A Magnetotelluric Survey in Methana Peninsula (Greece)

Theodora Volti

Doctor of Philosophy
University of Edinburgh

1996

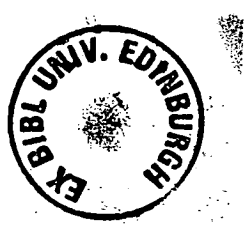

Declaration

I hereby declare that the work presented in this thesis has been composed by me unless otherwise stated in the text, and that has not been submitted for any other degree.

Theodora Volti

Acknowledgements

I wish to thank sincerely my supervisor Dr. R.J.Banks for his help and guidance throughout the course of this investigation, and his careful reading of the manuscript of this thesis. I also thank G.J.K. Dawes for his help in the fieldwork and in many technical aspects of this study, as well as to Dr. D. Livelybrooks for his assistance during the fieldwork and data processing.

I would like also to thank the members of the Department of Geophysics of Athens, particularly Dr. E. Lagios for initiating this project and my involvment with it, and Dr. A. Tzanis for his useful comments and his help during the fieldwork.

I am also grateful to the State Scholarship Foundation (SSF) of Greece of providing me financial support during my postgraduate studies.

By working the same period of time with Dr. O. Ritter and Dr. P. Ritter, I had the opportunity to exchange many ideas with them. I thanks particularly Dr. O. Ritter for many useful suggestions he made on my work.

I thank Prof. K.Whaler, Dr.B.Hobbs, Dr.I.Main, Dr.T.Danelian, Dr.D. Galanopoulos, D.Nascimento and G.Balasis for their advice in particular subjects of my work, all the members of the MT group, Dr.D.McKirdy and Dr. P.C.Jones for their help concerning the thin sheet modelling, and Dr.M.Ingham for his suggestions in the 2-D inversion.

S.Voss and I.Chisholm are thanked for their help concerning the computing facilities, without whom my thesis would never have come to an end.

G.J.K Dawes and his wife Alicia are also thanked for their hospitality which helped me a lot to settle into my new environment.

Above all I wish to thank my parents and my sister Valia who supported me in my difficult times. I thank also Robu, for providing me emotional support and his car during the last 3 months, and my cat PcPc for let me play with her whenever I was feeling tired.

Abstract

As a first deep geophysical survey, thirteen magnetotelluric (MT) and magnetovariation (MV) soundings in the period range 0.0085-6000 s have been carried out in the Methana Peninsula and Trizina area (Greece) which form a part of the active Hellenic Volcanic Arc (HVA). The intensity of artificial disturbances in Methana prevented the acquisition of good quality data, and led to the exclusion of data in the 10-100 s range from further interpretation.

The measured data are first processed using robust methods, then decomposed using the methods of Groom and Bailey and of Bahr. Thin sheet modelling follows with the aim of detecting effects due to the surrounding seas. All the data show anisotropy and were found to be distorted by galvanic distortion, facts which become more apparent at periods below 1 s. At these longer periods, effects from the sea also become important. The above problems indicated : (i) the insufficiency of 1-D modelling (ii) that the data are at least 2-D and (iii) that a careful consideration of all the above effects must be given in order to provide a meaningful electrical model.

The analysis of distortion effects and the measured induction arrows enable the determination of a regional azimuth to which subsequently the data are rotated. Seven sites are used, and a 2-D model is proposed. The model indicates a zone of high conductivity (7-32 ohm m) beneath the centre of the peninsula at a depth of 1-5 km, which is interpreted as being connected with the volcanic history of Methana, as a cooler remnant of former magmatic activity.

Although with the long period MT data it was not possible to locate a deep magma source connected with the indicated anomaly, induction arrows at $T > 2400$ s taken from the regional area point towards the South and South West, perpendicular to the strike of the well known deep structure of the Hellenic Volcanic Arc. Further attempts to integrate the results from Methana with other areas along the HVA lead to correlation of the regional azimuths with horizontal stress directions in the South Aegean sea.

TABLE OF CONTENTS

6. Inversion and modelling

LIST OF FIGURES

LIST OF TABLES

Chapter 1

Introduction

1.1 The magnetotelluric method of geophysical prospecting

Geophysical methods aim to infer the subsurface structure of the Earth by measuring fields at the Earth's surface which are due to certain physical properties. Electrical and electromagnetic (EM) methods, in particular, are based on remote measurements of the electrical conductivity. EM methods employ fields which are used to penetrate the Earth, giving in that way information about its subsurface in terms of electrical conductivity. One method uses natural electromagnetic fields, the magnetotelluric (MT) method. It is the method used in this work, in a small area of Greece (Methana), to infer its electrical substructure because of its geothermal interest.

The use of the natural electromagnetic (or magnetotelluric) field as a geophysical tool was first suggested by Tikhonov (1950), Rikitake (1950) and Cagniard (1953). The theory as well as the method have been further developed and described by, (among others), Wait (1962), Bostick and Smith (1962), Price (1962), Madden and Swift (1969) and Vozoff (1972).

With the MT method it is possible to determine the electrical conductivity distribution within the Earth's crust and upper mantle based on measured data at the Earth's surface. The technique consists of simultaneous measurements of the orthogonal components of the time-varying electric and magnetic fields at the Earth's surface. The period range used is restricted by the length of the recording time at one extreme, and the sampling rate at the other. For targets in the crust and possibly upper mantle, periods in the range 10^{-3}-10^{4} s are appropriate. In this way information is provided at a range of depths. The depth of penetration of the electromagnetic (EM) field depends on the frequency and the electrical conductivity of rocks; the lower the frequency and the conductivity, the greater the penetration.

In addition to the horizontal electric and magnetic fields, simultaneous recording of the 3 components of the magnetic field (geomagnetic variation or magnetovariation method) can provide a useful check on the MT method, and supply

additional information. For this reason the vertical magnetic field is usually recorded at the same time as the 4 horizontal components of the MT field.

1.2 Electrical conductivity and other rock parameters

The conductivity is a measure of the ease with which electrical currents can pass through a medium (i.e. rock) and is sensitive to a broad range of rock parameters. It can therefore be used to gain a better understanding of the subsurface lithology. A study of the electrical conductivity in rocks implies the knowledge of the mechanisms of electric conduction.

Electrical currents can flow mainly by three conduction mechanisms (Jacobs, 1989):

a. Metallic: Metals are the best electric conductors and with significant economic importance, but apart from the Earth's core, they are relatively rare in the crust and mantle.

b. Semiconduction: Carriers are electrons or "holes" which are thermally activated. Oxide and sulphide minerals fall into this category, but again they exist in deposits too small to be of global significance (possible exceptions can be serpentine and black shales). At normal temperatures most silicate minerals have very low conductivities.

c. Electrolytic: Rocks relatively close to the Earth's surface contain fluids which in their turn contain dissolved ionic salts. Conduction in the pore fluids is very common in the crust and a very important influence on Earth's conductivity.

d. Conduction due to diffusion of ions: Random movements of ions and "holes" due to porosity, saturation and permeability of the rocks.

Conductivity in Earth materials is controlled mainly by three parameters: water content, temperature and partial melting. In the uppermost crust, water content controls mainly the conduction mechanism, whereas temperature plays a most important role in regions of anomalous high heat flow or geothermal gradient. At great depths (> 100 km), high conductivities can be due to the partial melting of rocks. Temperature and partial melting are almost certainly the controlling factors under most of the ocean floor.

a. Upper crust

Most rocks at normal temperatures are generally poor conductors, having resistivity values up to 10^7 Ohm m. Without the fluids contained in pores within the

rock structure, the resistivities of most rocks would be considerably higher than they actually are. In the upper crust the rocks are porous and fractured which is favourable for water and fluid circulation. The governing conduction process is electrolytic. The main controlling parameter is porosity which may be intergranular (volcanic ash beds), in the form of joints (igneous rocks), or in the form of large irregular cavities (limestones and some volcanics). The conducting medium is an aqueous solution of common salts distributed through the pore structure of the rock. Therefore, the electrical behaviour of rocks at the surface is also determined by the concentration, interaction, charge number and mobility of ions in the solution as well as by the density, viscosity, dielectric constant, pressure and temperature of the water (Berktold, 1983). An empirical relationship was found by Archie (1942) which shows that the conductivity of porous, fluid bearing rocks can be predicted quite well using the empirical formula:

$$\sigma_r = \sigma_p \eta^m \qquad (1.1)$$

where σ_r is the overall conductivity of the rock, σ_p the conductivity of the pore fluid, η the porosity, and m a constant which depends on the texture of the rock. Typical values of m are in the range 1-2.

Sea water, which has a very high conductivity, can be encountered either in the form of small water intrusions near to the Earth's surface, or as sea water itself (see chapter 5). Attention must be paid in the interpretation of conductivity anomalies to the presence of sea water near measurement sites.

b. Lower crust

Archie 's Law is valid as long as water is the predominant factor for the electrical conductivity. As depth increases, porosity and permeability decrease as the increasing pressure reduces the pore space of the rocks, and cracks and fractures close by compaction. Some of the water is driven into hydration of the rock-forming minerals, and the remaining free water enters the vapour phase because of the higher temperature and pressure. Water content diminishes in general and the conductivity depends now primarily on ions of the solid matter which become the only carriers of the charges (semiconduction mechanism). The process of conduction through rocks follows an equation of the form (Tozer, 1959):

$$\sigma = \sum \sigma_i \exp(-E_i / kT) \qquad (1.2)$$

where σ is the conductivity of the rock at temperature T and k is Boltzmann's constant. The summation is over different semiconduction mechanisms in the rock, each with a different conductivity σ_i and activation energy E_i. Eq.1.2 suggests an increase of the conductivity with temperature.

The conductivity of major phases due to semiconduction is very low. As with the upper crust, the bulk σ is due to minor phases, possibly fluids, graphite or other minerals.

c. Upper mantle

Increasing temperature with depth has a definite effect on the conductivity. But apart from that, at great depths the melting of rocks in the asthenosphere can significantly increase the conductivity. For example, in laboratory tests, the conductivities of dry basalts are found to increase by 2-3 orders of magnitude on melting at 1200-1400^{0}C (Khitarov et al., 1970).

Conductivity anomalies are commonly found associated with subduction zones. One feature associated with subduction is the andesitic volcanism. The magma may come from partial melting of the subducted oceanic crust (Ringwood, 1975) and the shearing that takes place at the top of the descending plate may provide the heat required for partial melting and release of fluids. Nevertheless, one should not underestimate the influence of water in conductivity at depth, because with the subduction of sediments, substantial amounts of water can be transported to great depths (Scholl et al., 1977).

Table 1.1 summarises electrical conductivity values for the most common rock types found at the Earth's surface and at depth.

1.3 Geothermal systems and the MT method

The location of geothermal fields is normally associated with surface expressions such as volcanic activity, geysering, fumaroles and thermal springs. A classification aiming at including all possible types of geothermal systems has been created by Muffler (1976). According to him, geothermal systems can be broadly divided into the following categories:

1. Geothermal systems with convective heat transfer (natural fluid circulation)

a. Hydrothermal systems in environments of high porosity and permeability, related to shallow, young intrusions. This group is subdivided:

(i) vapour dominated systems (e.g. The Geysers, California; Landrello, Italy).

(ii) liquid dominated systems (e.g. Imperial Valley, California; New Zealand).

Rock type	Resistivity range (Ωm)
Granite	3×10^3–10^6
Granite porphyry	4.5×10^3 (wet)–1.3×10^4 (dry)
Feldspar porphyry	4×10^3 (wet)
Albite	3×10^2 (wet)–3.3×10^3 (dry)
Svenite	10^2–10^6
Diorite	10^4–10^5
Diorite porphyry	1.9×10^3 (wet)–2.8×10^4 (dry)
Porphyrite	$10–5 \times 10^4$ (wet)–3.3×10^2 (dry)
Carbonatized porphyry	2.5×10^3 (wet)–6×10^4 (dry)
Quartz porphyry	3×10^3–9×10^3
Quartz diorite	2×10^4–2×10^6 (wet)–1.8×10^5 (dry)
Porphyry (various)	60–10^4
Dacite	2×10^4 (wet)
Andesite	4.5×10^4 (wet)–1.7×10^2 (dry)
Diabase porphyry	10^3 (wet)–1.7×10^5 (dry)
Diabase (various)	$20–5 \times 10^7$
Lavas	10^3–5×10^4
Gabbro	10^3–10^6
Basalt	$10–1.3 \times 10^7$ (dry)
Olivine norite	10^3–6×10^4 (wet)
Peridotite	3×10^3 (wet)–6.5×10^3 (dry)
Hornfels	8×10^3 (wet)–6×10^7 (dry)
Schists (calcareous and mica)	20–10^4
Tuffs	2×10^3 (wet)–10^5 (dry)
Graphite schist	10–10^3
Slates (various)	6×10^2–4×10^7
Gneiss (various)	6.8×10^4 (wet)–3×10^6 (dry)
Marble	10^2–2.5×10^8 (dry)
Skarn	2.5×10^2 (wet)–2.5×10^8 (dry)
Quartzites (various)	$10–2 \times 10^8$

Rock type	Resistivity range (Ωm)
Consolidated shales	$20–2 \times 10^3$
Argillites	$10–8 \times 10^2$
Conglomerates	2×10^3–10^4
Sandstones	$1–6.4 \times 10^8$
Limestones	50–10^7
Dolomite	3.5×10^2–5×10^3
Unconsolidated wet clay	20
Marls	3–70
Clays	1–100
Alluvium and sands	10–800
Oil sands	4–800

Rock	% H_2O	ρ(Ωm)	Rock	% H_2O	ρ(Ωm)
Siltstone	0.54	1.5×10^4	Pyrophyllite	0.76	6×10^6
Siltstone	0.44	8.4×10^6	Pyrophyllite	0.72	5×10^7
Siltstone	0.38	5.6×10^8	Pyrophyllite	0.7	2×10^8
Coarse grain SS	0.39	9.6×10^3	Pyrophyllite	0	10^{11}
Coarse grain SS	0.18	10^6	Granite	0.31	4.4×10^3
Medium grain SS	1.0	4.2×10^3	Granite	0.19	1.8×10^6
Medium grain SS	1.67	3.2×10^6	Granite	0.06	1.3×10^8
Medium grain SS	0.1	1.4×10^8	Granite	0	10^{10}
Graywacke SS	1.16	4.7×10^2	Diorite	0.02	5.8×10^3
Graywacke SS	0.45	5.8×10^4	Diorite	0	6×10^8
Arkosic SS	1.26	10^3	Basalt	0.95	4×10^4
Arkosic SS	1.0	1.4×10^3	Basalt	0.49	9×10^4
Organic limestone	11	0.6×10^3	Basalt	0.26	3×10^7
Dolomite	2	5.3×10^3	Basalt	0	1.3×10^8
Dolomite	1.3	6×10^3	Olivine-pyrox.	0.028	2×10^4
Dolomite	0.96	8×10^3	Olivine-pyrox.	0.014	4×10^4
Peridotite	0.1	3×10^3	Olivine-pyrox.	0	5.6×10^7
Peridotite	0.03	2×10^4			
Peridotite	0.016	10^6			
Peridotite	0	1.8×10^7			

Table 1.1: Resistivity ranges for different rock types (From Telford et al., 1976).

b. Circulation systems in environments of low porosity but sufficient fracture permeability for water circulation (deep circulation of meteoric waters in fault and fracture zones).

2. Geothermal systems with conductive heat transfer

a. Low temperature aquifers ($T<150^0C$) in environments of high porosity and permeability (e.g. in deeper parts of sedimentary basins).

b. "Hot Dry Rock" (high temperature, low natural porosity and permeability, e.g. Carnmenellis granite).

The capacity of the rocks to transmit heat by convection in the formation water is generally higher than that by conduction through the rocks. Shallow young intrusions associated with high porosity and permeability include almost all geothermal systems which have been developed for electrical power production.

There are certain geological conditions favourable for a geothermal field to exist, which must be examined. According to Facca and Tonani (1962) the following formations must be present:

a. A sequence of layers heated by an underlying magmatic stock (magma source) which in turn heats the overlying strata.

b. A strongly permeable layer with thickness, porosity and permeability of such an order as to allow the formation and permanence of a system of convection currents in the water filling the pores of the rock (reservoir).

c. An impermeable layer overlying the reservoir (caprock), with low permeability in order to prevent the escape of the hot water out of the reservoir.

A model for an ideal geothermal field is shown in fig.1.1:

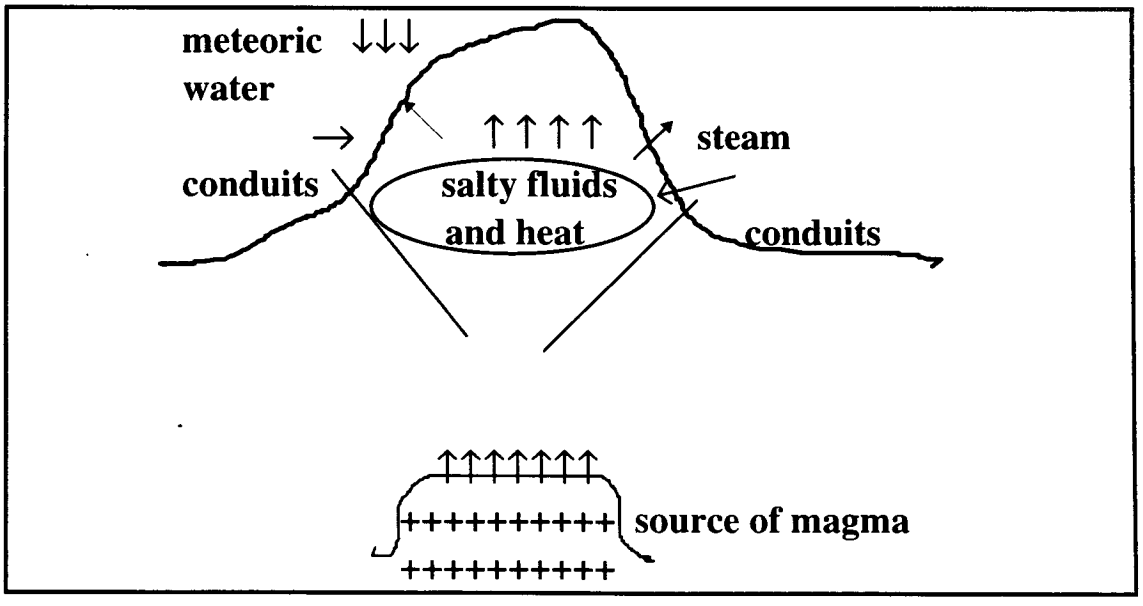

Fig.1.1: An idealised model of a geothermal field

In fig.1.1 the layered structure has been omitted, and only the magma source situated at depth and the reservoir at shallower depth are shown. The reservoir, which is composed of permeable rocks (for example limestone), is filled with salty fluids and heated up by the source underneath. Cracks, conduits and faults are the means by which hot material coming from the source is directed upwards, creating in this way surface manifestations of the hot fluids (or steam) which are present in many geothermal areas. Meteoric waters replenish the aquifer and maintain a permanent circulation inside the reservoir.

The MT method, as well as all electrical and EM methods, is suitable for geothermal exploration because the physical parameter to be measured (i.e. the electrical conductivity) is strongly temperature-dependent (Keller et al., 1974) and sensitive to the presence of fluids. The advantage of the MT method is that the natural EM field is rich in the needed low frequencies ($f < 0.1$ Hz), avoiding the cost and effort involved in generating a powerful artificial field. These low frequencies provide a penetration depth of a few km to a few tens of km into the Earth, so that the resistivity of rocks at depth, where temperatures near the melting point might be encountered, can be tested.

The MT method has been widely used for geothermal prospecting around the world. Table 1.2 summarises some of the MT surveys that have been successfully applied to some geothermal areas apart from Greece, where the MT method has been applied continuously in recent years.

ITALY	Travale Landarello	Celati et al. (1973) Haak and Schwarz (1980)
GERMANY		Berktold et al. (1980) Richards et. al (1980)
ICELAND		Hersir et al. (1984) Hermance et al. (1974)
Reunion island		Benderitter et al. (1984)
U.S.A	Oregon Long valley caldera	Long et al. (1980) Wannamaker et al. (1991) Park et al. (1988)

Table 1.2: Geothermal surveys around the world.

1.4 Aim of this thesis

The purpose of the present thesis is the application of the MT method in a small volcanic area in Greece, the so-called Methana Peninsula, which is part of the geologically active South Aegean sea, and comprises the western end of the Hellenic Volcanic Arc. As no geophysical work aiming to investigate the deep electrical structure has been undertaken before, the present MT survey hopes to throw some light on the electrical subsurface structure of this area. The 4 subsidiary aims of this work can be listed as follows:

1. By using short period measurements (AMT), to provide some information about the shallow structure which may be connected with the volcanic history of the area.

2. By using long period measurements (LMT), to attempt an interpretation of the deeper structure.

3. To examine the possible effect that the sea around the peninsula may have on the results.

4. To compare the outcome with already existing results from other areas along the same belt.

In the next chapter the essential theory underlying the MT method will be given. In chapter 3 the study area will be described, together with the method as it has been applied in the field. Chapter 4 deals with the analysis of the data obtained from the fieldwork. In chapter 5 further analysis of the data is made, to investigate the distortion due to 3-D inhomogeneities, particularly the sea effect. In chapter 6 inversion and modelling of the data are presented, resulting in a final 2-D model. Finally, in the last chapter, results from Methana are compared with those from other volcanic islands along the arc, in order to: (i) assess the importance of conductivity anomalies for Methana in comparison with the other areas and (ii) supply some information about the electrical structure of the regional area of which Methana Peninsula forms a part (i.e. the Hellenic Volcanic Arc and the South Aegean sea).

Chapter 2

The magnetotelluric method

2.1 Origin of the natural electromagnetic field

The sources of the EM variations which are considered are located outside the Earth. In order to study the conductivity of the Earth by using the natural EM field, one needs to know the variations of the natural field. According to Rokityansky (1982), the EM field variations are classified:

1. Regular daily variations (T between 0.2 s and 1 day).
2. Disturbances including magnetic storms (T between 1 hour and 11 years).
3. Pulsations (Pc1-Pc5) ($0.2 < T < 1000$ s).
4. Atmospherics (ELF) ($0.2 < T < 10^{-5}$ s).

For MT purposes variations in the 3 last groups are considered. More specifically:

At T>0.2 s, there are variations in the Earth's magnetic field caused by interactions of the Earth's permanent magnetic field with the flow of plasma (solar wind) which is directed towards the Earth. The charged particles from the Sun interact with the Earth's main magnetic field and the ionosphere. On their way towards the Earth, they are deflected and set up current systems which in their turn induce secondary magnetic fields according to Ampere's law. These fields cancel the effect of the Earth's main field at the magnetosphere's boundary known as the magnetopause. The interactions result in time-varying magnetic fields at the Earth's surface which are the source for the MT method or the so-called "primary field". The primary field diffuses within the Earth and induces electric currents, according to Faraday's law. The induced electric currents have associated magnetic fields, which appear with the primary magnetic field at the surface of the Earth and are superimposed on it.

At T<0.2 s, thunderstorm activity (lightning strokes) occurring in the Earth-ionosphere cavity, are the cause of the EM field variations. The EM fields generated by a lightning stroke (atmospherics) travel around the Earth trapped in a wave guide. They are large amplitude broad frequency band EM waves, which produce a number of peaks (at 8, 14, 20, and 25 Hz), known as the Schumann frequencies which are

determined by the properties of the waveguide. Fig.2.1 shows samples of the atmospherics recorded in the Schumann resonance range.

Atmospherics depend strongly on the distance from the storm location. If they occur close to the measuring site, they can saturate the recording system amplifiers and generally fail to produce an acceptable MT signal. Atmospherics from very distant thundershowers provide a spatially uniform source of noise. There are 3 storm centres in the equatorial regions - Brazil, Central Africa and Malaya - with an average of 100 storm days per year.

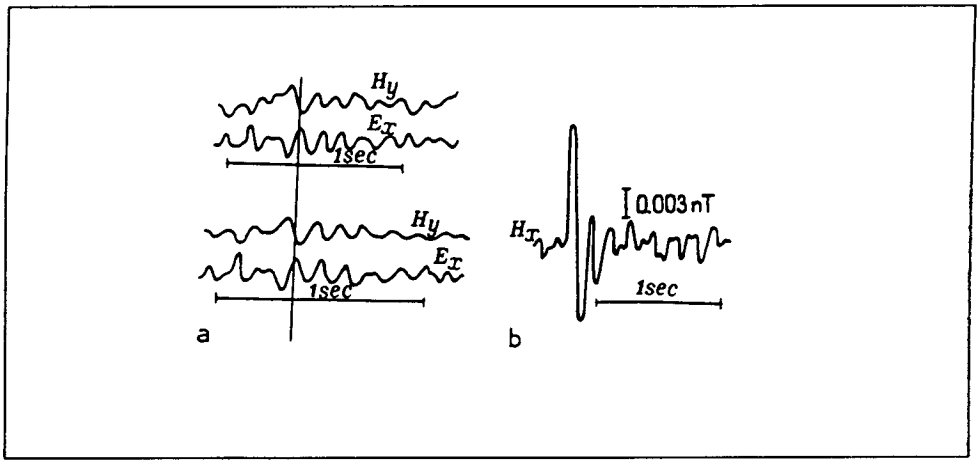

Fig.2.1: Samples of the atmospheric records a: in a remote zone of the source. Simultaneous records at two points 70 km apart. b. remote source field is superposed by a signal from nearby lightning discharge (Krylov, 1971).

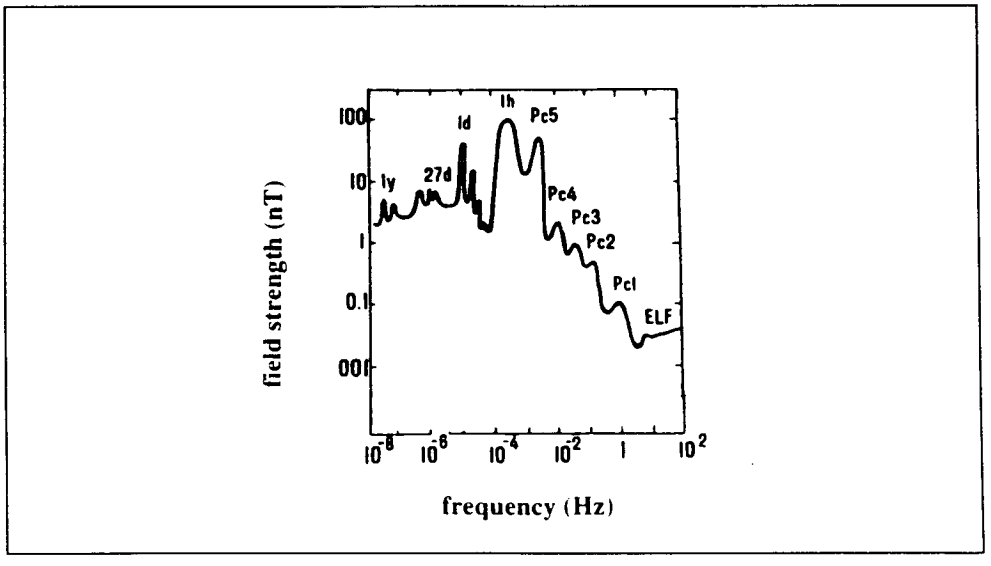

Fig.2.2: Typical amplitudes of natural variations in the geomagnetic field. **d**: day, **h**: hour, **Pc1-Pc5**: pulsations, **ELF**: atmospherics (from Serson, 1973).

An amplitude spectrum for geomagnetic variations including atmospherics at the highest frequency end of it, is shown in fig.2.2. It is noticeable that the magnetic field strength is higher in the lower frequencies, and low at $f>10^{-2}$ Hz.

2.2 Maxwell's equations

The propagation and attenuation of EM waves inside the Earth is based on Maxwell's theory of EM induction, through the fundamental equations:

$$\text{curl}\mathbf{E} = -\frac{\partial \mathbf{B}}{\partial t} \qquad (2.1)$$

$$\text{curl}\mathbf{H} = \mathbf{J} + \frac{\partial \mathbf{D}}{\partial t} \qquad (2.2)$$

$$\text{div}\mathbf{B} = 0 \qquad (2.3)$$

$$\text{div}\mathbf{D} = \rho' \qquad (2.4)$$

where **E** is the electric field intensity (Volt/m)
H is the magnetic field intensity (Ampere/m)
B is the magnetic flux density (Weber/m^2)
J is the current density (Ampere/m^2)
D is the dielectric displacement (Coulomb/m^2) and
ρ' is the electric charge density (Coulomb/m^3)

Faraday's law (eq.2.1) deals with the production of electric fields by changes in magnetic fields. Ampere's law (eq.2.2) shows that if an electric current already flows, a magnetic field will be associated with it which is proportional to the total current flowing. Eqs.2.3 and 2.4 state that in the case of a magnetic field, flux never diverges from a point source, but charge can accumulate during current flow. The relation between the magnetic and electric components of a typical plane EM wave is shown schematically in fig.2.3.

Three more equations relate the above quantities:

$$\mathbf{D}=\varepsilon\mathbf{E} \quad \mathbf{B}=\mu\mathbf{H} \quad \mathbf{J}=\sigma\mathbf{E} \qquad (2.5)$$

where ε : dielectric permittivity (Farad/m)
μ: magnetic permeability (Henry/m)
σ: electrical conductivity (S/m)

Except for ferromagnetic materials, in the Earth μ is usually taken equal to $\mu_0 = 4\pi x10^{-7}$ (H/M) (its value in free space). The dielectric constant of free space is $\varepsilon_0=8.85x10^{-12}$ and its value in the Earth varies from approximately $9\varepsilon_0$ to

$80\varepsilon_0$ in sea water. But the most important parameter in MT prospecting is the conductivity σ (or its reciprocal, resistivity which can vary from less than 1 up to 10^7 Ohm m, table 1.1).

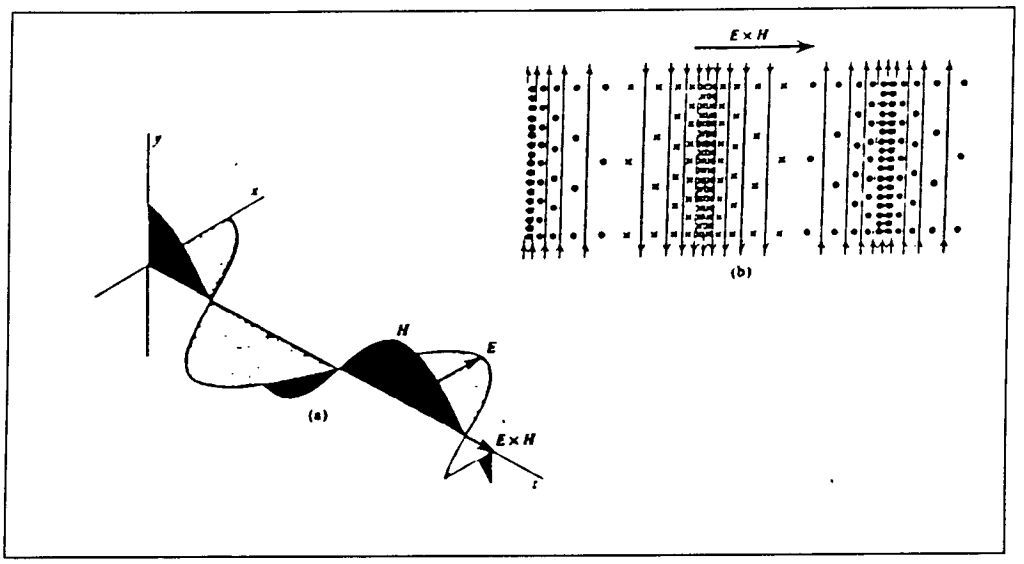

Fig.2.3: A plane EM wave travelling in the positive direction along the z-axis. (a) The magnetic (**H**) and electric (**E**) vectors are in phase but perpendicular to each other. (b) The corresponding lines of force as seen from the xz plane. The lines represent the electric field. **dots:** magnetic lines of force coming out of the paper. **crosses:** magnetic lines of force going into the paper. The vector **E x H** gives the direction of propagation (Lorrain and Corson, 1970).

In eq.2.2 the second term represents the total current present, conduction and displacement. The ratio between these two types of current is $\frac{\partial \mathbf{D}/\partial t}{\mathbf{J}} = \frac{\varepsilon / T}{\sigma} \approx \frac{10^{-11}\rho}{T}$ where T is the period of oscillation and ρ ($=1/\sigma$) the resistivity. Periods used in MT soundings vary from 10^{-2}-10^4 s. Taking into account also the range of resistivities in Earth materials, it is obvious that displacement currents can be neglected for MT purposes. Also, charge does not accumulate during current flow in a uniform conductive Earth and eq.2.4 becomes div**D** = 0.

Thus, Maxwell's equations simplify to the form:

$$\text{curl}\mathbf{E} = -\frac{\partial \mathbf{B}}{\partial t} \qquad (2.6)$$

$$\text{curl}\mathbf{H} = \mathbf{J} \qquad (2.7)$$

$$\text{div}\mathbf{B} = 0 \qquad (2.8)$$

$$\text{div}\mathbf{D} = 0 \qquad (2.9)$$

From eqs. 2.6, 2.7 and 2.8, using the vector identity $\mathrm{curl}(\mathrm{curl}\mathbf{E}) = \mathrm{grad}(\mathrm{div}\mathbf{E}) - \nabla^2\mathbf{E}$, and since $\mathrm{div}\mathbf{E} = (\mathrm{div}\mathbf{D}/\varepsilon_0) = 0$ we have:

$$\mathrm{curl}(\mathrm{curl}\mathbf{E}) = -\frac{\partial}{\partial t}\mathrm{curl}\mathbf{B} = -\mu_0\sigma\frac{\partial \mathbf{E}}{\partial t} = -\nabla^2\mathbf{E} \Rightarrow \nabla^2\mathbf{E} = \mu_0\sigma\frac{\partial \mathbf{E}}{\partial t} \qquad (2.10)$$

Assuming variations of the form $E(t) = E_0 e^{-i\omega t}$ the frequency domain equivalent of (2.10) is: $\nabla^2\mathbf{E} = -i\omega\mu_0\sigma\mathbf{E}$ (2.11)

A similar equation can be obtained for the magnetic field:

$$\nabla^2\mathbf{H} = -i\omega\mu_0\sigma\mathbf{H} \qquad (2.12)$$

Eqs.2.11 and 2.12 are diffusion equations for the electric and magnetic field vectors, respectively, inside the Earth.

In the air or in very poorly conductive mediums ($\sigma \approx 0$), the above equations simply reduce to the Laplace' equation:

$\nabla^2\mathbf{H} = 0$ and $\nabla^2\mathbf{E} = 0$ (2.13)

This shows that while in the air the EM field propagates without attenuation, in the conductive Earth the energy is absorbed by the rocks, and the induced electric currents dissipate.

2.2.1 Boundary conditions and further assumptions

Eqs.2.11 and 2.12 are valid as long as the Earth is considered homogeneous. But this is far from the case normally, and it is often assumed for convenience that σ, ε and μ are uniform everywhere except at boundaries. This would break the validity of the equations, unless continuity conditions are applied to the vector quantities at the interface:

1. The tangential components of **E** and **H** are required to be continuous on the interface separating the two media.

2. The normal components of **J** and **B** are required to be continuous across the boundary.

3. The general mathematical description of the phenomenon (Cagniard, 1953) requires that the primary field is a plane wave propagating vertically towards the Earth, which is true only when the source field is far from the area of observation (i.e. the distance of the source is large compared with the penetration depth).

Two more assumptions are also necessary for the mathematical treatment to be tractable:

1. For the frequency range used for MT prospecting (>10^{-4} Hz), the influence of the curvature of the Earth can be neglected ($\delta << E_{radius}$), where δ is the skindepth and E_{radius} the radius of the Earth.

2. The Earth is a passive system which can only absorb or dissipate the EM energy.

2.3 Electromagnetic induction in a homogeneous Earth

A simple Earth model is considered in which the conductivity is a function only of depth, i.e. $\sigma = f(z)$ i.e. the Earth is homogeneous and horizontally layered. Maxwell's eq.2.6 for the two electric field components simplifies to:

$$\frac{\partial E_x}{\partial z} = -i\omega\mu_0 H_y \quad \text{and} \quad \frac{\partial E_y}{\partial z} = -i\omega\mu_0 H_x \tag{2.14}$$

Eq.2.11 also simplifies to the form:

$$\frac{\partial^2 \mathbf{E_x}}{\partial z^2} + i\omega\mu\sigma \mathbf{E_x} = 0 \tag{2.15}$$

Similar expressions can be found for the magnetic field from eqs.2.7 and 2.12.

A general solution to eq.2.15 is $E_x = E_0 e^{kz}$ (2.16)

where E_0 is the surface value of the electric field and

$$k = \pm\sqrt{i\omega\mu_0\sigma} \tag{2.17}$$

is referred as the propagation constant or wavenumber.

By substitution of the mathematical equivalent of $\sqrt{i}$ with $e^{i\pi/4}$, eq.2.17 becomes:

$$k = \pm\sqrt{\frac{\omega\mu_0\sigma}{2}}(1+i) \tag{2.18}$$

A very useful factor derived from eq.2.18 is the "skin depth" which is defined as the depth in a uniform Earth at which the field is reduced to 1/e of its original value at the surface:

$$\delta = \sqrt{\frac{2}{\omega\mu_0\sigma}} \tag{2.19}$$

In practice

$$\delta \approx 500\sqrt{\frac{\rho}{f}} \tag{2.20}$$

where ρ is the resistivity ($\rho = 1/\sigma$) expressed in Ohm m and f the frequency (Hz). The penetration depth is inversely proportional to the square root of the frequency of the signal, and so investigation using relatively low frequencies is needed in order to obtain information about the deep Earth.

From eqs.2.16 and 2.18 it can be seen:

$$E_x = E_0 e^{-az(1+i)} \tag{2.21}$$

where

$$a = \sqrt{\frac{\omega\mu_0\sigma}{2}} \tag{2.22}$$

and from eqs.2.21, 2.14 and $(\partial/\partial t = -i\omega)$, the identity:

$$\frac{\partial E_x}{\partial z} = \frac{\partial}{\partial z}(E_0 e^{-az(1+i)}) = -a(1+i)E_x = -i\omega\mu_0 H_y \qquad (2.23)$$

The last two terms of eq.2.23 provide a very useful expression for the ratio $E_x/H_y = Z$, where Z is defined as the impedance.

2.4 Electromagnetic induction in 2-D structures

2-D models seem to be a better approximation to the real heterogeneous Earth because lateral inhomogeneities in one direction are allowed, i.e. $\sigma = f(x,z)$ where we have y be the horizontal direction in which the electrical conductivity remains constant (strike direction). Considering that the variation occurs in the x and z directions, eqs.2.6 and 2.7 can be expressed in terms of the field components:

$$-\frac{\partial H_y}{\partial z} = \sigma E_x \qquad (2.24)$$

$$\frac{\partial H_y}{\partial x} = \sigma E_z \qquad (2.25)$$

$$\frac{\partial E_x}{\partial z} - \frac{\partial E_z}{\partial x} = i\omega\mu H_y \qquad (2.26)$$

$$\frac{\partial H_x}{\partial z} - \frac{\partial H_z}{\partial x} = \sigma E_y \qquad (2.27)$$

$$-\frac{\partial E_y}{\partial z} = i\omega\mu H_x \qquad (2.28)$$

$$\frac{\partial E_y}{\partial x} = i\omega\mu H_z \qquad (2.29)$$

By combining eqs.2.24, 2.25 and 2.26 on one hand, and eqs.2.27, 2.28 and 2.29 on the other, we arrive at the following second order differential equations:

$$\frac{\partial^2 E_y}{\partial x^2} + \frac{\partial^2 E_y}{\partial z^2} = i\omega\mu\sigma E_y \qquad (2.30)$$

$$\frac{\partial^2 H_y}{\partial x^2} + \frac{\partial^2 H_y}{\partial z^2} = i\omega\mu\sigma H_y \qquad (2.31)$$

These two equations represent two different modes of EM induction. In the first case, the transverse electric mode (TE), the electric field is polarised parallel to the strike of the structure, whereas the magnetic field is perpendicular to the structure. In the second case, the transverse magnetic mode (TM), the magnetic field is polarised parallel to the strike. The TE mode comprises electric fields (currents) parallel to strike, while in the TM mode the electric fields are perpendicular to strike. In the absence of noise (section 3.3.5), the TM mode may be more complicated due to the electric charge distributions (section 5.2) arising whenever the electric field crosses boundaries of different electrical conductivity.

Analytical solutions cannot be obtained for eqs.2.29 and 2.30 in general, but only for some specialised cases.

In a 3-D Earth, the conductivity changes along three Cartesian coordinates, i.e. $\sigma = f(x,y,z)$. In this case no strike direction exists and there is always some surface

exposed to charge accumulation. There are no further simplifications of Maxwell's equations.

2.5 Impedances for conductivity models

2.5.1 One dimensional models

With the Earth considered as a linear system, a change in the time-varying magnetic field results in induced electric currents which flow inside the Earth. What is important in the MT method, is the Earth's response to these variations (i.e. the measurements). The MT method starts with the definition of the response of a 1-D Earth model or impedance Z as the ratio of one horizontal component of the electric field (E_x) to its perpendicular component of the magnetic field (H_y) measured at the Earth's surface :

$$Z = \frac{E_x}{H_y} \quad \text{or} \quad E_x = ZH_y \tag{2.32}$$

where the pair (E_x, H_y) is equivalent to the pair (E_y, H_x) and leads to the same absolute impedance value.

This is the definition of impedance as first proposed by Cagniard (1953), and applies to the ideal case of a plane wave incident on a homogeneous and isotropic Earth. Eq.2.32 states that the electric field in one direction, say E_x is linearly related to the orthogonal magnetic field H_y. The ratio E/H is independent of the direction of the coordinate axes and of position, and the horizontal fields are always at right angles to each other. The impedance is a complex scalar quantity and its value as a function of frequency is characteristic of the properties of the medium.

Rearranging the two last terms of eq.2.23 gives:

$$\frac{E_x}{H_y} = \frac{i\omega\mu_0}{a(1+i)} \tag{2.33}$$

From eqs.2.32 and 2.22 one has:

$$Z = \frac{E_x}{H_y} = \sqrt{\frac{\omega}{\mu_0\sigma}}e^{-i\pi/4} \tag{2.34}$$

In the above definition the impedance is measured in Ohms. Eq.2.34 shows that Z is a complex number which can be expressed in terms of its magnitude and phase. The magnitude is directly related to the conductivity (or resistivity) of the rocks which the EM fields penetrate. For a halfspace there is a 45^0 phase difference between the oscillating electric and magnetic fields.

Rather than working directly with the impedance elements, two useful functions derived from eq. 2.34 are often preferred:

the apparent resistivity ρ_a :

$$\rho_\alpha = \frac{1}{\omega\mu_0}|Z|^2 \qquad (2.35)$$

and the phase difference between the electric and the magnetic fields

$$\phi = \tan^{-1}(\mathrm{Im}(Z)/\mathrm{Re}(Z)) \qquad (2.36)$$

The apparent resistivity (Ohm m) of a halfspace is the true halfspace resistivity. For a 1-D structure $\rho(z)$, $\rho_a(f)$ is a function related to $\rho(z)$. A well known rule of thumb (Fischer, 1985, 1992) states that for a two-layer structure $\phi>45^0$ if the lower layer is a better conductor, whereas the condition $\phi<45^0$ reveals a poorer conductor at depth. Apparent resistivity and phase are widely used in the interpretation of MT data.

2.5.2 Two dimensional models

When lateral inhomogeneities in rocks' resistivity occur, the total electric field measured at the Earth's surface is linearly dependent on both components of the horizontal magnetic field. The electric field is generally not perpendicular to the magnetic field and the impedance depends on both the orientation of the coordinate system and the position. This happens because around an inhomogeneous Earth the induced currents are polarised arbitrarily with respect to the incident fields. In the frequency domain the equations which describe the linear relationship between the EM field components are as follows:

$$E_x = Z_{xx}H_x + Z_{xy}H_y \qquad (2.37)$$

$$E_y = Z_{yx}H_x + Z_{yy}H_y \qquad (2.38)$$

or in matrix form:

$$\begin{bmatrix} E_x \\ E_y \end{bmatrix} = \begin{bmatrix} Z_{xx} & Z_{xy} \\ Z_{yx} & Z_{yy} \end{bmatrix} \begin{bmatrix} H_x \\ H_y \end{bmatrix} \text{ or } \mathbf{E=ZH} \qquad (2.39)$$

Here $\mathbf{Z} = \begin{bmatrix} Z_{xx} & Z_{xy} \\ Z_{yx} & Z_{yy} \end{bmatrix}$ is the impedance tensor. It contains 4 complex elements.

Eq.2.39 is the general form of eq.2.32 which has been introduced by Cantwell (1960) and Rokitiansky (1961) and accounts for the lateral inhomogeneities in an heterogeneous Earth. The diagonal elements Z_{xx} and Z_{yy} generally show the presence of lateral effects. All the impedance elements are complex numbers and frequency dependent.

In a 1-D case where no lateral effects exist, $Z_{xx} = Z_{yy} = 0$, $Z_{xy} = -Z_{yx} = Z$ and eq.2.39 reduces to the form of eq.2.32.

In 2-D and 3-D cases all the elements of the impedance tensor are in general no-zero. However, for 2-D structures simplifications can be made because the elements of the impedance tensor vary as the measuring axes are rotated with respect to the electrical strike. A coordinate system in which one axis coincides with the strike direction would result in zero diagonal elements, while the off-diagonal elements are unequal ($Z_{xy} \neq Z_{yx}$) and correspond to TE and TM modes respectively.

$$\begin{bmatrix} E_x \\ E_y \end{bmatrix} = \begin{bmatrix} 0 & Z_{xy} \\ Z_{yx} & 0 \end{bmatrix} \begin{bmatrix} H_x \\ H_y \end{bmatrix} \tag{2.40}$$

The tensor can be rotated to any direction θ using the transformation:

$$\mathbf{Z'} = \mathbf{R}\,\mathbf{Z}\,\mathbf{R}^{T} \tag{2.41}$$

where $\mathbf{Z'}$ is the new rotated impedance tensor and $\mathbf{R} = \begin{bmatrix} \cos\theta & \sin\theta \\ -\sin\theta & \cos\theta \end{bmatrix}$ is the rotation tensor. Each element of $\mathbf{Z'}$ can be expressed in terms of elements of the unrotated tensor:

$$Z'_{xx} = 1/2\{Z_{xx} + Z_{yy} + (Z_{xx} - Z_{yy})\cos 2\theta + (Z_{xy} + Z_{yx})\sin 2\theta\} \tag{2.42a}$$

$$Z'_{xy} = 1/2\{Z_{xy} - Z_{yx} + (Z_{xy} + Z_{yx})\cos 2\theta - (Z_{xx} - Z_{yy})\sin 2\theta\} \tag{2.42b}$$

$$Z'_{yx} = 1/2\{-Z_{xy} + Z_{yx} + (Z_{xy} + Z_{yx})\cos 2\theta - (Z_{xx} - Z_{yy})\sin 2\theta\} \tag{2.42c}$$

$$Z'_{yy} = 1/2\{Z_{xx} + Z_{yy} - (Z_{xx} - Z_{yy})\cos 2\theta - (Z_{xy} + Z_{yx})\sin 2\theta\} \tag{2.42d}$$

One approach which has been chosen for the interpretation of measured tensors is to find a rotation angle for which the tensor is as close as possible to the 2-D form. Swift (1967) proposed the maximisation of $|Z'_{xy}|^2 + |Z'_{yx}|^2$, leading to a rotation angle θ′ given by:

$$\tan 4\theta = \frac{Z_1 Z_2^* + Z_1^* Z_2}{Z_1 Z_1^* - Z_2 Z_2^*} \tag{2.43}$$

where $Z_1 = Z_{xx} - Z_{yy}$, $Z_2 = Z_{xy} + Z_{yx}$ and * means the complex conjugate.

If the rotation angle θ′ is applied, then Z'_{xy} and Z'_{yx} are the maximum and minimum ("principal") impedance estimates respectively. Attention must be paid to the fact that two angles with a difference of 90^0 one from the other can satisfy eq.2.43. Additional information will be needed in order to decide which angle may represent the true strike.

2.5.3 Three dimensional models

As was mentioned before, the secondary or anomalous EM fields induced around a 3-D body may be polarised arbitrarily with respect to the incident fields. Therefore,

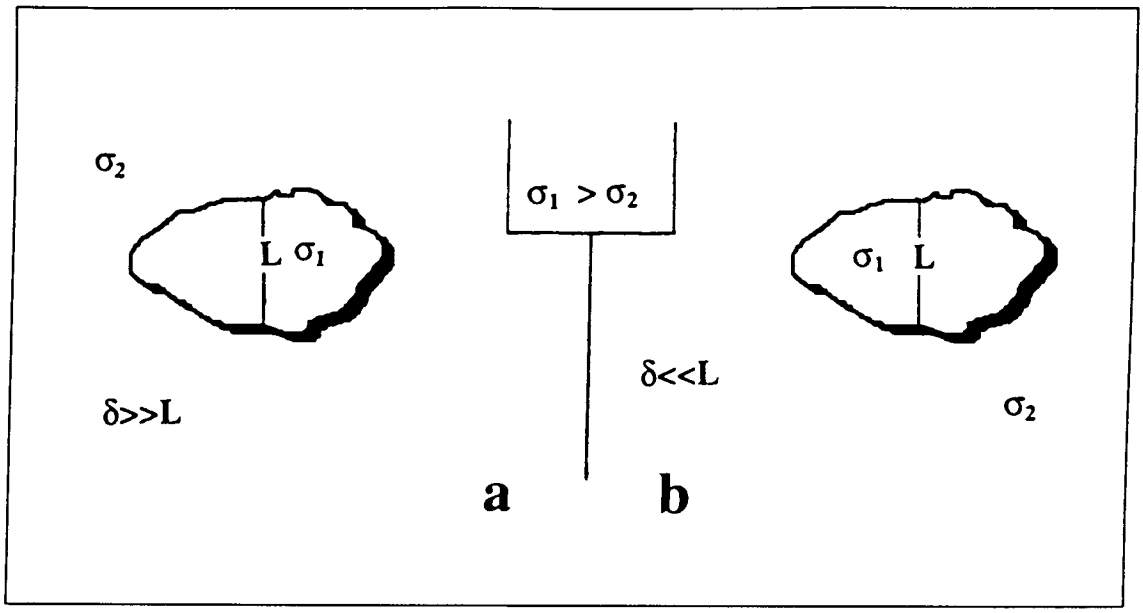

Fig.2.4: A 3-D body embedded in a larger structure **a.** Galvanic effect **b.** Inductive effect.

the relation between the total electric and magnetic fields measured at the Earth's surface must be the full expression of eq.2.39, without further simplifications.

A description of the complex processes in the neighbourhood of a 3-D body is given by Berdichevsky et al. (1973) who classifies the problem into two major effects, namely galvanic and inductive. The difference between these two effects depends mainly on frequency (which in its turn controls the skin depth), and the dimensions of the 3-D local body. In fig.2.4 a 3-D body (delineated structure) of conductivity σ_1 is embedded in a larger (regional) body of conductivity σ_2, where $\sigma_1>\sigma_2$, δ is the skin depth and L a measure of the dimensions of the 3-D local body.

In the first case (fig.2.4a), the skin depth is much larger than the dimensions of the body. The 3-D conductive body is considered only as a local effect which distorts the true (regional) conductivity (galvanic effect).

In fig.2.4b, the depth of penetration is very small compared with the dimensions of the body. In that case, induction inside the body occurs and no information is possible from the regional area (inductive effect or local induction).

Galvanic distortions do not affect the phase observations, but only the apparent resistivity responses. On the contrary, inductive distortion produces a frequency dependent distortion of both apparent resistivity and phase functions. The galvanic effect and associated static shift will be further discussed in chapter 5.

There are two kinds of 3-D modelling procedures:

a. Those using a 3-D body embedded in an otherwise homogeneous Earth or a layered halfspace (Ting et al, 1981; Hohmann, 1983).

b. Those using the thin sheet approximation, where the inhomogeneity is confined to a thin sheet at the surface (Dawson et al., 1979; Vasseur et al., 1977). They are mainly used to study the effect of conductivity contrasts between the land and the sea or contrasts due to conductive sediments.

2.5.4 Dimensionality indicators

Very often it is useful to have an indication of the complexity of the data, to indicate which of the 3 cases (1-D, 2-D or 3-D) they are likely to represent. A possible indicator of the "dimensionality" of the data is the skew defined by Swift (1967):

$$S = \left| \frac{Z_{xx} + Z_{yy}}{Z_{xy} - Z_{yx}} \right| \qquad (2.44)$$

Skew is a rotationally invariant parameter as we can see from eq.2.41 (the quantities $Z_{xx} + Z_{yy}$ and $Z_{xy} - Z_{yx}$ are independent of θ). For 1-D and 2-D structures, S=0, while S>0 indicates the presence of 3-D effects. For a meaninful 2-D interpretation to be conducted, S should not be above 0.3 (Swift, 1967).

Dealing with real data, care should be taken in the following situations:

a. When the structure is 1-D, the diagonal terms should vanish. However, measuring noise can affect the results and S is almost never exactly zero.

b. In a 2-D situation the diagonal elements exist unless rotation of the impedance tensor is applied. If the resistivity contrast across strike is low, i.e. $|Z_{xy} - Z_{yx}| \cong 0$ the skew can be large even for a structure which is "almost 2-D".

More recent estimates of skew, less affected by galvanic distortion are discussed in chapter 5.

In order to minimise 2-D and 3-D effects, an approach based on average values was introduced by Berdichevsky and Dmitriev (1976) who suggested the following rotationally invariant elements:

The arithmetic or Berdichevsky average:

$$Z_{berd} = 0.5(Z_{xy} - Z_{yx}) \qquad (2.45)$$

and the effective impedance:

$$Z_{eff} = (Z_{xx}Z_{yy} - Z_{xy}Z_{yx})^{1/2} \qquad (2.46)$$

Averaging two different modes of induction will not always give an accurate representation, especially if the XY and YX components of Z differ considerably from each other.

2.6 The vertical magnetic field

As was mentioned in the introduction, the magnetovariation method (MV) can be used simultaneously with the MT method in order to control or provide additional information about the conductivity structure of the subsurface, as it has been proved that the vertical magnetic field is particularly sensitive to lateral variations in conductivity. In the frequency domain, a linear relationship exists between the vertical H_z and the two horizontal (H_x and H_y) components of the magnetic field (Parkinson, 1962):

$$H_z = AH_x + BH_y \tag{2.47}$$

The quantities A and B are complex, with $A=A_R+iA_I$ and $B=B_R+iB_I$ .They can be combined to form the 2-D vector (A, B) called the "induction arrow" or the "Tipper".

The real parts of A and B and the imaginary parts of A and B may be combined to form the induction vectors $\pm(A_R, B_R)$ and (A_I, B_I) respectively, which can be represented as arrows on a geographic map. Their magnitude and azimuth are defined by the relationships:

$$|R| = (A_R^2 + B_R^2)^{1/2}, \quad \theta_R = \tan^{-1}\frac{B_R}{A_R} \tag{2.48}$$

$$|I| = (A_I^2 + B_I^2)^{1/2}, \quad \theta_I = \tan^{-1}\frac{B_I}{A_I} \tag{2.49}$$

where $|R|$, θ_R, $|I|$ and θ_I are the magnitude and angle of the real and imaginary parts of the vector respectively.

Attention must be paid on the sign of the real vector (A_R, B_R). The (+) vector (Wiese convention) tends to point away from areas of high conductivity, whereas the (-) vector (Parkinson convention) tends to point towards areas of high conductivity. In the next chapters, the Parkinson convention will be adopted.

A number of points should be mentioned for a meaningful interpretation of the induction arrows to be conducted:

(i) Unless the external field is non-uniform, in 1-D cases there is no vertical magnetic field component, whereas H_z can be induced in any of the other multidimensional cases. (ii) In 2-D cases the induction vectors align consistently in a plane perpendicular to the strike. (iii) Large amplitude of the vertical field suggests a 3-D environment.

Chapter 3

The study area and the fieldwork

3.1 Description and geological history of the Aegean Sea

3.1.1 The geotectonic model

The collision between the African and Eurasian plates during the last 70 m.y. is a generally accepted model accounting for the geodynamic evolution of the East Mediterranean (Papazachos and Komninakis, 1971). After the main Tertiary phase of that collision, an important episode led to the segmentation of part of the Eurasian plate in that area, creating the so called 'Aegean' microplate. The subduction of the African plate beneath the Aegean microplate (fig.3.1) is an active process in the East Mediterranean which started in the Middle-Upper Miocene (14-11 m.y) (Fytikas et al., 1976; Mackenzie, 1978; Le Pichon and Angelier, 1979). The general features of this zone (fig.3.2) are:

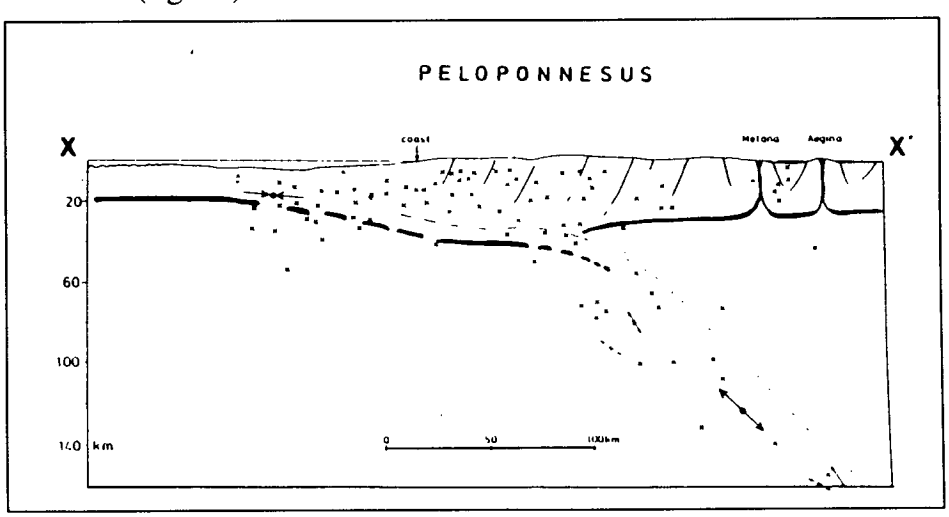

Fig.3.1: Subduction of the African plate under the Aegean microplate (section X-X', fig. 3.2). Data are based on deep seismic soundings, seismic profiles and surface geology (Berckhemer, 1977). **Vertical and oblique lines:** surface faults. **x:** position of earthquakes. **solid thick line:** depth of Moho. **dashed thick line:** hypothetical continuation of Moho depth. **dashed line:** limit of the subducting slab. **convergent arrows:** compressional tectonics. **divergent arrows:** extensional tectonics.

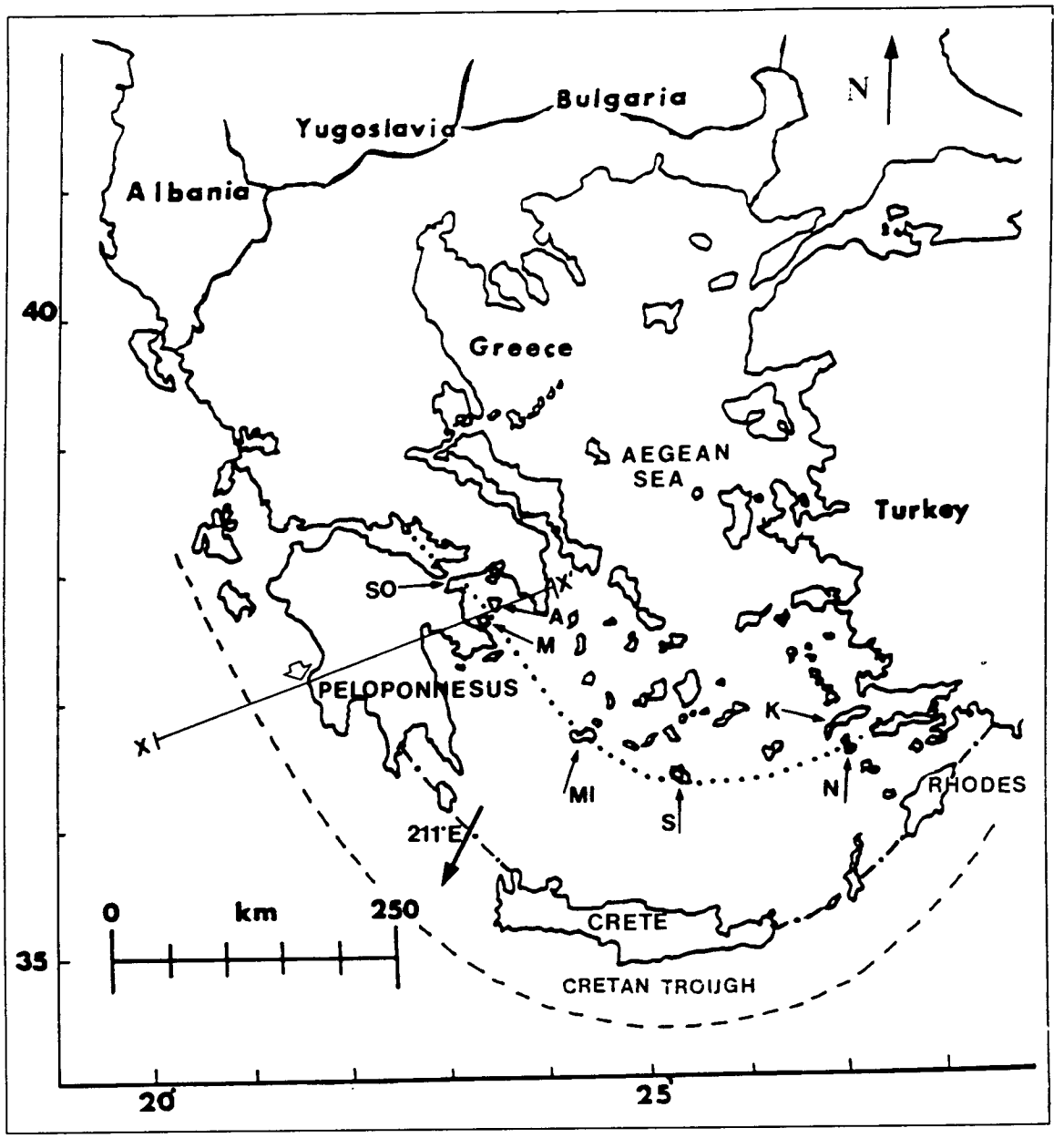

Fig 3.2: Map of Greece. Emphasis is given to the South Aegean sea. **Dotted line:** Hellenic Volcanic Arc (HVA). **Dashed and dotted line:** sedimentary Arc. **Dashed line:** Hellenic trench. **Big black arrow:** direction of the relative motion between the Aegean and African plates. **White arrow:** position "coast" marked in fig.3.1. Areas from NW to SE along the HVA: **SO**: Sousaki. **A:** Aegina. **M**: Methana. **MI**: Milos. **S:** Santorini. **K:** Kos. **N:** Nisyros. **X-X' line:** section across Peloponnesus shown in fig 3.1.

a. The Hellenic trench, a deep trench (4000 m depth) which marks the zone boundary :

b. The sedimentary arc, about 220 km behind and parallel to the trench, which comprises the SW Peloponnesus, Crete, up to the island of Rhodes:

c. The Hellenic Volcanic Arc (HVA), 120 km behind, which comprises from W to E mainly the areas of Sousaki, Methana, Aegina, Milos, Santorini, Kos and Nisyros;

d. The direction of the relative motion between the two plates is 211^0E (McKenzie, 1978a).

e. Rapid extension is taking place in the Aegean (chapter 7).

3.1.2 Composition of the volcanic rocks

The Aegean region is characterised by volcanic activity starting in the Eocene in the N. Aegean sea (Papanikolaou, 1984), whereas in the S.Aegean volcanism became active during the Pliocene (Fytikas, 1989).

The composition of rocks in the HVA is characteristic of volcanic arcs. It is of the calc-alkaline type, varying in composition from basaltic andesites to rhyolites, with andesites and dacites as the most common rocks. In general, andesites and dacites predominate on Methana, Aegina and Nisyros, while Kos and Milos are dominantly rhyolitic. Santorini is the only island of the arc with extensive basaltic members. There is indication (Nichols, 1971) that in the SW part of the arc (Sousaki, Methana, Aegina, Milos), differentiation occurred dominantly at high pressure forming lava domes and loose pyroclastic products. In Santorini and Nisyros central volcanoes forming calderas prevail. The different stress regimes are probably responsible for the differences in composition along the HVA.

3.2 Description and geological background of Methana Peninsula

As was seen from fig.3.2, Methana Peninsula is part of the western termination of the HVA. It occupies a small area of about 45 km^2 and is located to the NE of the Peloponnesus (Greece), connected with it through a narrow isthmus (approximately 250 m wide). Although geophysical studies including MT surveys have been carried out in other areas of the arc (Milos, Kos, Nisyros), in Methana some geological studies have been made but only one geophysical survey (section 3.3.1).

3.2.1. Geological formations

In fig.3.3 a sketch of Methana Peninsula with its southward continuation depicts the geology of the area. The information is taken from Institute of Geological and

Mineralogical Exploration of Greece (IGME), concerning the geological mapping of Methana (IGME: Suesskoch, 1974, Fytikas and Innocenti, 1972), and from a final report concerning areas of geothermal interest in Greece (IGME, 1984).

Although in the regional area few outcrops of igneous intermediate rocks such as trachyte and ultrabasic such as serpentine and peridotite can be found, the surface of the area of investigation is covered mainly by four geological formations:

1. A Mesozoic crystalline basement
2. Flysch of Mesozoic-Tertiary age
3. Late Tertiary-Quaternary volcanic products
4. Quaternary alluvium deposits

The Mesozoic basement consists of sedimentary rocks which outcrop only to the W and to the S of the peninsula. To the W, faulting has revealed a group of carbonate rocks of Triassic age called the "Pantokrator limestones". Along their contact with the volcanics, very few tectonised lenses of serpentinites, shales and ophiolithes of Jurassic age can be found. In the S, Cretaceous limestones outcrop together with intercalated conglomerates and marls consisting of quartz, quartzites and volcanics. These limestones form complicated karst systems suitable for water circulation (Yannetakis et al.,1972).

On the top, the volcanic rocks which cover almost the whole Methana Peninsula, vary from basaltic andesites to rhyolites but the most common rocks are dacites and andesites forming lava domes and flows, especially in the central part. Other volcanic products are agglomerates formed by the crumbling of lava domes, as well as loose reworked breccia and conglomerates cemented with fine grains of the same material. The latter reach the NE sea edge overlying the andesites. The distribution of volcanic centres of Methana is controlled by the NW-SE and NNE-SSW main tectonic trends.

Above the volcanics, Quaternary beach and river deposits consisting of sand and loam present very few outcrops, mainly in the town of Methana.

Southwards outside the peninsula, the so-called Trizina graben is a large WNW assymetrical graben formed as a result of the extensional tectonics in the S.Aegean (section 7.4). The main formation is flysch of Mesozoic-Tertiary age which predominates for several kilometres, and only some alluvium deposits appear near to the sea. The flysch generally consists of marls, sandstones, breccia, conglomerates and shales. The formations appearing in the peninsula (Triassic and Cretaceous carbonates, Jurassic ophiolithes and serpentines) are also recognized to the W of Trizina graben, but in a rather complicated pattern. The volcanic products are strictly confined to the Methana Peninsula (fig.3.3).

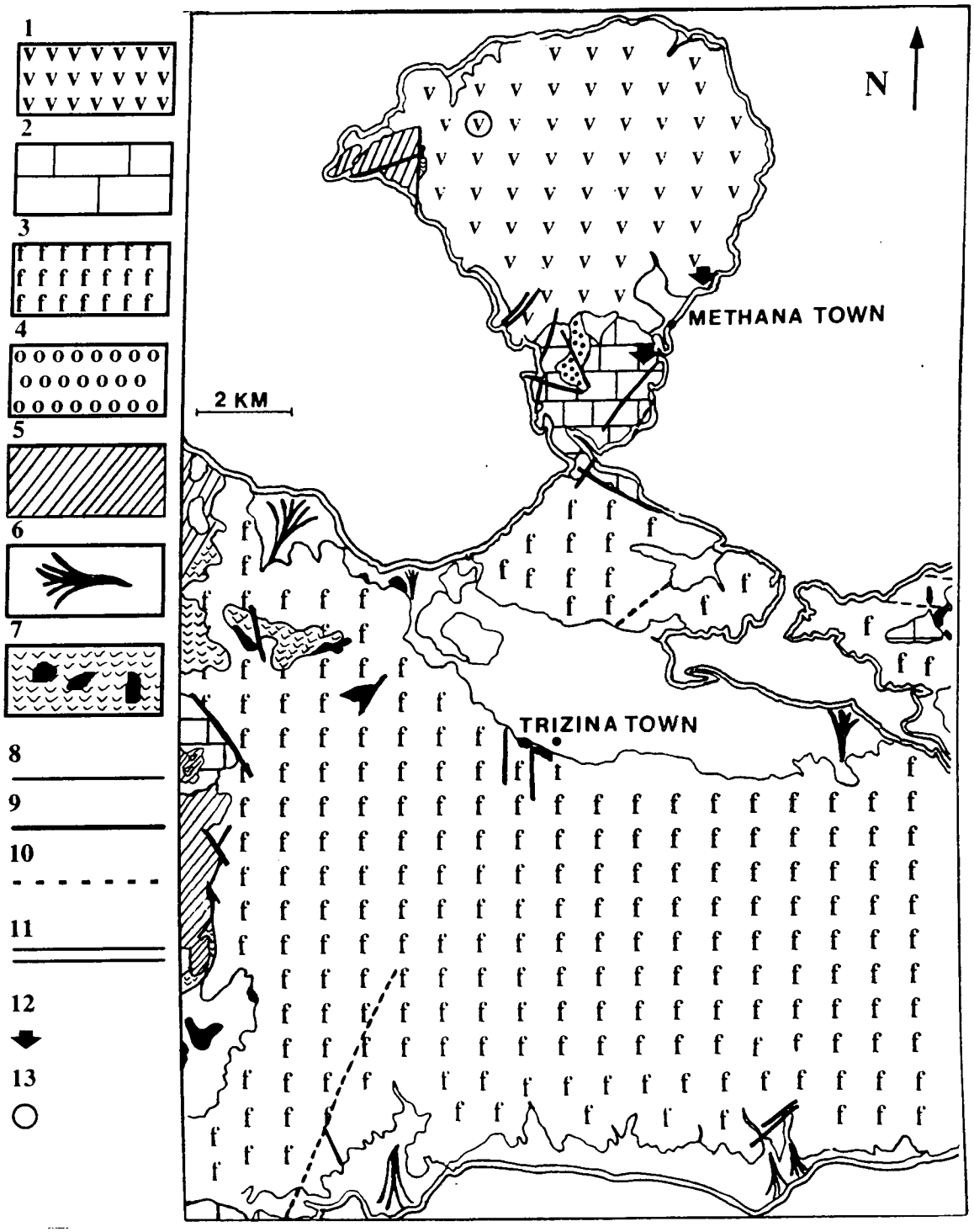

Fig.3.3: Geological map of Methana and surrounding regions. **1:** volcanics of Quaternary age **2:** limestones of Cretaceous age. **3:** flysch of Mesozoic-Tertiary age. **4:** conglomerates (Cretaceous). **5:** carbonates (Pantokrator limestones) of Triassic age. **6:** quaternary alluvia. **7:** serpentines and ophiolithes of Jurassic age found within the Mesozoic carbonates and the flysch series. **8:** geological boundary. **9:** fault. **10:** fault probable or covered. **11:** coastline. **12:** thermal springs. **13:** location of the most recent eruption.

3.2.2. Volcanic activity

Almost all of the surface is very irregular and covered by volcanics forming several domes of viscous lava which reach up to 750 m. The most recent eruption occurred about 250 years B.C and has been recorded by Strabo in his "Geographica" (Pe,1974). It forms the extrusive dome of Kammeno Chorio in the NW of the peninsula (fig.3.3).

Radiometric data indicate that volcanic activity started in the late Tertiary or Quaternary. K-Ar dating suggests an age of 0.9-0.32 my (Fytikas et al.,1976)

The volcanics can be grouped into 4 differentiation series ranging from basaltic andesites to rhyodacites: Old series, Malisa series, Chelona series and Late series. The Late series laves are more acid compared with the Old series (Pe, 1974).

3.2.3. Thermal springs

Seven thremal springs have been recorded in the Methana Peninsula (Georgoulis, 1983), which are located to the N and to the SE near Methana town (fig.3.3). In five out of seven, water flows out from volcanic rocks, whereas the other two are situated near carbonates. All of them are situated near the sea and as a result they are influenced by sea movements. Their existence is possibly connected with the recent age of volcanism and the tectonics of the area. The temperature range of the water is between 20 and 44^0C, and they have alkaline-chloride composition with B/Cl and Li/Cl ratios much higher than sea water (IGME, 1984), which shows that water-rock interaction might take place at relatively high temperatures. The number of springs is high in relation to the small extent of the area and the annual rainfall (400 mm/y). Therefore it is probable that part of the springs' water is juvenile rather than meteoric.

Six more springs have been recorded in the Trizina graben, to the NW and SE of Trizina town. Their temperature, by being less than 20^0C, indicate that that they are possibly related to tectonic activity (Georgoulis, 1983).

3.3. The fieldwork

3.3.1. Previous work

Methana is one of the relatively unexplored regions of the HVA. Some previous geological work comprises geological mapping (Fytikas et al., 1984), petrologic analysis of the volcanic rocks (Pe, 1974), a paleomagnetic study of the volcanic rocks (Orlicky, 1984), and a geochemical and isotopic analysis of the thermal springs carried out by IGME (1982).

Previous geophysical exploration in Methana includes only a number of SP measurements along a curved line of 30 km and a geoelectric profile consisting of 10 DC resistivity soundings (Thanasoulas et al.,1991), both taken in positions around the peninsula. The results have shown apparent resistivity values less than 10 Ohm m, and locally in places associated with the presence of hot water of less than 2 Ohm m, whereas in the NE part these low values were interprated as due to the penetration of sea water into the rocks. According to that work also, many minor faults exist within the volcanics, and there is a contrast in resistivity in the proximity of Methana town, which was interpreted as due to a NE-SW faulting zone which exists in positions corresponding approximately to the sites 120 and 121 (fig.3.5).

Another profile consisting of 74 DC resistivity soundings, has been carried out in the Trizina graben (IGME, 1982). The apparent resistivity curves have shown a shallow conductive layer of small thickness (<50 m) and a variable resistivity basement (100-2000 Ohm m). The interpretation was confined to the top 1 km and resistivity values typical of alluvium deposits and flysch formations were recognised. Variation of values within the flysch was most likely due to the different proportions of marls, sandstones and shales. The high resistivity values as well as the low temperatures of springs (section 3.2.3) in Trizina graben did not suggest the existence of a geothermal anomaly.

The first attempt to investigate Methana Peninsula using a geophysical method which allows an interpretation at greater depth, was in October 1991. 13 MT soundings were carried out in an approximately N-S profile. 2 additional soundings were done extending a few km southwards into the Trizina graben.

3.3.2. Instrumentation

Data were recorded over a broad frequency range in order to provide information for a wide range of depths. To achieve this aim, two different kinds of instrumentation have been used:

1. The Short Period Automatic Magnetotelluric data acquisition system SPAM IIb, designed and developed by Dawes (1984), covering the frequency range 0.016-128 Hz (AMT equipment)

2. The long period data acquisition system (NERC pool) covering the frequency range 0.02-0.0001 Hz (LMT equipment).

3.3.2.1. AMT equipment

SPAM IIb is an in-field real-time data acquisition system measuring natural electromagnetic signals over a broad frequency range. Data are captured and analysed in 4 frequency bands:

Band 0: 128-16 Hz

Band 1: 16-2 Hz

Band 2: 2-0.25 Hz

Band 3: 0.25-0.016 Hz.

The lower the frequency, the greater the acquisition time but the greater the depth of penetration.

The equipment can be divided into 2 sub-systems (fig.3.4):

a. The SPAM box which comprises the analogue box and the computer box.

b. The sensor system, which comprises the cables, the sensor distribution box, and the magnetic and telluric sensors.

a. 1. Analogue box

The analogue box comprises 7 identical channels: 3 magnetic (H_x, H_y, H_z), and 4 electric (E_x, E_y, E_x^R, E_y^R) two for base and two for remote sites respectively (the "remote" telluric site technique is discussed in section 3.3.3), and performs pre-amplification filtering, notch filtering, switchable band filtering and analogue to digital conversion.

All the signals are fed into a fixed gain input amplifier and a broad band filter. The band pass filtering consists of a high pass and a low pass filter. It is used to eliminate high frequencies and DC levels from the measured signal. Notch filters eliminate the electrical power frequency of 50 Hz and its first odd harmonic, 150 Hz.

Finally an analogue to digital converter converts the signals into digital form and sends them to the computer system.

a. 2. Computer box

The output from the analogue section is fed into the computer box which samples the data, carrying out preliminary analysis, including impedance tensor estimation and stores the time series data and the results on floppy discs. Power is provided through 3 12V batteries, one for the analogue and two for the computer boxes. A small portable terminal connected with the computer box is powered by internal batteries.

Before any data were recorded, a program called "test" was run in order to check if everything was set up correctly. All bands, notch filters, amplifier gains, were checked. The band pass filters were checked by measuring their responses using a signal generator. A portable oscilloscope was used for a view of the test signals as well as of the real signals.

b.1. magnetic sensors

Induction coils measure the rate of change of magnetic field strength. They have a high output at high frequencies but a very large number of turns must be used to provide a measurable voltage at the lower frequencies. 3 CMIIE induction coils incorporating pre-amplification and feedback systems were used, two for the horizontal components and one for the vertical component of the magnetic field. The horizontal coils were levelled, oriented by compass, and then buried with their connected cables at about 20 cm depth in order to reduce vibration noise caused by wind. The vertical coil was buried completely where possible because it is the most sensitive to wind-generated vibrations. The coils were separated a few meters from each other and attention was paid to avoiding any kind of interference from passing vehicles, power lines etc.

b.2. telluric sensors

Electrodes measure the potential difference between two points in the ground. There are two types of electrodes available, polarising and non-polarising, but non-polarising are essential to lower frequency measurements. In the fieldwork, two pairs of grounded, non-polarising lead-lead chloride ($Pb\text{-}PbCl_2$) electrodes were used.

Lead-lead chloride electrodes are made of a lead wire placed into a container with a porous base. Water saturated with $PbCl_2$ and NaCl fills the container.

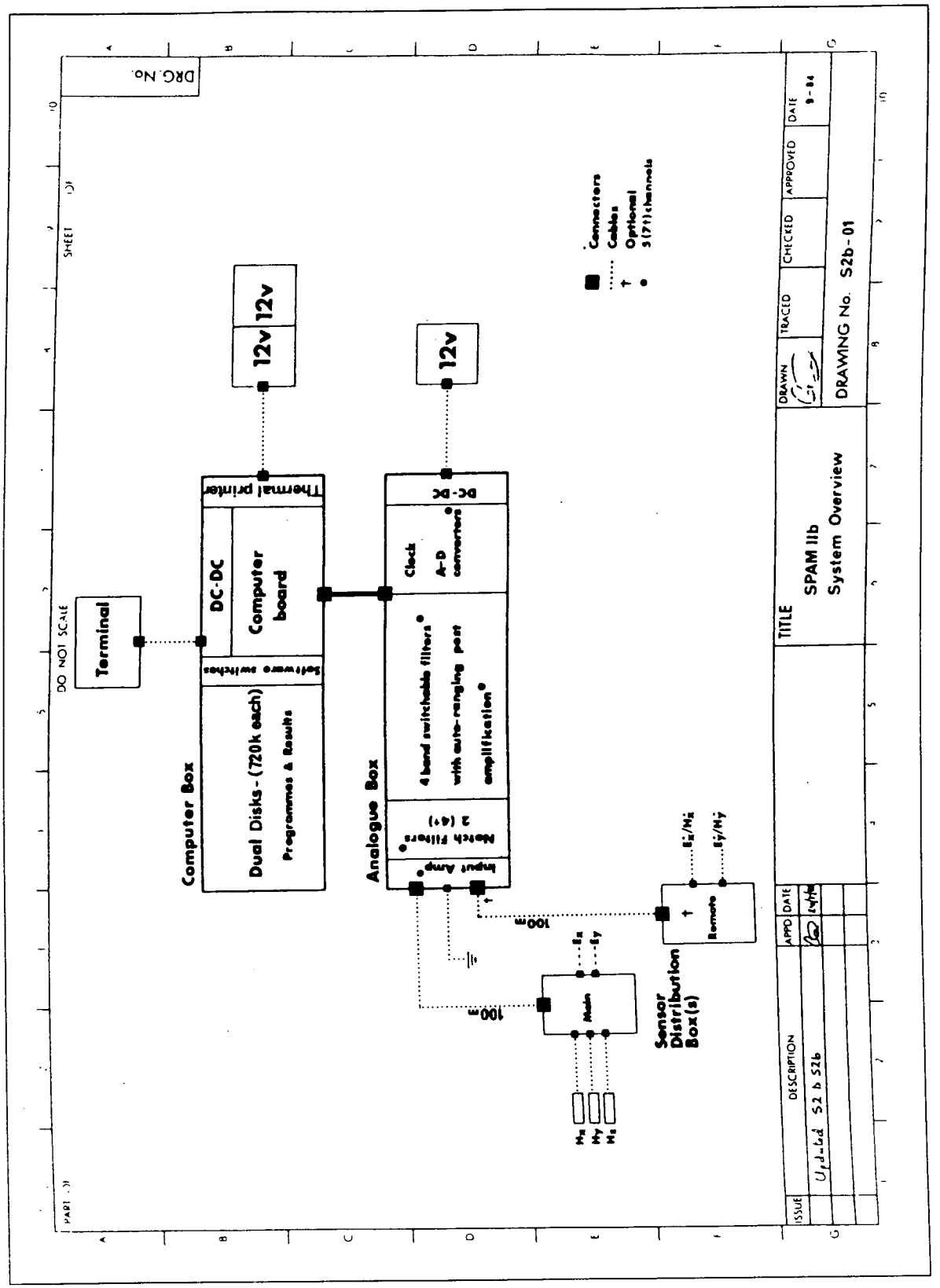

Fig.3.4: Block diagram showing the Short Period Audio Magnetotelluric (SPAM) system. (Dawes, 1984).

Typically, their stabilisation time does not exceed 0.5-1 h, the noise spectrum is low enough (0.4 mV at 1 Hz, 1.2 mV at 0.01 Hz), the temperature coefficient is -40 mV/^{0}C and the polarisation about 1 mV/month (Petiau and Dupis, 1980). An increase in separation distance results in an increase of signal to noise ratio, which is usually compensated for by increase in noise due to wind moving the long cables.

b.3 sensor distribution box

All the sensors, electrodes and induction coils, were connected to the common sensor box. The very low amplitude telluric signals were amplified and then sent to the analogue box through a 50 m cable. The power needed to supply the induction coils and the telluric amplifiers was also passed through the sensor box.

3.3.2.2. LMT equipment

For the long period measurements, a three-component fluxgate magnetometer was used, incorporating a NERC geologger for recording the signals (Valiant, 1976), covering the frequency range 0.02-0.0001 Hz. The system was designed by the NERC geophysical pool. The fluxgate head was levelled and aligned accurately so that the sensors pointed North, East and vertically Down. The drum containing the fluxgates was fixed in a pit in the ground and buried 1 m under the surface in order to reduce daily temperature variations (about 2^{0}C/day), as well as vibration noise. Power was sent through a 20 m cable and the signals went back along the same cable. The electric sensors were the same as for the AMT equipment. The telluric signals were passed through an amplifier with a fixed gain of 100 before any filtering was performed. A sampling rate of 10 s was chosen. A 3000 s high pass filter was incorporated to remove variations connected with diurnal temperature changes, longer period telluric signals, and the slow drift in self potential of the electrodes.

3.3.3 Site preparation

Given that the present survey was a reconnaissance study, and allowing for limitations imposed by the geological and topographical features, it was decided to accommodate the AMT sites wherever it was possible (i.e., where vehicle access, sufficiently flat areas, remoteness from power lines and sea water could be achieved). Unfortunately the only areas far enough from the sea and from power lines were steep, and also the only flat areas were at the edges of the peninsula or near villages. Nevertheless, a profile in an approximately N-S direction was made extending southwards to the Trizina graben (fig.3.5).

It was possible at all the sites to align the sensors in the magnetic N-S and E-W directions, except for one where in-situ rotation from the magnetic North was applied.

The steps in preparing an AMT site were as follows:

a. Find a suitable area to accommodate the site: Relatively flat areas at least 50x50 m and away from cultural noise as well as from the sea, were recommended.

b. Determine the centre

c. Prepare the holes for the magnetic sensors, a few meters away from the centre, and bury the coils: one vertical (H_z) and two horizontal (H_x, H_y). The coils were levelled and placed along three directions, magnetic North (H_x), East (H_y) and Downward vertical (H_z).

d. Preparation of the telluric lines: Lay out the cables which must be held down to prevent vibration from rocks, bushes, rugged or steep terrain. Wind or plant vibrations may cause noise problems in the electric channels. Depending on the characteristics of the investigation area, an electrode configuration in the form of "L"(3 electrodes),"T" or "X" (4 electrodes) was adopted, with a length of about 50-100 m for each direction (E_x,E_y). The electrodes were inserted into the ground, the telluric cables attached, and measurements of the self potential between two electrodes and contact AC resistance were made. In order to reduce the contact resistance between the electrodes and the ground, water was used to moisten the soil around the electrodes. The self potential (SP) which can saturate the DC coupled telluric pre-amplifiers did not exceed a few millivolts in the survey. The contact resistance also was less than 10 KOhms, as the SPAM system requires.

e. Connect the sensors to the sensor distribution box and the sensor box to SPAM.

A second sensor distribution box was used for a second remote telluric site (fig. 3.6). When possible, this procedure was adopted at a number of sites. Under the assumptions that the magnetic field is homogeneous over short distances and that the telluric field is more sensitive to noise, the remote site technique serves as a control of static shift. A multicore cable 100-150 m long was used in order to connect the sensor box to the SPAM box. A final electrode was buried near the SPAM box for the earthing of the system.

After some preliminary tests and filter calibration the system was ready for recording.

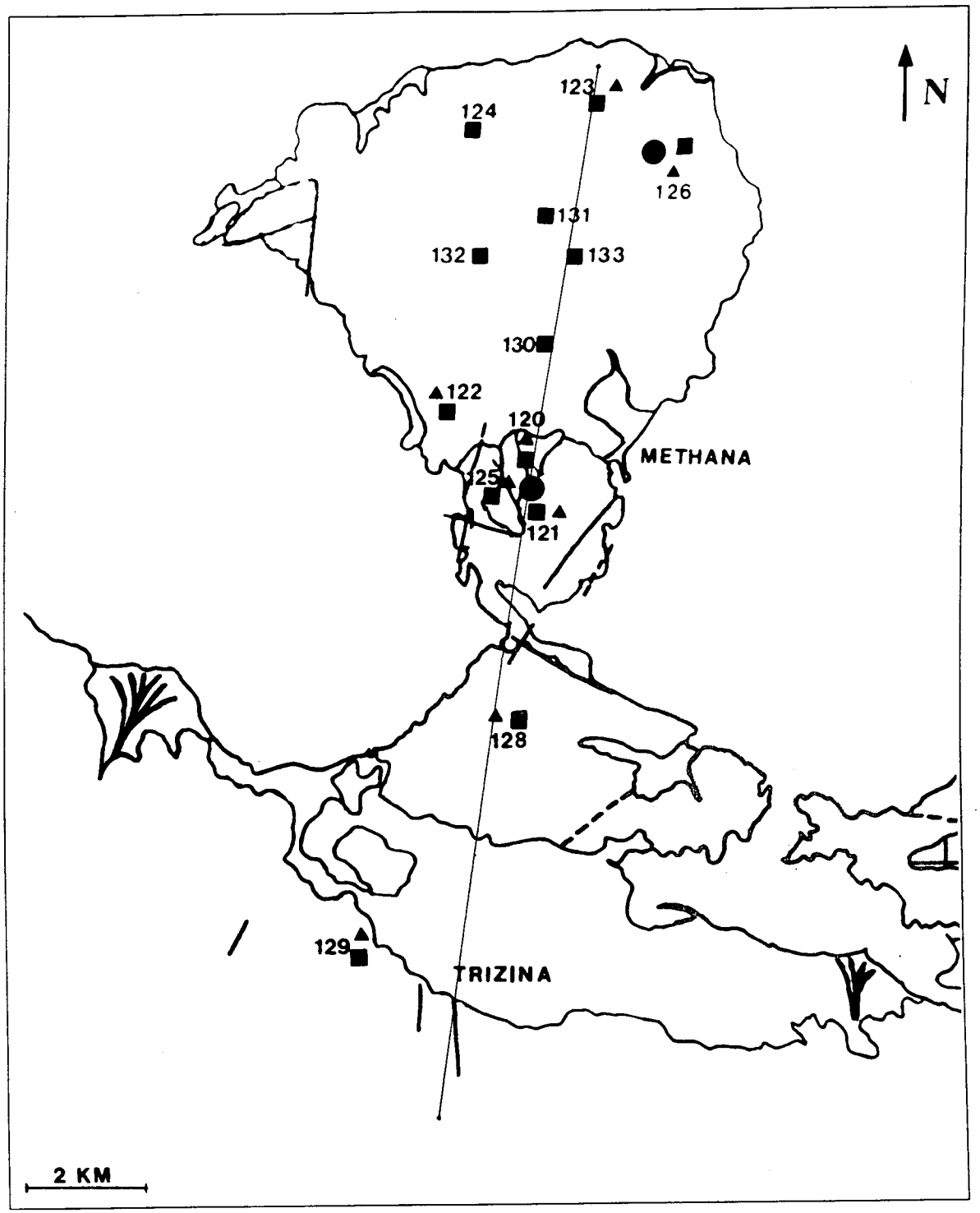

Fig.3.5: Distribution of sites during the fieldwork. **Squares:** base 5-component AMT sites. **Triangles:** remote electric AMT sites. **Circles:** LMT sites.

AMT range: 0.0085 - 23 s

LMT range: 24 - 6000 s

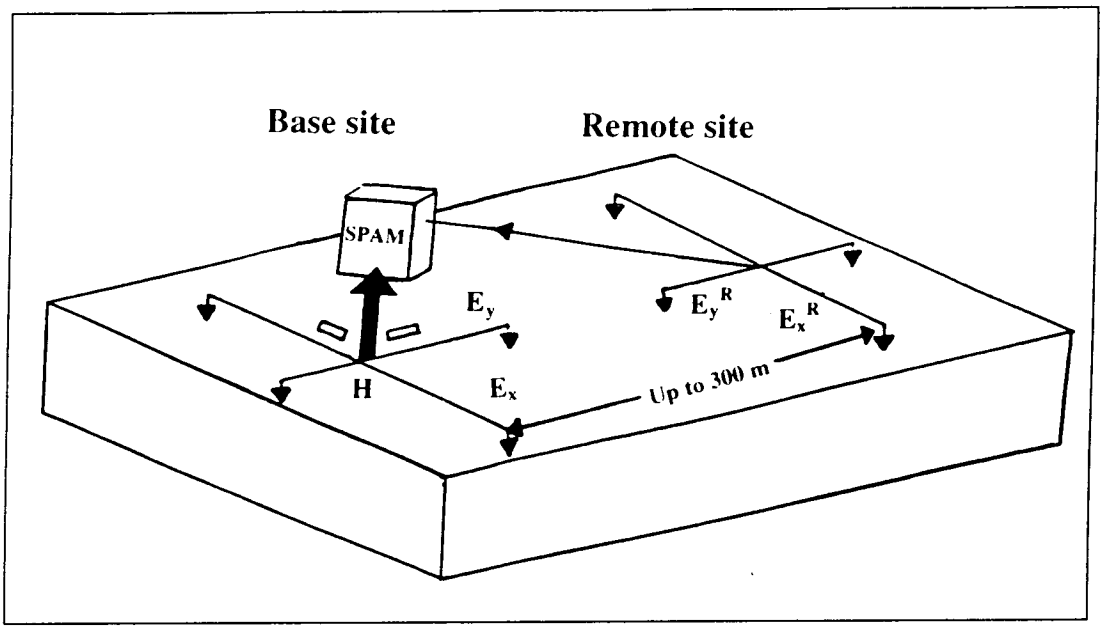

Fig.3.6: "Remote site" method of data acquisition. It involves "hardwiring" of the electric observations to the SPAM from an auxiliary site located up to 300 m away.

3.3.4 Data recording

14 base and 8 remote sites in the AMT frequency range were distributed in a N-S profile along the peninsula. Data for each site were recorded during one day , so that every day a new site was prepared. The natural signals were initially amplified by a fixed gain, the same for all channels. The data were then digitised at a sampling rate related to each frequency band: 512 Hz for band 0, 64 Hz for 1, 8 Hz for 2 and 1 Hz for band 3. The time series consisted initially of 256 point windows. An example of a typical in-field time series window is shown in fig.3.8. The time series was converted into the frequency domain using a Fast Fourier Transform (FFT) routine. Impedance tensors were calculated from cross and auto spectral averages over many data windows (more about data processing in chapter 4).

Spikes in the data coming from power lines (mainly 50 or 60 Hz and their odd harmonics), were unavoidable especially in locations near villages.

The acquisition time depended primarily on the frequency band as high frequency data are recorded much more quickly than low frequency data. Recording on bands 0 and 1 was preferable early in the morning, avoiding in that way very much interference from the switching on of domestic power. For bands 2 and 3 more time was needed and the recording sometimes lasted until late evening, in order to obtain a satisfactory number of windows.

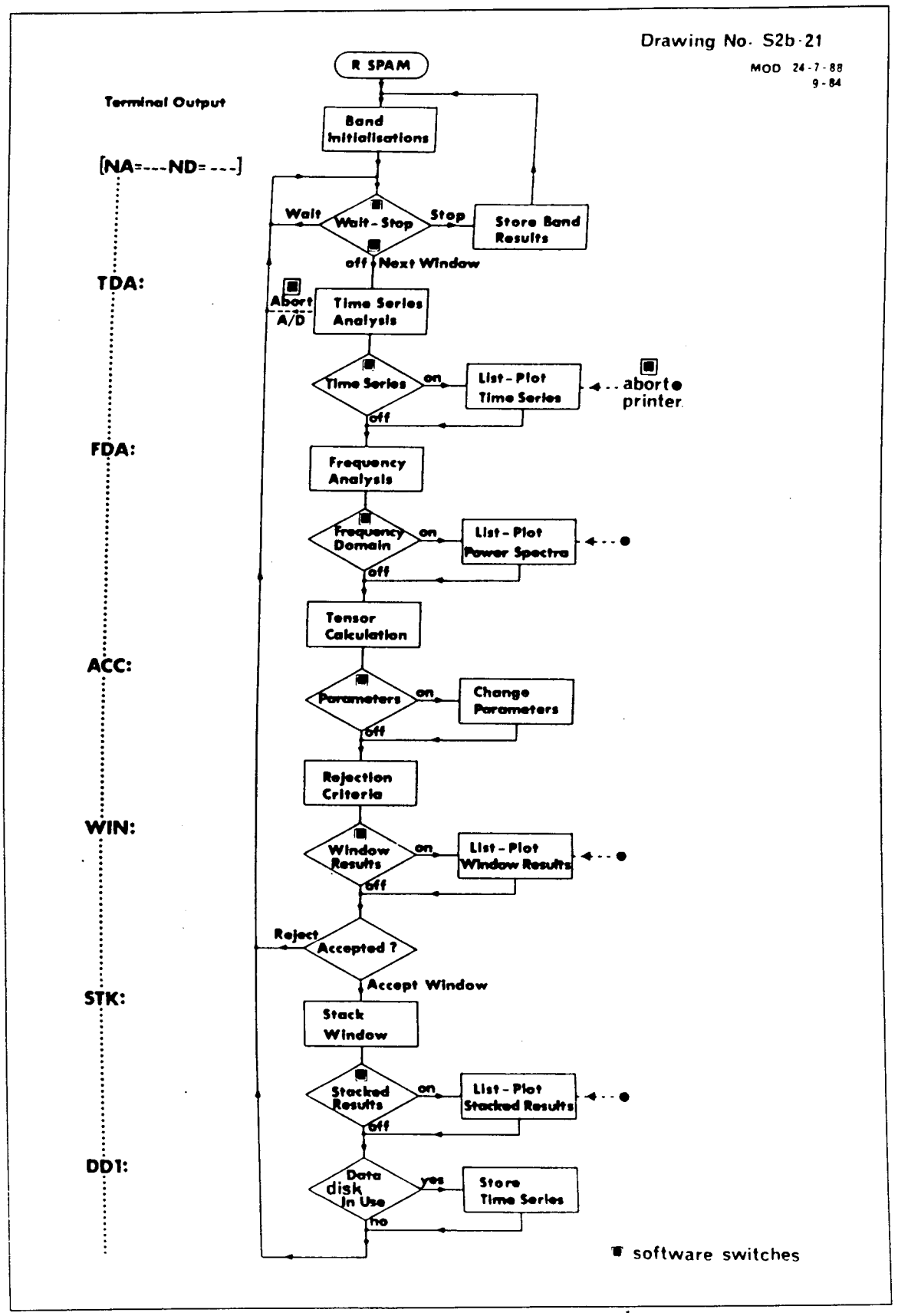

Fig. 3.7: Spam IIb - flowchart of the main analysis program (from Dawes, 1984).

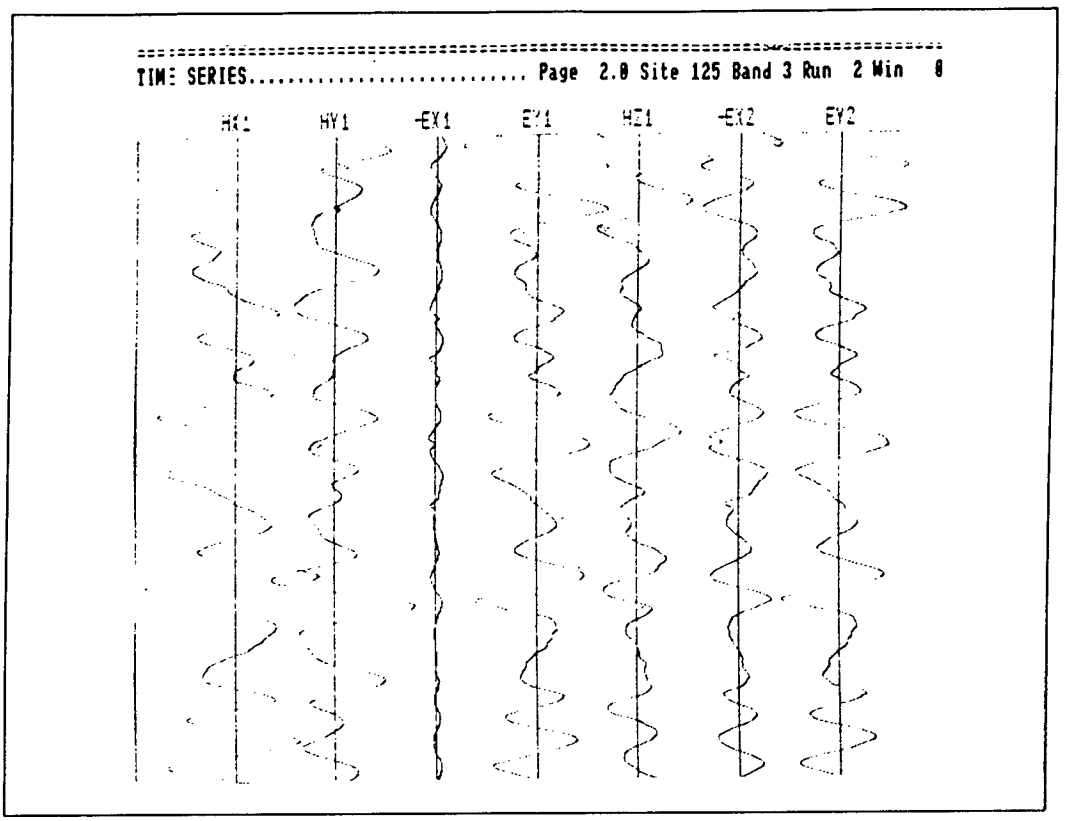

Fig.3.8: Recording of 7 components of the MT field. High activity in all channels, except the E_{x1} component. The time interval in the above window is 256 s.

A very useful measure of the data quality used in the data acquisition as well as in the data processing (chapter 4), is called the predicted coherence (Swift, 1967) and is the coherence between the measured electric field and the theoretical electric field as it is predicted by the eqs.2.37 and 2.38. The predicted coherence is widely used as a measure of noise in the field data:

$$\mathrm{coh}(E_x, E_{xp}) = \frac{(E_x E_{xp}^*)}{((E_x E_x^*)(E_{xp} E_{xp}^*))^{1/2}} \qquad (3.1)$$

where E_x and E_{xp} are the observed and theoretical (or predicted) values of the electric field, respectively. Predicted coherence values lie between 0 and 1, and measure the degree of correlation between the measured and the predicted value of the electric field.

During recording not all the data windows were accepted because natural signals can be very poor in frequency content, or have very low power, or low coherence. For that reason certain rejection criteria were imposed on the input data windows and 3 parameters were defined:

(a) the minimum number of accepted frequencies for a window to be accepted;

(b) the minimum coherence for an accepted frequency;

(c) the minimum power for the horizontal magnetic field for an accepted frequency;

The rejection criteria were set higher for bands 0 and 1, as it was generally easier to obtain good data quality on those bands than in the lower frequency bands. A low coherence (e.g. 0.7) would accept data of lower quality which proved necessary when the signal level was low, whereas a high coherence (e.g. 0.95) is more desirable but can also be generated by coherent noise (section 3.3.5). It was decided to set values of 0.95-0.90 for bands 0 and 1, while a minimum of 0.85-0.75 was kept for bands 2 and 3, whenever possible. For band 3 with the lowest sampling rate, all windows were usually recorded.

In order to provide the necessary resolution at depth, MT activity at as many frequencies as possible was desirable. Also, a large number of estimates was necessary to obtain a mean response based on a sufficient amount of data. A distribution of events from different times of the day could also minimise any bias in the response due to the polarisation of the source field. For bands 0 and 1, more than one run of 100 requested windows each, was recorded. For bands 2 and 3, a minimum of 50 windows was saved. Finally, all the accepted windows were stacked, and results could be plotted in order to assess the quality of the data. A flow chart of the SPAM analysis program is given in fig.3.7.

During recording, the occurrence of different kinds of noise was noticed. For example, pure 50 Hz harmonics, radio transmissions, seismic vibration arising from automobile traffic near a sensor, instrument malfunction and unexpected sheep flocks which had to pass through a measuring area. When zero signal amplitude or large and rapid changes in amplitude occurred, they were simply avoided by aborting the window. A discussion on noise is given in the next section.

Additionally, for the long period measurements, 2 stations were selected to the N and to the S of the peninsula, fairly close to AMT sites 126 and 121. 2 fluxgate magnetometers were installed, each with an "L" electrode configuration, and data were logged for about 3 weeks.

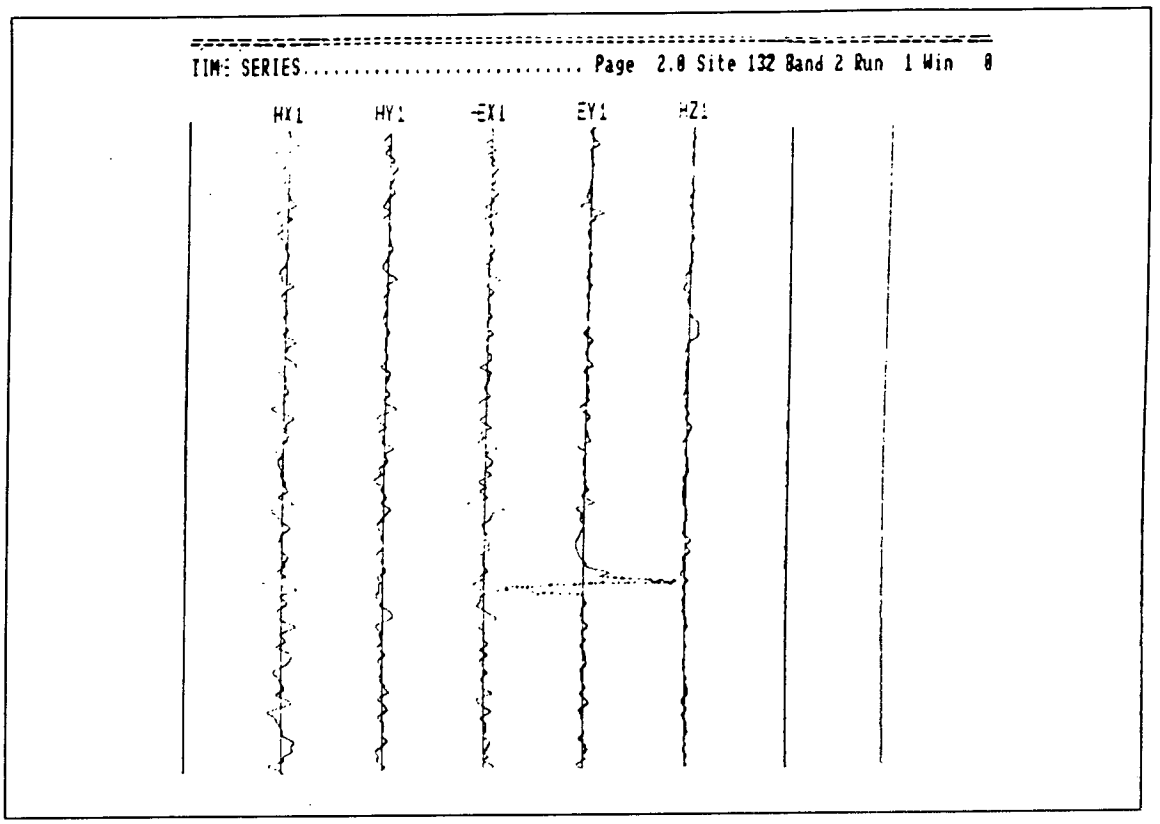

Fig.3.9: High amplitude noise in the E_y1 channel superimposed in an otherwise low signal activity.

3.3.5 Noise in the data recording

In the recording of MT signals, the natural EM fields do not normally occur as single frequencies which produce strong narrow peaks in the spectrum, but rather as random oscillatory functions. Only when there are fields of non-natural origin, such as those generated by power distribution systems at 50 or 60 Hz, do very strong peaks occur in the spectrum. These peaks can cause problems even with long sample lengths or application of notch filters.

Noise can be defined as that part of the EM field which is not induced or homogeneously induced. Two kinds of noise can be distinguished, incoherent and coherent, although real data may contain a superposition of both:

a. Incoherent or random noise is generally aperiodic and occurs when the noise in the magnetic field is independent of that in the electric field. Examples are the noise in the acquisition system itself, the vibration of cables or induction coils caused by the wind or microseismic activity, moving vehicles which produce magnetic but no electric disturbances, and electrochemical changes within the electrodes. Fig.3.9 shows an example of noise in one of the electric components.

b. Coherent noise is correlated with the natural signal, subsequently it is very difficult to detect and to extract from the measurements. It is caused by inhomogeneously induced fields such as the man-made EM fields of electric power lines. Also a breakdown in the uniform source field assumption can create coherent noise whose variance in dependent upon the strength of the signal, for example induction by a nearby source (whose distance is less than 3 skin depths). Coherent noise appears in both magnetic and electric channels. The result can be perfectly correlated signals with a high coherency, nevertheless far from natural. A clear indication of the presence of coherent noise may only be noticed after data processing, e.g. the apparent resistivity and phase curves may exhibit unrealistic slopes (such a case will be shown in section 6.4) or provide unreasonable Earth models.

Noise can also be due to systematic errors such as equipment not properly calibrated, sensors not exactly aligned or incorrect measurement of a telluric line length. Electric sensors are usually regarded as being noisier than magnetic sensors. They can be affected by leakage currents that may be present, electric railways, local lightning discharges, electric fences, power lines, domestic switch on equipment. The impulsive nature of some of these sources can saturate the equipment amplifiers, and the recording of the lower amplitude signals can become very difficult.

Chapter 4

Data processing and presentation of results

4.1 Introduction

The procedure adopted for the analysis of the field data was mainly based on robust techniques. The programs used were different for the AMT and the LMT sets. For the AMT data the robust code of Egbert and Booker (1986) was used, while for the LMT data a technique called "complex demodulation" was found to be more appropriate for dealing with high magnetic noise level in the period range 20-200 s.

SPAM IIb AMT data were stored in the field on 3,5" floppy discs. They were read and split into individual files containing different bands and runs, by using programs READ and FILE written by Dawes (1991). For the long period data which were obtained on cassette tapes, a cassette reader interfaced to a portable computer was used to extract the raw data which were then re-stored on floppy discs.

An initial step, similar for both AMT and LMT data, consisted of the use of the programs XFER and CASROB respectively, which read the data files. The output was a time series in standard ASCII format ready for subsequent processing.

4.2 Processing of AMT data

The robust processing of AMT data consisted of cleaning the time series, transforming them into the frequency domain, and computing the robust Earth Response Functions (ERFs). The programs were written by Egbert and Booker and modified by Livelybrooks (1991).

The first step was the cleaning of the time series. This was accomplished with program CLEAN. First, the running mean average deviation (MAD) was computed; then all points which varied from the MAD for several adjacent points by more than a threshold value were replaced by a new predicted estimate. In this way, isolated outliers that could influence the whole data set were excluded from further processing.

Windowing and transformation of the cleaned data segments into the frequency domain was accomplished by program DNFF. Input to this program was the cleaned time series and a number of system parameters including sampling rates, sensor orientations, electrode line lengths, clock drifts, instrument analogue filter corrections and factors to convert the data from counts to physical units. DNFF is a Fourier transforming scheme based on standard FFT (Cooley et al., 1965, 1969; Brigham, 1974), and cascade decimation (Wight et al., 1977). The latter provides spectral values at frequencies separated at logalithmic intervals, rather than linearly equal intervals as with the FFT. Transformation is accomplished by multiplying data points by weighted sine and cosine coefficient and accumulating the results.

The basic goal was to use data segments which are as short as possible to avoid problems caused by the non-stationarity in the data. The cleaned data were divided into 128 point overlapping windows. For the first decimation level (level 1), a 16 s window was used and by taking samples every point the highest frequencies were obtained. In order to obtain lower frequencies a longer time window was needed. For this reason the program digitally low passed the input series and re-sampled every 4th point (decimation level 2). The 128 point segments obtained were then windowed and FFTed. The same procedure was followed for two more decimation levels which were obtained by sub-sampling every 8th and every 16th point, respectively. In this way Fourier coefficients for 28 frequencies (from 117.6 to 0.042 Hz) were produced.

Before the transformation into the frequency domain, each window was de-meaned and a pi-prolate funtion was applied for tapering the data to avoid spectral leakage. Then program DNFF calculated the Fourier coefficients for each window, which after correction for the system response, were written into a binary file ordered by frequency and according to increasing power in the horizontal magnetic fields.

The robust estimation of the ERFs was accomplished by using program TRAN.

4.3 Estimation of the Earth Response Functions

All the procedures aimed at estimating the tensor elements are based initially upon the equations:

$$E_x=Z_{xx}H_x + Z_{xy}H_y \qquad (2.37)$$

and

$$E_y=Z_{yx}H_x + Z_{yy}H_y \qquad (2.38)$$

One way of estimating the impedance tensor elements is by least squares cross-spectral analysis (Sims et al., 1971). Multiplication of each term of the eqs.2.37 and 2.38 by the complex conjugates of each component (E_x*, E_y*, H_x* and H_y*), leads to

4 equations for each of eqs.2.37 and 2.38. In this overdetermined problem, these equations can be solved for any of the impedance elements. For example, for Z_{xy} , 6 different solutions can be provided:

$$Z_{xy} = \frac{(H_x E_x^*)(E_x E_y^*) - (H_x E_y^*)(E_x E_x^*)}{(H_x E_x^*)(H_y E_y^*) - (H_x E_y^*)(H_y E_x^*)} \tag{4.1a}$$

$$Z_{xy} = \frac{(H_x E_x^*)(E_x H_x^*) - (H_x H_x^*)(E_x E_x^*)}{(H_x E_x^*)(H_y H_x^*) - (H_x H_x^*)(H_y E_x^*)} \tag{4.1b}$$

$$Z_{xy} = \frac{(H_x E_x^*)(E_x H_y^*) - (H_x H_y^*)(E_x E_x^*)}{(H_x E_x^*)(H_y H_y^*) - (H_x H_y^*)(H_y E_x^*)} \tag{4.1c}$$

$$Z_{xy} = \frac{(H_x E_y^*)(E_x H_x^*) - (H_x H_x^*)(E_x E_y^*)}{(H_x E_y^*)(H_y H_x^*) - (H_x H_x^*)(H_y E_y^*)} \tag{4.1d}$$

$$Z_{xy} = \frac{(H_x E_y^*)(E_x H_y^*) - (H_x H_y^*)(E_x E_y^*)}{(H_x E_y^*)(H_y H_y^*) - (H_x H_y^*)(H_y E_y^*)} \tag{4.1e}$$

$$Z_{xy} = \frac{(H_x H_x^*)(E_x H_y^*) - (H_x H_y^*)(E_x H_x^*)}{(H_x H_x^*)(H_y H_y^*) - (H_x H_y^*)(H_y H_x^*)} \tag{4.1f}$$

Similar expressions can be derived for the other impedance elements.

However, because the real data contain noise the above estimates are not equivalent. Two of them are shown to result in the apparent resistivity being biased down by random noise on the electric field (eqs.4.1a and 4.1b), two are biased upwards by random noise on the magnetic field (eqs.4.1e and 4.1f) and the remaining two are unstable (Sims et al. 1971). It is generally accepted that the magnetic field is less susceptible to measurement noise, and so eq.4.1f which contains autopowers of H (HH*) would be the most acceptable. However, a more accurate estimate is provided by an average of the up and down estimates based on the following formula (Jones, 1977):

$$Z_a = \frac{\frac{Z_u}{e_u^2} + \frac{Z_d}{e_d^2}}{\frac{1}{e_u^2} + \frac{1}{e_d^2}} \tag{4.2}$$

where Z_u and Z_d are the up and down biased impedance estimates and e_u, e_d the errors on the impedance tensor elements with up and down estimates, respectively. Program TRAN calculated separately the up and down estimates for each frequency band, weighted them by their errors and averaged them at a final stage.

4.3.1 Least square (LS) methods of analysis

The basic assumption underlying the MT theory is that for signal sources far enough from the observation area and in the absence of noise, the relationship between the orthogonal magnetic and electric field measured at the Earth's surface is given by the matrix eq.2.39 and between the horizontal and vertical components of the magnetic field, by eq.2.47. In practice, however there is always an error (**r**) in the observed values and the above equations for the ith estimate become:

$$\mathbf{E}_i = \mathbf{Z}\mathbf{H}_i + \mathbf{r}_i \tag{4.3}$$

$$\mathbf{H}_{zi} = \mathbf{T}\mathbf{H}_{oi} + \mathbf{r}_i \tag{4.4}$$

where **E** and **H** are the vectors of the electric and magnetic fields, $\mathbf{H}_z$ and $\mathbf{H}_o$ are the vectors of the vertical and horizontal magnetic components respectively, and i=1...N .

If E_i is the measured electric field and E_{pi} the predicted electric field as calculated from eq.2.37 or eq.2.38, the error or residual (r) is:

$$r_i = E_i - E_{pi} \tag{4.5}$$

LS methods are based on the assumption that the errors have a Gaussian distribution. They attempt to minimise the sum of squared residuals. Eq.4.3 can be written:

$$\sum_{i=1}^{2N} \mathbf{r}_i^{\,2} = \sum_{i=1}^{2N} (\mathbf{E}_i - \mathbf{H}_i^{\mathrm{T}}\mathbf{Z})^2 \tag{4.6}$$

where T denotes Hermitian transpose.

Application of the $\min\Sigma r^2$ leads to the same equations as those in section 4.3.

4.3.2 The need for robust methods analysis

The Gaussian distribution is a general statistical model which in a number of cases seems to be violated:

(i) Actual data frequently contain a small fraction of data points, or "outliers". Such data could in principle be modelled by distributions which are Gaussian at the centre but with tails which are "heavier" than those of a Gaussian distribution. Estimators such as the arithmetic mean and the standard deviation which are used in LS methods, are very poor if the data set contains outliers, because a single gross outlier can have a very strong effect on their values and distort the estimate.

(ii) For relatively short period data the error variance is independent of signal power and ordinary LS would be justified. For longer periods, however, the noise power tends to increase with the signal power (Egbert et al., 1986).

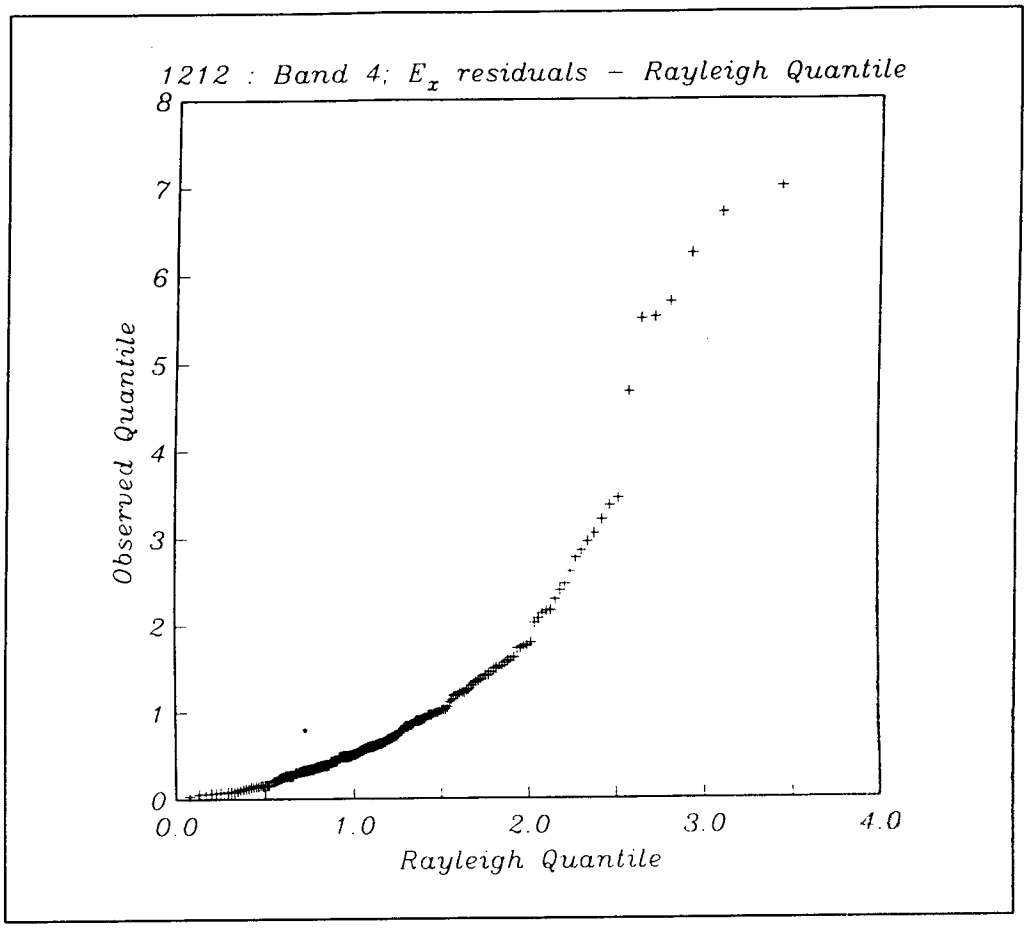

Fig.4.1: Example of a Q-Q plot for site 125 at T=100 s.

The Gaussian error assumption can be tested by plotting the distribution of actual residuals observed against the distribution of residuals expected from a Gaussian error distribution. Such plot are called Q-Q plots (see Egbert and Booker, 1986; Goodall, 1983). For example, data are taken from site 125 at T=100 s and the observed residuals for E_x are plotted against the predicted ones (fig.4.1). If the residuals are consistent with a Gaussian distribution, the plot should approximate a straight line of unit slope. Obviously, this is not the case, and although for small residuals (<1) the line is almost straight, as the magnitude increases, the largest residuals are much larger than expected.

Robust techniques involve estimation methods which are generally insensitive to outliers. An *ad hoc* remedial action after examining the data is to downweight (or removing) the outliers and then apply conventional LS methods. This is a weighted least square (WLS) estimation in the sense that it minimises a weighted sum of squared residuals. Eq.4.6 can be written:

$$\sum_{i=1}^{2N} \mathbf{w}_i \mathbf{r}_i^2 = \sum_{i=1}^{2N} \mathbf{w}_i (\mathbf{E}_i - \mathbf{H}_i^T \mathbf{Z})^2 \qquad (4.7)$$

where **w** is the weighting factor matrix. The weights are chosen in such a way as to repress the influence of large residuals.

4.3.3 The robust code of Egbert and Booker

Several methods have been developed for the identification and removal of outliers (Kleiner, Martin and Thomson, 1979; Chave et al., 1987; Chave and Thomson, 1989). In this work the robust code of Egbert and Booker (1986) has been used, and the so-called "regression M-estimate" has been applied. This technique which is flexible and easy to implement includes the most widely used class of robust parameter estimators.

M-estimators are similar to LS-estimators in that they both attempt to minimise the difference between predicted and observed data values. The misfit, however, is measured in such a way that outliers do not dominate the estimate.

Instead of eq.4.6, an expression of the following form is minimised:

$$\sum_i \rho \left(\frac{\mathbf{E}_i - \mathbf{H}_i^T \mathbf{Z}}{\sigma} \right) \qquad (4.8)$$

where (Huber, 1981):

$$\rho(r) = r^2 / 2 \qquad |r|<r_0 \qquad (4.9a)$$

$$\rho(r) = r_0 |r| - r_0^2 / 2 \qquad |r|>r_0 \qquad (4.9b)$$

with $r_0 = 1.5$ and σ is the scale parameter used for normalising the residuals.

The procedure used was the following:

A LS estimate of Z_0 and a robust estimation of the error scale σ_0 were initially used to compute the predicted (E_{p0i}) electric field and residual (r_{i0}):

$$E_{p0i} = ZH_i \quad \text{and} \quad r_{i0} = E_i - E_{p0i} \qquad (4.10)$$

Then the modified observation was computed:

$$E_{pi} = E_{p0i} + w\,(r_{i0} / \sigma_0)\, r_{i0} \qquad (4.11)$$

where

$$w(r) = 1 \qquad |r|<r_0 \qquad (4.12a)$$

$$w(r) = r_0 / |r| \qquad |r|>r_0 \qquad (4.12b)$$

so that for small residuals ($|r|<r_0$) the modified observations were identical to the original observations, while for larger residuals the observations were pulled towards their predicted values. The modified observations then were used to compute a new LS estimate of Z_1 and a new error scale estimate σ_1, leading to a new modified observation. The procedure was iterated until convergence was achieved. This

algorithm was, in effect, equivalent to eq.4.7, with $w_i = w(r_i)$. The weights were determined by the data, with the outliers given smaller weights.

Weights were applied uniformly to all channels. There was an automatic adaptive downweighting of high power events in program TRAN. Also after the Fourier coefficients were ordered, there was an option of "power cut-off percentage" which was used to eliminate the lowest and highest power events from further processing.

4.4 Processing of the LMT data

As was mentioned before, the LMT data were not processed by the same code of robust analysis as the AMT data. The LMT data were generally more difficult to handle, as a large number of noisy and corrupted windows was found. A more careful selection of good quality data segments was needed, and this was provided by the complex demodulation method.

4.4.1 The complex demodulation technique

Complex demodulation is a technique in which the amplitude and phase of selected frequency components of a time series can be examined as a function of time. The process of complex demodulation as applied to a time series x(t), is defined by two mathematical operations (Banks, 1975). Each frequency of interest in the spectrum is shifted to zero frequency by multiplying each term of the time series by the function $\exp(-i\omega' t)$, where ω' is the central frequency of the shifted band. A new series is produced for each frequency band:

$$X_s(\omega',t) = x(t)\exp(-i\omega' t) \qquad (4.13)$$

By using a set of weights a_k ($-m<k<m$) the frequency shifted series is low-pass filtered, giving the complex demodulated time series:

$$X_d(\omega',t) = \sum_{k=-m}^{k=+m} a_k X_s(\omega', t + k\Delta t) \qquad (4.14)$$

or more conveniently

$$X_d(\omega',t) = |X_d(\omega',t)|\exp(-i\phi(\omega',t)) \qquad (4.15)$$

in terms of the modulus and phase of $X_d(\omega',t)$.

While power and cross spectra calculated by conventional means are averages over the whole length of the data series, spectra calculated by complex demodulation can be taken over some specially selected subsets of data.

In practise, a more convenient method of calculating demodulates using the FFT is employed (Banks, 1975). The Fourier spectrum is divided into appropriate frequency bands, each band in turn is shifted to zero frequency, a new Nyquist frequency is defined, and an inverse transform is applied to obtain the demodulated series.

4.4.2 The complex demodulation code

A series of programs were used in order to obtain the impedance tensor estimates and magnetic transfer functions. Results were obtained for 5 out of 7 cassettes recorded during the fieldwork. First, from the file containing the time series of the magnetic and electric field a selected portion was extracted. For each cassette, up to 7 pieces of the time series (each containing 5400 data points) could be extracted and processed. After visual examination of the time series, 4 or 5 pieces of data were extracted from each cassete, because for the rest the signal to noise ratio was low. An example of a good quality LMT data window is shown in fig.4.2. The frequency structure for the demodulation was given in a separate file (13 bands ranging from 24 up to 6000 s) and subsequently the separate pieces of data were transformed into the frequency domain. Then the demodulates (up to 7 demodulates for each frequency band), were merged together. Each merged demodulate contained the number of time series points, and values for each of the 5 MT components.

A first estimate of the ERFs was obtained by following a LS procedure. Estimates for running segments of data were computed, by taking averages over windows of finite length. For each data segment, the median and a robust scale parameter (Chave, 1988) which gives the standard deviation, were estimated. The median was taken as a robust initial estimate of the ERFs. Shorter period data (bands 8 to 13) have shown initially very low coherency values. Therefore, for the above frequency bands a coherence-based test was used, and only data with coherences above a threshold value (>0.8) were accepted.

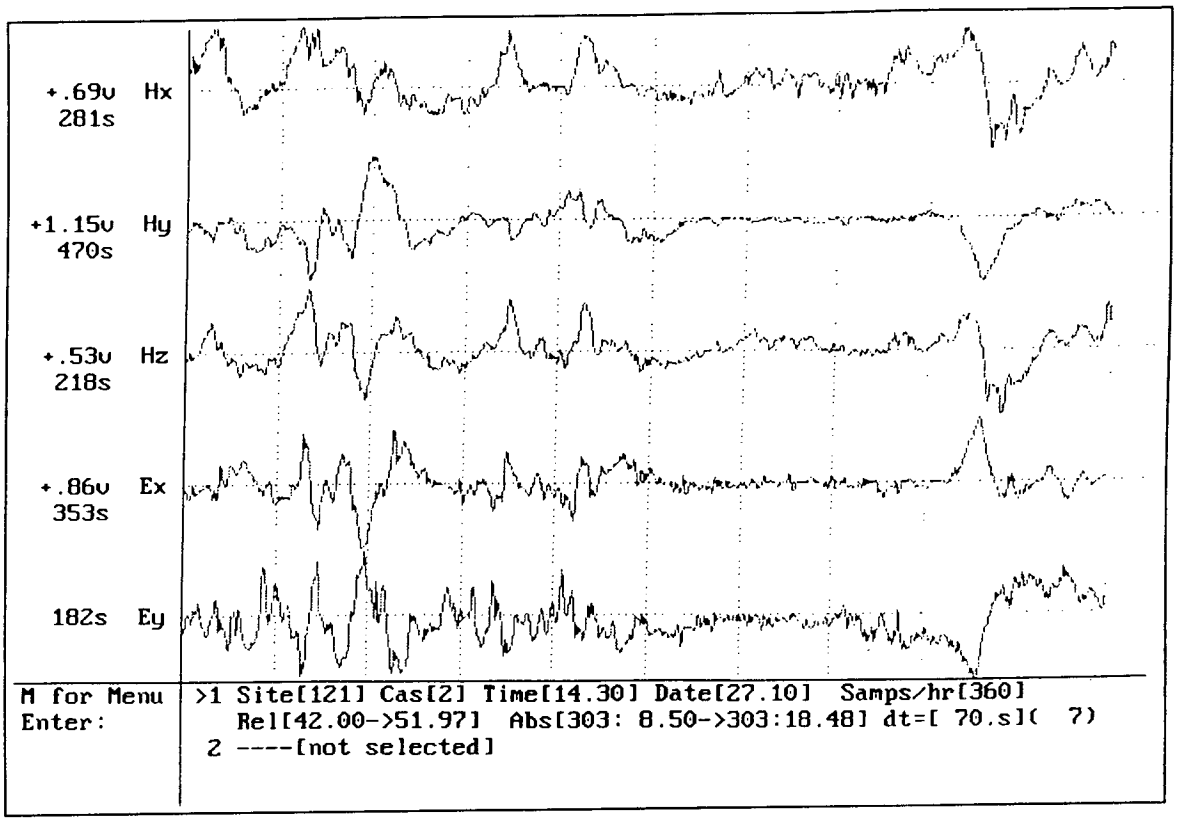

Fig.4.2: Example of a good quality data window from the LMT data. Site 125, cassete 2.

The residuals between the observed demodulates and the predicted values were computed, scaled by the standard deviation of the predicted value and used to generate a set of weights: if the difference exceeds a set value, zero weight is assigned to that point, whereas to the remaining points a uniform weight one is applied. In that way, data whose residuals were more than 1.5 standard deviations (1.5 S.D), were rejected. Despite this, the 3 shorter period bands (25-100 s), even after the above rejection criterion, failed to produce acceptable responses, and so a most severe limit of 1.0 S.D was imposed. And although the majority of the data points were rejected for these bands, the remaining few estimates succeded in providing continuous response curves over all the bands.

Based on the weights generated, the final step of the LMT processing package was to use a WLS procedure which led to a new weighted estimate of the ERF's.

4.5 Presentation of results

Results for the 14 base and 8 remote AMT sites as well as for the LMT data (fig.3.5) are presented in the form of :

a. XY and YX apparent resistivities and phases

b. Number of estimates and predicted coherence

c. pseudosections of apparent resistivity and phase

d. induction arrows magnitude and direction.

4.5.1 Apparent resistivities and phases

Apparent resistivities and phases for the two measured directions at all the sites are shown in fig.4.3(1-21). For the AMT range some general comments can be made:

1. Data are very noisy in the period range 3-10 s. This range actually belongs to the "dead band", where the signal level is so low that noise predominates in the recording. Sites such as 121, 124 and 132, show almost no results for $T > 0.5$ s.

2. Noise is more pronounced in the phase curves.

3. Above 1 s, the XY and YX components for each site show a split in the resistivity curves. In the phase curves the split occurs earlier ($0.1 < T < 1$ s).

4. Some components at the base sites are shifted compared to the corresponding remotes (XY for site 129, 128 and 122, YX for 121, XY and YX for 120, 125 and 126), while their phases remain unaffected. This suggests that there must be a "static shift" problem (chapter 5).

5. Sites at the centre show apparent resistivity values relatively higher (~100 Ohm m at the highest frequency) than those close to the edges of the peninsula (~50 Ohm m).

The 2 LMT sites were linked to AMT sites 125 and 123 in the S and in the N of the peninsula respectively (fig.4.3.19-20). For the LMT part the following are mentioned:

6. The XY component of 125l and the YX of 123l reach resistivity values up to 1000 Ohm m, while for the other two the values are less than 100 Ohm m. This suggests an anisotropy at the depth corresponding to these periods.

7. The phase curves do not decrease as the resistivity increases, but they follow a more complicated pattern.

The mismatch between the AMT and LMT curves may be due to the application of different processing techniques for the two data sets respectively.

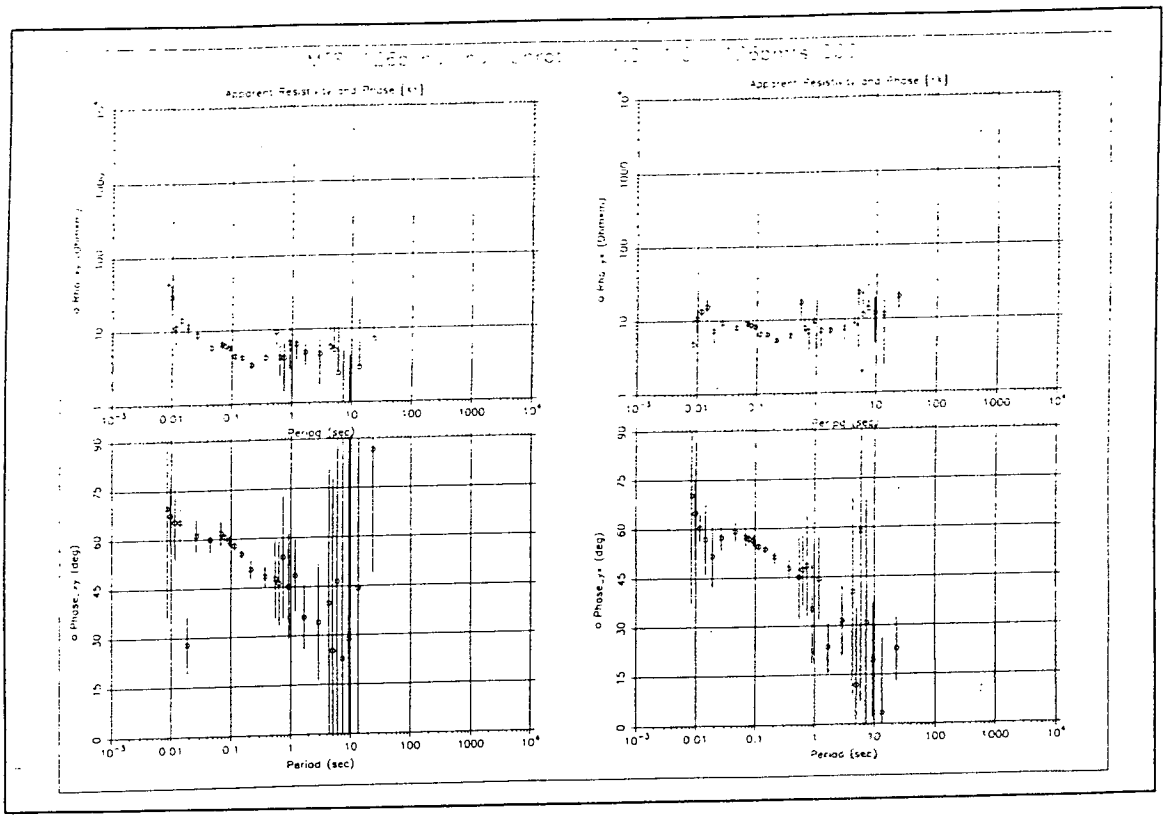

Fig.4.3.1

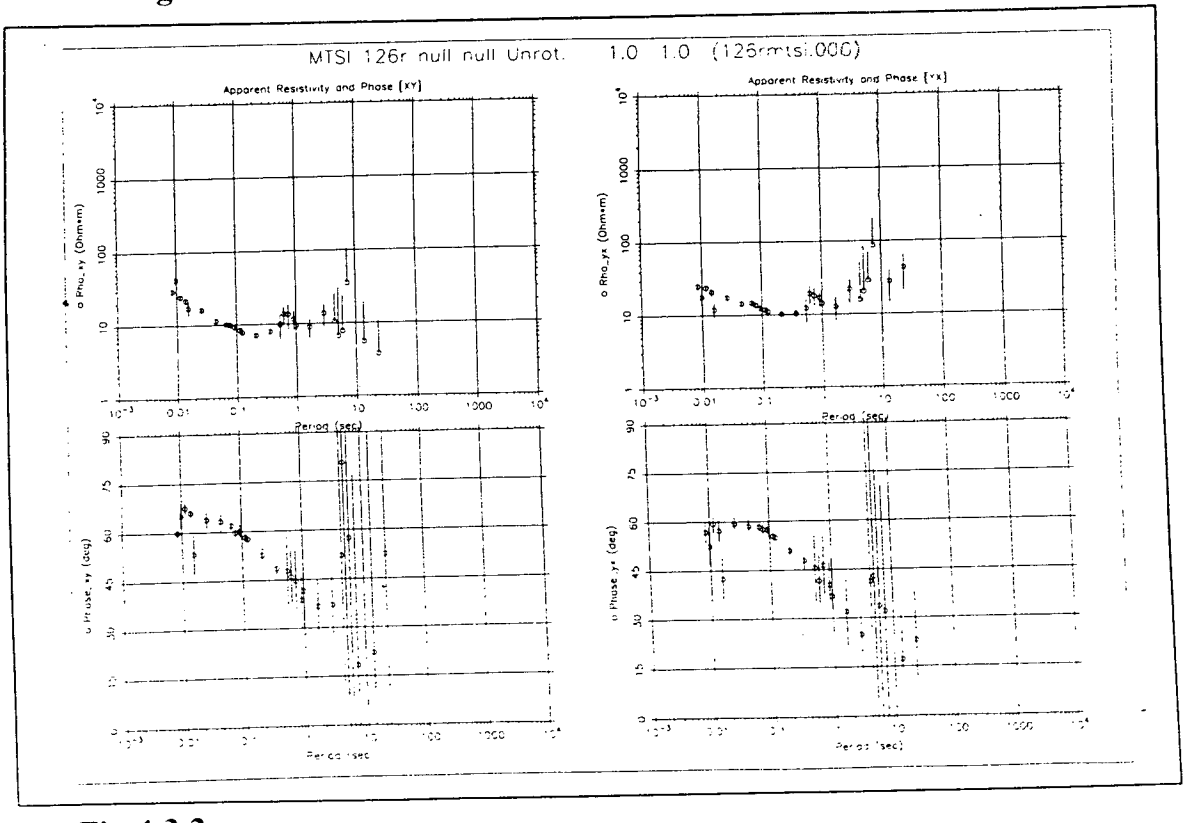

Fig.4.3.2

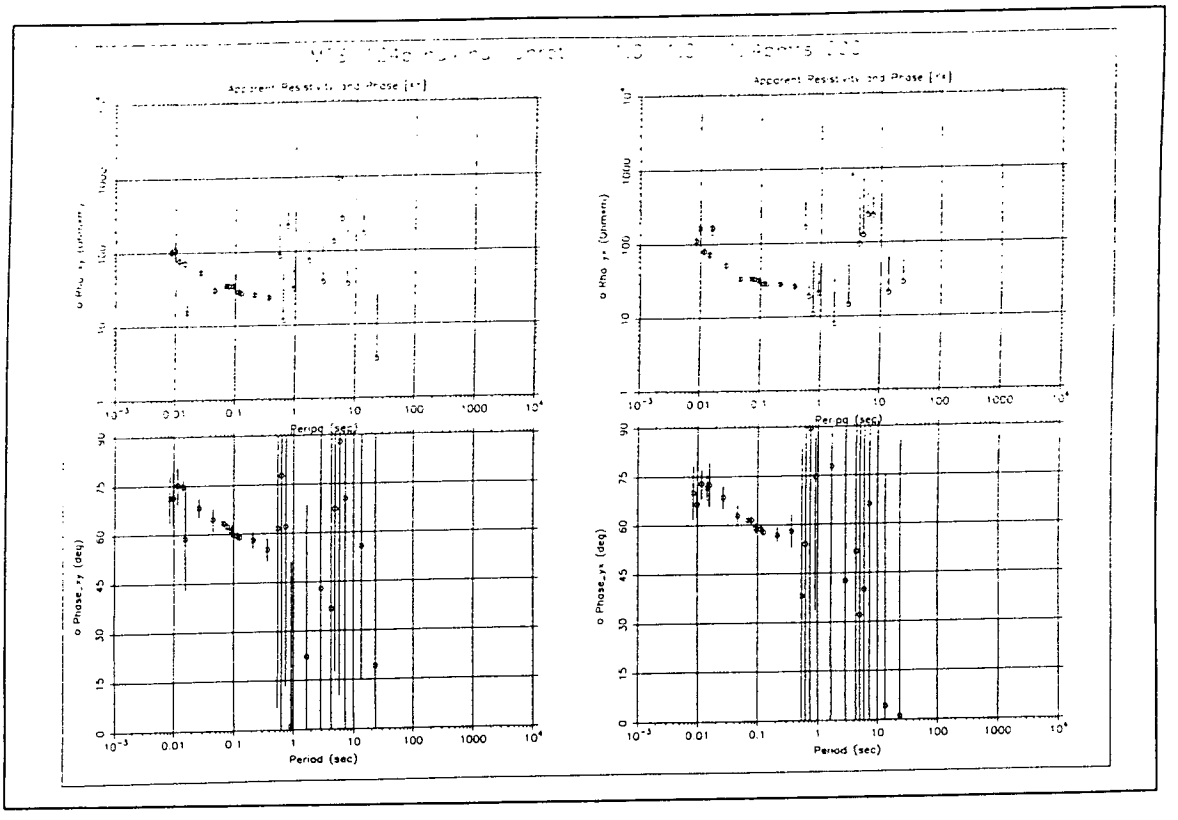

Fig.4.3.3

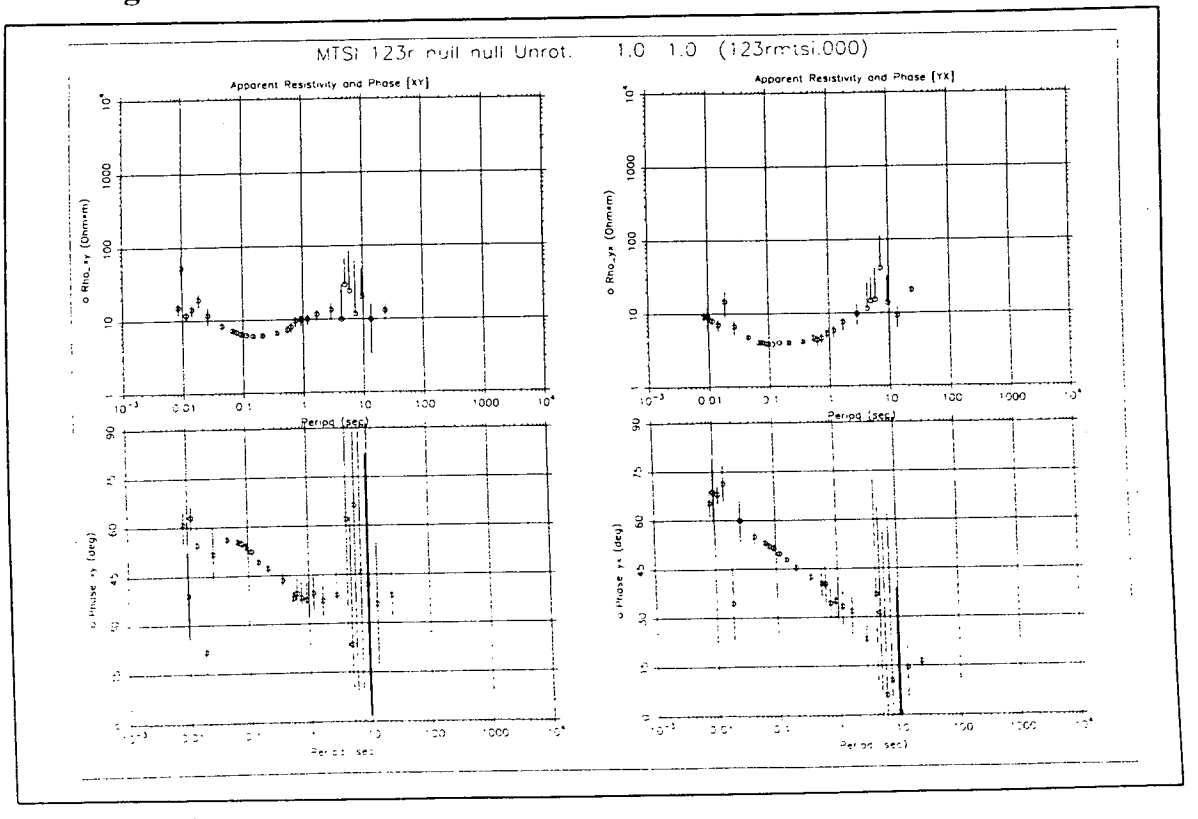

Fig.4.3.4

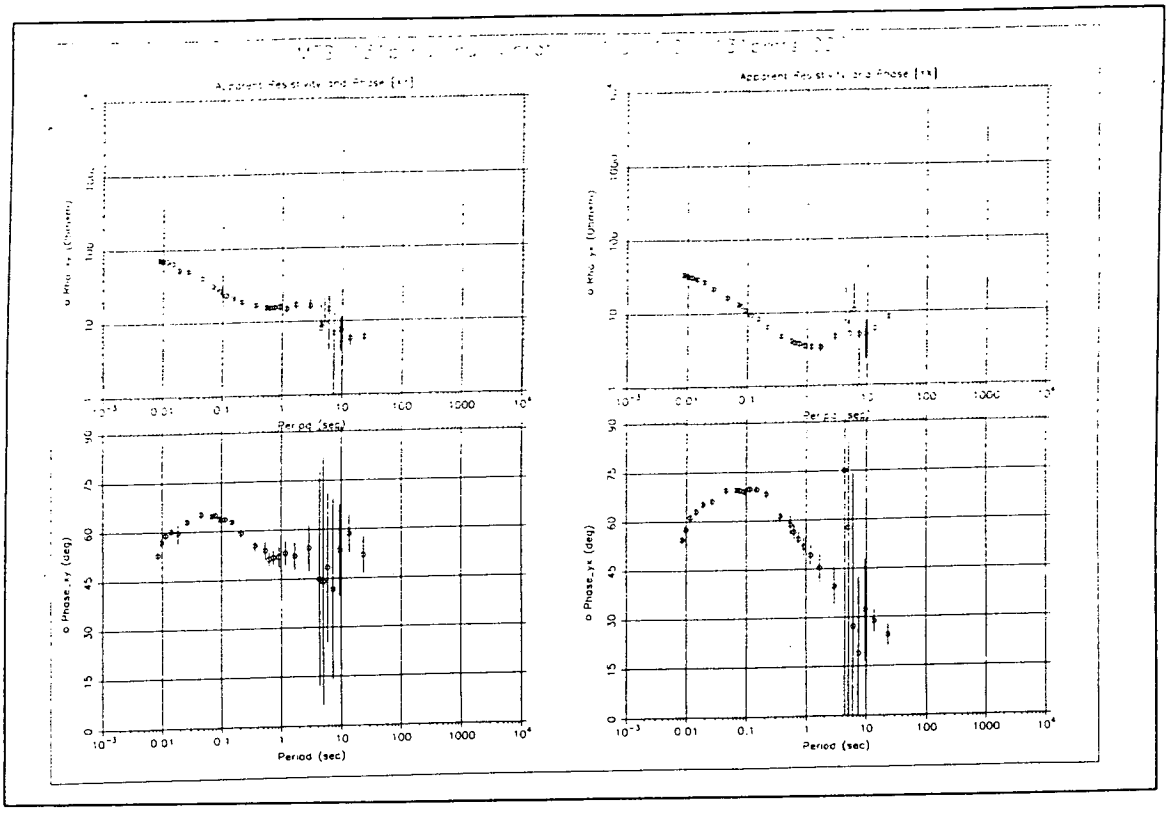

Fig.4.3.5

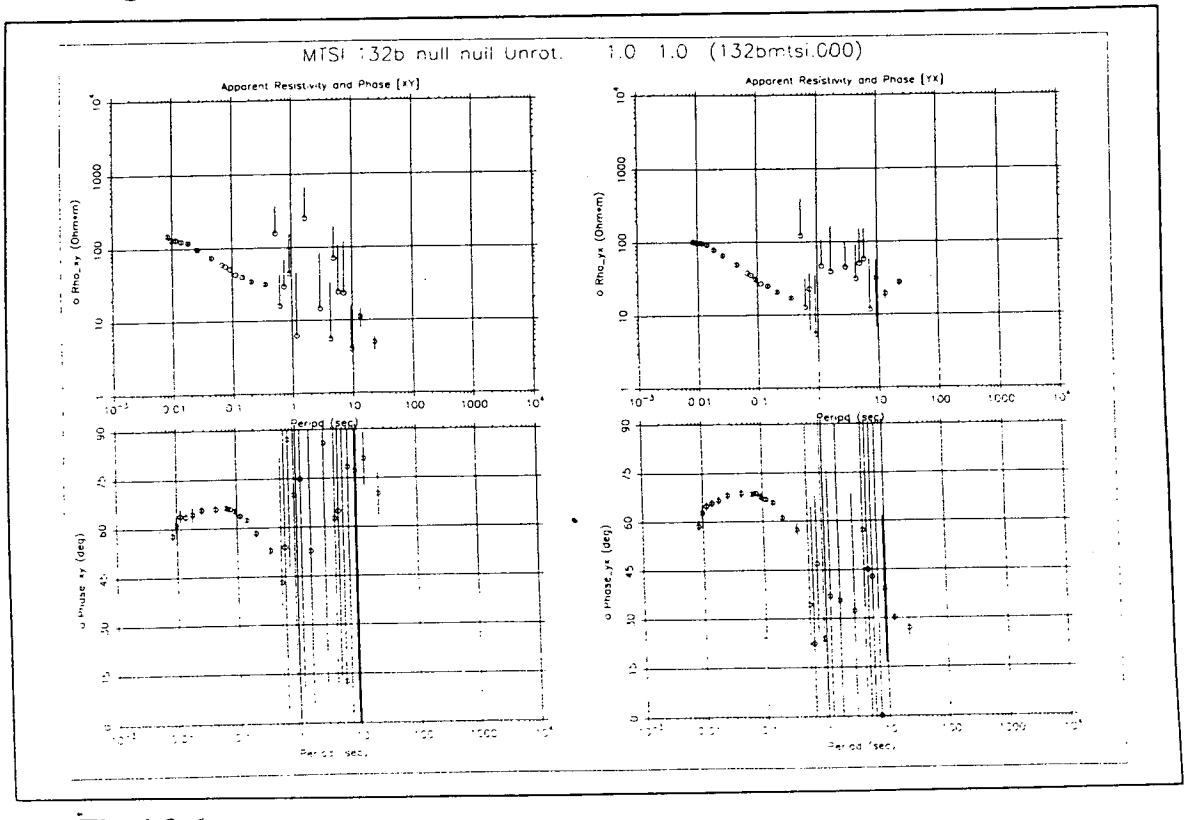

Fig.4.3.6

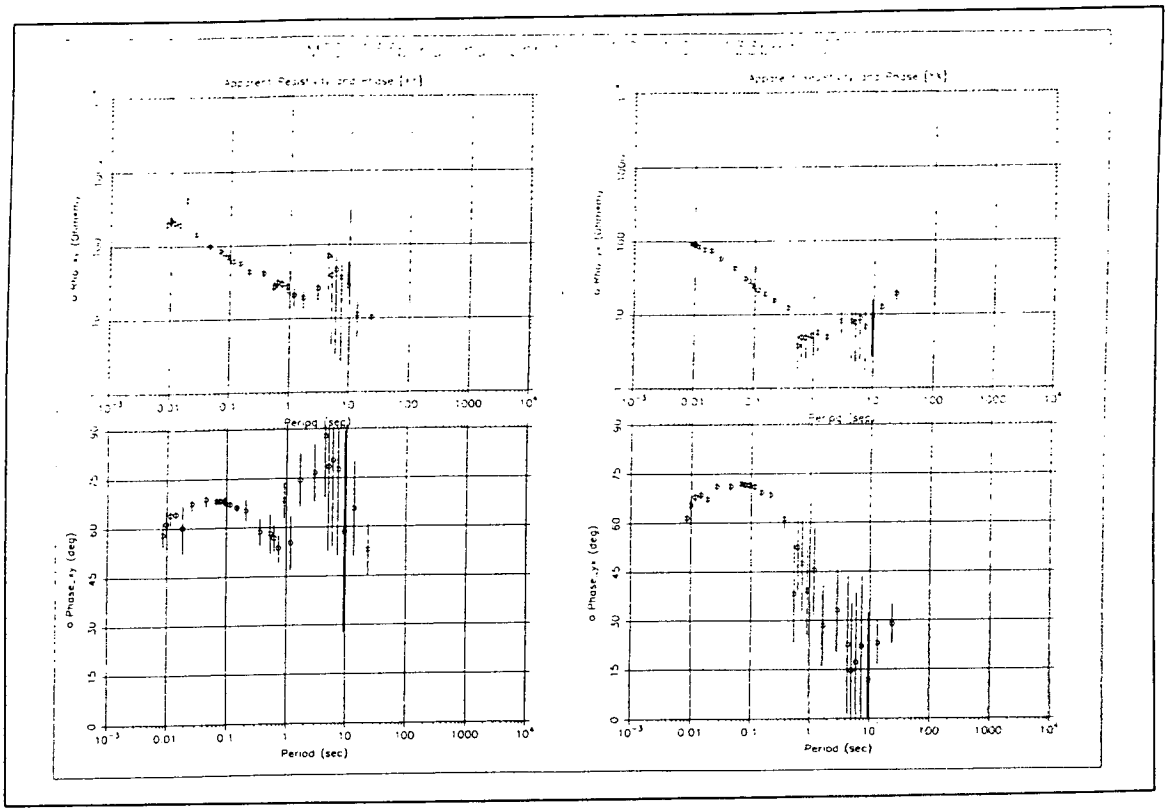

Fig.4.3.7

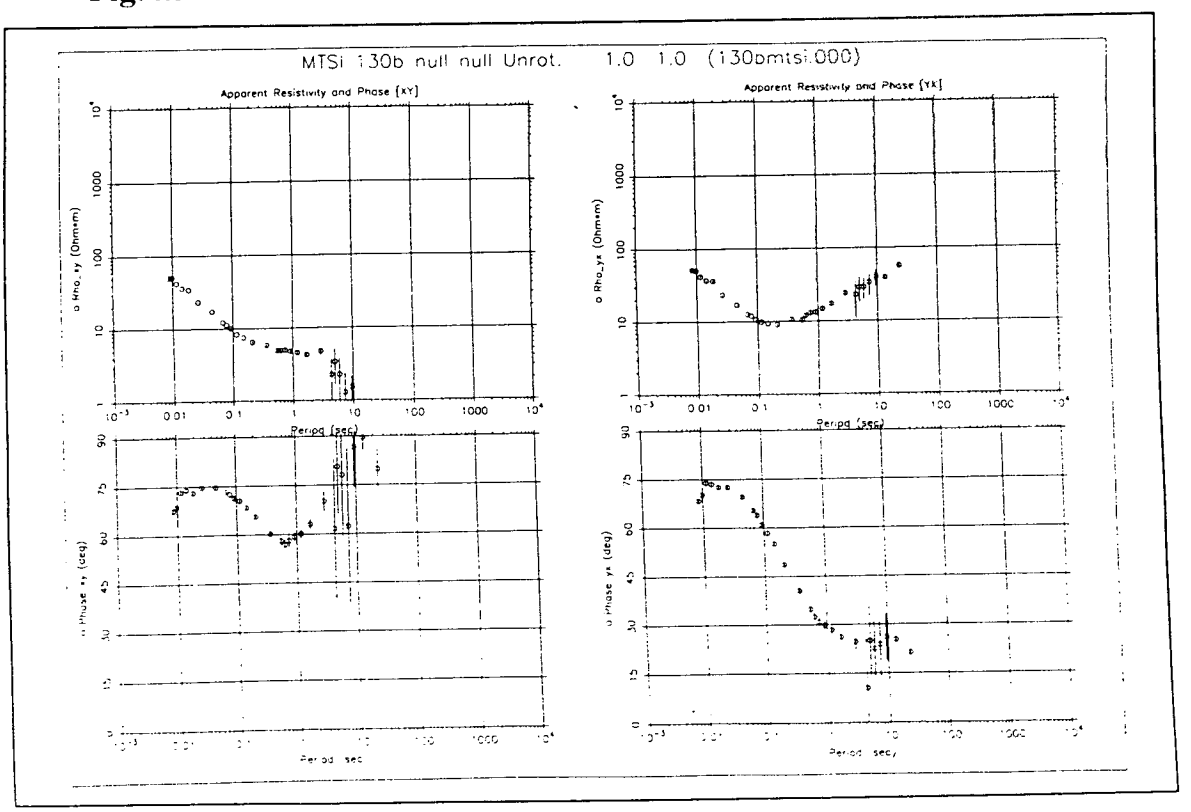

Fig.4.3.8

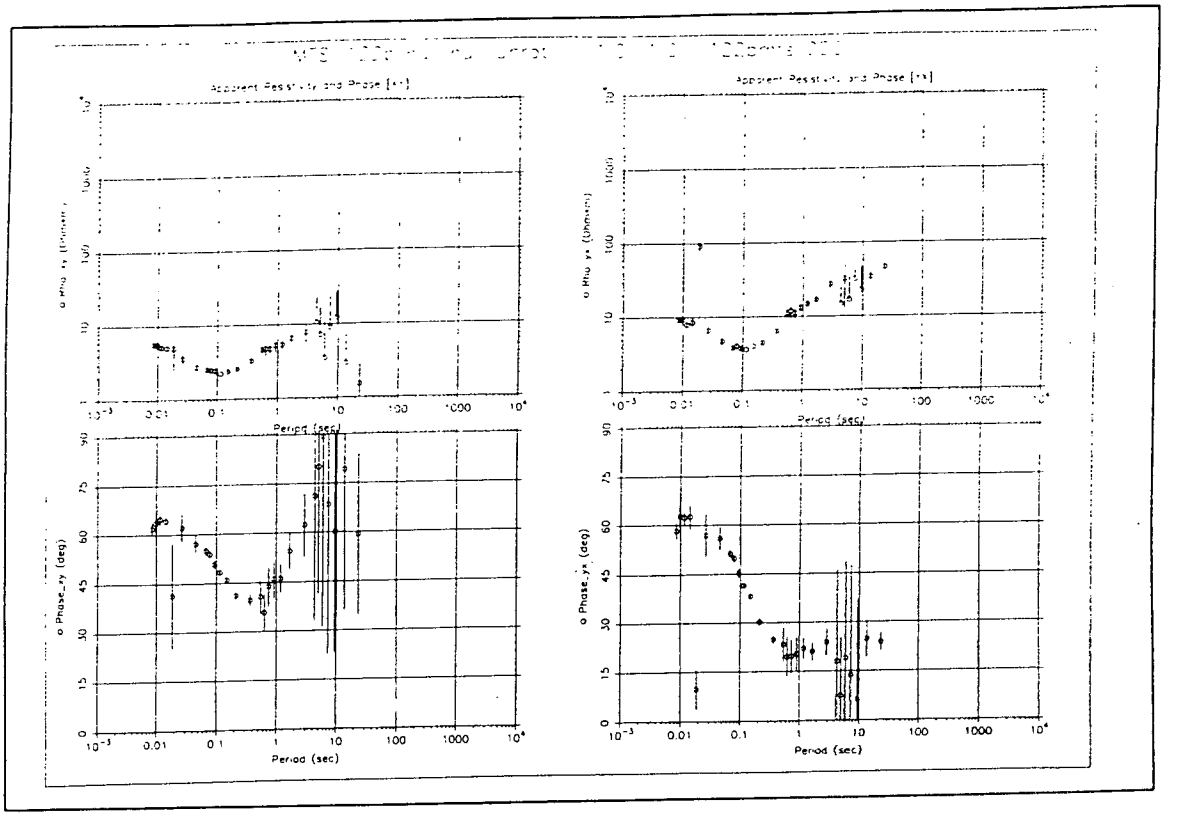

Fig.4.3.9

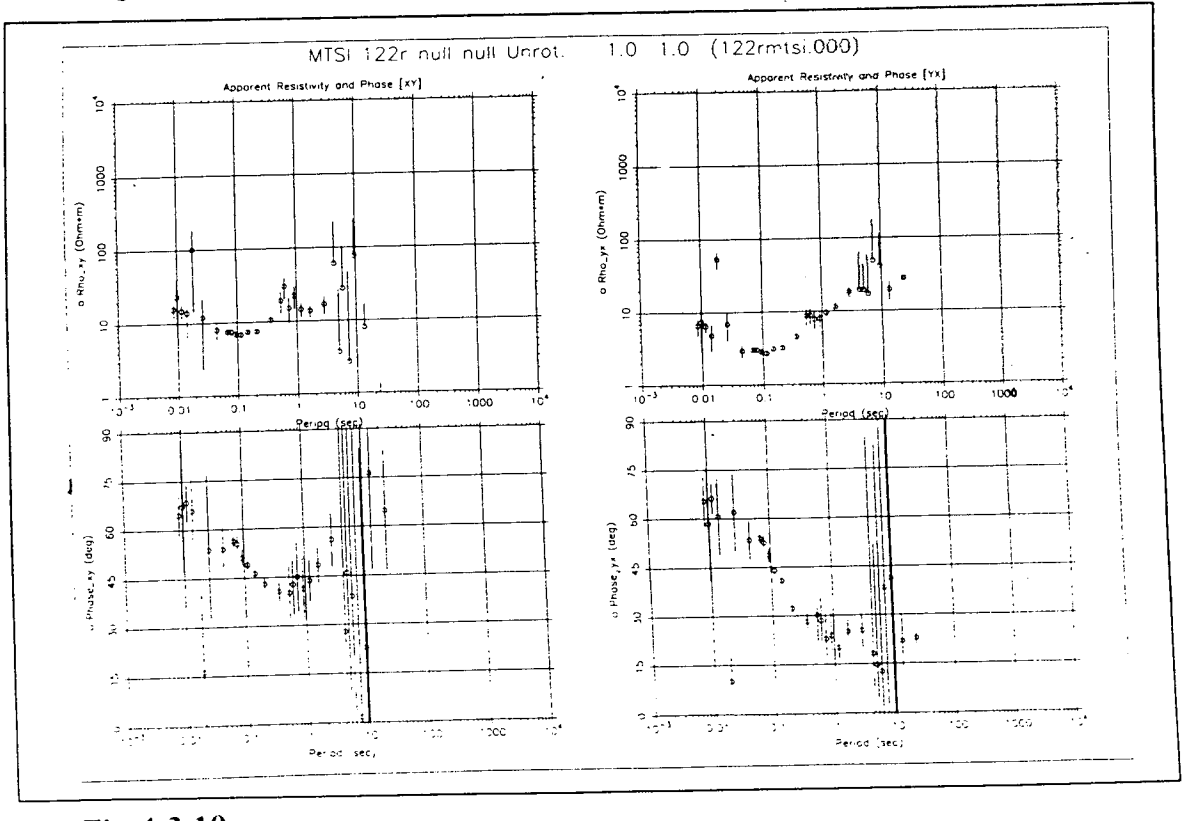

Fig.4.3.10

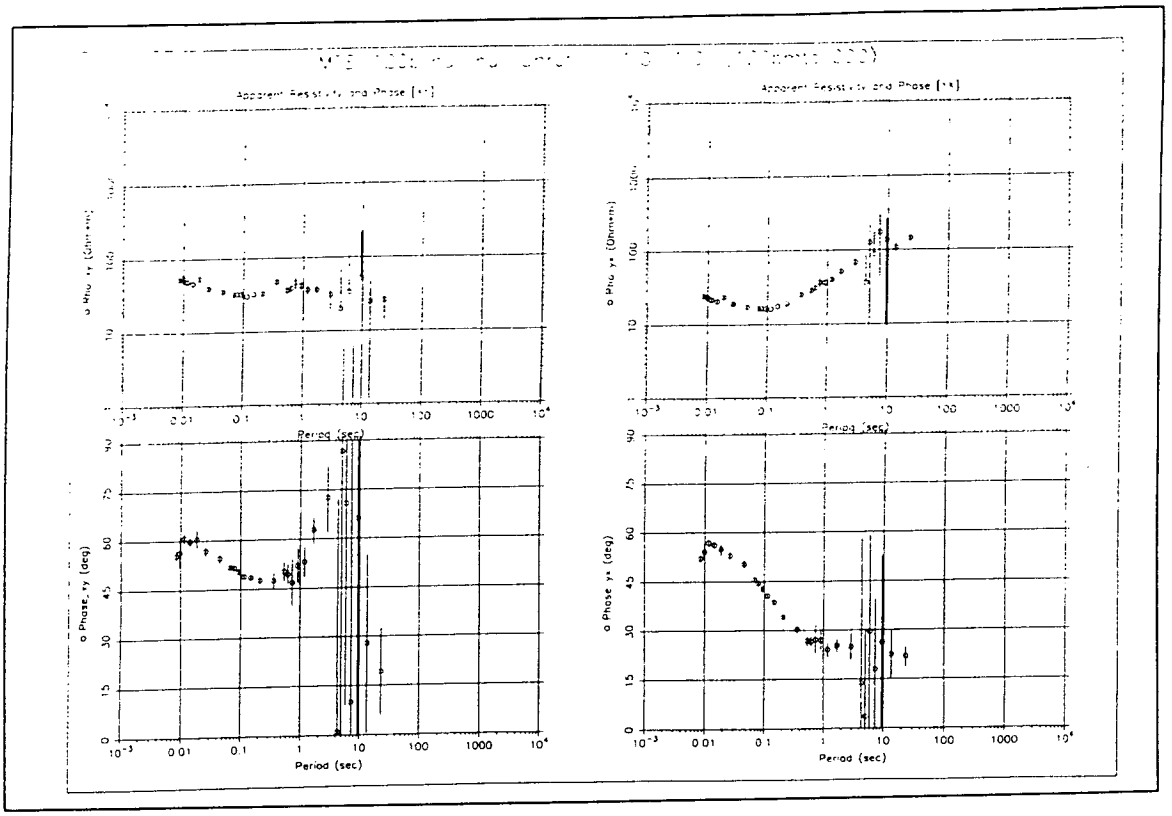

Fig.4.3.11

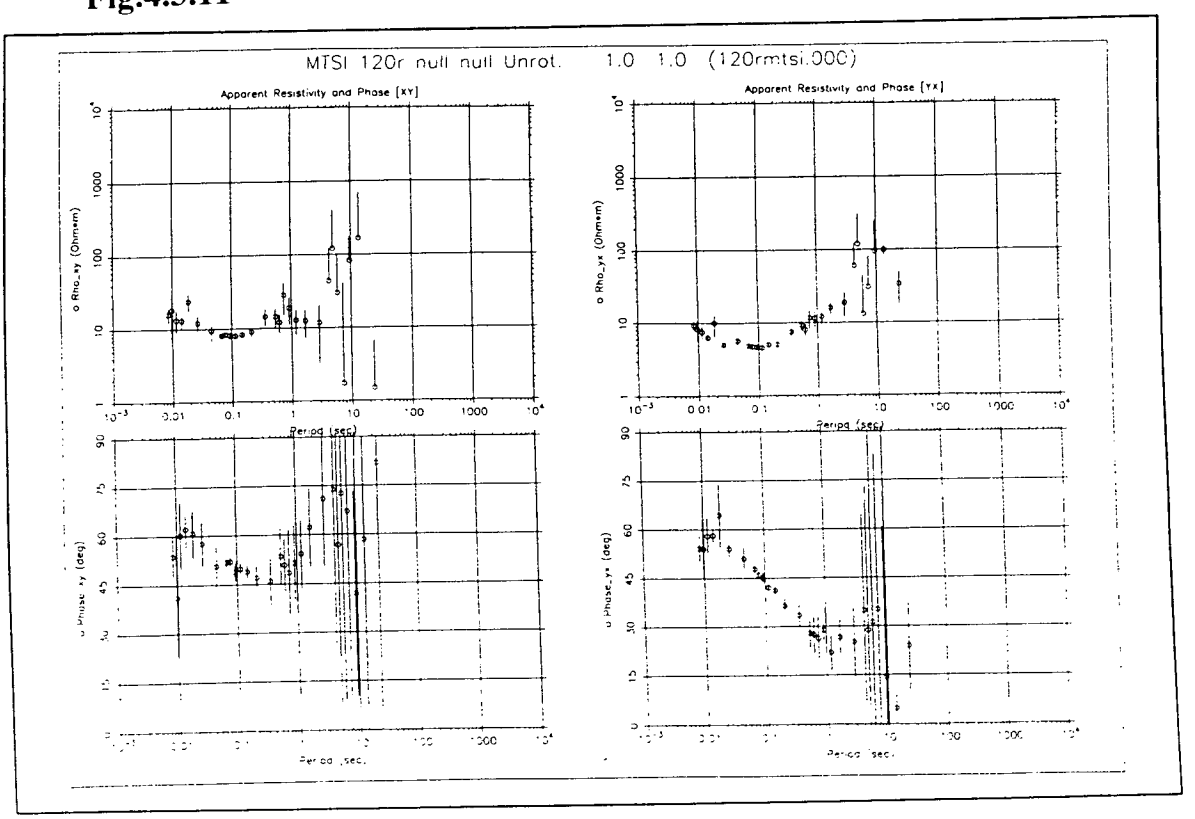

Fig.4.3.12

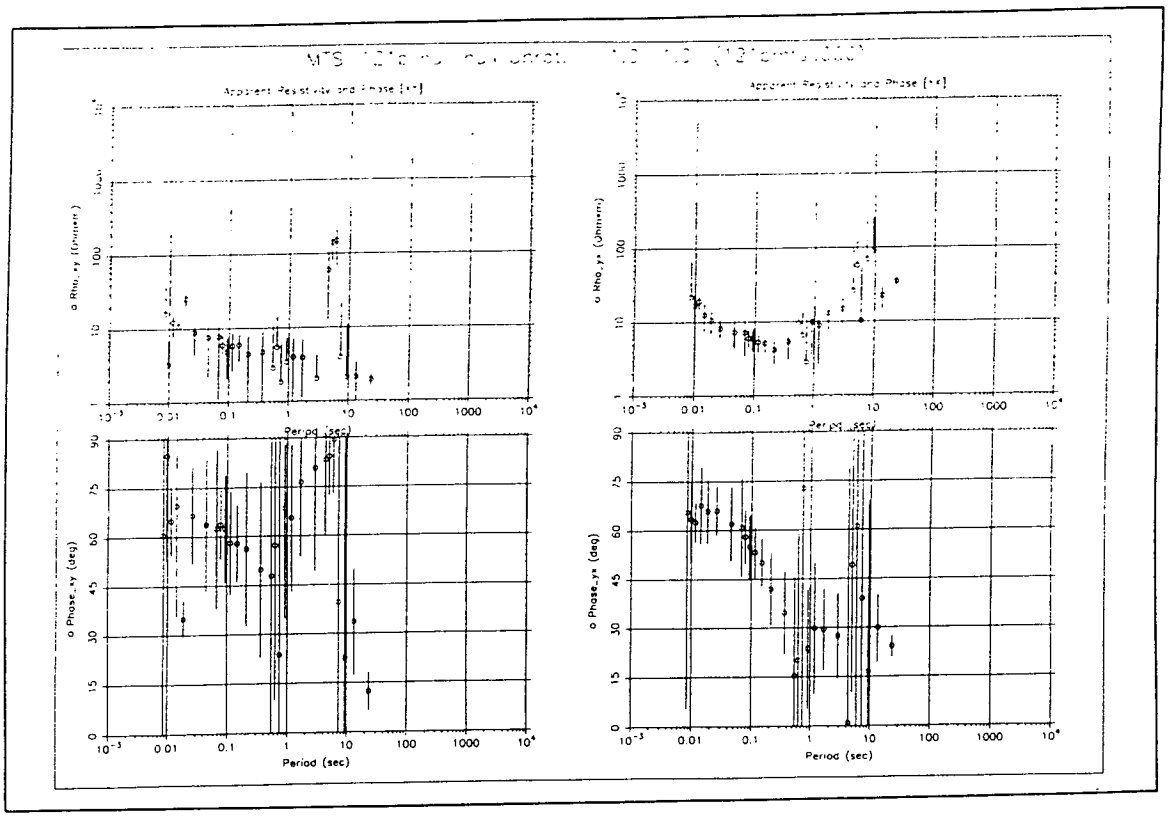

Fig.4.3.13

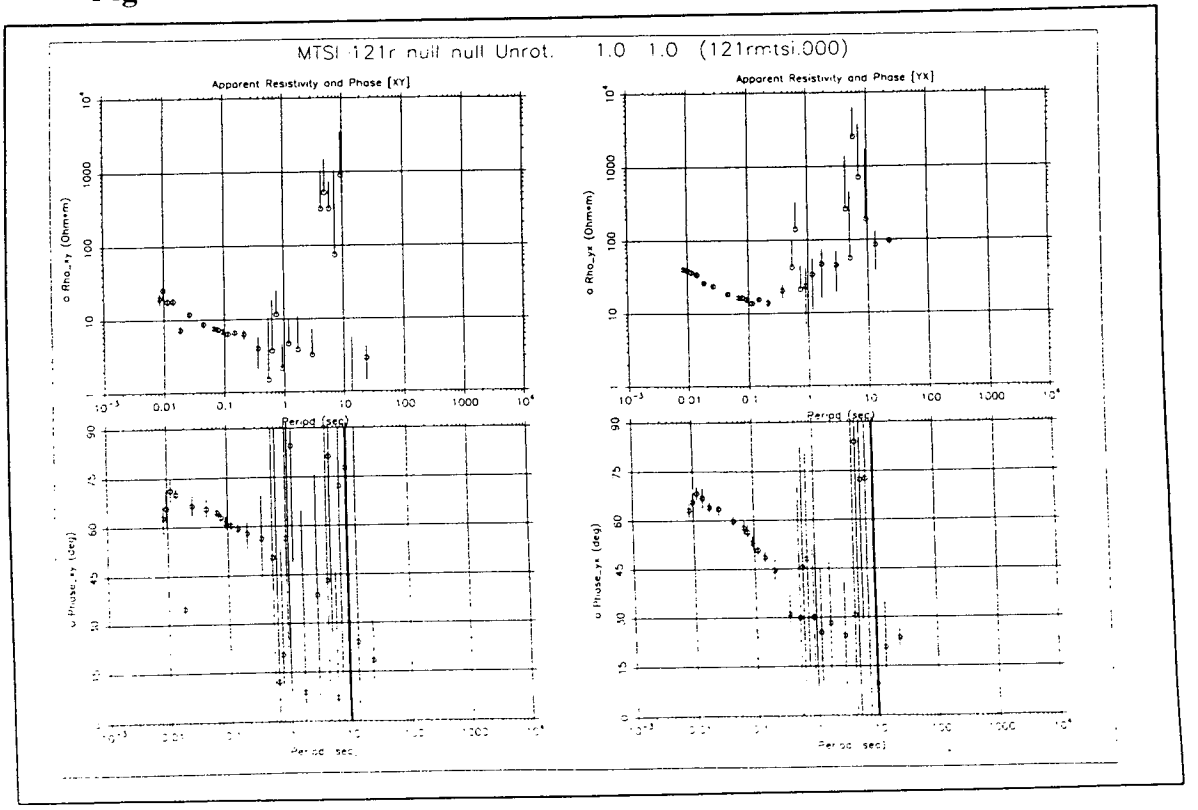

Fig.4.3.14

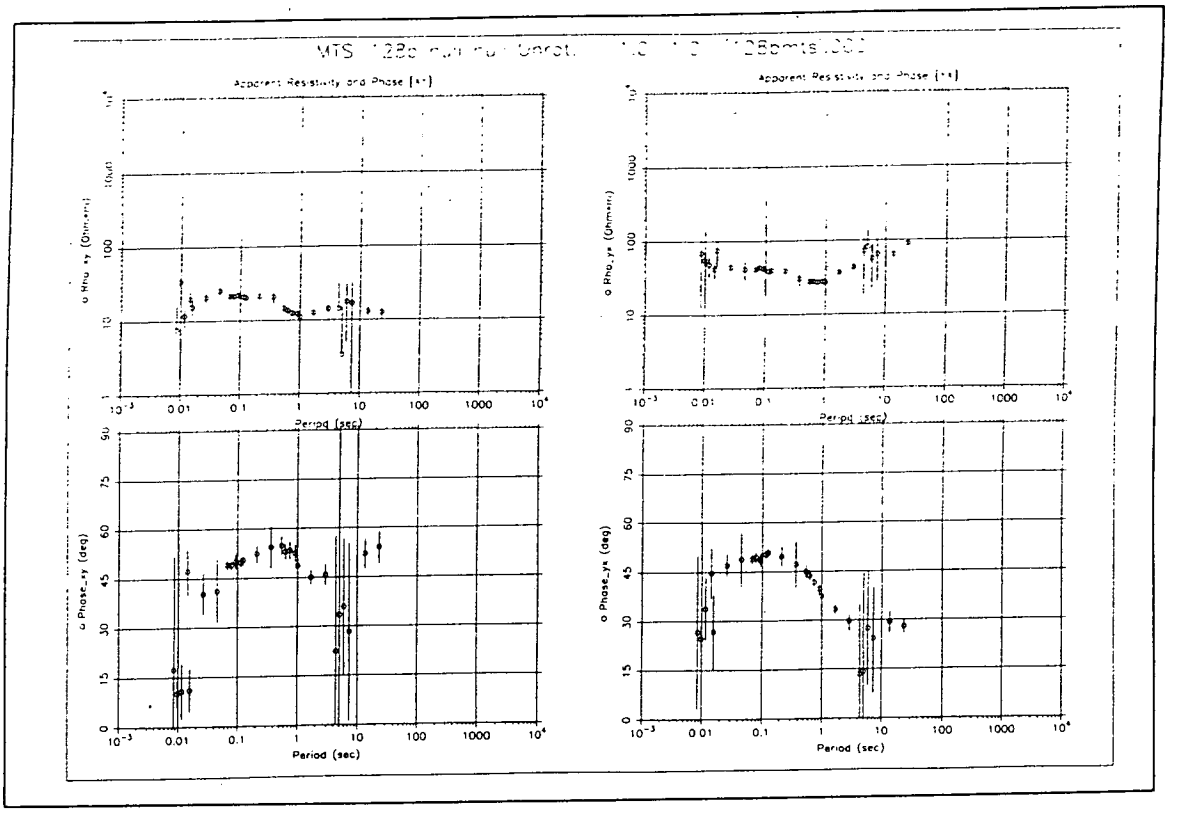

Fig.4.3.15

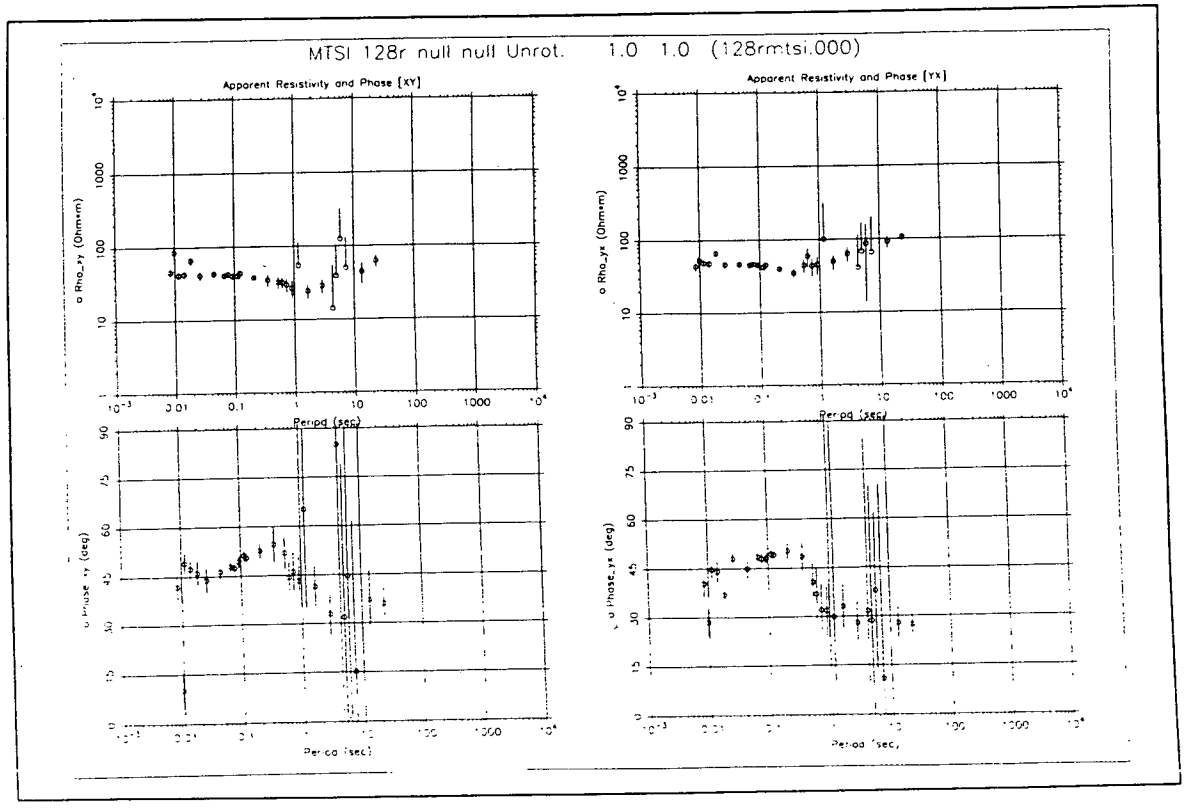

Fig.4.3.16

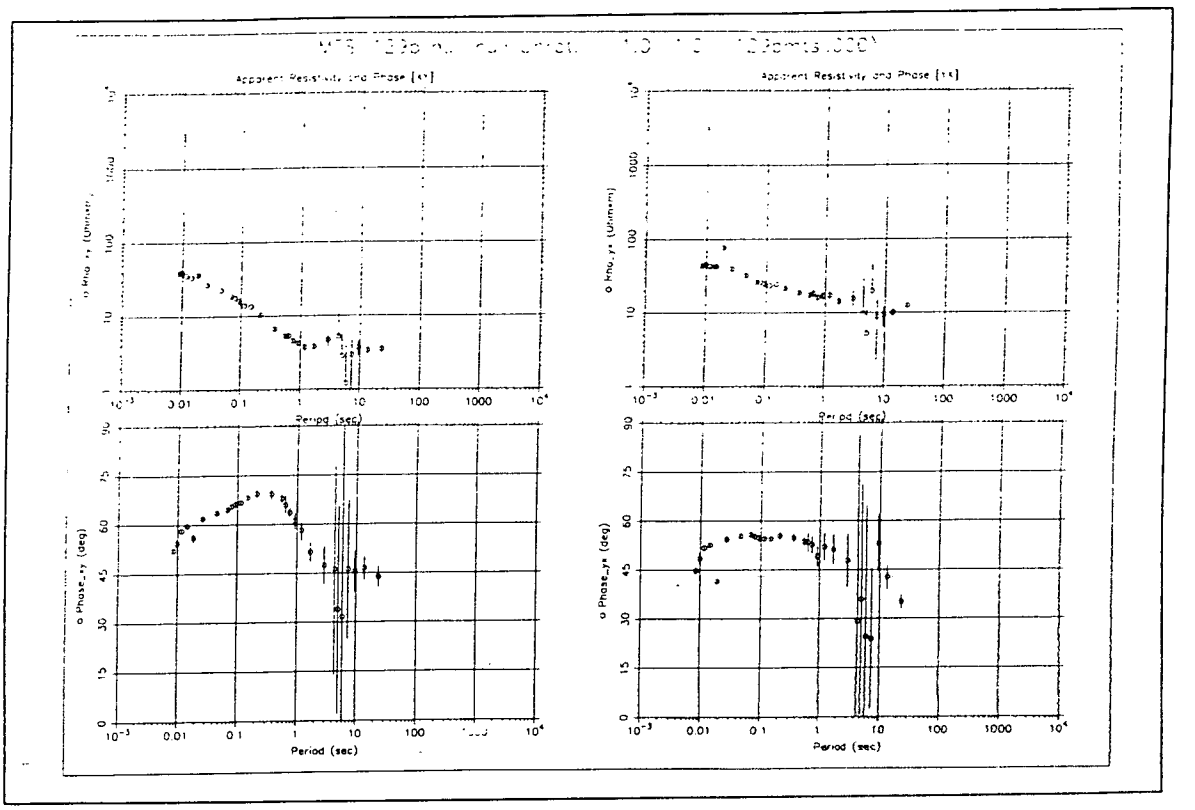

Fig.4.3.17

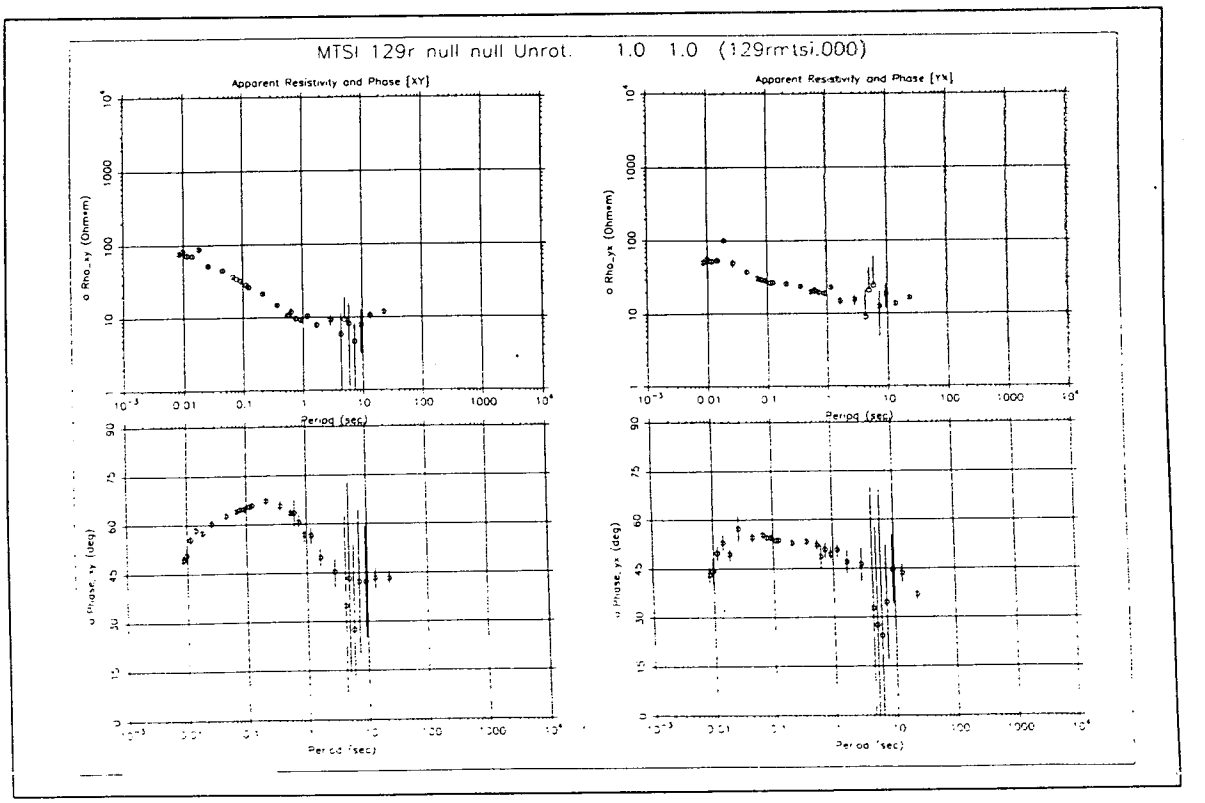

Fig.4.3.18

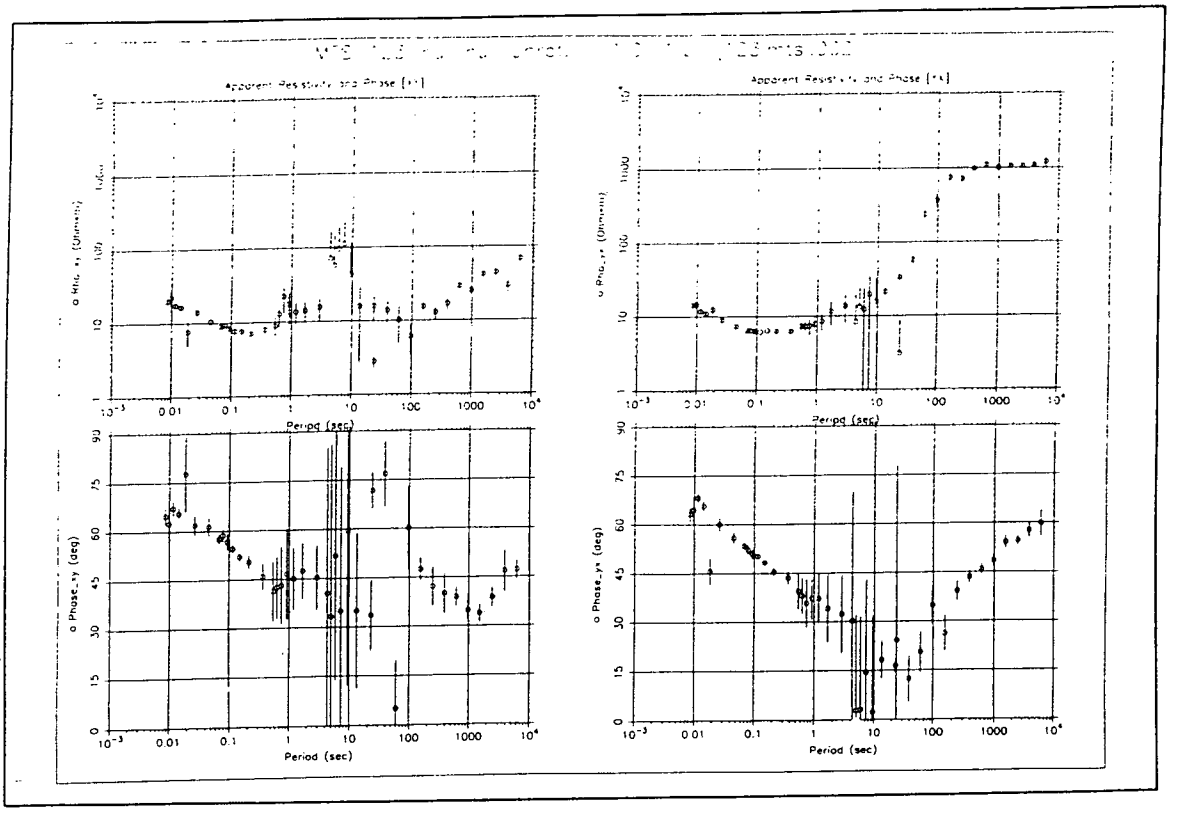

Fig.4.3.19

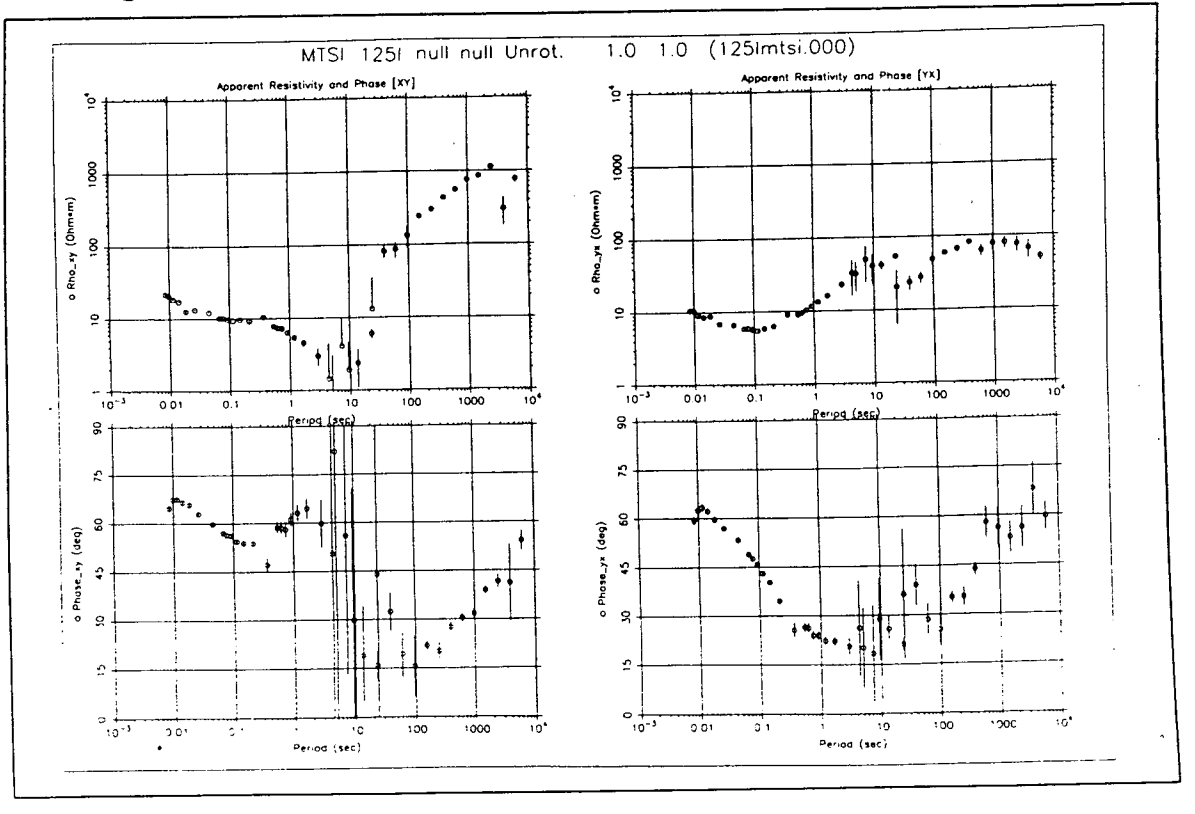

Fig.4.3.20

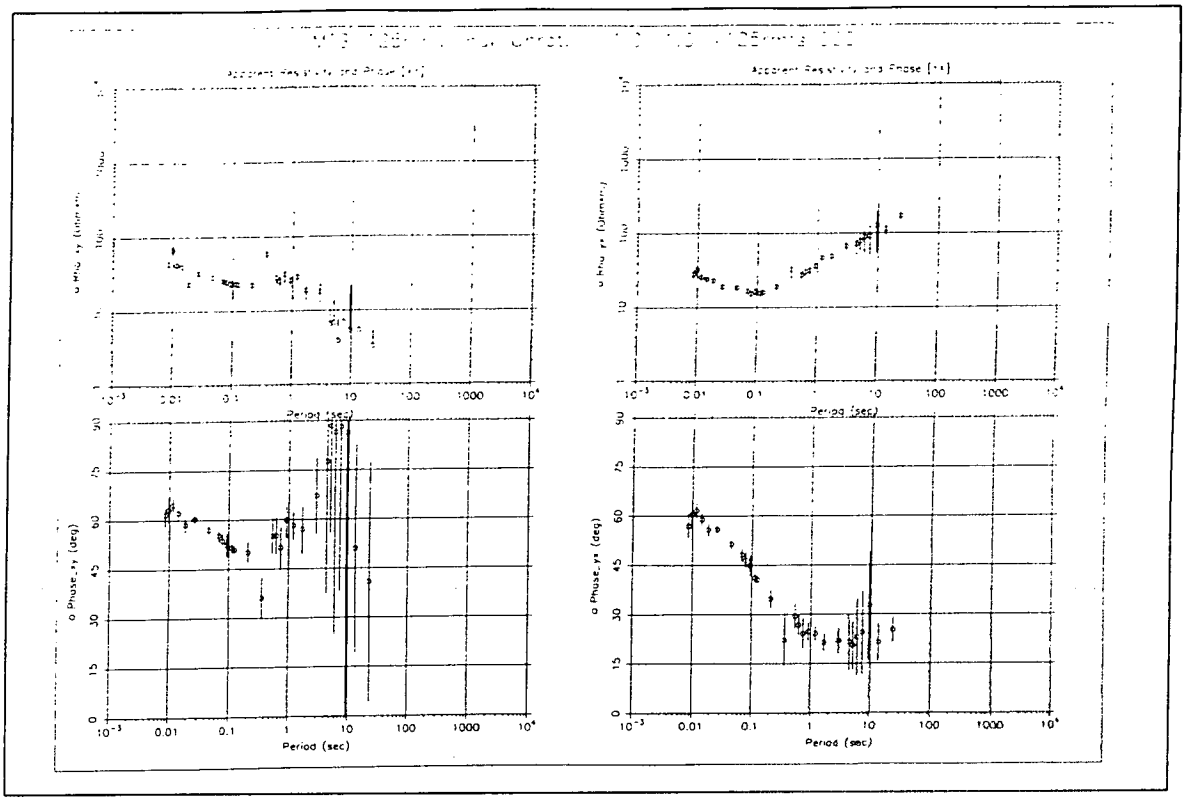

Fig.4.3.21

Figs.4.3.1-4.3.21: Unrotated apparent resistivities and phases for the two measured directions. Results are presented for all the sites.

XY: N-S direction. **YX:** E-W direction. **b:** base site. **r:** remote site.

4.5.2 Number of estimates and predicted coherence

The number of estimates (fig.4.4) decreases as the period increases, because of the longer recording time needed and also because of the difficulty in obtaining good data quality at these periods. The minimum number was recorded at periods between 3 and 10 s. Predicted coherence values are above 0.9 (except at a few periods) for all the sites, for periods up to 1 s and the last two AMT periods. In contrast, between 1 and 10 s the data quality is very poor for the majority of sites showing very low coherency values. Also it is generally higher for the YX than for the XY component (fig.4.4).

For the LMT data, in which more severe selection criteria were applied, the predicted coherence is good (>0.78) over all the period range, but the number of estimates is generally small, especially at the shorter periods (table 4.1).

Sites →		**125l**		**123l**	
Band	**T (s)**	**coh**	**P**	**coh**	**P**
1	6143	0.9375	90.3%	0.9925	68.5%
2	3839	0.9775	86.4%	0.9372	81.2%
3	2457	0.9930	85.4%	0.9905	82%
4	1536	0.9268	85.1%	0.9536	81.9%
5	975	0.9495	89.6%	0.9171	83.1%
6	614	0.8975	88%	0.9061	84%
7	389	0.8906	89%	0.9288	83.5%
8	245	0.8908	3.36%	0.8912	7.13%
9	154	0.7851	2.6%	0.9112	2.2%
10	97	0.8438	2.46%	0.7851	0.8%
11	61	0.8729	1.73%	0.9904	0.5%
12	39	0.9999	0.6%	0.8609	0.6%
13	24	0.9525	0.9%	0.9943	0.7%

Table 4.1: Predicted coherence values and percentage of the amount of data used for the two LMT sites. **Coh:** predicted coherence.**P:** percentage of the data used.

From the above table it is quite clear that for bands 8-13, in order to keep the predicted coherence at the same level as for the other frequency bands, and therefore to have more reliable estimates for the period range between 24-250 s, it was necessary to throw away a great part of the data.

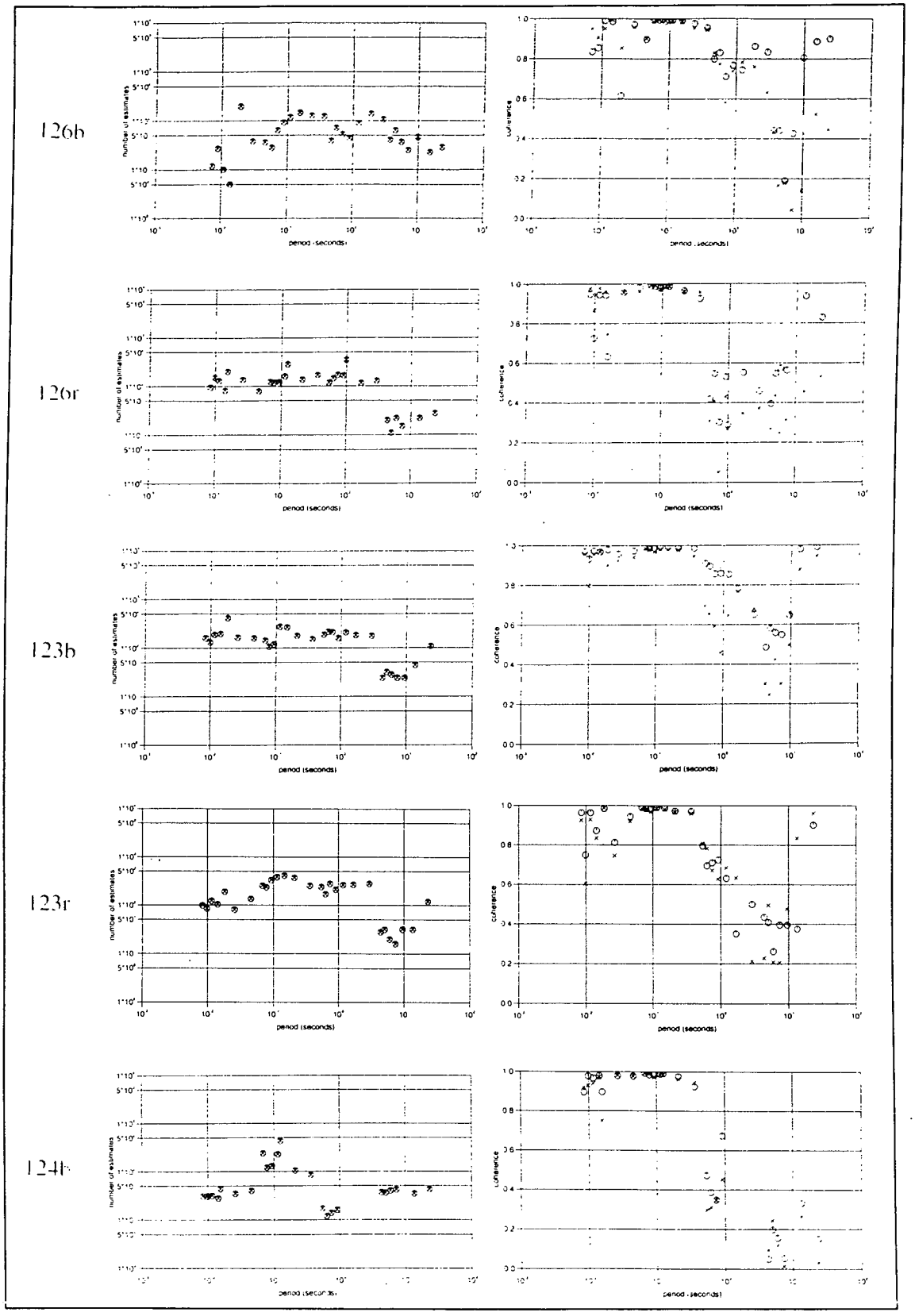

Fig.4.4(continued): Number of estimates and predicted coherence for the AMT data. (The scale for the number of estimates is 1-10^4).

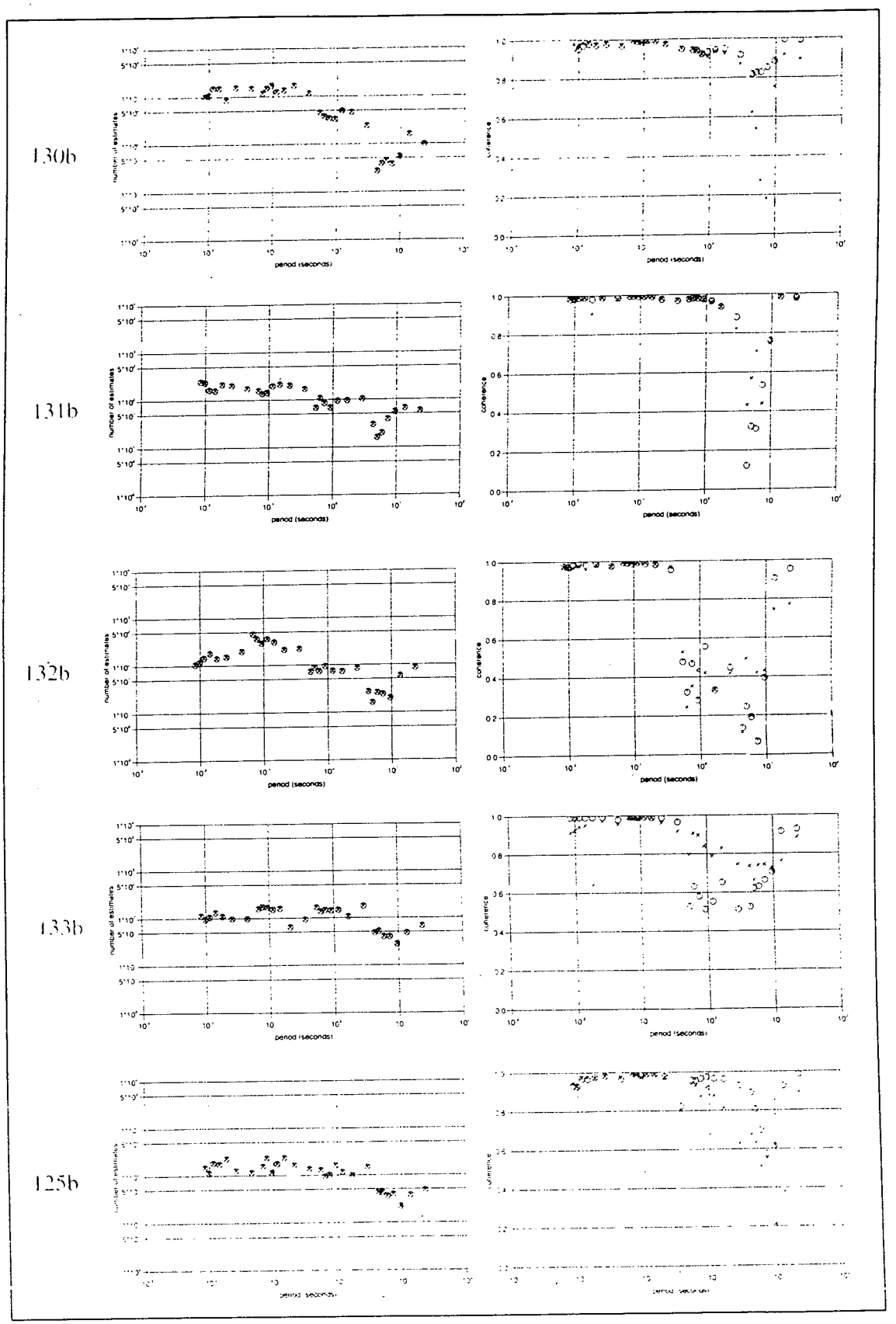

Fig.4.4 (continued): Number of estimates and predicted coherence for the AMT data.

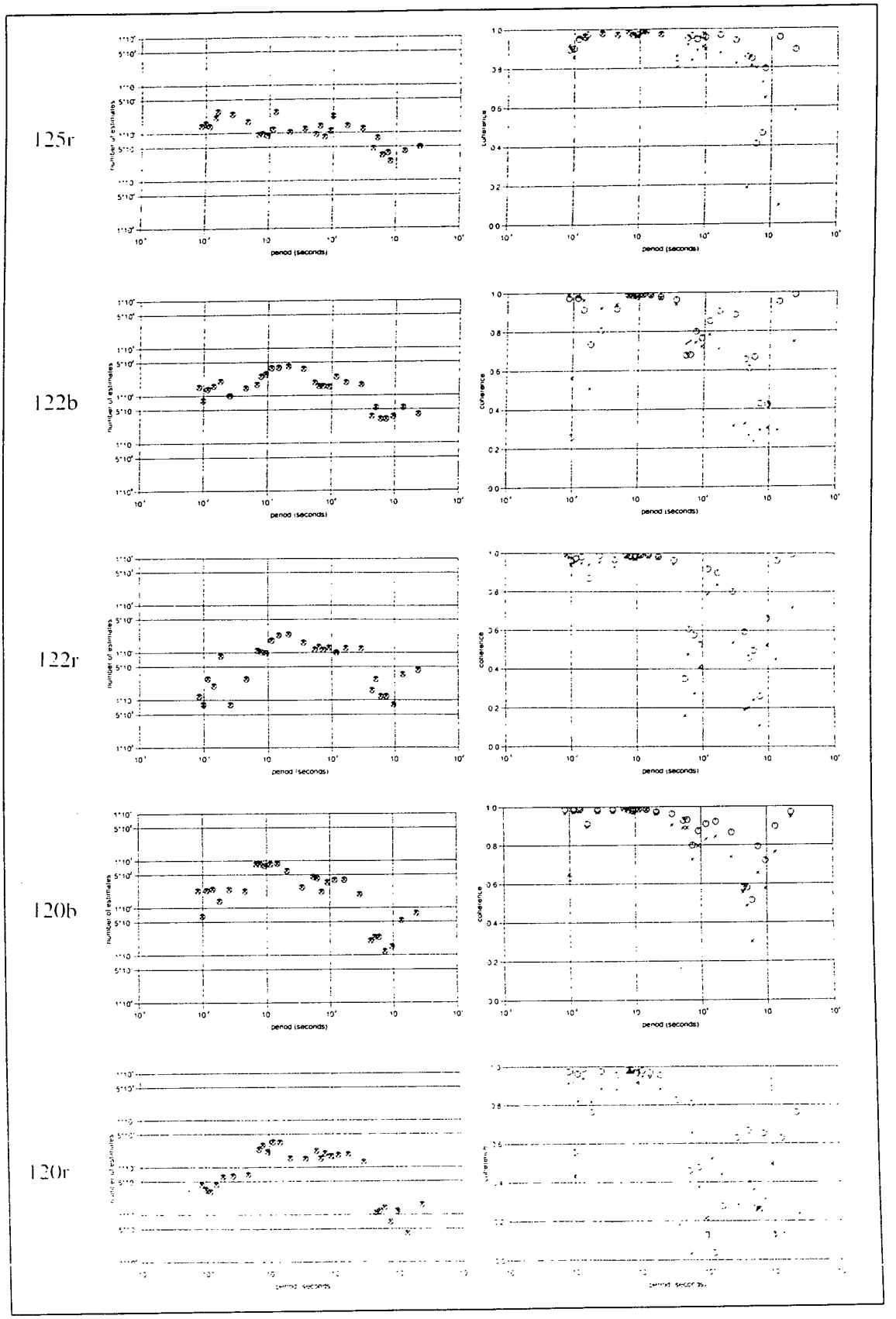

Fig.4.4 (continued): Number of estimates and predicted coherence for the AMT data.

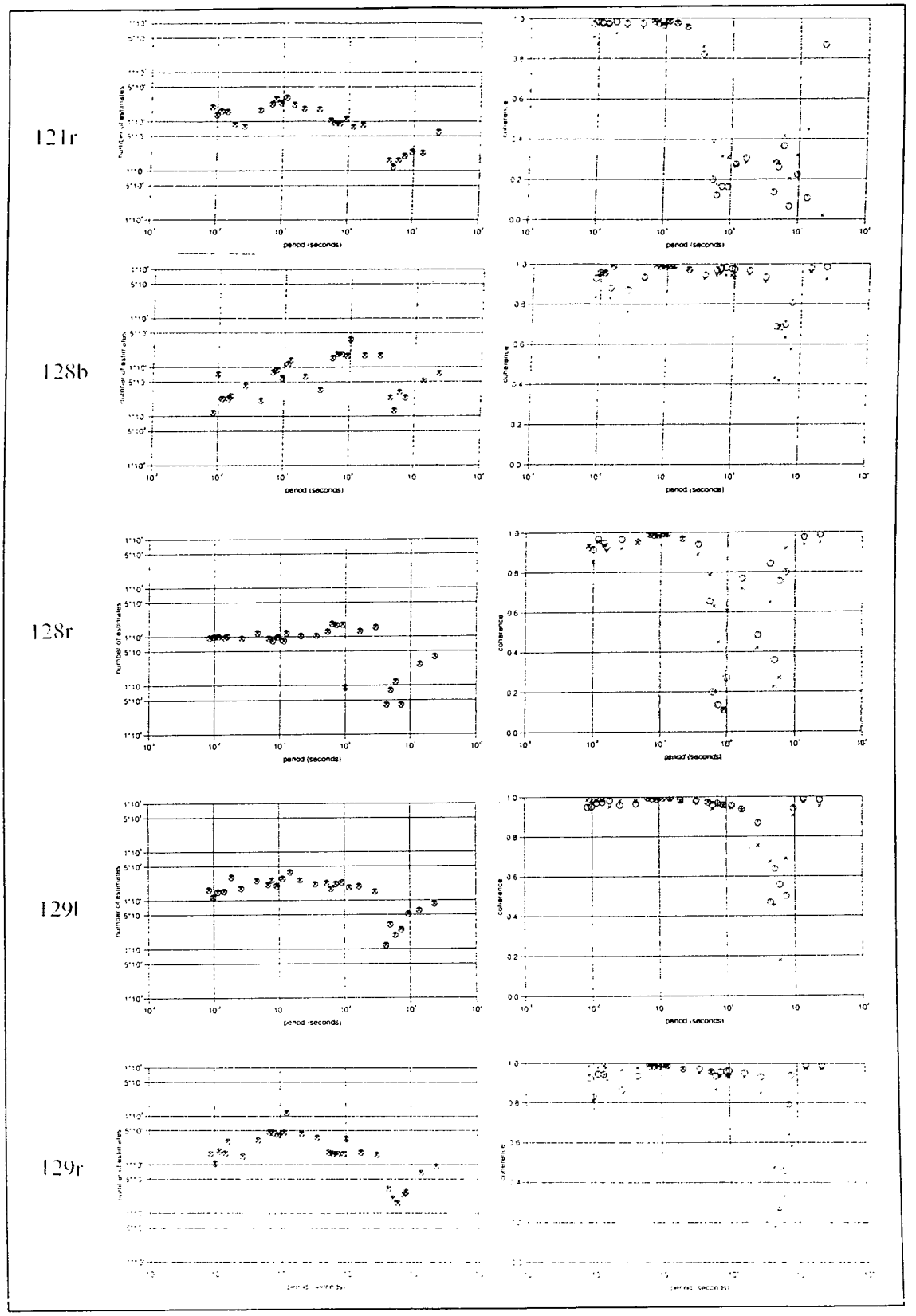

Fig.4.4 (end): Number of estimates and predicted coherence for the AMT data.

b: base site. **r:**remote site. **oblique crosses:** XY component. **circles:** YX component.

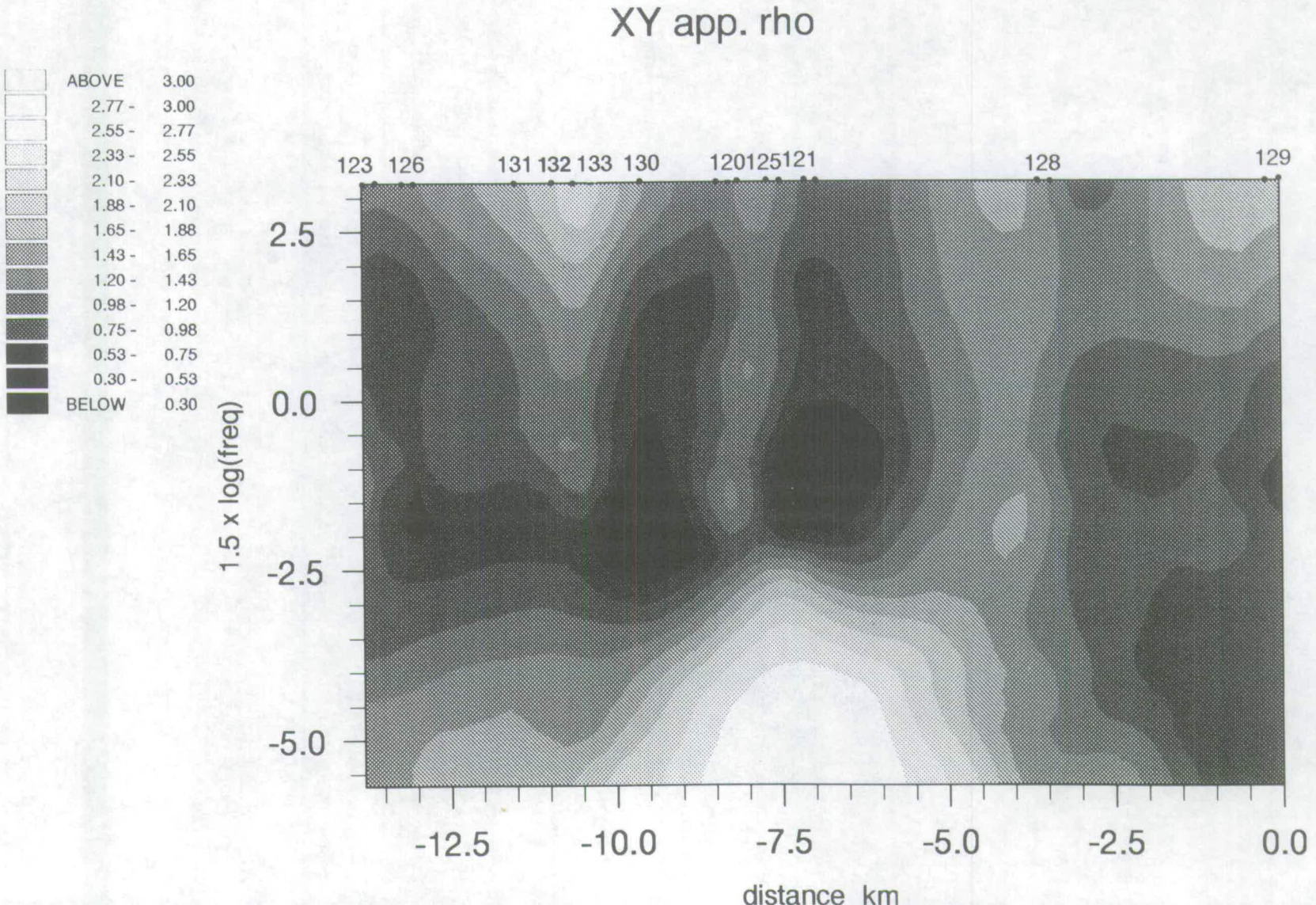
XY app. rho
ABOVE 3.00
2.77 - 3.00
2.55 - 2.77
2.33 - 2.55
2.10 - 2.33
1.88 - 2.10
1.65 - 1.88
1.43 - 1.65
1.20 - 1.43
0.98 - 1.20
0.75 - 0.98
0.53 - 0.75
0.30 - 0.53
BELOW 0.30
123 126 131 132 133 130 120 125 121 128 129
2.5
0.0
-2.5
-5.0
1.5 x log(freq)
-12.5 -10.0 -7.5 -5.0 -2.5 0.0
distance km

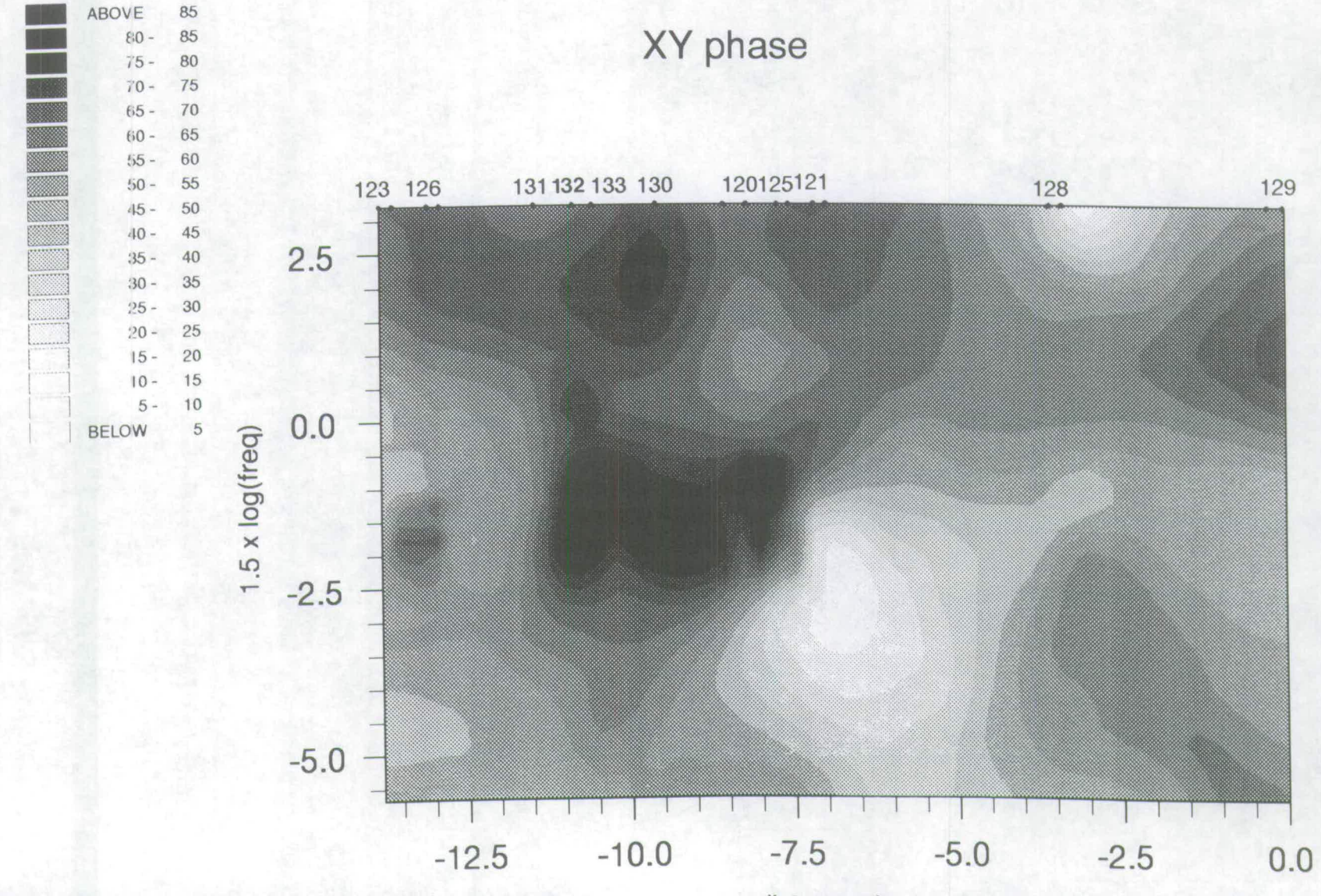
XY phase
ABOVE 85
80 - 85
75 - 80
70 - 75
65 - 70
60 - 65
55 - 60
50 - 55
45 - 50
40 - 45
35 - 40
30 - 35
25 - 30
20 - 25
15 - 20
10 - 15
5 - 10
BELOW 5
123 126 131 132 133 130 120 125 121 128 129
2.5
0.0
-2.5
-5.0
1.5 x log(freq)
-12.5 -10.0 -7.5 -5.0 -2.5 0.0

YX app. rho
ABOVE 3.00
2.77 - 3.00
2.55 - 2.77
2.33 - 2.55
2.10 - 2.33
1.88 - 2.10
1.65 - 1.88
1.43 - 1.65
1.20 - 1.43
0.98 - 1.20
0.75 - 0.98
0.53 - 0.75
0.30 - 0.53
BELOW 0.30
123 126 131 132 133 130 120 125 121 128 129
2.5
0.0
-2.5
-5.0
1.5 x log(freq)
-12.5 -10.0 -7.5 -5.0 -2.5 0.0

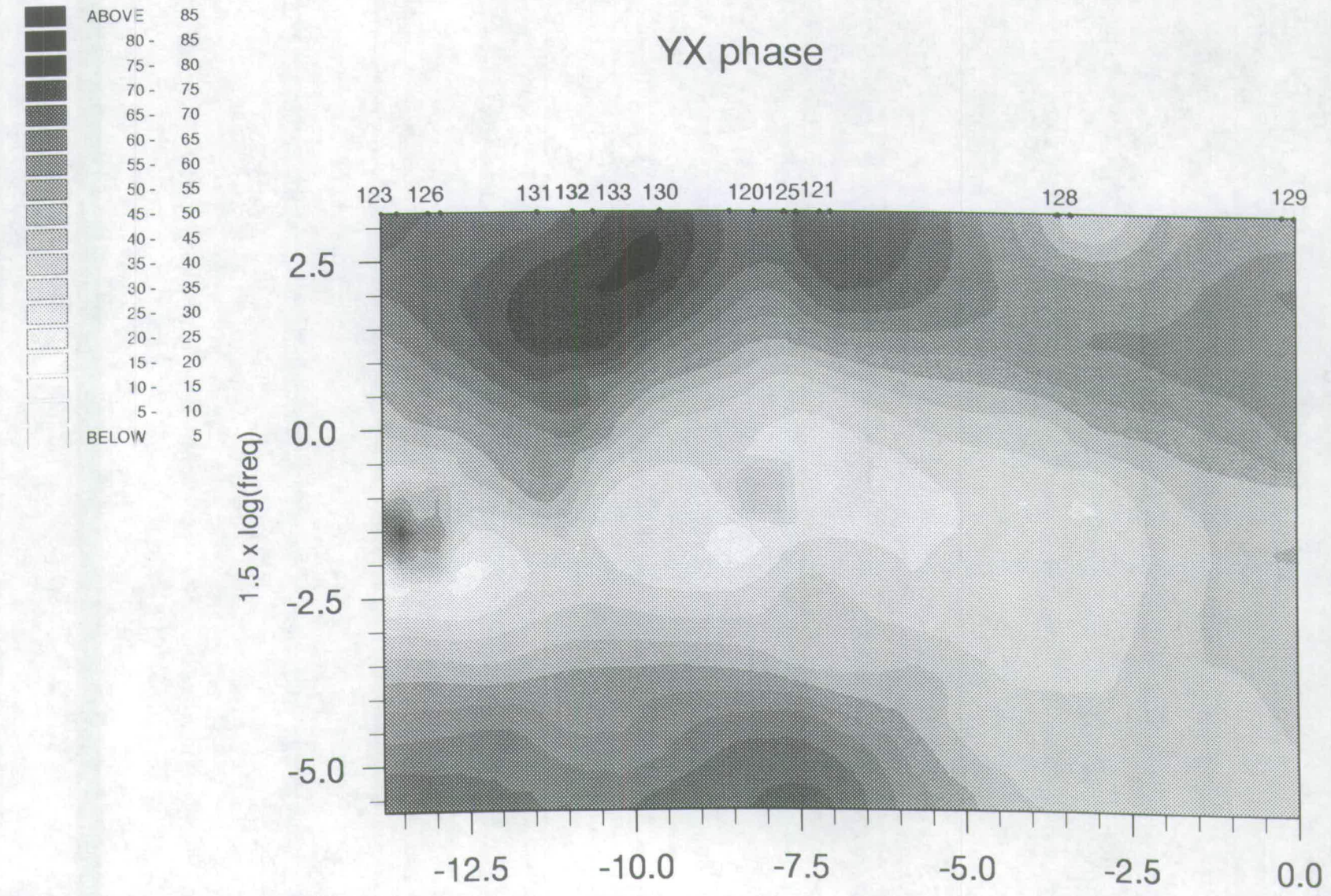
YX phase
ABOVE 85
80 - 85
75 - 80
70 - 75
65 - 70
60 - 65
55 - 60
50 - 55
45 - 50
40 - 45
35 - 40
30 - 35
25 - 30
20 - 25
15 - 20
10 - 15
5 - 10
BELOW 5
123 126 131 132 133 130 120 125 121 128 129
2.5
0.0
-2.5
-5.0
1.5 x log(freq)
-12.5 -10.0 -7.5 -5.0 -2.5 0.0

4.5.4 Induction arrows

Induction arrows magnitudes and directions for all base sites are shown in figs.4.6(1-13). From these plots the following can be seen:

1. The magnitude of the real and imaginary parts of the induction arrows increases with period, although the imaginary part is usually smaller than the real. Real arrows show values from 0.1 at 0.01 s, to greater than 0.3 at 20 s, and around 0.5 in the LMT band. The increasing magnitude with period shows that at depth one has to deal with multi-dimensional environment. Also, the magnitude at central sites is smaller than at sites close to the coast, which suggests that influence by the sea may be important.

2. The direction of the real arrows changes considerably with the period. The imaginary arrows are antiparallel to their real parts in many AMT periods, whereas in the LMT band there is always an angle $<90^0$ between the real and imaginary arrows.

In order to see more clearly the most important patterns revealed by the induction arrows, in figs.4.7a-d profiles for 4 selected periods, 0.06, 0.1, 1 and 23 s are shown. The following points are worth mentioning:

1. At T=0.06 and 0.1 s the real arrows at the sites 133, 131, 132 and 120 point to around the centre of the peninsula, while the remaining point towards the sea (figs.4.7a and b)

2. At T=1 s, the real arrows point towards the sea (fig.4.7c).

3. At T=23 s the real arrows show a tendency to orientate 50^0-70^0E on the peninsula rotating up to 80^0E at the very S (fig.4.7d).

For the LMT data, the direction of the real arrows is around 60^0E for site 1231 at T=100 s, while they gradually rotate to170^0E at T=6000 s. For site 1251 the same pattern is followed, a rotation from 80^0E to 185^0E (figs.4.6.11 and 4.6.12).

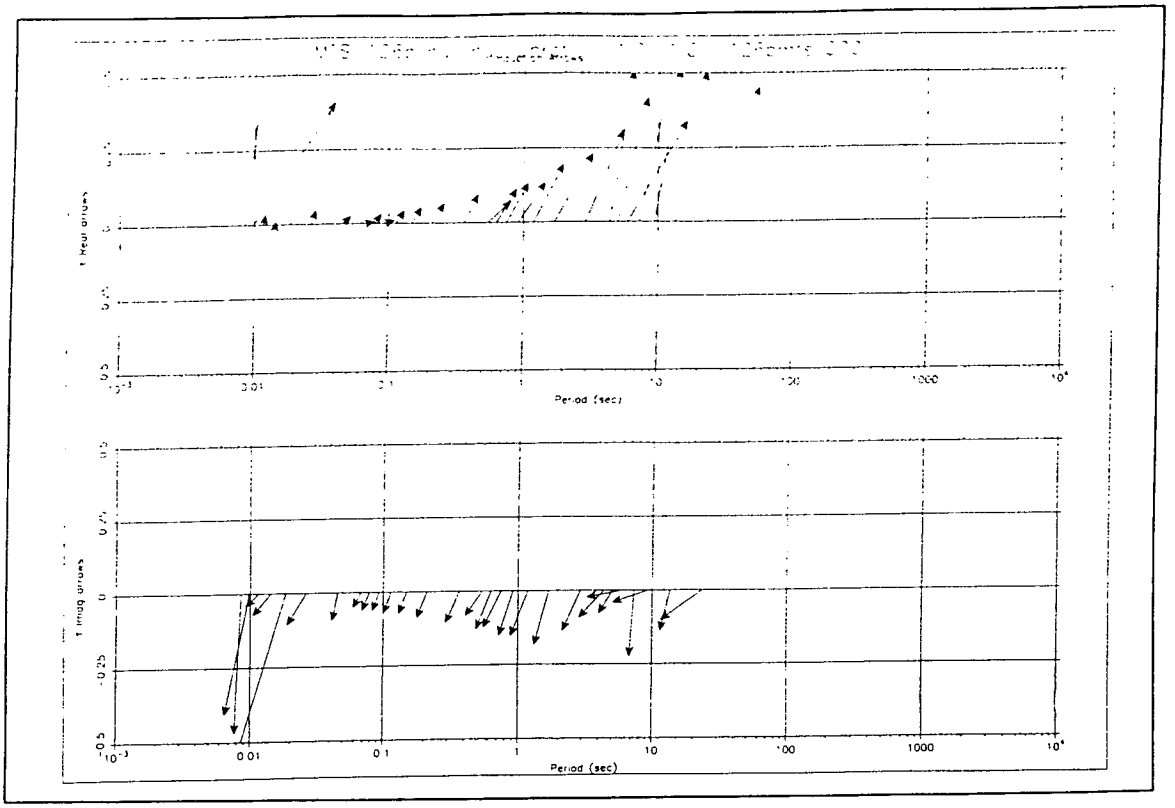

Fig.4.6.1

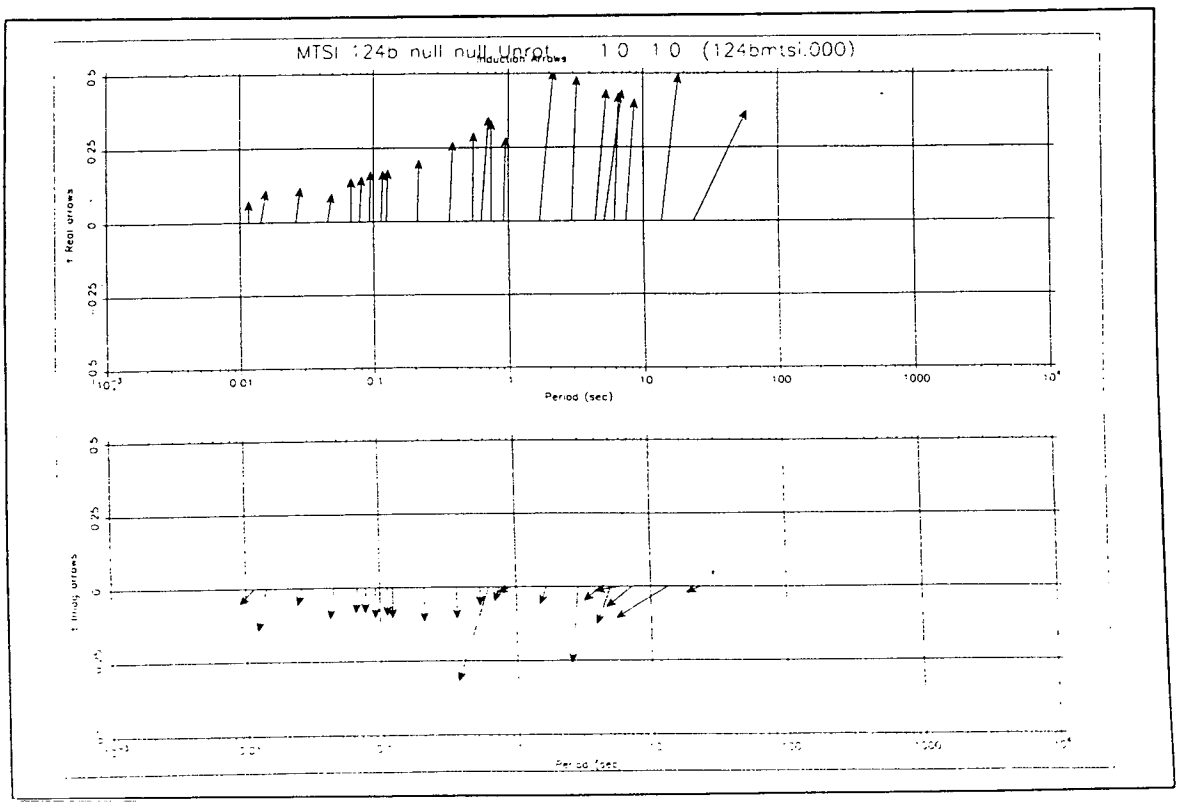

Fig.4.6.2

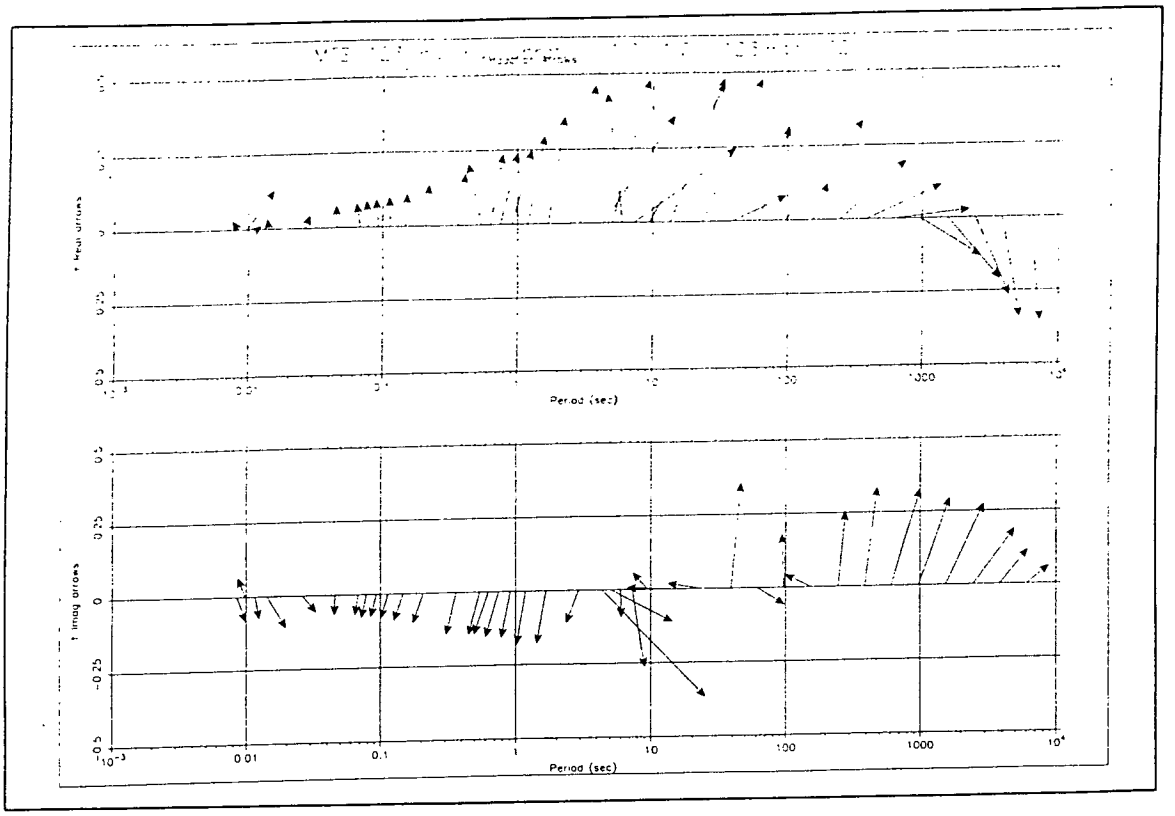

Fig.4.6.3

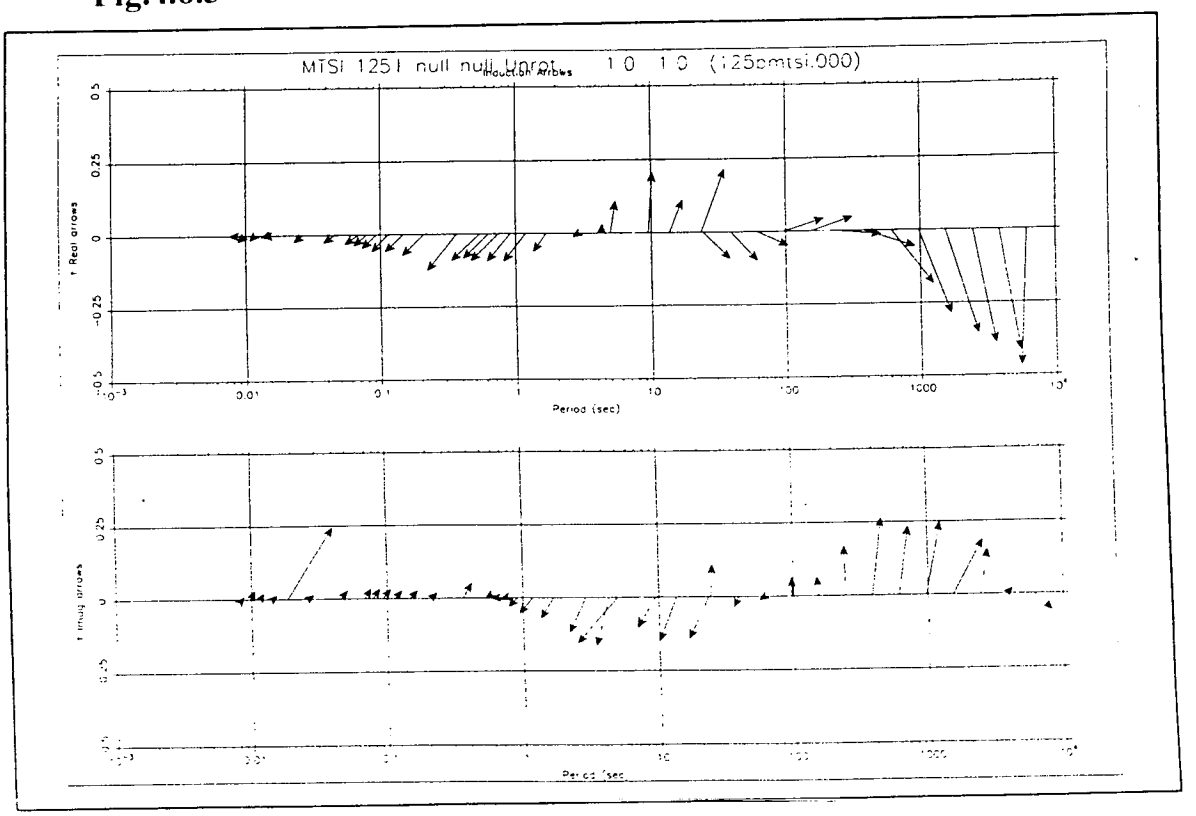

Fig.4.6.4

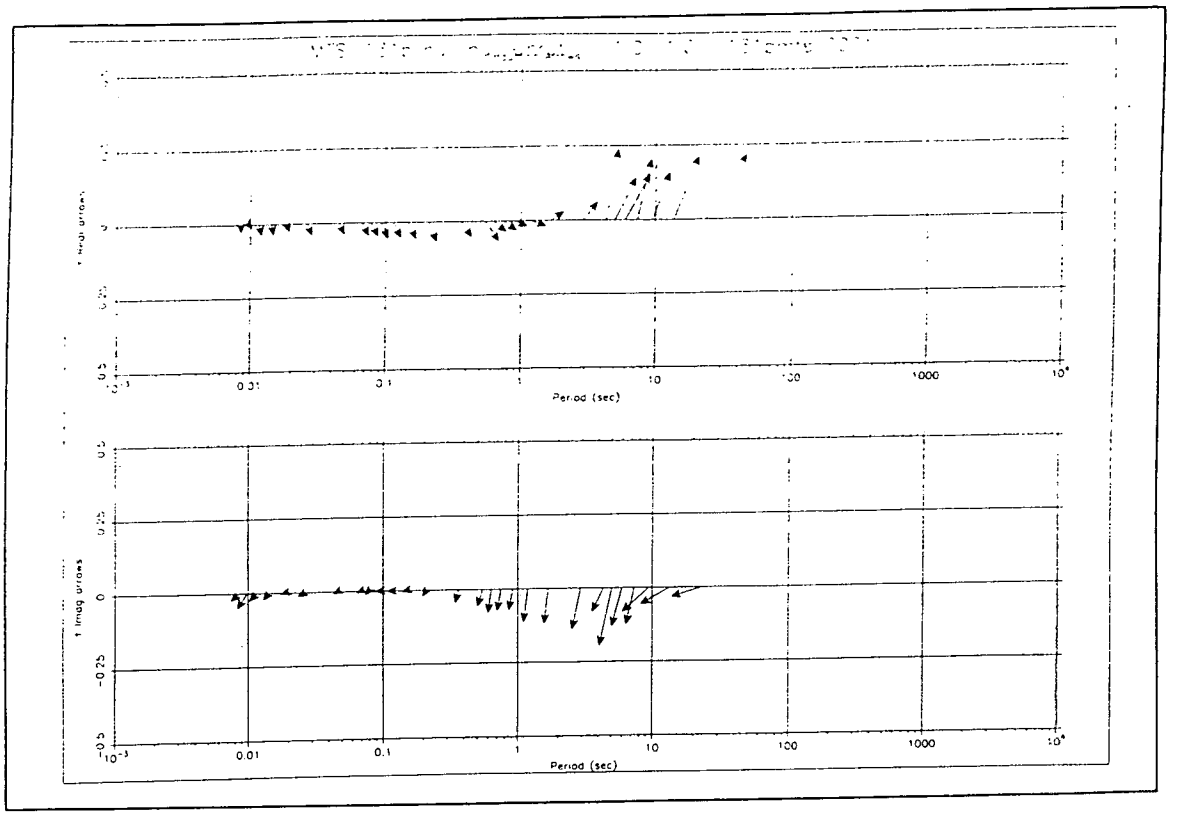

Fig.4.6.5

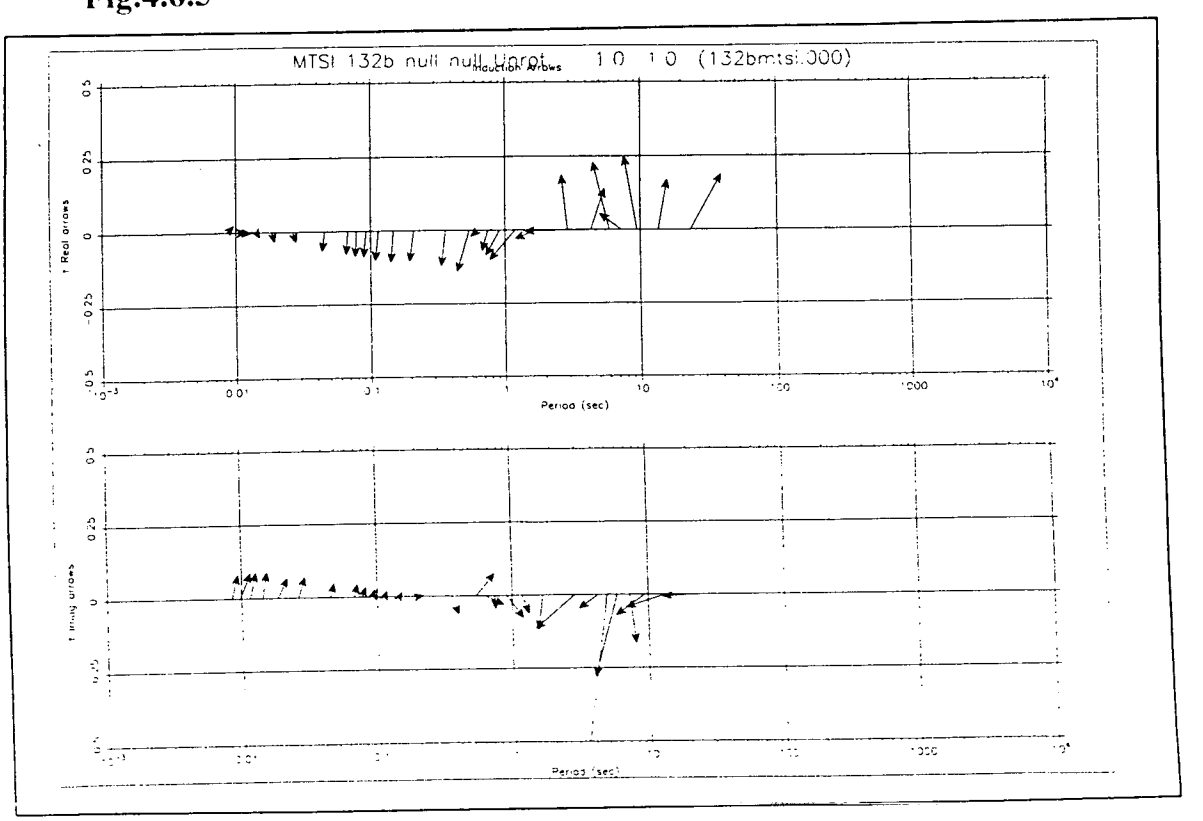

Fig.4.6.6

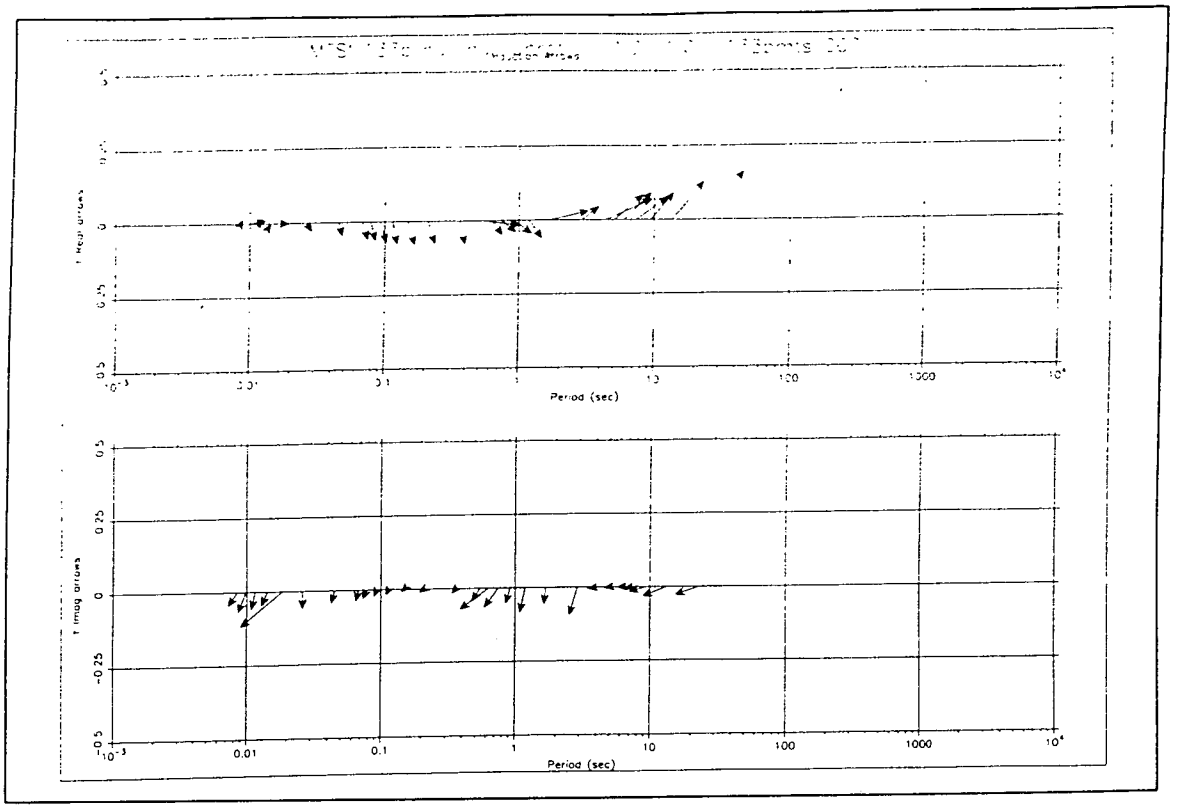

Fig.4.6.7

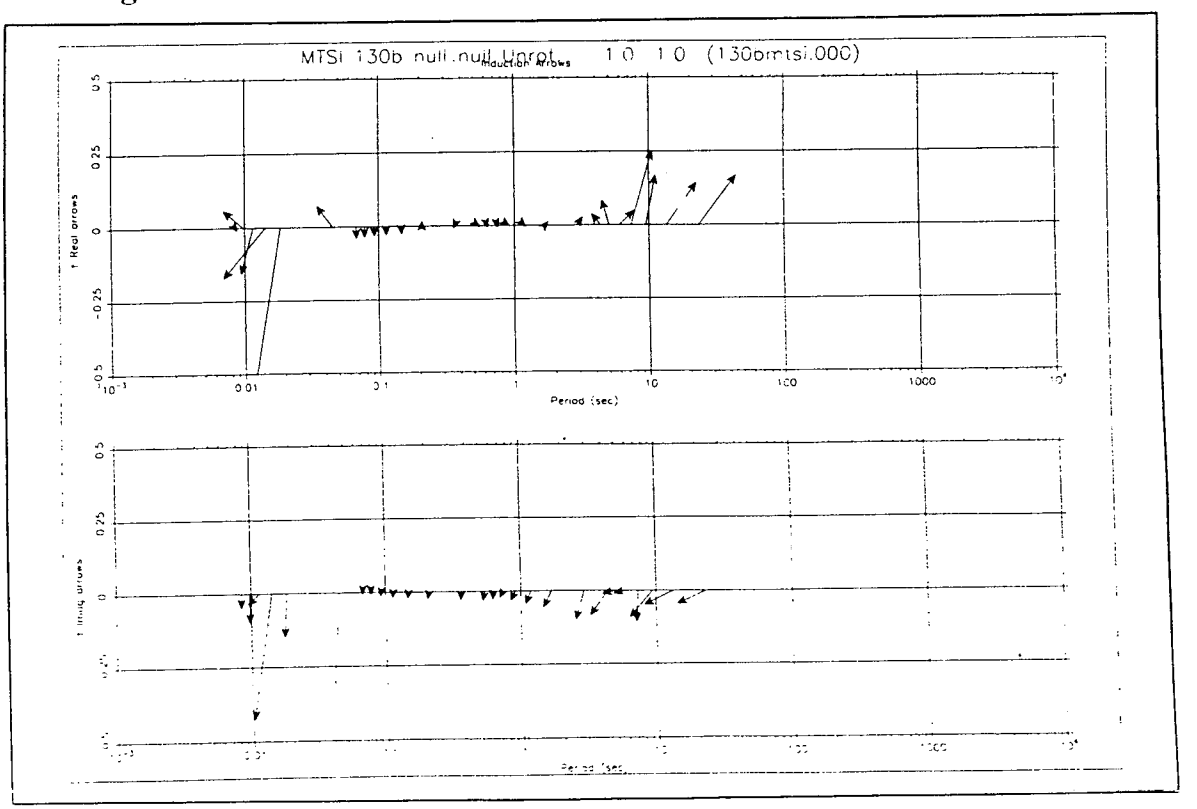

Fig.4.6.8

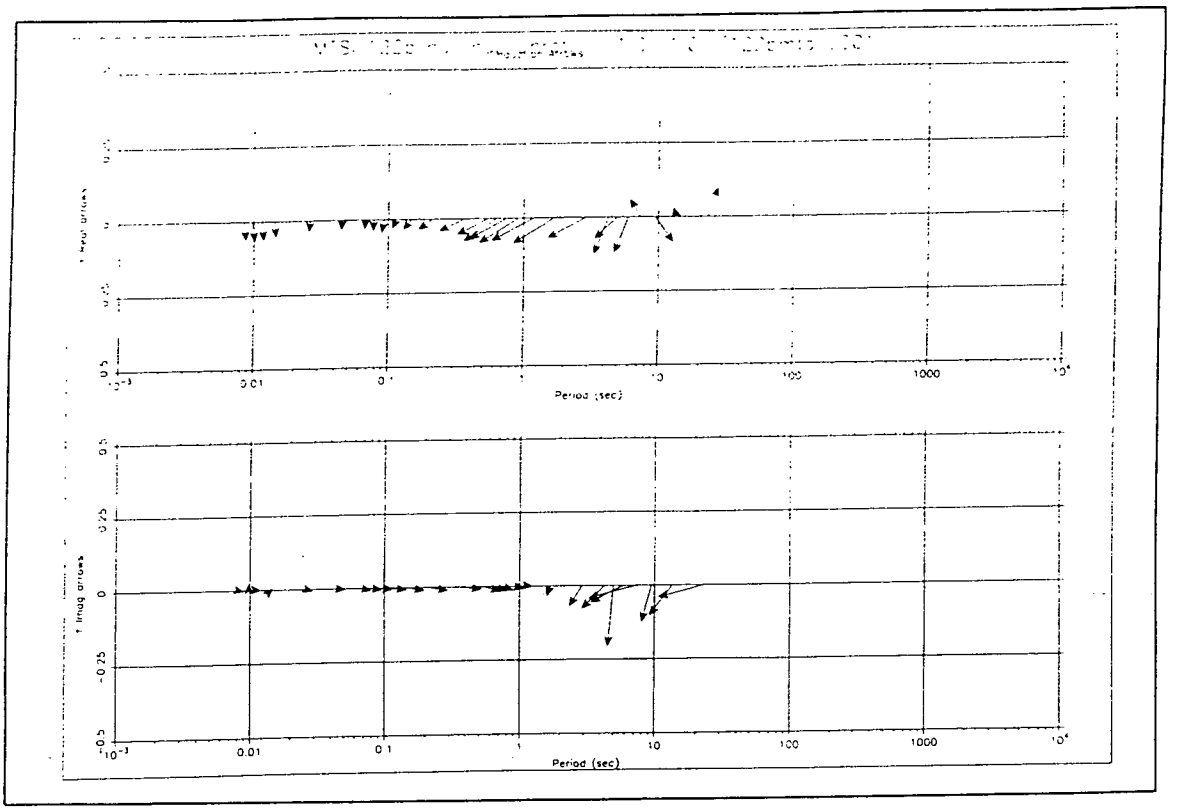

Fig.4.6.9

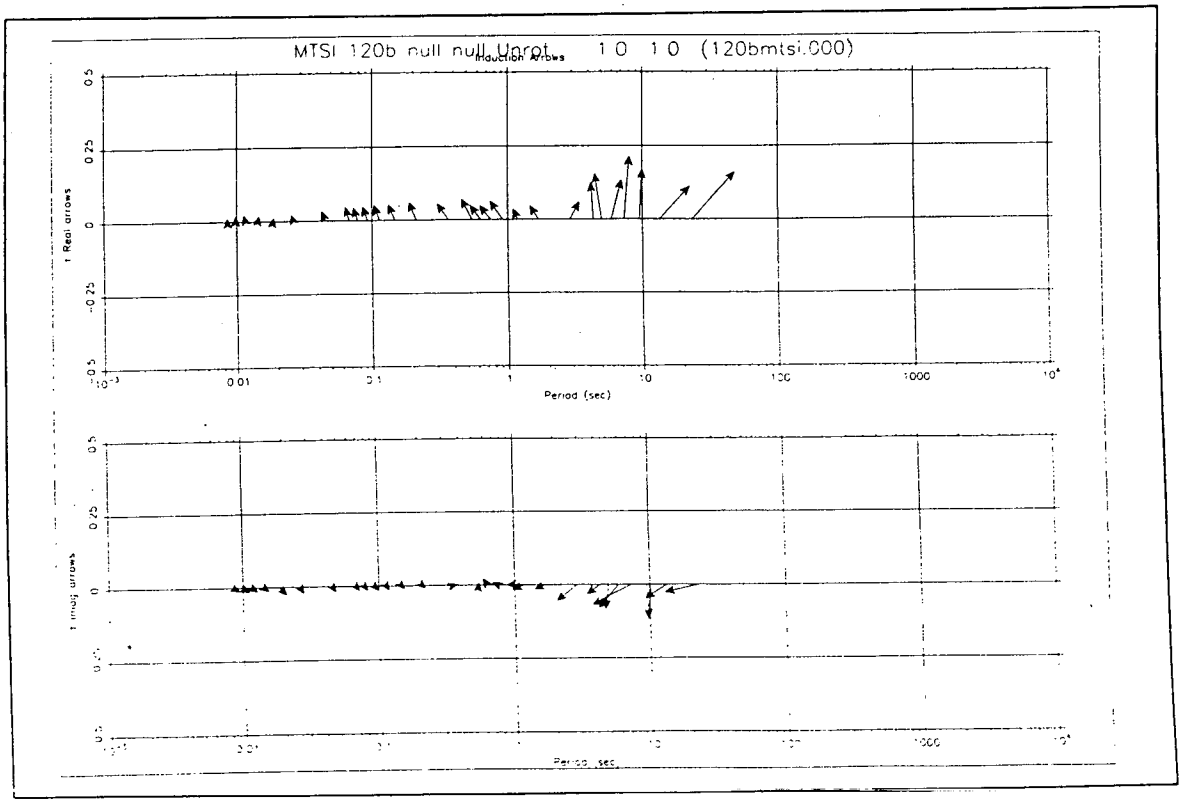

Fig.4.6.10

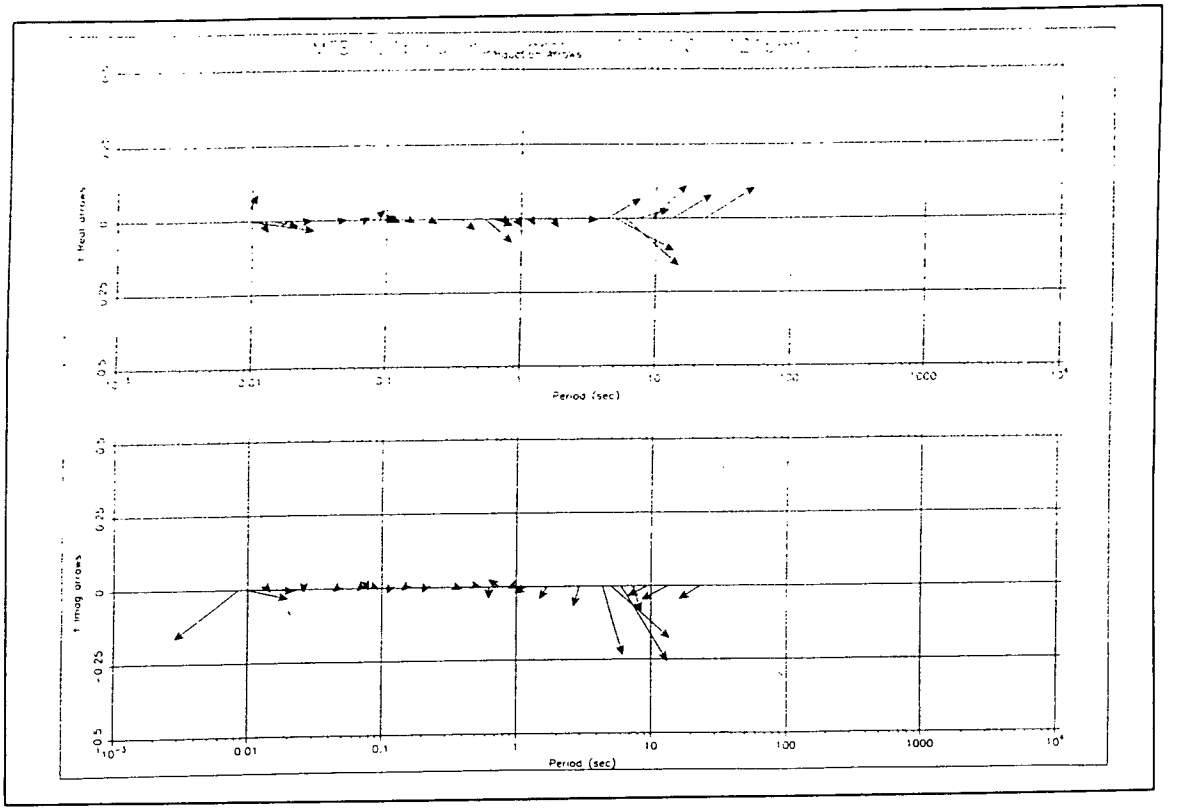

Fig.4.6.11

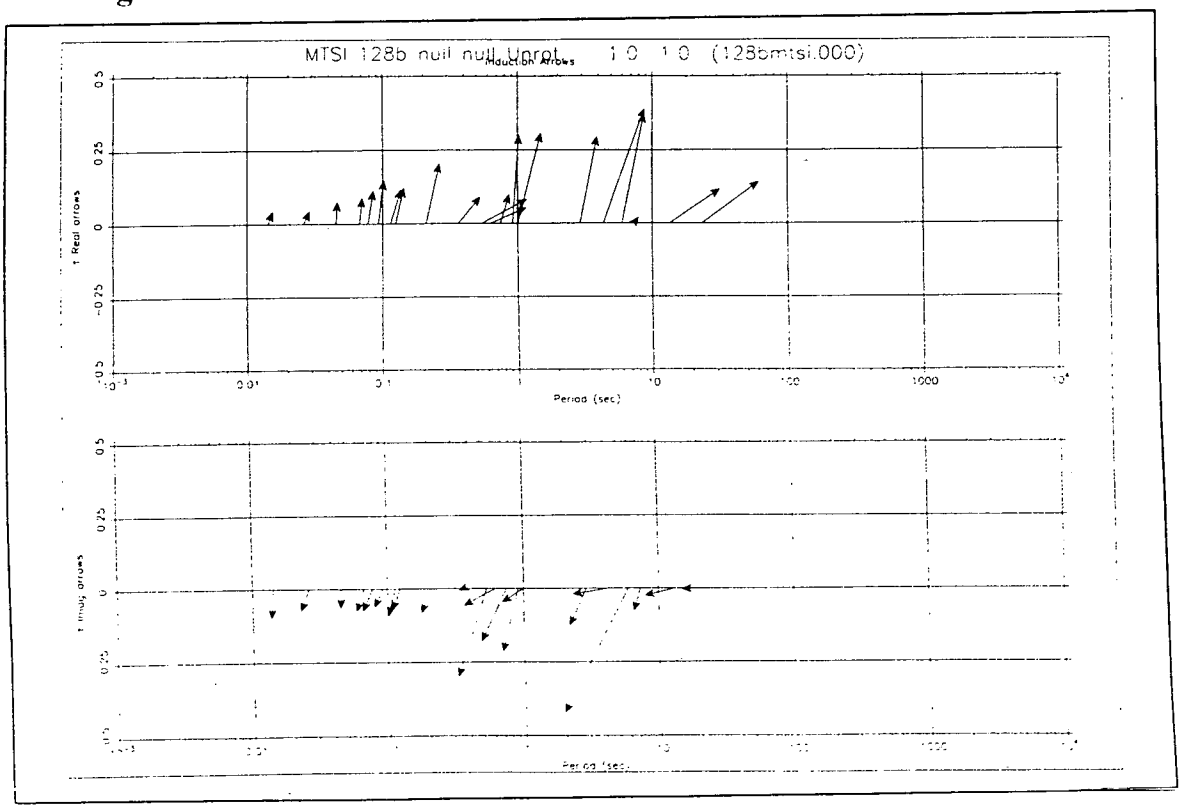

Fig.4.6.12

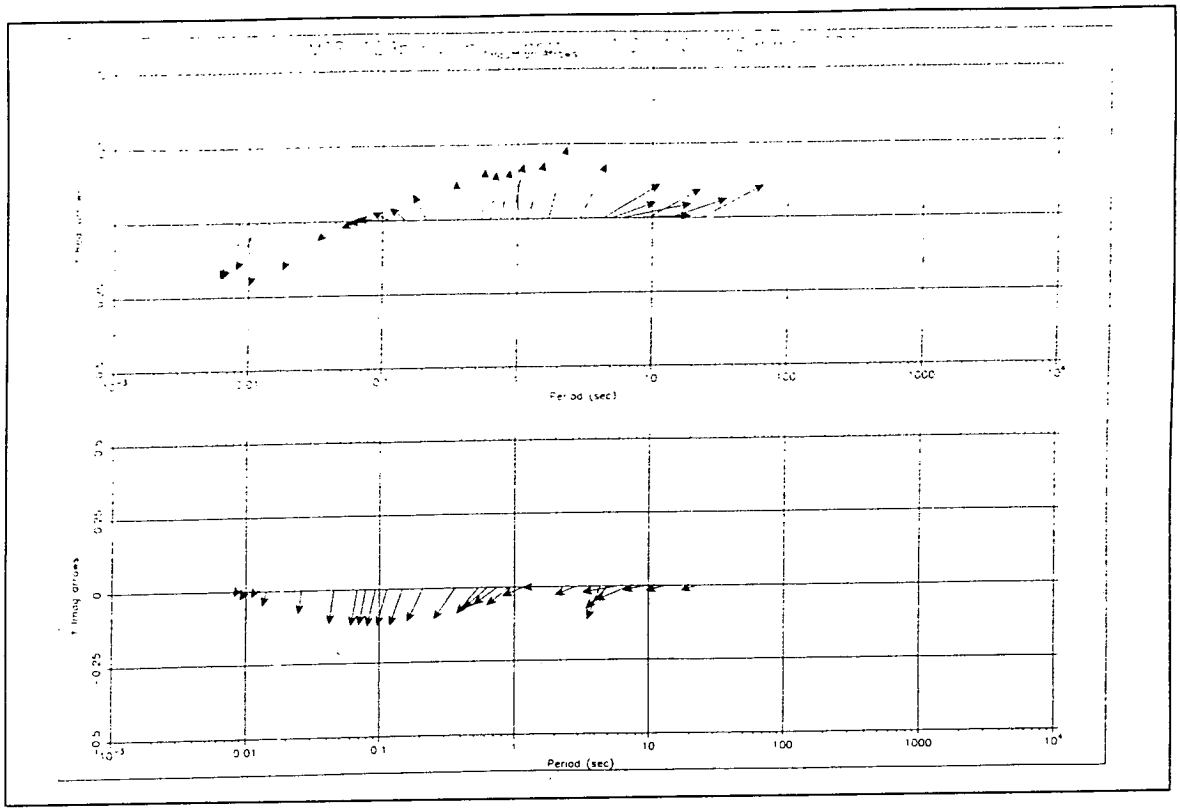

Fig.4.6.13

Figs.4.6.1-4.6.13: Real and Imaginary Parkinson induction arrows. Magnitude and azimuth for all the base sites. For each site, the real and imaginary parts are shown in two plots, respectively. For each plot, the magnitude and direction of the arrow are shown.

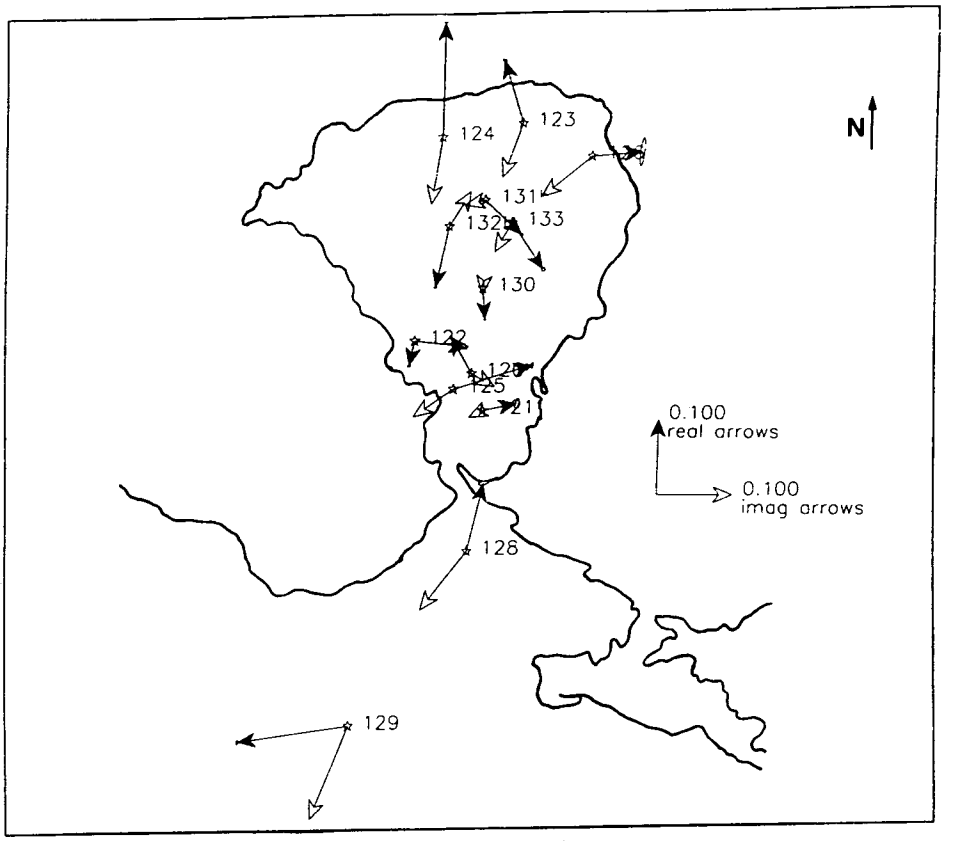

Fig.4.7a: Parkinson arrows for all sites, at f= 5 Hz

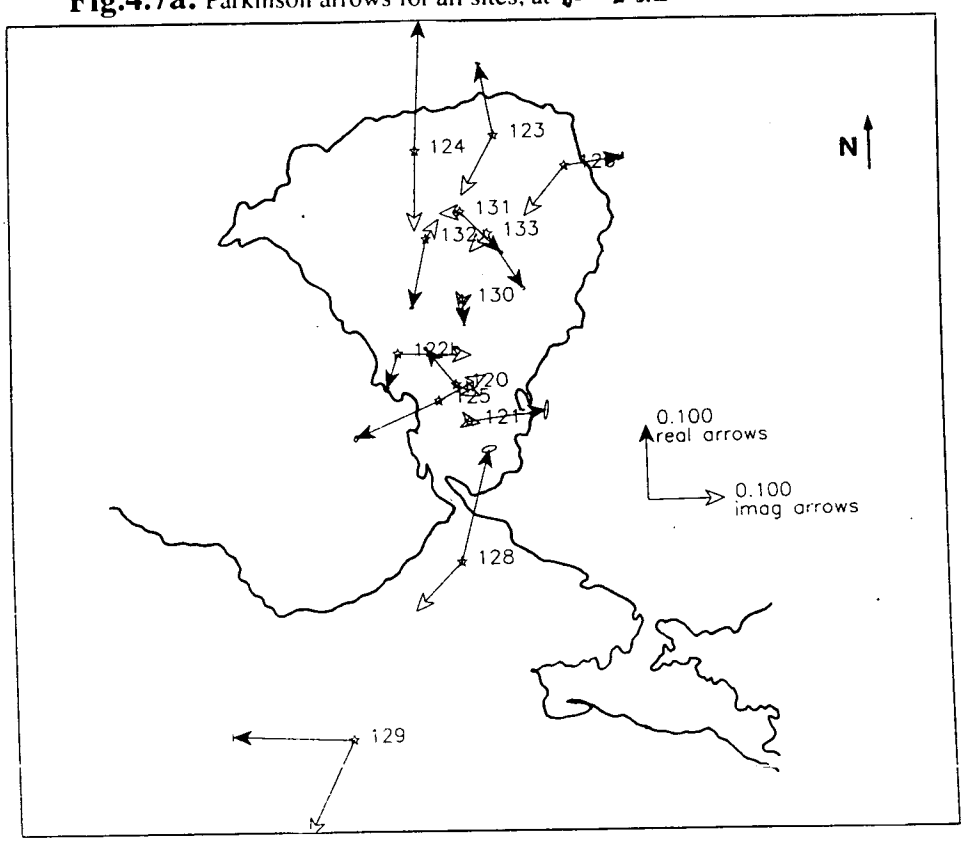

Fig.4.7b: Parkinson arrows for all sites, at T=0.1 s

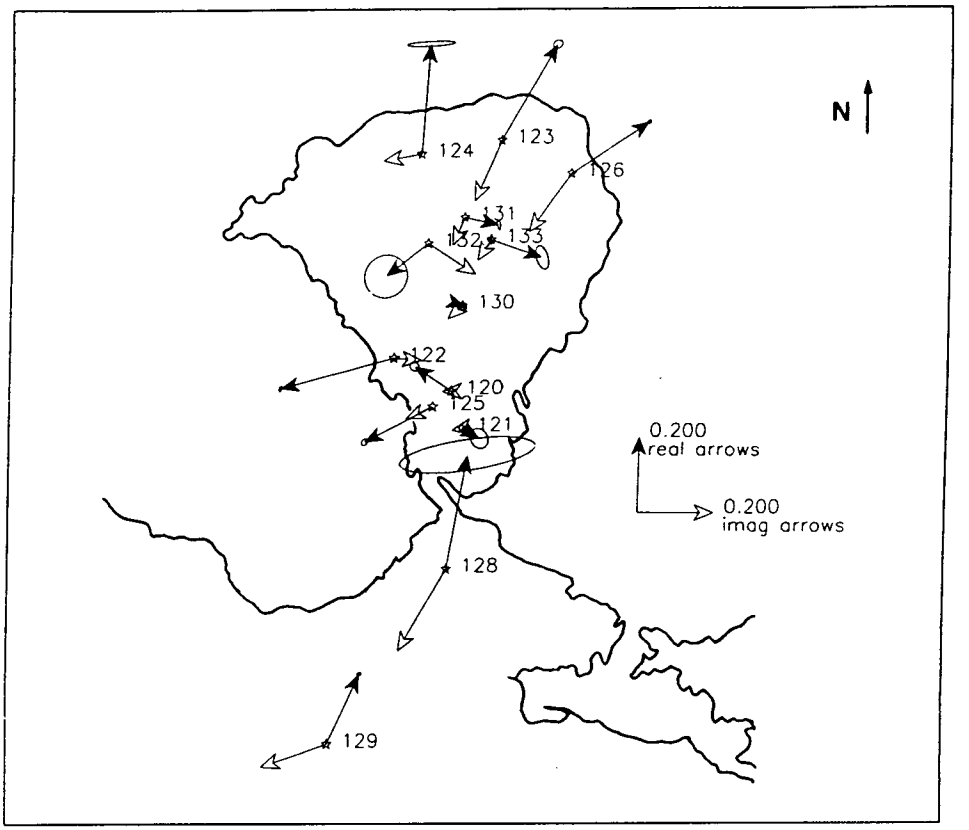

Fig.4.7c: Parkinson arrows for all sites, at T=1 s

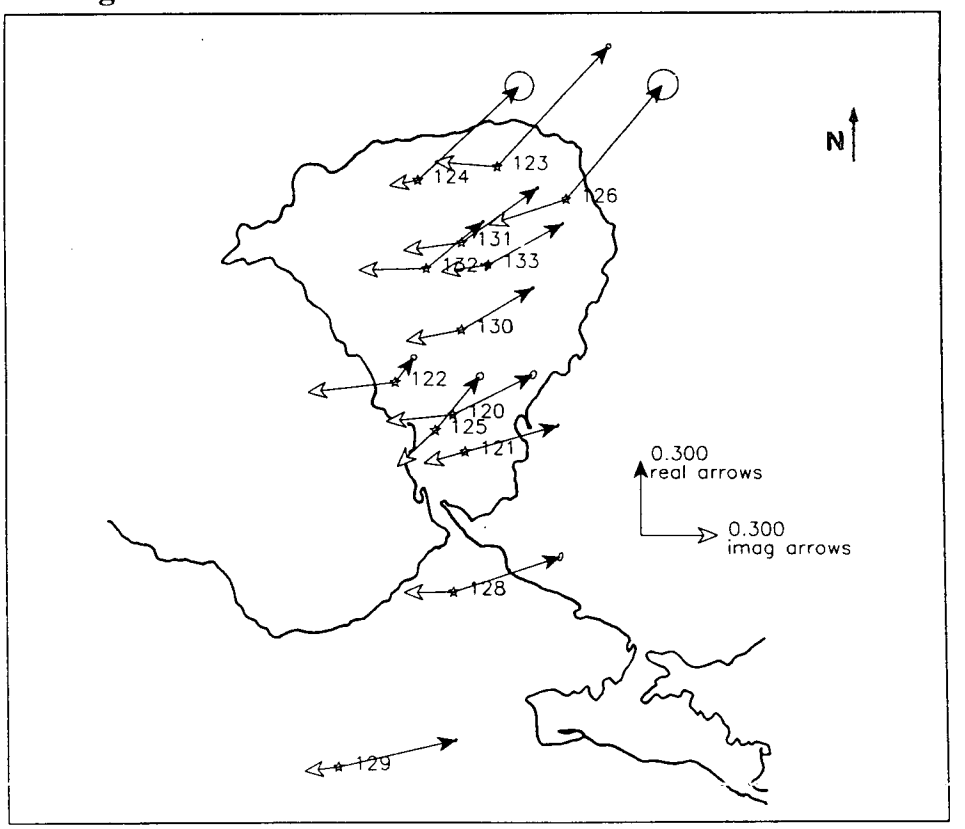

Fig.4.7d: Parkinson arrows for all sites, at T= 23 s.

4.6 Summary

From the results presented in the sections 4.5-4.6 of this chapter, the following should be kept in mind:

1. Concerning the MT data:

a. The presentation of pseudosections for the XY and YX components has shown that although the MT data at relatively short periods show no significant differences between the two measured components, this is not the case at the longer periods. At T>1 s, there is an obvious anisotropy between Z_{xy} and Z_{yx}, indicating contrasts in the electrical conductivity of at least a 2-D character.

b. The number of estimates, as well as the predicted coherence at the range 3-10 s is quite low (especially for the XY component), which means that any interpretation in that range must be considered very carefully.

c. There is a "shifting" of the resistivity curves among neighbour sites, which is possibly connected with 3-D local inhomogeneities.

2. Concerning the MV data:

a. The MV data are of a much better quality than the MT data and so they can provide more reliable information.

b. It seems that at periods between 0.05 s and 0.3 s, the real Parkinson arrows at a number of sites point towards somewhere around the peninsula centre, although at sites closer to the coast they point towards the sea.

c. Generally, the behaviour of the induction arrows is rather complicated through the whole period range and therefore deserves more attention, as it can be connected with conductive features of interest, or possibly undesirable effects such as influence by the surrounding seas.

As the data were found to be affected by static shifts and also hints of influence by the surrounding seas were suggested, a more careful consideration of these effects is considered necessary. In the next chapter an extended analysis of the data in terms of local distortions including the sea effect will be done, after which, a decision about the gross electrical strike direction for the deep structure under Methana will be taken.

Chapter 5

Strike direction and electrical distortion

5.1 Introduction

As the number of MT investigations increases and experience is gained through fieldwork and data processing, it has become clear that experimentally determined impedance tensors rarely conform to the ideal 2-D tensor. For example, the apparent resistivity curves are sometimes shifted vertically from their values expected on the basis of other independent information (e.g. well logs). This displacement, which does not appear on the phase curves, is broadly called "static shift" and it has been thoroughly analysed by many scientists (Berdichevsky and Dmitriev, 1976; Jones and Price, 1970; Jones, 1983; Jiracek, 1990).

The underlying cause for the observed static shifts is the galvanic effect. This is the accumulation of charges at the edges of a small surficial body or simply a contrast in conductivity (section 2.4.3). Is has been proved (Kaufman, 1985) that the volume charge density (ρ_v) is given by:

$$\rho_v = -\frac{\varepsilon_0}{\sigma + i\omega\varepsilon_0}\mathbf{E}.\nabla\sigma \qquad (5.1)$$

where

ε_0 : the electrical permittivity of free space

ω : the angular frequency of the electromagnetic field

σ : the electrical conductivity of the material

$\mathbf{E}$: the primary electric field

From eq.5.1, it can be seen that:

1. Electric charges do not appear in regions where the medium is uniform ($\nabla\sigma = 0$).

2. In MT applications, where $\sigma >> \omega\varepsilon_0$, the imaginary part of eq.5.1 vanishes, i.e. there is no phase difference between the primary electric field and the galvanic distortion.

The boundary charge build-up results in a reduction or an enhancement of the total electric field at different locations. It also distorts the direction of the electric

field. Magnetic field variations due to galvanic current deviations are small for small inhomogeneities. However they can become significant in the case of large galvanic distortion (Groom and Bailey, 1989).

5.2 Distortion of the impedance tensor

5.2.1 Distortion due to local inhomogeneities

Layered Earth models simply neglect the diagonal elements of the impedance tensor, attributing any non-zero values to noise. Also, the off-diagonal elements are assumed to be equal but of opposite sign. Swift 's rotation is valid as long as the regional structure does not depart significantly from a 2-D model. There are a number of more mathematical manipulations (Eggers, 1982; La Torraca et al., 1986; Cevallos, 1986), which attempt a decomposition by extracting certain characteristics of the impedance tensor. These methods also are valid if the response is 2-D, but it is not clear what happens when departures from a regional 2-D structure exist.

There is a different category of possible manipulations of the galvanically distorted impedance tensor (Bahr, 1988, 1991, and Groom and Bailey, 1989), which is adopted in the present chapter. These methods consider the possibility of small 3-D effects which may distort the regional 2-D impedance tensor. By separating these local galvanic effects from the measured impedance tensor, the regional inductive response can be recovered.

5.2.2 Distortion due to the sea

One particular kind of near-surface distortion is caused by the continent-ocean interface. Given that the conductivity of sea water is considerably higher from that of crustal rocks, the electrical currents may flow in the seawater instead of flowing into the deep Earth. In fact, in the present study, all the sites are surrounded by shallow conductive sea water and that makes it necessary to examine the influence the sea may have on the MT components. In section 2.6 it was mentioned that particularly sensitive to lateral variations in conductivity is the vertical magnetic field H_z. Observations have shown (Parkinson, 1962; Honkura, 1974) that along the coastline induction arrows are perpendicular to the coastline. Induction arrows and other MT parameters are examined in the second part of this chapter (section 5.5) by using a thin sheet approximation.

5.3 The decompositions of Groom-Bailey (G-B) and Bahr

5.3.1 The model

First, a model which takes into account small galvanic distortions superimposed over a larger scale 2-D structure is considered.

Under the assumption that the fields are measured in the principal directions (// and $\perp$ to the strike direction) the regional electric field ($\mathbf{E}_r$) is defined by the equation:

$$\mathbf{E}_r = \mathbf{Z}_r \mathbf{H}_r \qquad (5.2)$$

where $\mathbf{Z}_r = \begin{bmatrix} 0 & Z_\perp \\ -Z_{//} & 0 \end{bmatrix}$ and $\mathbf{H}_r$ are the regional impedance tensor and the regional magnetic field respectively.

In the case of a small body, the regional electric field is scattered by an amount which is given by a scattering tensor $\mathbf{C}$ operating on the regional electric field to produce the measured electric field ($\mathbf{E}_m$):

$$\mathbf{E}_m = \mathbf{C}\mathbf{E}_r \qquad (5.3)$$

where $\mathbf{C} = \begin{bmatrix} C_{xx} & C_{xy} \\ C_{xy} & C_{yy} \end{bmatrix}$.

The scattering field is in phase with the regional electric field, so the elements of $\mathbf{C}$ are all real.

5.3.2 Groom and Bailey's local distortion parameters

Assuming that the regional impedance tensor ($\mathbf{Z}_r$) is distorted by a 2x2 scattering tensor ($\mathbf{C}$), and that the measured magnetic field is not distorted (i.e. $\mathbf{H}_m=\mathbf{H}_r$) the measured impedance tensor ($\mathbf{Z}_m$) is given by:

$$\mathbf{Z}_m = \mathbf{C}\,\mathbf{Z}_r \qquad (5.4)$$

By performing a rotation through an angle called the regional azimuth (θ), we obtain the measured impedance tensor in a general coordinate system:

$$\mathbf{Z}_m' = \mathbf{R}(\theta)\,\mathbf{C}\,\mathbf{Z}_r\,\mathbf{R}^T(\theta) \qquad (5.5)$$

The last equation contains 4 real parameters from the distortion tensor, 2 real and 2 imaginary from the regional tensor and one azimuth, i.e. 9 parameters. Yet the measured impedance tensor contains only 8 parameters (magnitude and phase of the 4 tensor elements). This factorisation cannot be unique. Also, although the scattering tensor can be considered real and independent of frequency for inductively weak (phase-free) galvanic distortions (Berdichevsky and Dimitriev, 1976; Jones, 1983;

Bahr, 1988) the multiplication will mix the elements of the regional impedance tensor, resulting in frequency dependence of all the elements, and the phases will be affected.

Groom and Bailey proposed a new factorisation:

$$\mathbf{C} = g\,\mathbf{T}\,\mathbf{S}\,\mathbf{A} \qquad (5.6)$$

where $\mathbf{C}$: the scattering tensor

g: scalar gain

$\mathbf{A}$: the anisotropy tensor

$\mathbf{S}$: the shear tensor

$\mathbf{T}$: the twist tensor

The mathematical definition of the new tensors can be found in Groom and Bailey (1989) together with the proof of the uniqueness of the factorisation. The definition contains three real numbers e, s, t associated with the **S**, **A**, and **T** tensors respectively.

Multiplying the regional impedance tensor by the splitting tensor **A** simply adds to the anisotropy already present. The shear tensor **S** also develops anisotropy, but with an angle called the shear angle (φ_e) that bisects the principal axes of the regional impedance tensor. The tensor **T** simply rotates the electric field through a clockwise angle called the twist angle (φ_t):

$$\varphi_e = \tan^{-1} e \qquad (5.7)$$

$$\varphi_t = \tan^{-1} t \qquad (5.8)$$

A further parameter, the local channelling angle (θ_L), summarises the above distortion parameters, and gives an estimate of the local current direction:

$$\theta_L = \theta + \varphi_e + \varphi_t \qquad (5.9)$$

where θ is the regional azimuth.

Following the above notation, skew is also expressed as an angle:

$$K = \tan^{-1}\kappa \qquad (5.10)$$

Eq.5.5 can be written now as

$$\mathbf{Z}_m' = \mathbf{R}(\theta)\,\mathbf{T}\,\mathbf{S}\,\mathbf{Z}_r'\,\mathbf{R}^T(\theta) \qquad (5.11)$$

where $\mathbf{Z}_r' = g\mathbf{A}\mathbf{Z}_r$ (5.12)

Eq.5.11 has only seven real parameters, the regional azimuth, the real and imaginary parts of the 2 elements of $\mathbf{Z}_r'$ and the shear and twist angles. A clear advantage of this factorisation of the distortion tensor **C** is that it allows the unknown parts of **C** to be absorbed into the regional impedance tensor without destroying the ideal 2-D form of that tensor (eq.5.12). If the galvanic distortion is truly frequency independent, the absorption of g**A** into $\mathbf{Z}_r$ will not change the shape of the apparent

resistivity and phase curves. Therefore, their determination will be correct except for the "static shift", represented by the factor g**A**.

The parameters e, s and θ can be extracted from the measured impedance tensor by using a set of non-linear equations, (Groom and Bailey, 1989):

$$Z_{xx}+Z_{yy}=tw+e\delta$$
$$Z_{xy}+Z_{yx}=(\delta-etw)\cos 2\theta-(t\delta+ew))\sin 2\theta \qquad (5.13a,b)$$
$$Z_{yx}-Z_{xy}=-w+et\delta$$
$$Z_{xx}-Z_{yy}=-(t\delta+ew)\cos 2\theta-(\delta-etw))\sin 2\theta \qquad (5.13c,d)$$

where

$$w=Z_{//}+Z_{\perp} \text{ and } \delta=Z_{\perp}-Z_{//} \qquad (5.14)$$

5.3.3 Bahr's azimuth, dimensionality indicators and subclasses of models

Up to now only Swift's azimuth (eq.2.43) and the dimensionality indicator named skew (κ) were mentioned:

$$\kappa=\frac{|S_1|}{|D_2|} \qquad (5.15)$$

where $S_1=Z_{xx}+Z_{yy}$ (5.16a)

and $D_2=Z_{xy}-Z_{yx}$ (5.16b)

A new azimuth has been introduced by Bahr (1988) :

$$\tan\alpha=\frac{(|\mathrm{Im}(S_2S_1^*)|-|\mathrm{Im}(D_2D_1^*)|}{(|\mathrm{Im}(D_1S_1^*)|+|\mathrm{Im}(D_2S_2^*)|} \qquad (5.17)$$

where $S_2=Z_{xy}+Z_{yx}$ (5.18b)

and $D_1=Z_{xx}-Z_{yy}$ (5.18b)

also two rotationally invariant dimensionality parameters:

$$\Sigma=\frac{\left(D_1^2+S_2^2\right)}{D_2^2} \qquad (5.19)$$

and

$$\eta=\frac{\left(\left|\mathrm{Im}\left(S_2D_1^*\right)\right|-\left|\mathrm{Im}\left(D_2S_1^*\right)\right|\right)^{1/2}}{D_2} \qquad (5.20)$$

Bahr (1991) extended the 3 model classes of G-B into 7 sub-classes, by using the above parameters plus the G-B parameters, following the same methodology and emphasising the separation of galvanic distortion from regional induction :

Class 1: The simple 2-D anomaly characterised by $\Sigma>0.1$ and $\kappa<0.1$

Class 2: A local 3-D anomaly superimposed upon a layered Earth characterised by $\eta<0.05$

Class 3: A regional 2-D structure weakly distorted by local 3D inhomogeneities, characterised by either $\varphi_e-\varphi_t<5$ and $\varphi_e-\varphi_t<20$ or $\varphi_e-\varphi_t<20$ and $\varphi_e-\varphi_t<5$

Class 4: A regional 2-D anomaly in rotated coordinates characterised by $\varphi_t\approx 0$

Class 5: A regional 2-D anomaly with strong local distortion characterised by $\eta<0.3$ and large twist and shear angles

Class 6: A regional 2-D anomaly with strong channelling characterised by $\varphi_e\approx 45$

Class 7: A regional 3-D anomaly characterised by $\eta>0.3$

5.4 Data analysis based on the decomposition models

In sections 5.4.1-5.4.3 the data are examined according to Groom-Bailey and Bahr's methods.

5.4.1 Data analysis according to Bahr's methods

The degree of distortion of the data as well as the validity of a regional 2-D induction model can be examined using Bahr's 7 subclasses. The data were separated into 7 period sub-ranges, and a model class for each site was estimated (table 5.1).

The table was constructed according to the following methodology: First, data with $\eta>0.3$ (class 7) were examined in order to exclude them from subsequent analysis. A great part of the data estimated to belong to class 7 was found to be associated with periods greater than 10 s, as well as with the range 3-10 s, where the data quality is poor and the noise to signal ratio is high. Second, the twist and shear angles of the remaining data were examined in order to find to which distortion class (3 to 6) the data belong.The remaining data were searched for low values (< 0.05 and <0.1) of the parameter η and for values >0.1 of the parameter Σ. Consulting the table the following main points can be noticed:

S \ T	123b	123r	124b	126b	126r	131b	132b	133b	130b	122b	122r	120b	120r	125b	125r	128b	128r	129b	129r
a	3	7	5	5	5	2	2	4	3	2	3	5	5	3	3	5	3	4	5
b	3	5	5	3	3	2	2	4	3	3	3	4	5	3	5	5	3	4	5
c	3	3	5	3	3	5	2	4	3	4	3	4	5	3	5	5	3	4	5
d	5	4	5	5	5	5	5	5	3	5	5	5	5	5	5	5	3	5	5
e	5	3	5	5	5	5	7	7	5	5	5	4	5	5	5	5	5	7	5
f	5	7	5	7	7	5	7	7	5	5	5	5	5	5	5	5	5	7	5
g	7	7	7	7	5	7	7	7	5	7	7	7	7	5	7	7	7	7	7
h	7													5					
i	5													5					
j	5													5					
k	7													5					
l	7													7					

Table 5.1: Data classified into 7 sub-classes according to Bahr's methods. **S**:site **T**: period (s)

a-l: period ranges

a: 0.008-0.014	**d**: 0.2-0.63	**g**: 7.3-23	**j**: 400 - 1000
b: 0.018-0.067	**e**: 0.74-1.6	**h**: 25- 60	**k**: 1500-2500
c: 0.078-0.148	**f**: 3-6	**i**: 100- 250	**l**: 4000 - 6000

1. The model class 1 indicative of a simple 2-D structure is absent.

2. Almost all the data show characteristics of galvanic distortion, although it is weak at short periods at many sites (class 3).

3. A number of sites show almost zero twist angle at some frequencies (class 4).

4. There is a tendency at longer periods, for higher model classes 5 and 7 to predominate.

5. In the last AMT period range (g) most of the data belong to class 7.

6. Although most of the LMT data (range h-l) show $\eta<0.3$, their distortion parameters are large, which suggests strong galvanic effects.

7. In the longest LMT period range, the data show strong indication of 3-D induction.

Bahr's regional azimuth and skew together with Swift's are shown for sites 125b and 125r (fig.5.1.1-2). A comparison of the results from two closely-spaced sites shows the advantages of Bahr's approach. Bahr's method gives an azimuth from around -30^0 at short periods rotating to 30^0E at 23 s. Bahr's azimuths for the two adjacent sites are almost identical. In contrast, Swift's azimuth shows an angle of 0^0-20^0 for 125b and 35^0-55^0 for 125r, for the two first period decades.

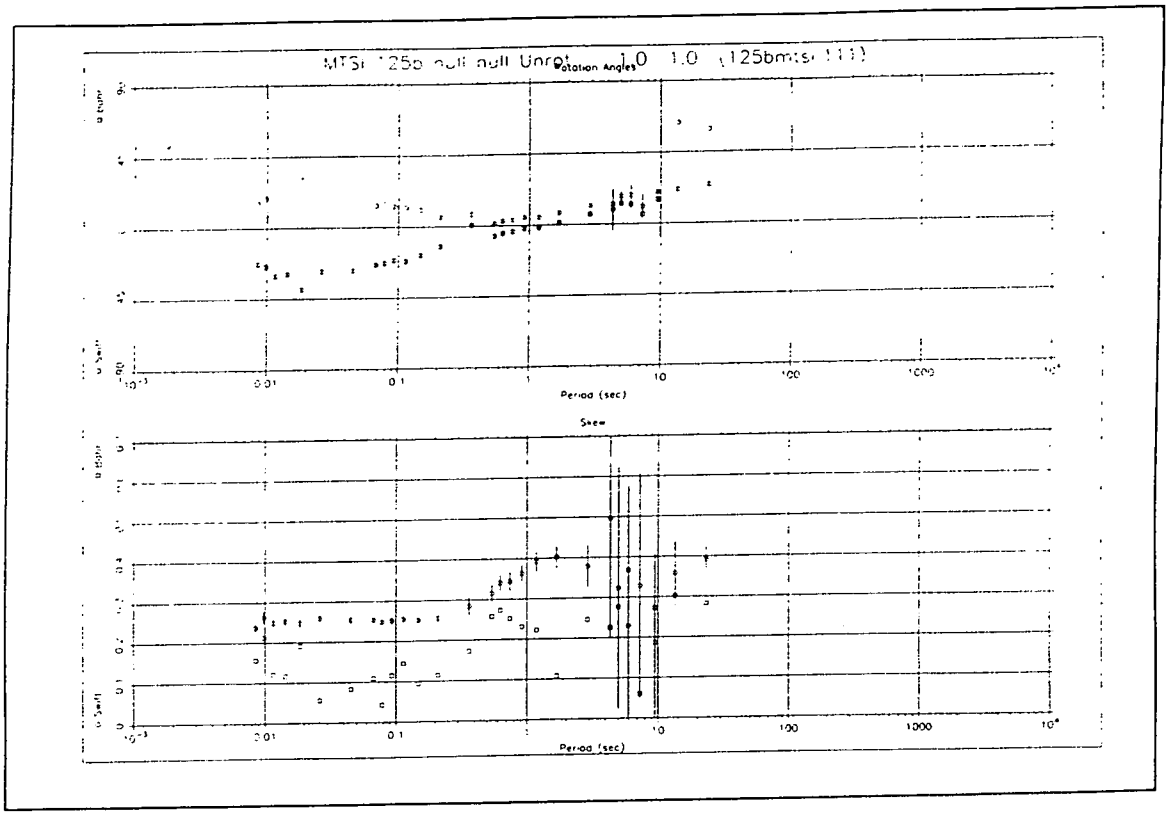

Fig.5.1.1

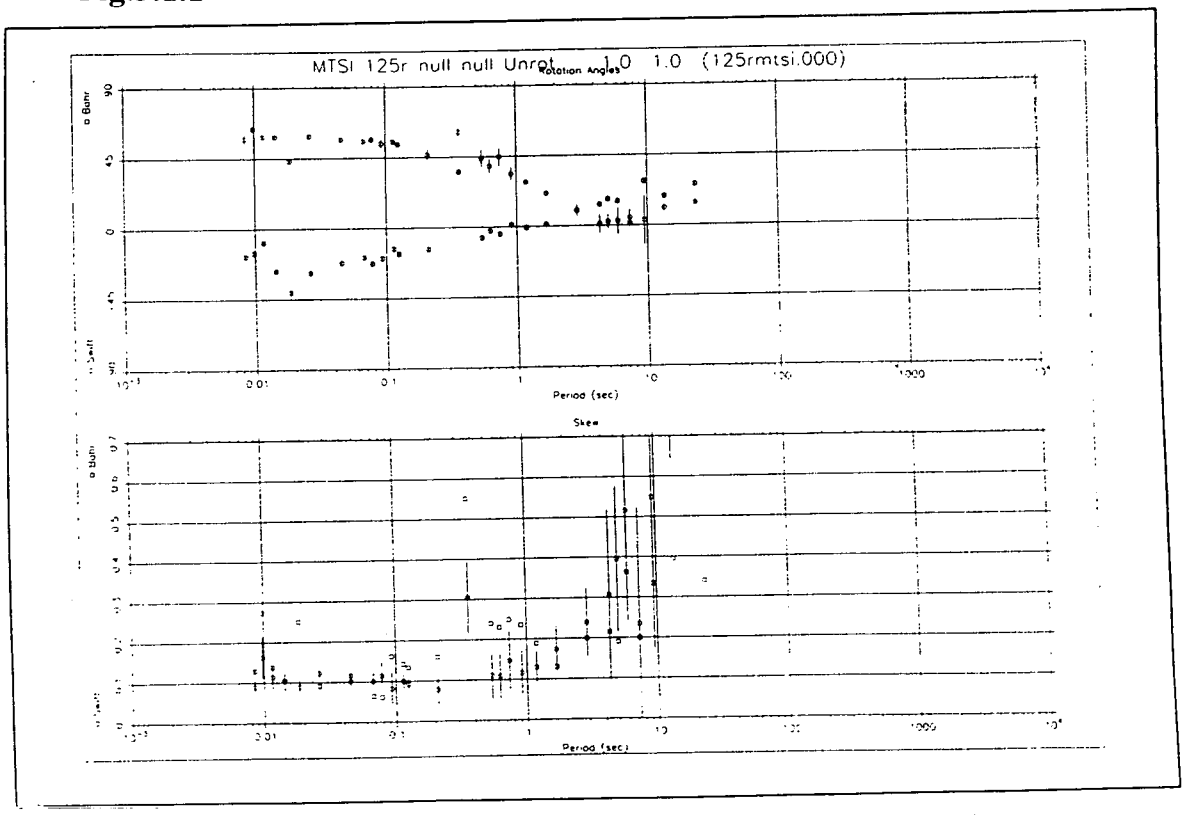

Fig.5.1.2

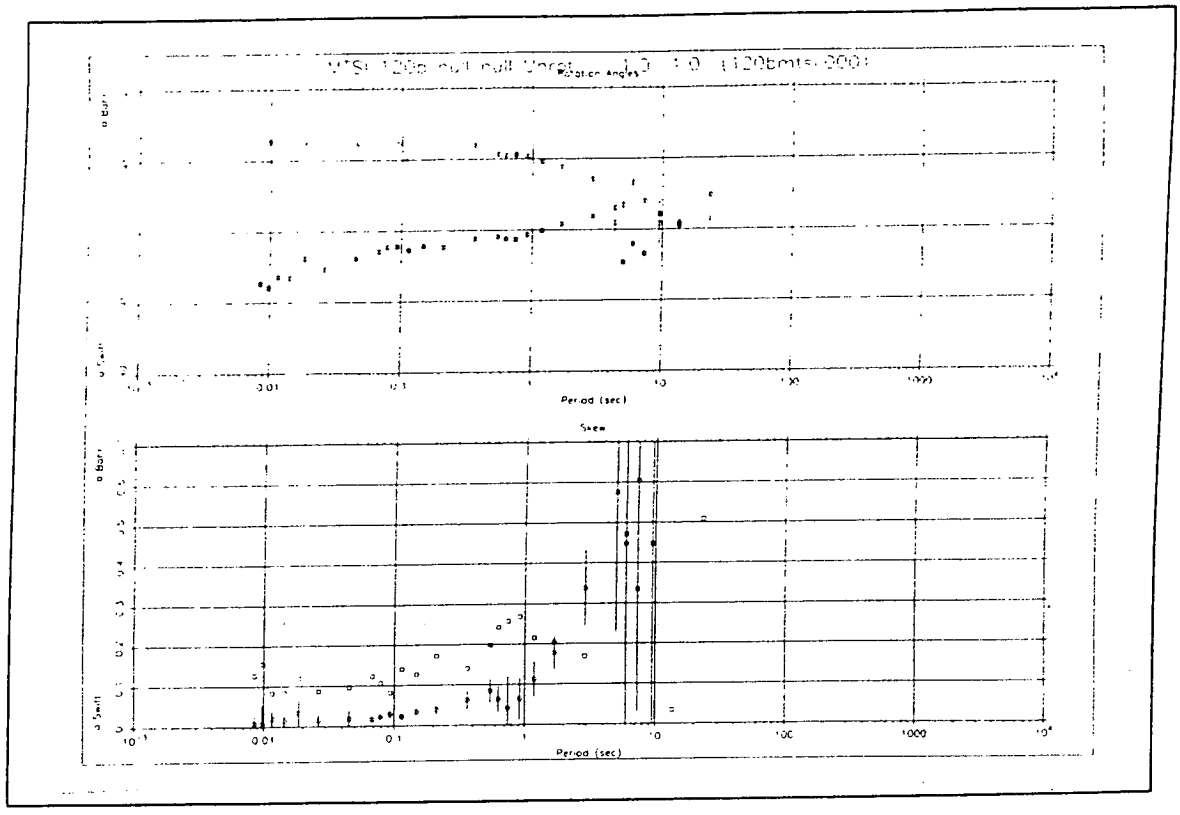

Fig.5.1.3

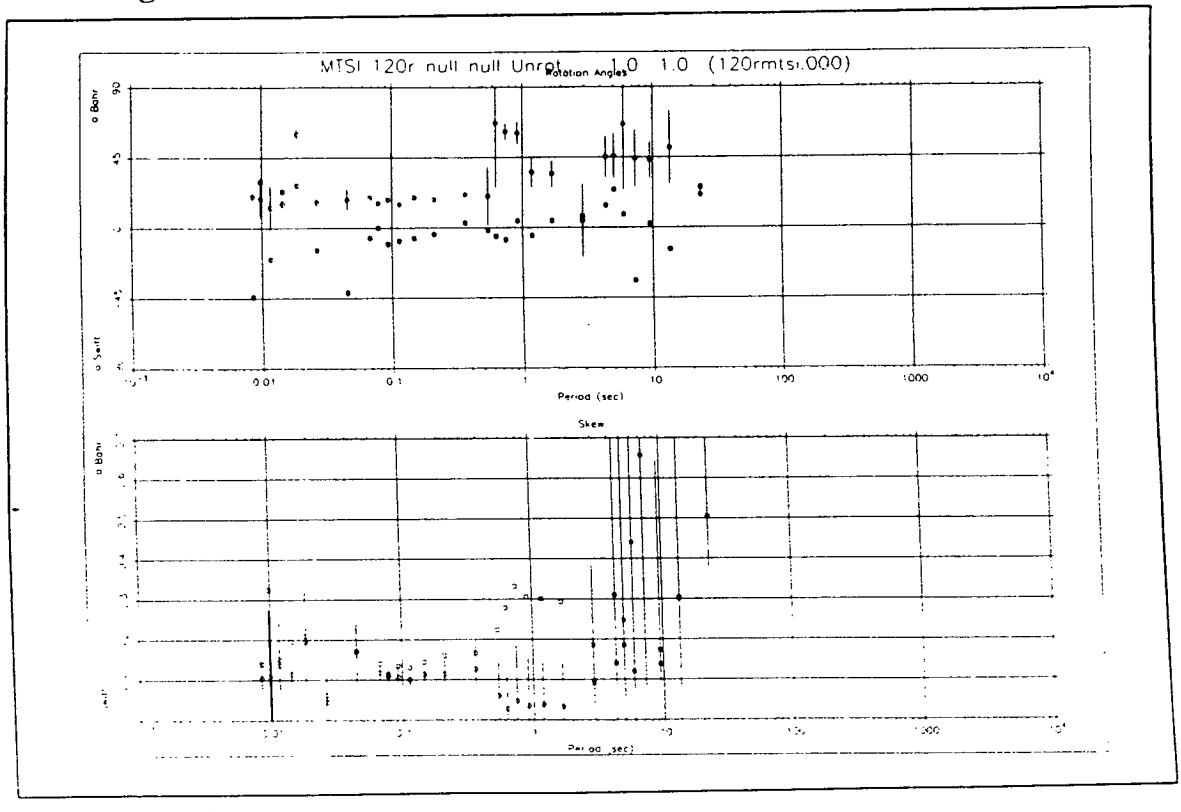

Fig.5.1.4

Figs.5.1.1-5.1.4: Azimuths and skew values as calculated by the methods of Swift and Bahr. **red squares:** Bahr's values, **circles:** Swift's values. No errors are shown for Bahr's skew values.

Bahr's skew for the same pair of sites (fig.5.1.1-2), is also more stable than Swift's. Similar effects can be observed for sites 120b and 120r (fig.5.1.3-4). Obviously local distortion is important on the scale of the site spacing (a few hundred metres).

Azimuths and skew values for the remaining sites are shown in appendix 1. Generally, Bahr's skew is relatively low (<0.2) at periods up to 0.5 s for all the sites, except 129, for which the skew increases rapidly with period. For a number of sites (128, 130, 131, 126), Bahr's skew is less than 0.2 up to 1 s. Above 1 s, it is generally higher and also more scattered, the latter probably due to bad data quality (sites 132, 124, 133).

5.4.2 Data analysis according to Groom and Bailey's methods

The subsequent manipulation of the data is based mainly on 3 Earth models:

1. The 1-D Earth, in which the conductivity varies only with depth. The solution involves calculation of only the off-diagonal impedance tensor elements.

2. The 2-D model, in which apart from the depth, the conductivity varies with one horizontal direction. The regional azimuth is defined according to the methods of Swift (1967).

3. A model which consists of a local 3-D distortion superimposed on a regional 2-D structure. This problem can be solved by separating the local effect as a frequency independent distortion of the regional response.

A useful tool which shows how well a model fits a particular set of data is the chi-squared (χ^2) residual error of fit normalised by the variances of the four elements of the measured impedance tensor:

$$\chi^2 = \frac{1}{4}\sum_{j=1}^{2}\sum_{i=1}^{2}\frac{\left|\hat{Z}_{ij} - Z_{ij}\right|}{\sigma_{ij}^2} \qquad (5.21)$$

where

Z_{ij} = measured data

$\hat{Z}_{ij}$ = modelled data

σ_{ij} = variance of the measured data

If the model is appropriate, it must fit each datum say within 3 standard deviations, so χ^2 should lie between 0 and 9. Attention must be paid to the fact that the misfit can be reduced for reasons other than that the particular model is

appropriate (data with large error bars or an increase in the number of free parameters within the model).

In the followings, sites 120b and 120r are examined in order to show how well the data fit to the proposed models.

5.4.2.1 Fit of 1-D models

Apparent resistivity and phase curves for the off-diagonal elements of the measured impedance tensor are shown in fig.5.2a, together with the chi-squared residual error of fit of the 1-D model to the data. The two tensor elements show a split at short periods and at longer periods for the resistivity and phase respectively. The first is probably due to a static shift for the resistivity which does not affect the phase, whereas the second shows a multidimensional environment at depth (split in the phases). The resistivity data are not so good at the longer periods. The inappropriateness of the 1-D model in this example is clearly shown by the very large chi-squared residual $\chi^2 > 200$ at most periods. The relatively low χ^2 at T>4 s can be explained by the dependence of χ^2 on the data errors as well as the low signal level (eq.5.21).

5.4.2.2 Fit of 2-D models

Fig.5.2b shows the fit of Swift's 2-D model to the data. The apparent resistivities are rotated through an angle, the regional azimuth, which is about 45^0E for the entire period range. While the phase for the two impedance elements is almost identical (except at a few low frequencies), the resistivity curves are separated by a factor of order 10. The chi-squared error of misfit is lower than before ($\chi^2<100$) but still not acceptable. The noise to signal ratio as well as the skew increases with period.

5.4.3.3 Fit of 3-D models

The G-B decomposition for site 120b is shown in fig.5.2c, where there is a significant decrease in the rms error of fit ($\chi^2<1$). This is not surprising since the number of free parameters has increased from 5 in the 2-D model to 7 (shear + twist angle). The resistivity curves are more homogeneous than before, while the phase curves show the same split towards longer periods. Indeed, the regional Swift's azimuth (fig.5.2b), seems closer to the local azimuth of G-B (fig.5.2c), while the regional azimuth for the latter gives angles 60^0-90^0E at the shorter periods and around 30^0E at the longer. The difference between the two azimuths (local and regional) can be explained by the large shear angle (>20^0), while the twist angle is around zero. The swing in shear angle is reflected also on the regional azimuth.

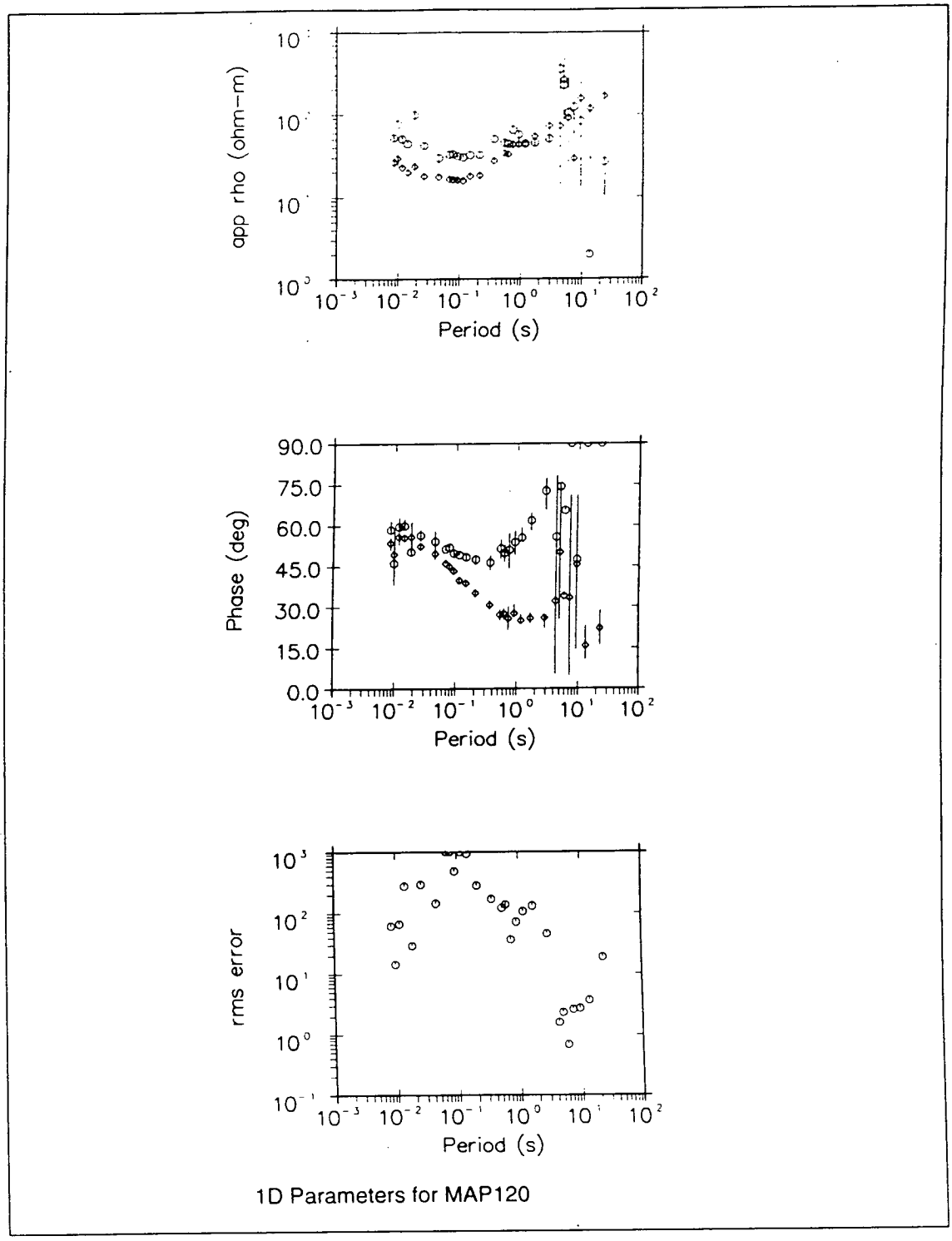

Fig.5.2a: Unrotated apparent resistivities and phases for site 120b, and rms misfit to 1-D model. **XY component**:circles **YX component**: diamonds.

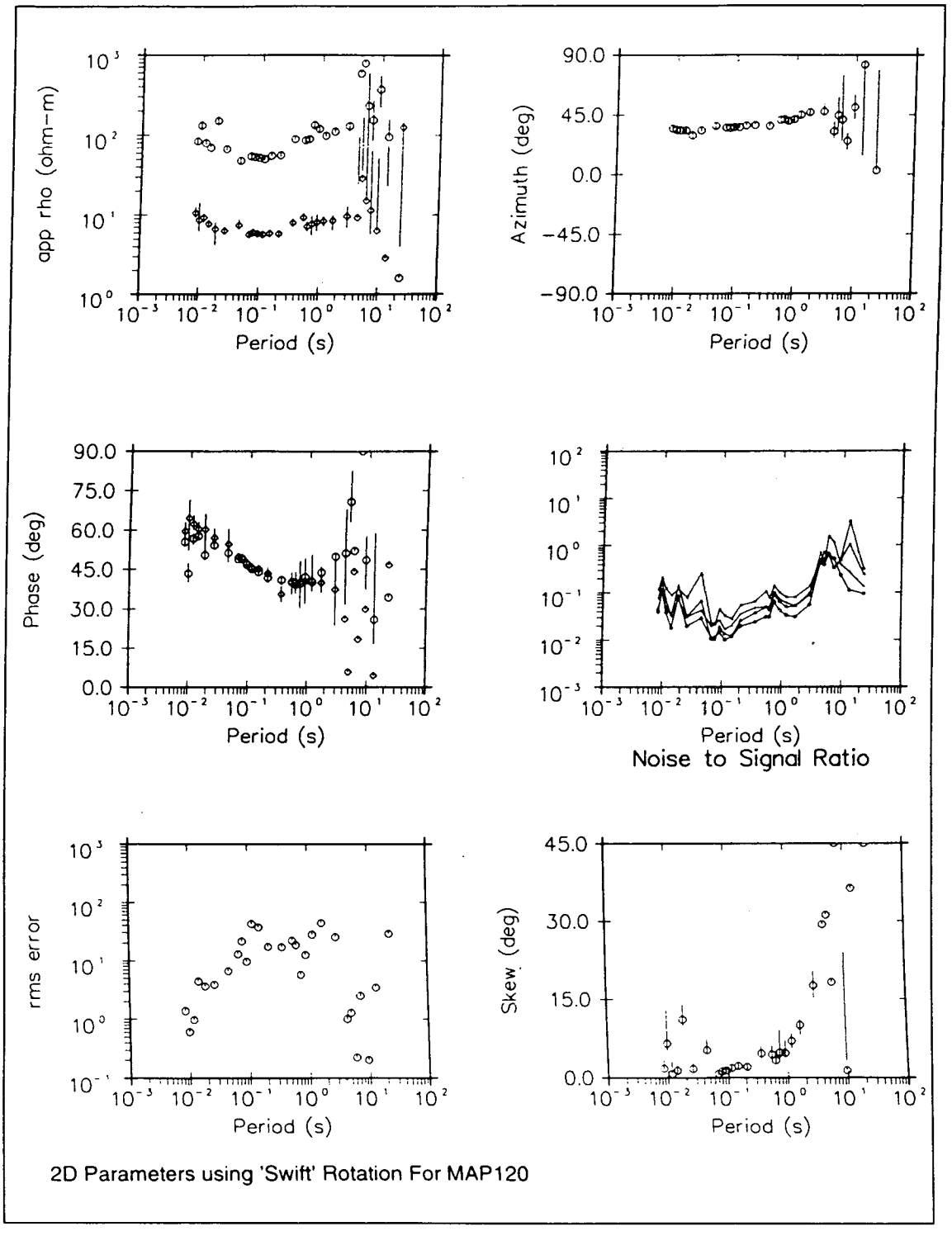

Fig.5.2b: Apparent resistivities and phases after Swift's rotation, for site 120b and rms misfit of the 2-D model to the data. **XY component:** circles. **YX component:** diamonds. The skew calculated from eq.(2.43) is shown in degrees according to eq.5.12.

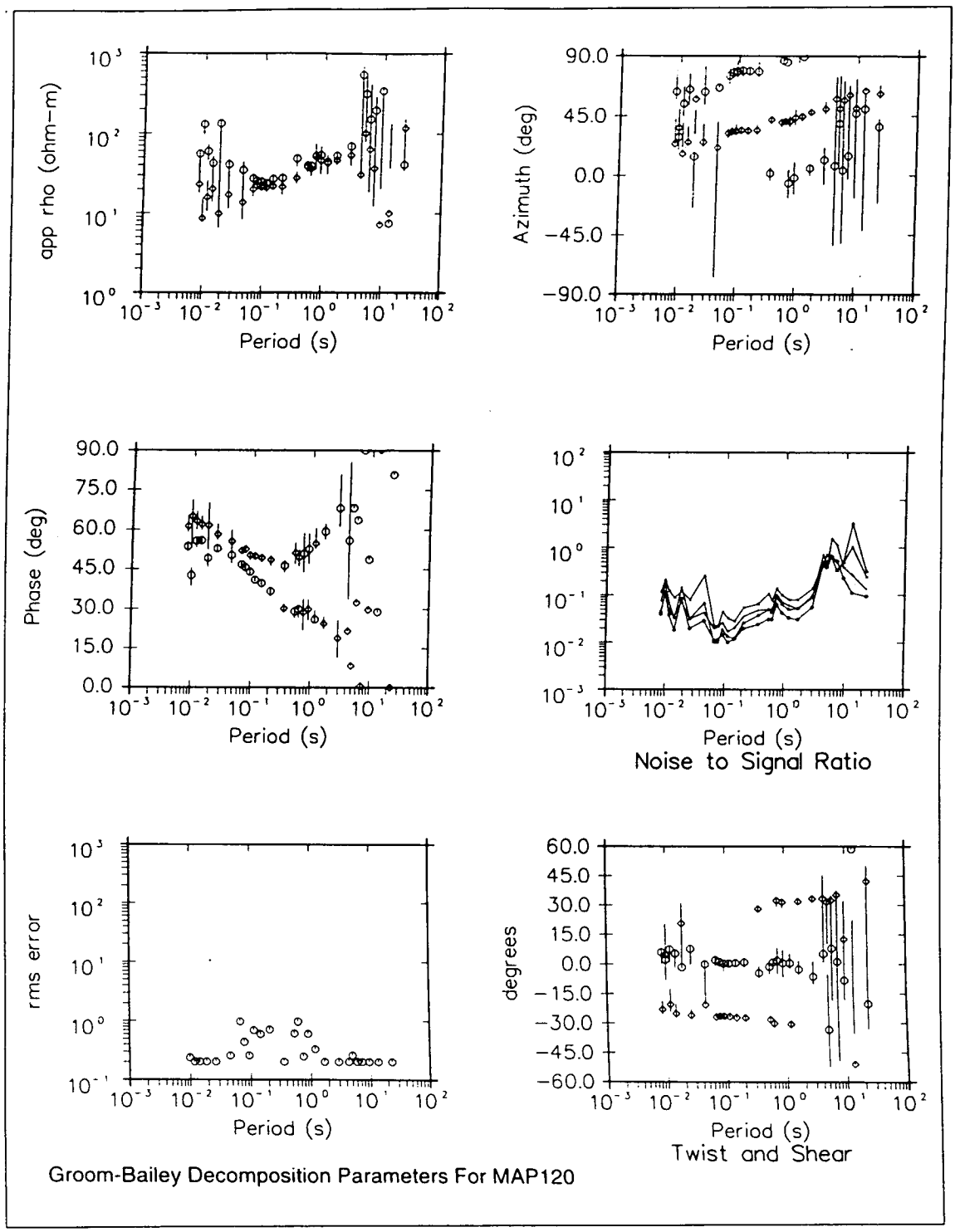

Fig.5.2c: Groom and Bailey's decomposition for site 120b and rms misfit of the G-B model to the data. **XY**: circles. **YX**: diamonds. **Regional azimuth:** circles. **Local azimuth**: diamonds. **Twist angle**: circles. **Shear angle**: diamonds.

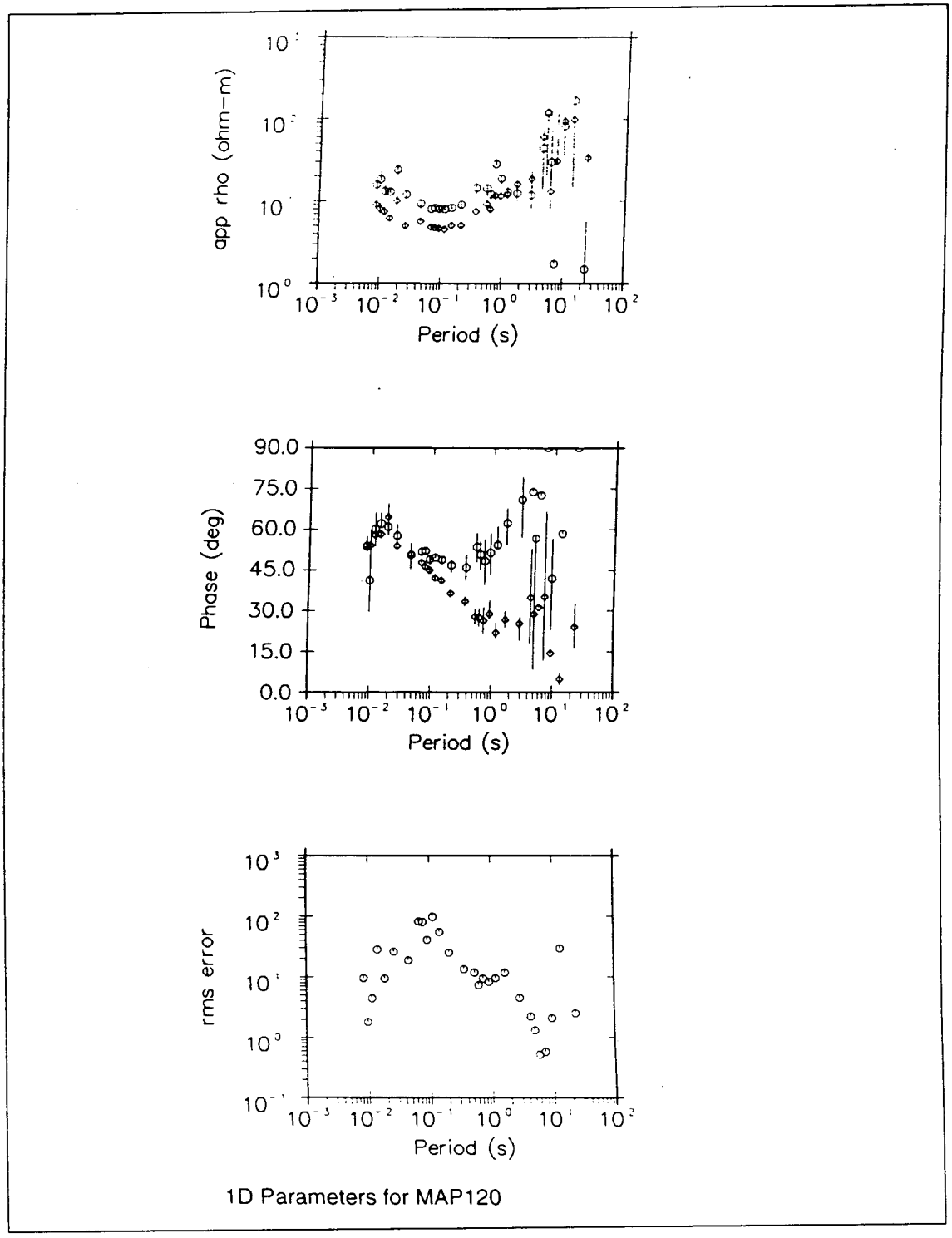

Fig.5.3a: Unrotated apparent resistivities and phases for site 120r, and rms misfit to 1-D model. **XY**:circles **YX**: diamonds.

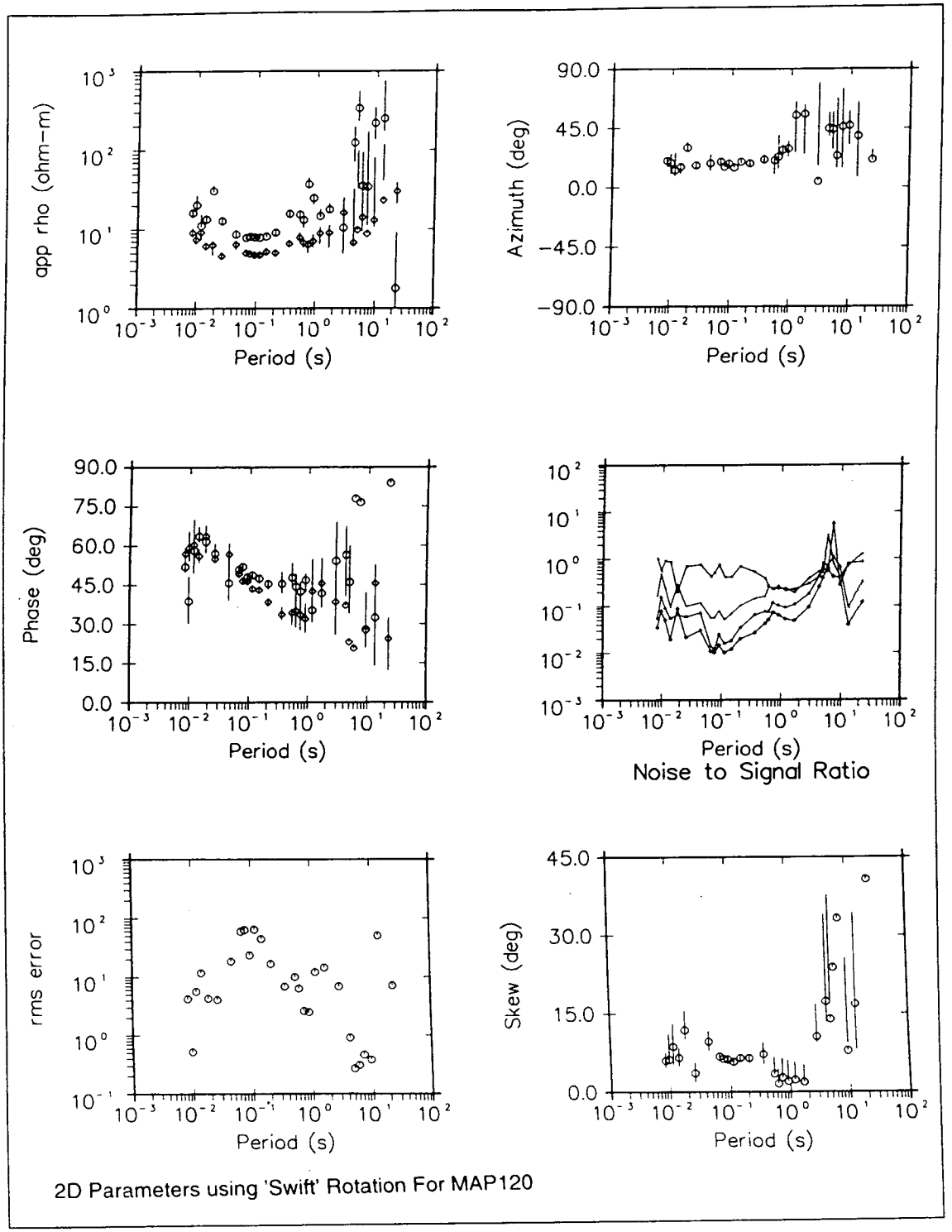

Fig.5.3b: Apparent resistivities and phases after Swift's rotation, for site 120r and rms misfit of the 2-D model to the data. **XY**: circles. **YX**: diamonds.

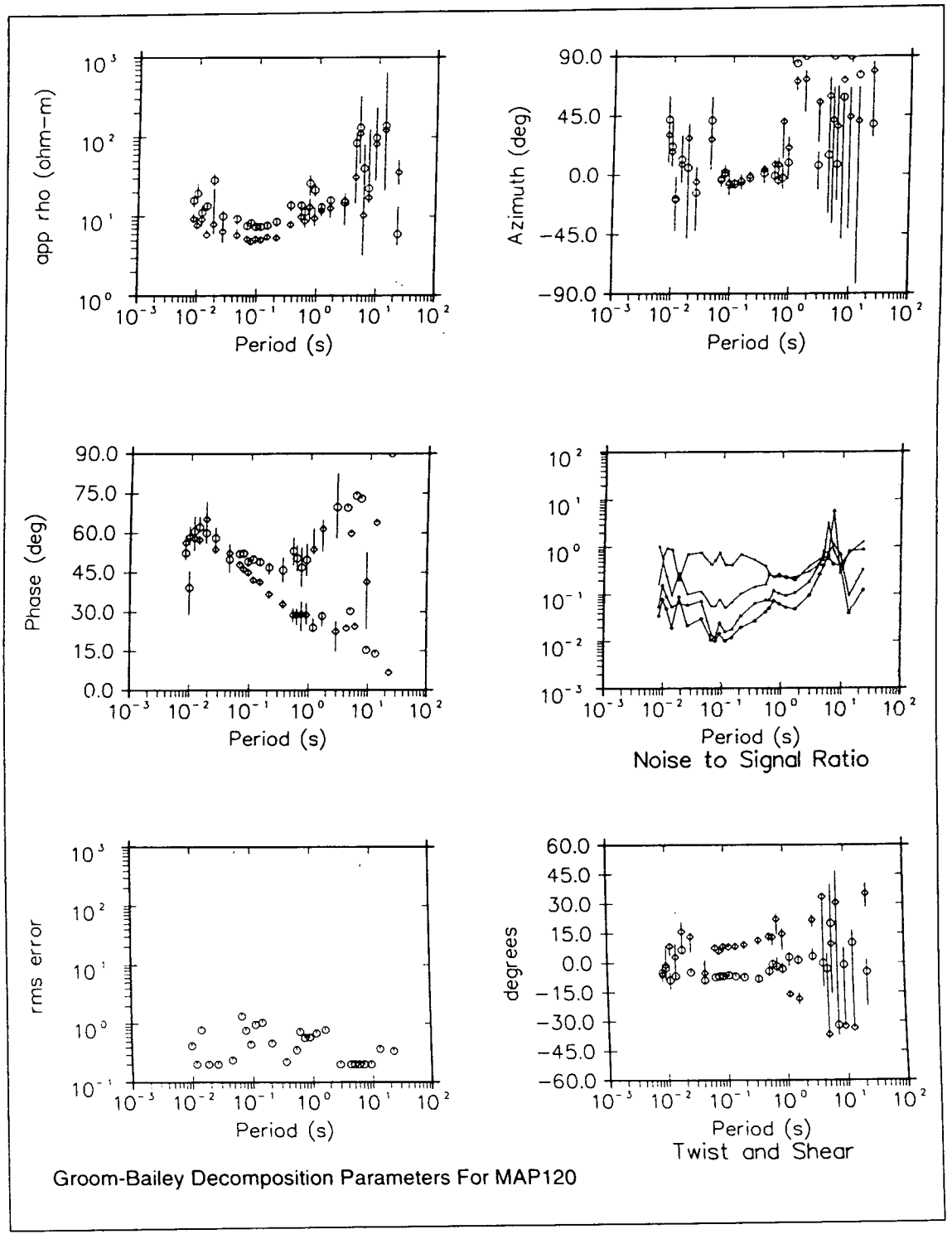

Fig.5.3c: Groom and Bailey's decomposition for site 120r and rms misfit of the G-B model to the data. **XY**: circles. **YX**: diamonds. **Regional azimuth**: circles. **Local azimuth**: diamonds. **Twist angle**: circles. **Shear angle**: diamonds.

Another site (120r) situated no more than 250 m to the N of 120b, shows quite different characteristics. As can be seen, for the 1-D analysis (fig.5.3a) the resistivity curves are shifted down to 30-60 Ohm m, compared with site 120b. The phase curves are identical with those of site 120b, but the chi-squared is much less (χ^2<100). The better fit of the 1-D model at site 120r is possibly due to the smaller diagonal impedance elements at 120r, compared with those at site 120b (being showed by the up-shifted resistivity values).

In contrast with 120b, the 2-D analysis shows no big difference compared with the 1-D, and the azimuth is slightly different from site 120b (fig.5.2b and 5.3b).

G-B decomposition (fig.5.3c) gives shear and twist angles around 10^0 for the shorter periods, while above 1 s the twist is around 0^0 and the shear increases towards 30^0. The azimuth is not well defined towards longer periods and this can be due to the large and scattered shear angles (>30^0) at T>4 s.

A few points can be drawn from this investigation:

1. Measurements done at two sites with a separation distance of less than 300 m and which use the same 3 magnetic components, should be identical. The difference observed can be attributed to purely telluric effects caused by near-surface local bodies.

2. Shear and twist angles should be frequency-independent. This is quite true for periods up to 0.2 s, above which the shear and twist angles increase with period and are more scattered, the latter possibly due to the bad data quality.

Results at all the sites show the above characteristic: For short periods (not exceeding 0.5 s), shear and twist angles are frequency independent and smaller than 15^0, which is not true for longer periods. Table 5.2 summarises shear and twist angles for all sites (only base sites are shown except 121, which was excluded due to very bad quality data), and for 3 different periods: 0.1, 1 and 13 s.

From table 5.2 it is clear that towards longer periods (i.e. greater depth), distortion effects due to 3-D regional induction (shown by the large shear and twist angles) become more important.

T →	0.1 s		1 s		13 s	
site	s	t	s	t	s	t
124	10	1	23	18	2	29
123	4	3	7	2	14	14
126	5	7	9	7	7	25
131	7	11	9	3	3	3
132	3	6	4	0	18	24
133	2	9	7	9	1	2
130	5	3	11	4	34	9
122	2	1	9	10	27	14
120	8	6	0	30	50	54
125	1	14	5	22	36	26
128	4	1	7	6	11	6
129	1	14	13	8	6	23

Table 5.2: Absolute values of shear and twist angles in degrees for 3 periods: 0.1, 1 and 13 s. **T**: Period. **s**: shear angle. **t**: twist angle. The sites are shown in the first column and are ordered from North (up) to South (down).

5.4.3 Groom-Bailey and Bahr 's azimuths

The azimuths calculated with the previous methods are shown in table 5.3 for a number of selected periods. For the longer periods site 124 was excluded, because the data were very scattered.

From the AMT data (table 5.3a), the following points can be observed:

1. For the majority of sites, and at all four periods, the two regional azimuths do not differ by more than 10^0, except for the 90^0 uncertainty.

2. For the majority of sites at 0.1 and 1 s, regional and local azimuths do not differ by more than 15^0. At 13 and 23 s differences between these two azimuths are considerably higher. This confirms the fact that while galvanic distortion does not significantly affect near-surface structures, the assumption that the Earth can be represented by a 2-D model breaks down at depth.

T →	0.1 s			1 s			13 s			23 s		
site	**R**	**B**	L	**R**	**B**	L	**R**	**B**	L	**R**	**B**	L
124	**56**	**-18**	46	**25**	**20**	-37						
123	**8**	**9**	14	**35**	**39**	41	**38**	**29**	11	**35**	**27**	31
126	**90**	**0**	78	**38**	**45**	40	**32**	**24**	0	**35**	**26**	81
131	**87**	**-4**	-78	**90**	**-15**	-77	**30**	**25**	30	**34**	**26**	29
132	**26**	**28**	17	**3**	**-37**	8	**32**	**28**	25	**40**	**31**	29
133	**90**	**0**	-80	**19**	**-10**	20	**24**	**23**	21	**38**	**30**	34
130	**73**	**-15**	82	**79**	**-10**	85	**27**	**22**	81	**33**	**30**	84
122	**90**	**0**	87	**73**	**-12**	73	**34**	**25**	64	**41**	**28**	69
120	**79**	**-10**	34	**89**	**-1**	45	**50**	**2**	64	**37**	**23**	68
125	**10**	**10**	24	**27**	**30**	48	**28**	**21**	41	**30**	**24**	41
128	**24**	**30**	20	**20**	**27**	22	**47**	**36**	52	**50**	**35**	40
129	**3**	**3**	19	**41**	**37**	46	**59**	**45**	42	**53**	**50**	31

Table 5.3a: Groom and Bailey's regional and local azimuths plus Bahr's regional azimuth in degrees to the East for 4 AMT periods 0.1, 1, 13 and 23 s. Regional azimuths are shown in bold. **T:** period. **R:** G-B regional azimuth. **B:** Bahr's azimuth. L: G-B local azimuth. The sites are shown in the first column and are ordered from North (up) to South (down).

Site →	123l			125l		
T(s)	**R**	**B**	L	**R**	**B**	L
250	**44**	**29**	90	**90**	**8**	-25
1000	**49**	**-28**	87	**47**	**-20**	87
2500	**90**	**-10**	81	**57**	**-20**	-24
6000	**53**	**-9**	-85	**63**	**40**	-85

Table 5.3b: Groom and Bailey's regional and local azimuths plus Bahr's regional azimuth in degrees to the East for 4 LMT periods, 250, 1000, 2500 and 6000 s. Regional azimuths are shown in bold. **T**: Period. **R:** G-B regional azimuth. **B:** Bahr's azimuth. L: G-B local azimuth.

3. The 90^0 uncertainty between the two methods occurs only at 0.1 and 1 s. There is a tendency for the azimuth, especially for sites at the centre and close to the discontinuity between the volcanics and the S block of carbonates, to orientate around 0^0 or 90^0 at T<1 s. The site 120, which is the closest to the geological boundary (fig.3.3), exhibits the largest difference between regional and local azimuths.

4. There is a tendency for the regional azimuths to rotate towards E from N to S along the profile. For example, at T=23 s, Bahr's azimuth is around 26^0E inside the peninsula, but reaches up to 50^0 southwards on the mainland. This suggests that a different electrical structure may exist in Trizina graben.

5. Bahr's azimuths are generally slightly lower than G-B. This becomes more obvious at the longer periods 13 and 23 s, where there is an indication of a possible strike direction at 24^0-35^0 for Bahr and at 33^0-40^0 for G-B.

For the LMT azimuths shown in table 5.3b, the following comments can be made:

6. The amount of local distortion is shown clearly by the large differences between regional and local azimuths

7. The regional azimuth cannot be defined, as different directions are suggested through the LMT range, due probably to the small number of LMT stations as well as to the deep 3-D structure of the area.

5.4.4 In search of a strike direction

In order to model the electrical structure under Methana by using a 2-D model, the regional strike direction is needed. This direction must give information about the deep electrical structure under Methana, not about local directions indicating near surface current concentration. The above decomposition techniques aimed to detect such small local effects, and extract the reliable information.

By examining the azimuths suggested, the angles of 90^0 and 25^0-40^0E were predominant for the AMT data (at T<1 s and T>10 s respectively). For the LMT bands it was not easy to select a predominant angle as only two sites were measured. However, given the instability in regional strike determination due to noise, and in the distortion parameters which were independent of frequency only at T<0.5 s, it would not be very wise to attempt to define a regional strike by considering the rotational properties or the decomposition results of the impedance tensor alone. Information from other independent methods is also necessary.

This information can be provided by the induction arrows and by the geology. In section 4.5.4 the behaviour of the induction arrows was discussed. A regional strike of 90^0E would require them to lie in a N-S plane, which is true for periods above 3000 s but not for periods up to 1 s. A strike of 25-40^0E suggested for T>10 s requires the induction arrows to lie in a plane of about 120^0E. Actually, for that particular period range the arrows show a direction of 50-70^0E. But the induction arrows (fig.4.7) at many sites point towards the sea around the peninsula. The remainder of this chapter is devoted to examine more specifically the effect that the sea can have on the data, and particularly at which periods the effect is more prominent. This can be done very effectively by modelling using a thin sheet approximation. Information on strike given by the geology of the area will be discussed at the end of the chapter.

5.5 Thin sheet modelling

Having examined the data from the point of view of Earth models (1-D, 2-D and 3-D local superimposed on 2-D regional), it remains to see the effect of the conductive sea water. For that, a model in which the region of the laterally varying conductivity is confined to a thin layer on the top of a halfspace, is considered. The thickness of the thin sheet represents the depth of the ocean at the surface of the Earth.

Thin sheet approaches have found their principal field of application in modelling situations that involve the channelling of induced electric currents in the sea around islands, peninsulas or other geographical features. (Notice that a layer may be regarded as a thin sheet if its thickness is much less than the skin depth in the underlying layer).

5.5.1 The algorithm

In this study, the modelling program based on the work of McKirdy, Weaver and Dawson (1985) is adopted. The mathematical model underlying the algorithm (fig.5.4) involves a thin sheet with negligible thickness on top of a halfspace which is in electrical contact with the overlying sheet. The surface sheet has a conductance of $\tau(x,y)$, so conductivity and depth values which correspond to surficial rocks and the sea water can be modelled. The structure of the thin sheet must become 2-D at infinity, in practice at the edge of the grid. This means that $\partial\tau/\partial x \rightarrow 0$ as $|x| \rightarrow \infty$ and $\partial\tau/\partial y \rightarrow 0$ as $|y| \rightarrow \infty$, and the solution will tend to an E-polarisation (H-polarisation) limit as $|x| \rightarrow \infty$ ($|y| \rightarrow \infty$), when the inducing field is in the y-direction as indicated in fig5.4.

The boundary conditions for induction in a thin sheet have been established by Price (1949). They are based on the equations:

$$E(r, 0^-) = E(r, 0^+) = E(r) \qquad (5.22)$$

$$H(r, 0^-) - H(r, 0^+) = 2\tau(r)\ \hat{z} \times E(r) \qquad (5.23)$$

$$Z(r, 0^-) = Z(r, 0^+) = Z(r) \qquad (5.24)$$

where:

E, H and Z are the horizontal electric, horizontal magnetic and vertical magnetic component respectively, at the top surface of the thin sheet $(r, 0^-)$ or the bottom surface $(r, 0^+)$;

τ is the integrated conductivity of the thin sheet;

$\hat{z}$ is a unit vertical vector.

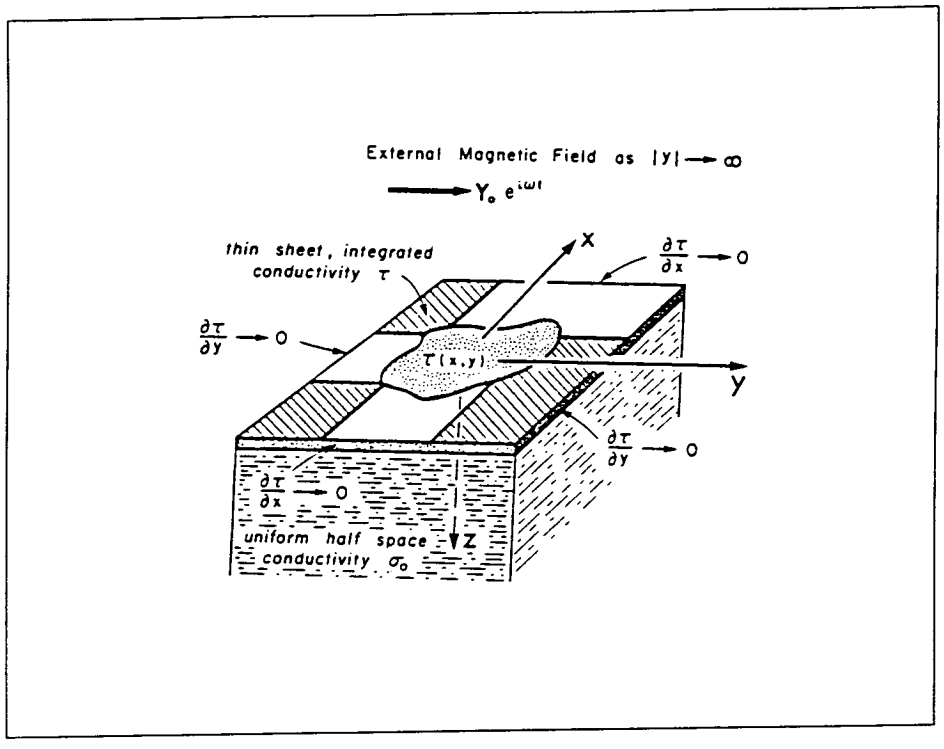

Fig.5.4: The mathematical model

Although the horizontal electric and vertical magnetic field are continuous across the sheet boundary, the horizontal magnetic field is discontinuous by an amount proportional to the density of the surface current flowing in the sheet.

In this algorithm, the magnetic field is expressed as a convolution of the electric field and an admittance tensor (Dawson and Weaver, 1979). The field equations can be solved analytically above and below the thin sheet, leaving only the sheet itself as the region where numerical methods are applied. For that, a N by N discretised numerical grid is first constructed and then surface integrals are evaluated at each grid point.

The regional magnetic field, by being in the y-direction (fig.5.4), reaches an E-polarisation limit as $x \to \infty$. By performing the calculations with the inducing field in the x-direction, the E-polarisation limit is reached at $y \to \infty$. In this way, the response of a regional field of arbitrary orientation can be calculated. In practice, the most convenient way of doing that is by rotating the model 90^0N clockwise, and then after the completion of the calculation for this new model, to transfer the results back to the original coordinate system.

5.5.2 Models and restrictions

The numerical model comprises all the area of investigation, i.e. the peninsula, an extension to the SW, and the surrounding sea (fig.5.5A). The conductivity values on the sheet were taken to be 0.25 Ohm m for the sea and 100 Ohm m for the land material, as was suggested by the MT data. The maximum depth of the sea water was taken to be 150 m as indicated by the bathymetric data (IGME, 1972). In the version installed on the departmental workstation the maximum grid size of the thin sheet was limited to 21 by 21. Field values were assigned to each of the 441 points of the grid. Although it would be desirable to model the area for the widest possible period range, there are certain restrictions which allow only a few models to be examined.

These restrictions are imposed on:

(i) The periods of the inducing field.

(ii) The shape and size of the model.

The condition under which a layer can be considered as a thin sheet restricts the lower limit of the period range. The skin depth of the sea water for T=0.1 s is 80 m. Unfortunately, this depth is less than the depth of the sea (150 m), so this period cannot be legitimately modelled, though the periods around 0.1 s belong to a range of interest (section 4.5.3). For T=1 s the skin depth is 250 m. Hence T=1 s will be the shortest period examined. (Nevertheless, an attempt to model the sea effect at T=0.1 s showed almost no difference from that at 1 s).

On the other hand it is necessary to keep conductivity gradients away from the edges of the grid, so that the assumption of two-dimensionality at infinity will be valid. It was suggested that a distance of δ_1 will be appropriate, where δ_1 is the skin depth of the layer beneath the thin sheet.

By taking each cell to be 1 km, an area of A=441 km^2 is delineated. According to Weaver (1994), the smallest possible node spacing is:

$$\frac{\sqrt{A}}{N-1} = \frac{22}{21} \approx 1 \text{ km}, \quad \text{which comes true for the examined case} \qquad (5.25)$$

The resistivity of the underlying structure plays an important role in the modelling results. As pointed out by Weaver (1994), the conductivity of the first layer beneath the thin sheet plays a dominant physical role, because it controls the leakage of poloidal currents from the thin sheet into the underlying half space and vice versa. An underlying medium with a conductivity of 20-50 Ohm m is chosen to represent the halfspace. With a halfspace of 20 Ohm m the upper limit of the period is 5 s for the above model.

In order to estimate the sea effect for longer periods, induction on a much larger scale must be considered. For that, the model shown in fig.5.5B is examined. As can be seen, the model retains the gross features of the coastlines, the peninsula occupies a very small place, and emphasis is given to the mainland to the W and S, and to the sea to the N and NE. Other islands in the area, i.e Aegina and Poros are omitted. The mean depth of the sea is taken to be 400 m. With a halfspace of 50 Ohm m and a grid spacing of 4 km, fields for a period of 13 s were calculated.

5.5.3 The parameters calculated and comparison with the data

The parameters which can be calculated from the thin sheet model are Parkinson arrows, Swift's impedance tensor directions, and the current arrows associated with surface current density.

5.5.3.1 Induction arrows

Induction arrows are calculated for 4 periods 0.1, 1, 5 and 13 s. Three periods are shown, T=1 s (fig.5.6), T=5 s (fig.5.7) and T=13 s (fig.5.8) calculated from model A (1 and 5 s) and model B (13 s), and the calculated arrows are compared with the measured data. Real and imaginary Parkinson arrows are drawn at a number of grid points whose position correspond approximately to the actual field stations.

1. At T=1 s there is a good agreement between the model and the data for the real arrows (fig.5.6A) at sites closer to the NE coast, which indicates that at the NE coast there is a distortion effect due to the sea. A fairly good agreement is seen for the site in the SW, but not at the centre, the S block and the mainland. The real arrows are larger closer to the sea and much smaller on the land and in the centre of the peninsula.

2. At T=5 s (fig.5.7A), there is generally less agreement, only two sites fit the model exactly. At this depth probably induction in the shallow seas is of less importance.

3. Comparison between the measured and the calculated imaginary arrows (figs.5.6B and 5.7B) does not show a good agreement. Very few sites fit the model, therefore it is possible that apart from the sea there are also other conductive features affecting the MV data.

4. At T=13 s (fig.5.8), the skin depth is much bigger, but the model now includes a much larger proportion of the surrounding deep sea, whose effect becomes obvious. The calculated real arrows point consistently to the NE (except in the SW part of the peninsula which is affected by the small channel separating Methana from the

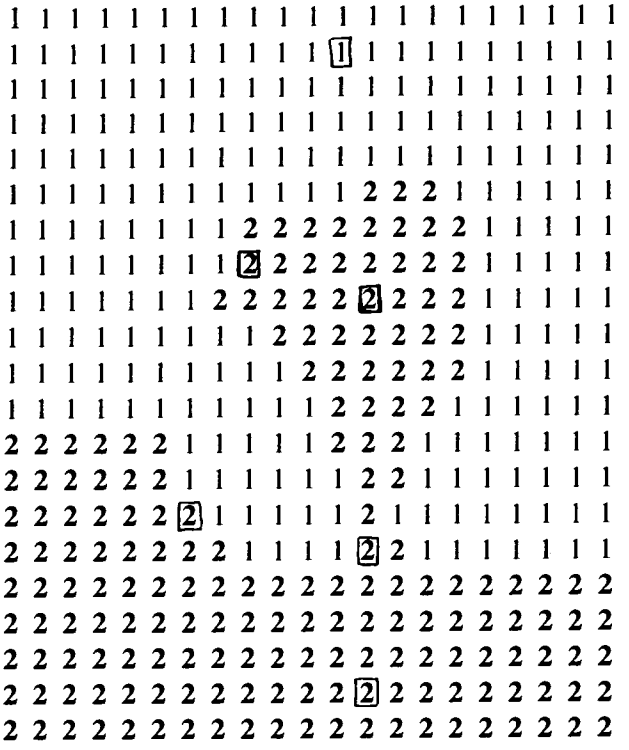

Fig.5.5A: Model A. 1:sea 2: land. Grid spacing is 1 km.

Open squares: points (1-6) discussed in section (5.5.3.3). From the right bottom and anti-clockwise: point 1 → point 6.

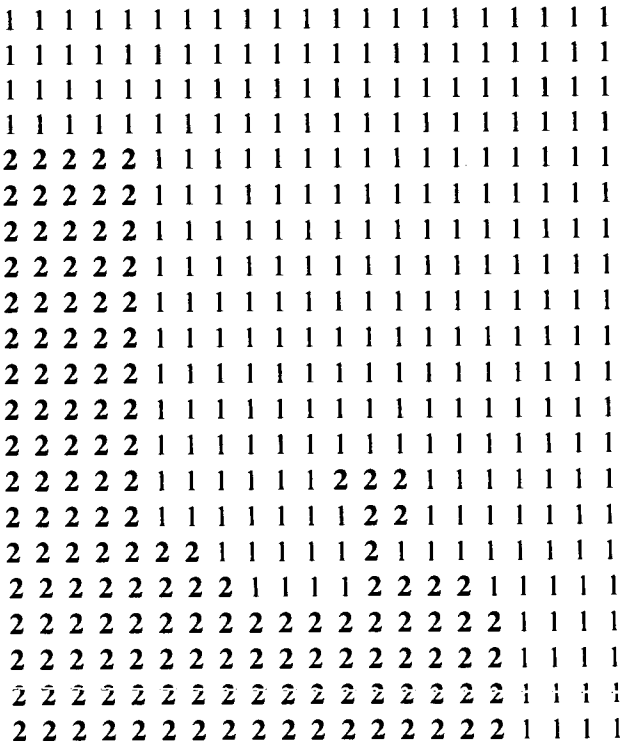

Fig.5.5B: Model B. 1:sea 2: land. Grid spacing is 4 km

Fig.5.5: Models of Methana used in the algorithm.

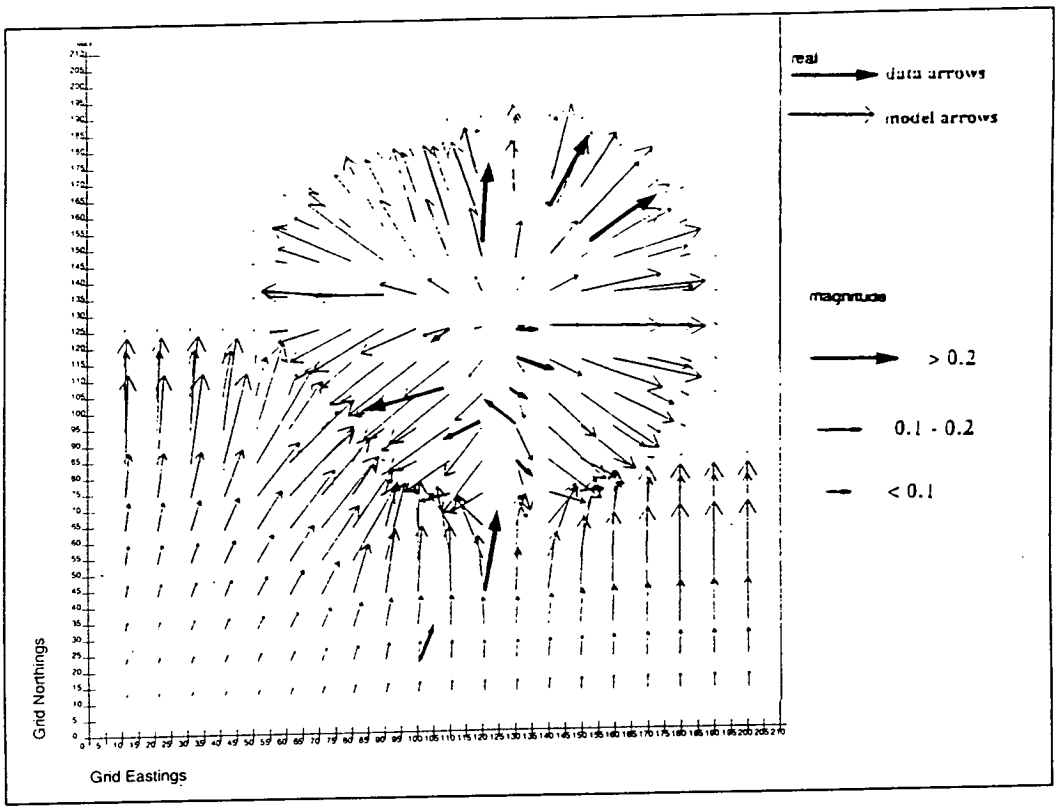

Fig 5.6A: Real induction arrows for T=1 s.

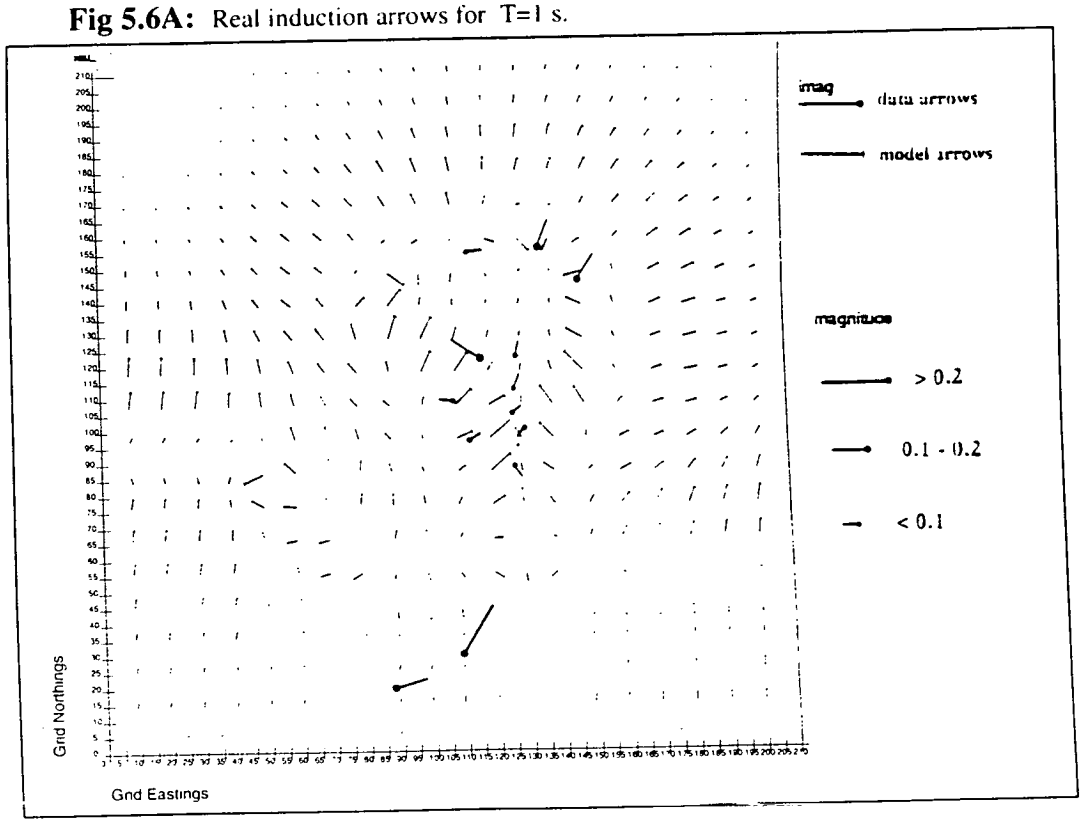

Fig 5.6B: Imaginary induction arrows for T=1 s.

Comparison of the model to the data. The measured induction arrows are superimposed on those calculated from the thin sheet modelling and are shown in bold.

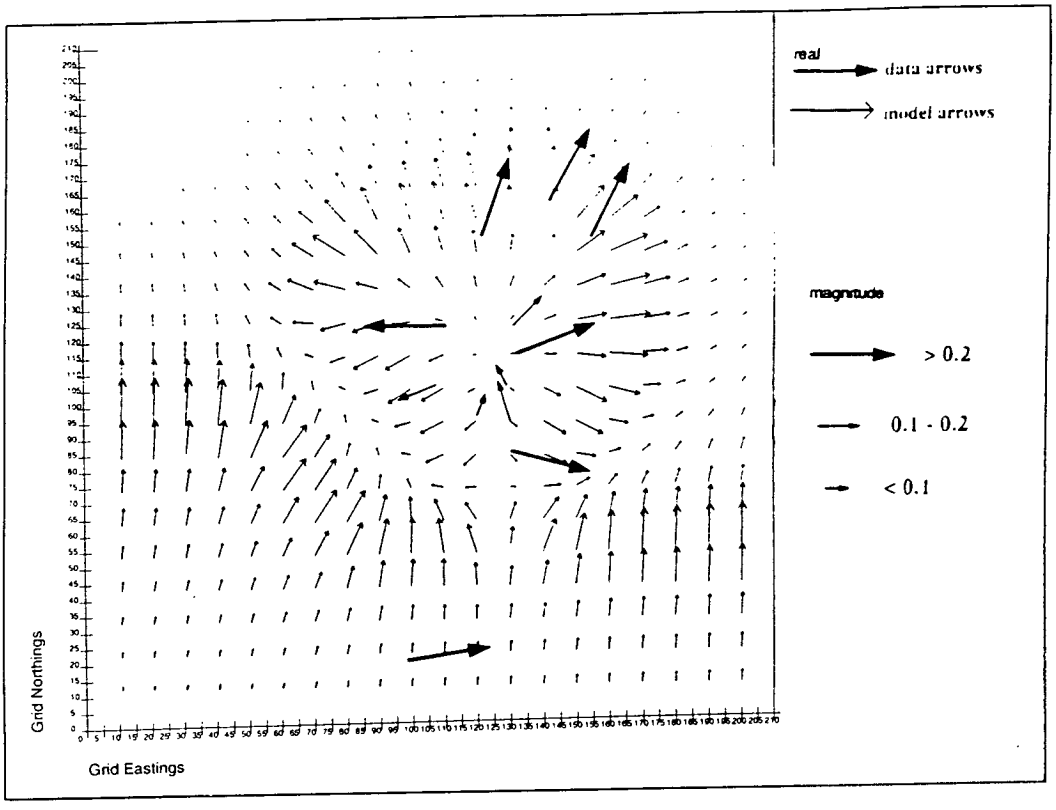

Fig.5.7A: Real induction arrows for T=5 s.

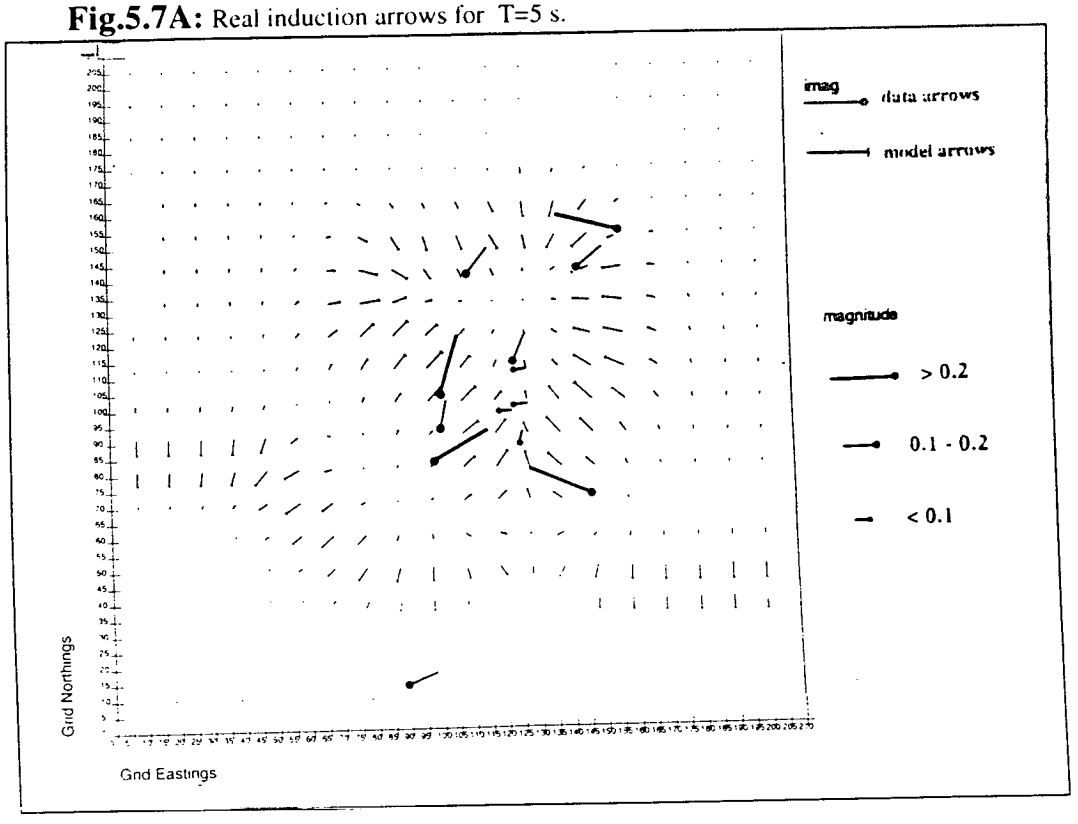

Fig.5.7B: Imaginary induction arrows for T=5 s.

Comparison of the model to the data. The measured induction arrows are superimposed on those calculated from the thin sheet modelling, and are shown in bold.

western mainland). There is a good agreement between the model and the data, as in both the tendency of the real arrows to point to the NE persists. In fact, the measured arrows point to the NE up to 23 s (fig.4.7D), but because of the computational restriction, it was not possible to model. Although this is a different induction problem from that of model A, the real arrows indicate a strong coast effect at T=13 s. In contrast with the shorter periods, the fit of the imaginary arrows with the data is better.

5.5.3.2 Impedance tensor directions

In figs.5.9A and B, strike directions as calculated by the method of Swift (1967) for the model A are compared with those calculated from the measured impedance tensor by using the same method, at T=1 s and 5 s. At T=1 s, the model shows agreement with the data at all sites except at the sites located in the S part of the peninsula. The anisotropy shown by the model reaches its maximum at the narrow isthmus which separates Methana from Trizina graben.

At T=5 s (fig.5.9B), there are not many changes in the model (compared with that calculated at T=1 s), although the data at all sites show consistent azimuth directions of 20^0-35^0E. As a result, the fit of the model to the data is generally poor.

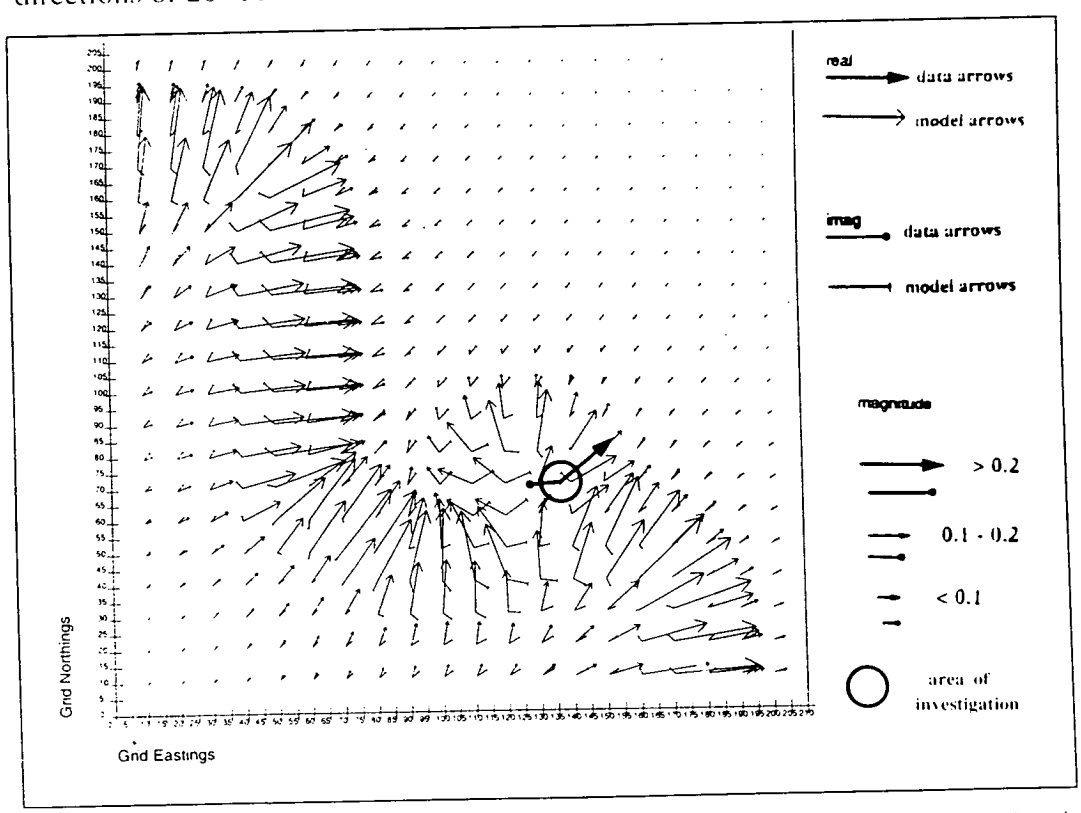

Fig.5.8: Real and imaginary induction arrows for T=13 s. Comparison of the model to the data. The measured Parkinson arrows are superimposed on those calculated from the thin sheet modelling and are shown in bold.

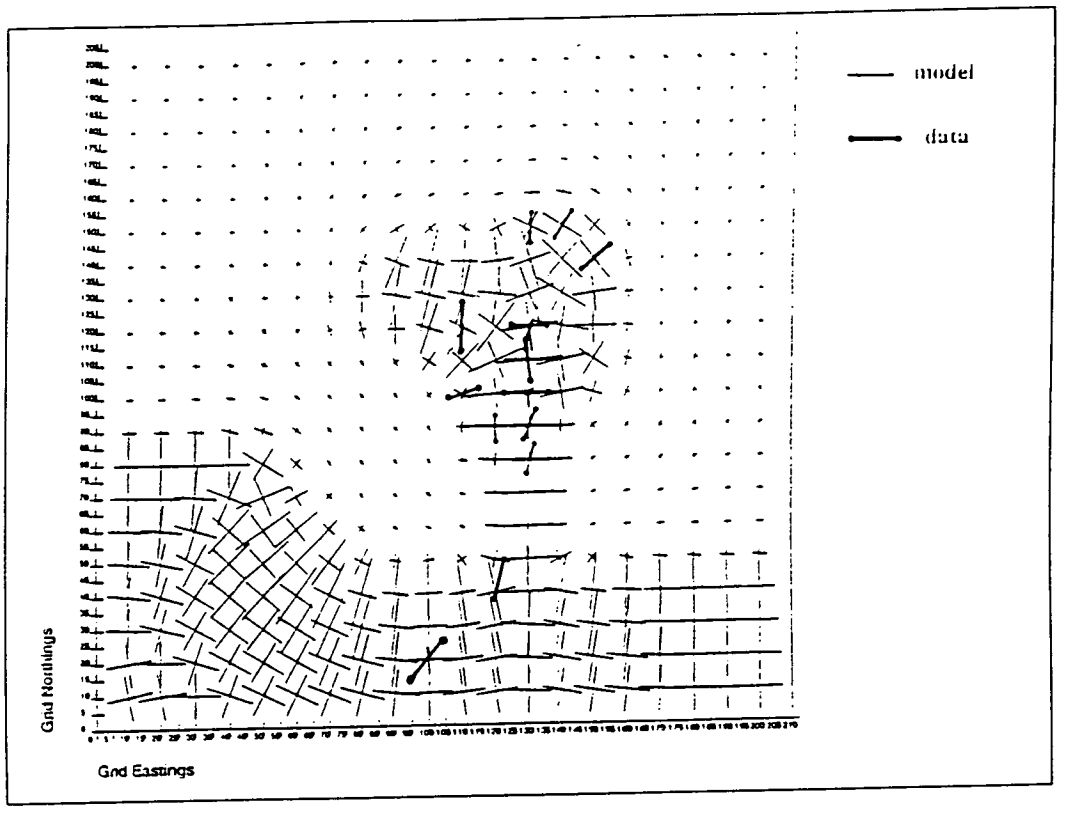

Fig 5.9A: Impedance tensor directions for T=1 s.

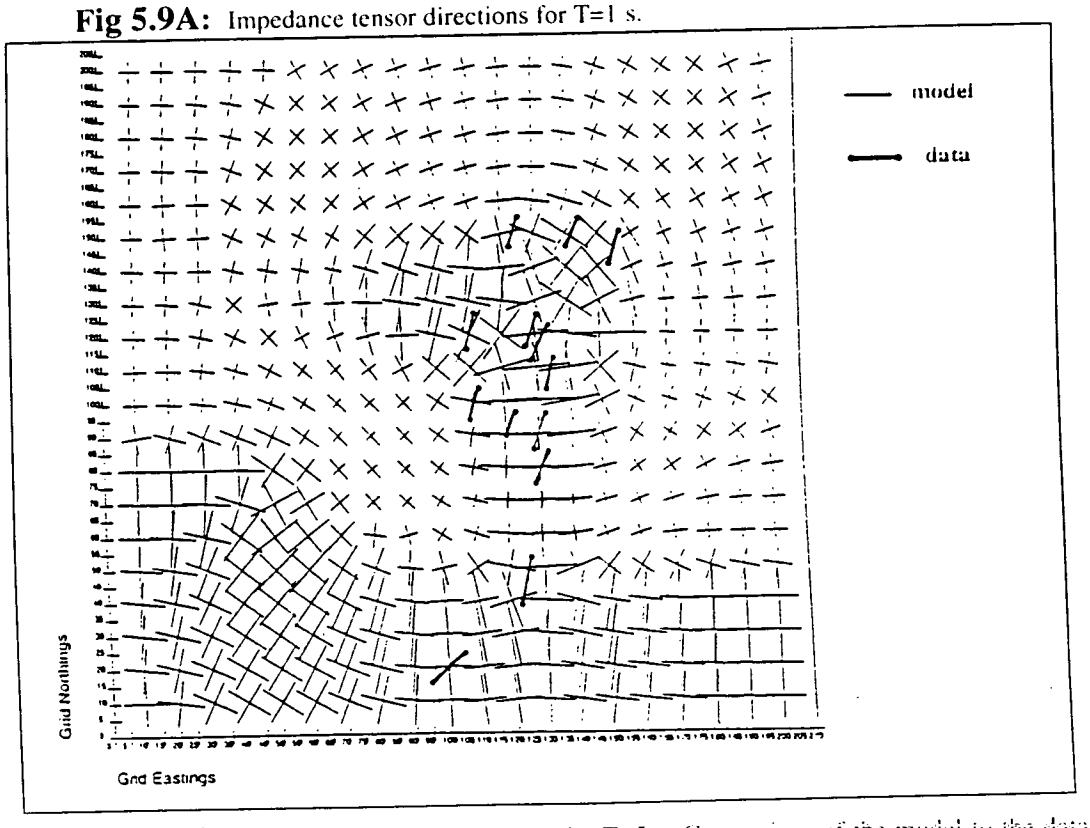

Fig 5.9B: Impedance tensor directions for T=5 s. Comparison of the model to the data. The azimuths as calculated from the measured tensor Swift (1967), are superimposed on those calculated from the thin sheet modelling by using the same method and are shown in bold.

5.5.3.3 Systems of current arrows

Regional currents which are induced by the primary magnetic field, flow in a direction perpendicular to the inducing field, and they are concentrated by (or deflected around) local conductive (or resistive) anomalies. The equivalent current arrows are hypothetical solenoidal currents that would produce the observed anomalous magnetic field, if the leakage into the medium under the sheet was small. Regional and equivalent current arrows are expressed as real and imaginary parts of a vector. The regional and equivalent current arrows are presented as calculated for model A.

Calculations were performed at 1 and 5 s, for two directions of the inducing field and the regional arrows are shown in fig.5.10A and 5.10B, respectively, with the electric field directed from E to W (the other direction is not shown). The deflection of regional current flow due to the presence of the peninsula, which is more pronounced at 1 s can be seen clearly. The imaginary arrows can only be seen close to coastlines and especially in the narrow channel between the peninsula and the mainland, to the SW, where they are oblique to the real arrows. The higher the frequency, the smaller the skin depth or adjustment distance, so the size of the peninsula cannot be considered small any more compared to the primary field. These additional out-of-phase currents are due to an inductive effect, where the induction takes place inside the body. In contrast to the galvanic effect, which adds to the primary field, the secondary field due to induction effect is not in phase with the primary one (sections 2.5.3 and 5.1).

The equivalent current arrows for the same two periods and the same direction of the electric field are shown in figs.5.11A and 5.11B. It is clear that they point in the opposite direction in land and inside the peninsula. At T=1 s, the arrows are bigger than those at T=5 s. Most of the real arrows follow the coast, turning around the tip of the peninsula. For both periods, imaginary arrows are much more pronounced close to the coastlines than at the centre or inland and point obliquely in respect to their real part.

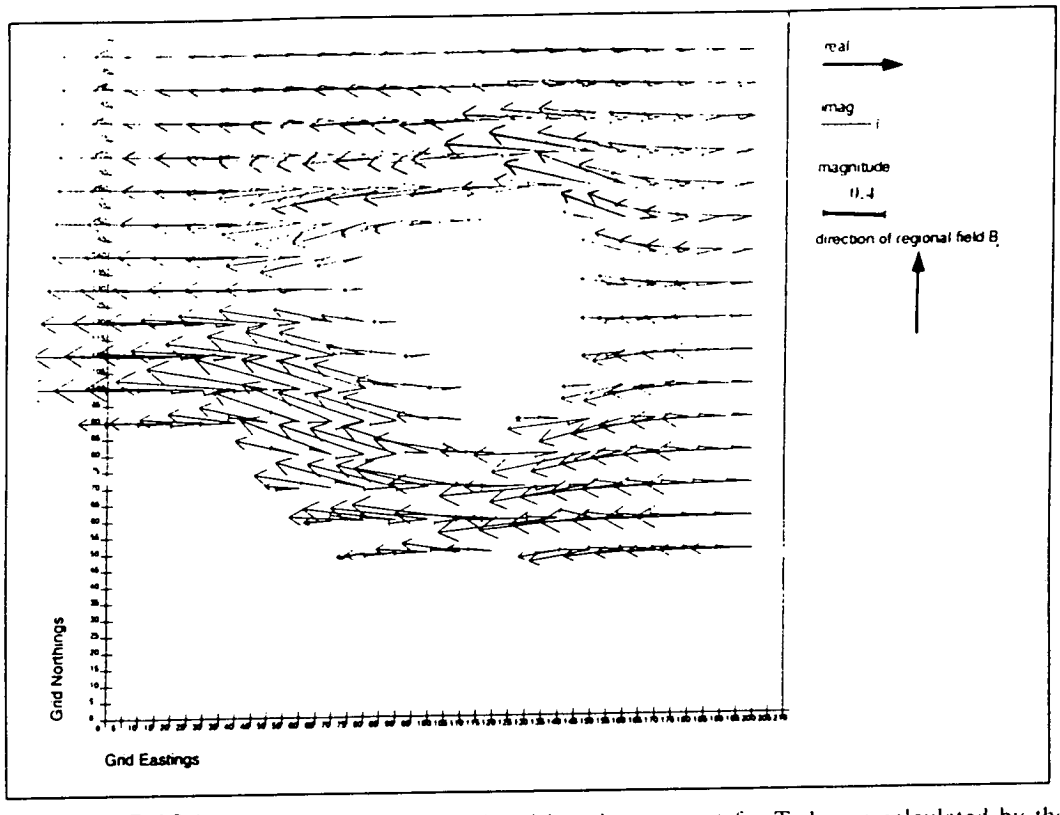

Fig.5.10A: Regional currents (real and imaginary parts) for T=1 s as calculated by the thin sheet modelling program (H-polarisation).

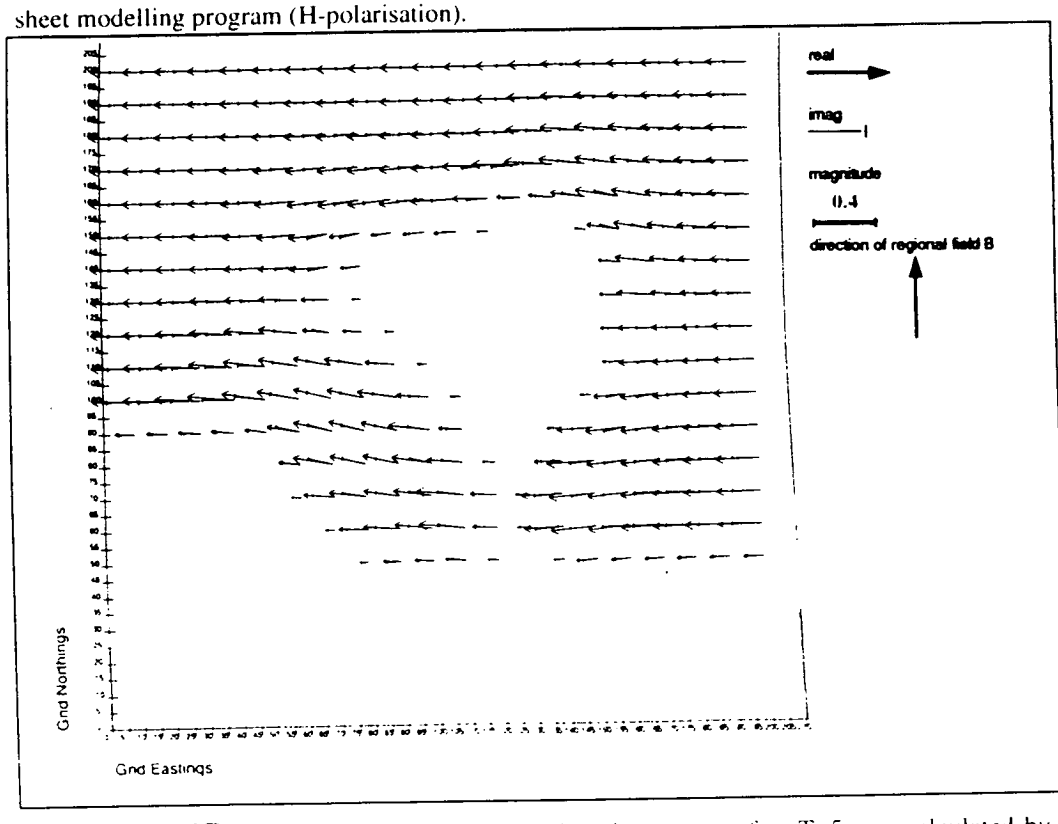

Fig.5.10B: Regional currents (real and imaginary parts) for T=5 s as calculated by the thin sheet modelling program (H-polarisation).

If the surface sheet were electrically insulated from the underlying medium, horizontal channelling of current flow would be the only kind of distortion due to the coastal boundary. However, because of the electrical contact with the underlying medium, vertical leakage of the electric currents into the underlying space take place.

A suitable measure of vertical leakage is provided by the 2-D surface divergence of the surface current density $\mathbf{J}=\sigma\mathbf{E}$ (Weaver, 1982):

$$\mathrm{div}_S\mathbf{J} = \frac{\partial J_x}{\partial x} + \frac{\partial J_y}{\partial y} \qquad (5.26)$$

In the absence of leakage $\mathrm{div}_S\mathbf{J}$ vanishes; in the absence of horizontal channelling $\mathrm{div}_S\mathbf{J}$ equals $\partial J_x/\partial x$ ($\partial J_y/\partial y$) for a regional electric field in the x (y) direction. A value between these two limits indicates both leakage and channelling. If both $\mathrm{Re}(\mathrm{div}_S\mathbf{J})$ and $\mathrm{Re}(\partial J_x/\partial x)$ (or $\partial J_y/\partial y$) are very small then channelling and leakage are negligible.

An example is given for the E-polarisation mode in table 5.4, with the regional electric field in the x-direction. The selected grid points are shown in fig.5.5A.

point	(l,m)	Re (divJ)	Re(∂Jx/∂x)
1	(9,2)	-0.0006	-0.0005
2	(9,6)	1.15	1.14
3	(9,13)	-0.001	-0.001
4	(9,21)	0.002	-0.008
5	(13,14)	0.01	0.84
6	(15,7)	-0.54	0.82

Table 5.4: Dimensionless values of Re (div_SJ) and $\mathrm{Re}(\partial J_x/\partial x)$ at selected grid points identified by the grid coordinates (l,m) at the low right corner. The 6 points are shown in fig.5.5A.

At the points 1 and 4, adjacent to the N and S grid boundaries respectively, both $\mathrm{Re}(\mathrm{div}_S\mathbf{J})$ and $\mathrm{Re}(\partial Jx/\partial x)$ are very small, which is quite expected since near the grid boundaries the induced current flow must be entirely regional. Similarly, neither channelling nor leakage is occurring in the middle of the peninsula (point 3).

In contrast, as the in-phase currents approach the coastlines, there is significant leakage into and out of the underlying medium. Points 5 and 6 show the importance of both channelling and leakage. At point 2 (isthmus), the values of $\mathrm{Re}(\mathrm{div}_S\mathbf{J})$ and $\mathrm{Re}(\partial Jx/\partial x)$ are large and equal, showing that vertical flow is of particular importance.

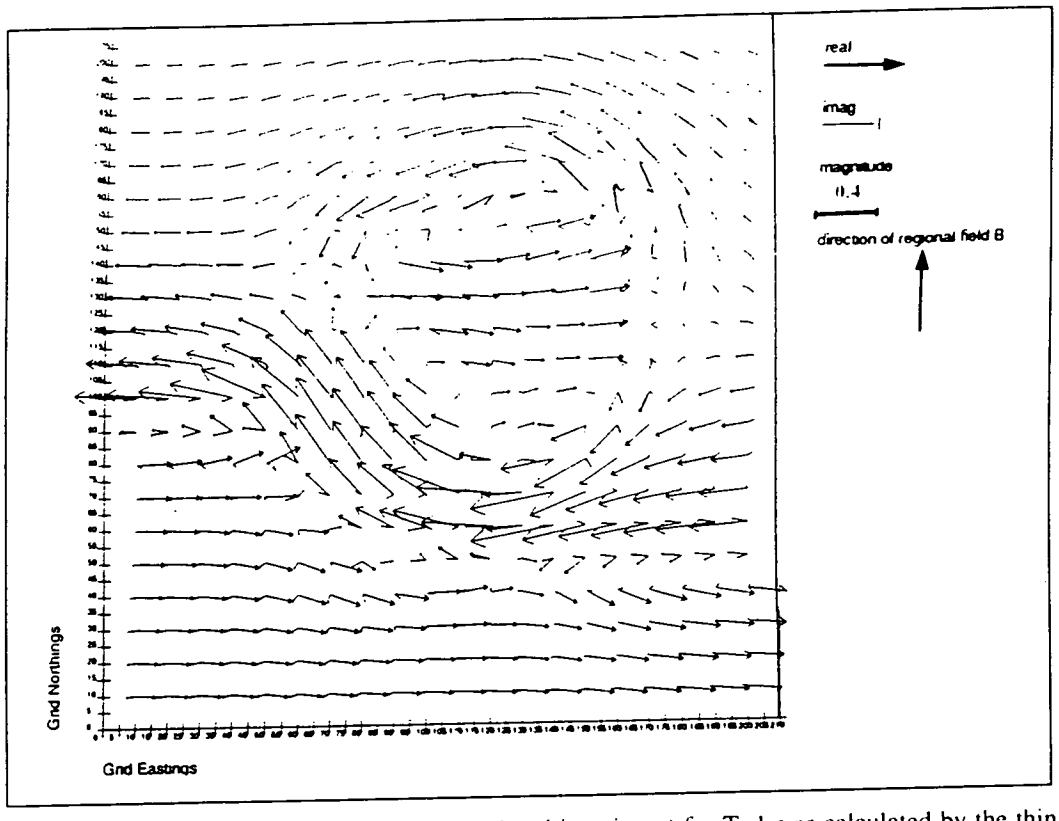

Fig.5.11A: Equivalent currents (real and imaginary) for T=1 s as calculated by the thin sheet modelling program (H-polarisation).

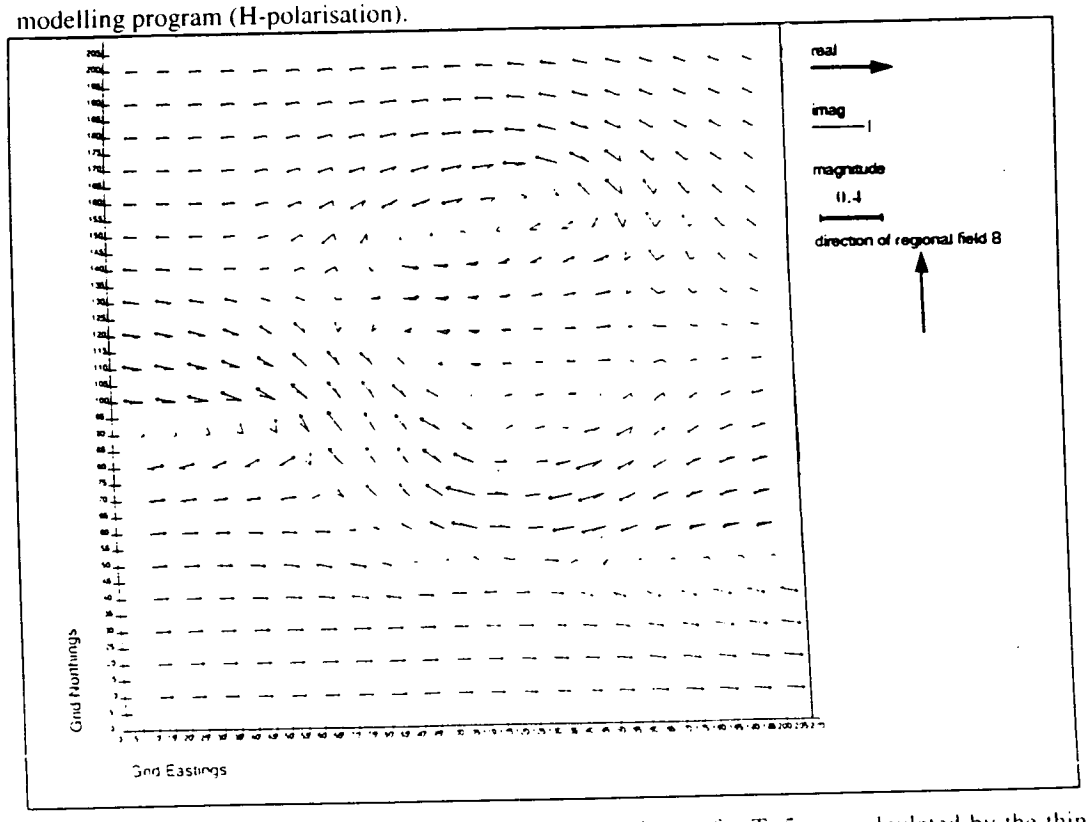

Fig.5.11B: Equivalent currents (real and imaginary) for T=5 s as calculated by the thin sheet modelling program (H-polarisation).

5.5.4 Summary

The thin sheet analysis generated induction arrows, impedance tensor directions and current arrows. From these parameters 3 main points can be deduced:

a. Theoretical induction arrows were calculated for periods in the range 1-13 s. And although it was not legitimately possible to model the sea effect for T<1 s, an attempt to do that showed that the theoretical real arrows point perpendicular to the sea, as it is actually expected. Comparison with the measured data showed that there is good agreement of the real arrows with those calculated from the thin sheet modelling at T>1 s, especially at sites close to the coast while the deep sea on the NE coast may have an effect at all sites at T=13 s. In spite of that, at the peninsula centre and inland sites the behaviour of the induction arrows cannot be attributed entirely to the coast effect, because the measured values do not fit the model so well, suggesting that there is complex structure in the geology beneath Methana which affects the field measurements. The latter can be possibly deduced at periods around 0.1 s (fig.4.7A and B).

b. Swift's azimuths calculated by the thin sheet modelling program suggested mainly N-S and E-W directions, with the maximum anisotropy at the isthmus, as it is affected by the sea from two sides. In fact, the E-W direction correlates with a number of sites at T=1 s, which shows that probably a strike of such a direction could reflect not only the surface geology (fig.3.3) but also the sea effect.

c. The analysis of current flow has demonstrated the horizontal as well as the vertical deflections of the induced currents, wherever there is discontinuity in conductivity due to the sea-land contrast. This behaviour of the current arrows is observed more at high frequencies, mostly in the isthmus and the small sea channel between the SW land and the SW end of the peninsula.

5.6 Conclusions

Data analysis presented in chapter 4 has shown clearly the need for analysis of distortion effects on the data. This problem has led to two different approaches for the distortion of the regional electric field: One caused by surficial local "patches" of conductivity significantly different from that of the surrounding rocks (approached by decomposition methods), and the other due to a particular conductor, the presence of sea water around the area of investigation (thin sheet analysis).

By examining the behaviour of the induction arrows through the whole period range, it was found that the measured real arrows at T>1 s lie perpendicular to the coast, as was actually expected by the modelling of the sea effect.

In sections 5.4.1-3 the regional azimuths as calculated by Groom-Bailey and Bahr's methods were presented and two possible strike directions were proposed: 90^0-130^0E up for periods up to 1 s and 0^0-40^0E for the longest AMT period range (>10 s).

First the 90^0E angle is considered. That E-W is a possible strike is fairly obvious from the geological map (fig.3.3), as the boundary between the volcanics and the carbonate basement lies in this direction. But this angle is suggested only for short periods (T<1 s). Moreover, the volcanics are relatively recent rocks whose vertical extent is not known, so it may be that the E-W unconformity is reletively surficial and that the volcanics, which are an isolated phenomenon compared with the regional area, do not extend very deeply.

A regional strike of 0^0-40^0E is suggested for the longer AMT periods (T>10 s). On the other hand, the induction arrows calculated for that range were found to be influenced by the deep NE sea, although they might also be associated with a known NW-SE tectonic trench. As the depth increases, the induction arrows rotate towards the SE and directions of 90^0-130^0E satisfy the condition for a 2-D strike of 0^0-40^0E. As was mentioned in the previous chapter, and can also be seen from fig.3.3, many faults lie in that direction as well as a deeper fault starting from the very S which probably extends up to the NE part of Methana. This fault has a direction of 30^0E. The relation of the induction arrows to the other known NW-SE deep structure will be discussed in the last chapter.

At longer periods, distortion parameters show increasing values, which is probably caused by 3-D effects at depth, but also by the poorer data quality. At the 4 longest LMT periods (T>2000 s), data quality is generally better, but the induction arrows are no longer perpendicular in respect to a 30^0E strike, which is indicative of the presence of 3-D effects at great depths.

Despite the indications for 3-dimensionality at depth, there is support for a 2-D structure at least up to a certain depth, and it was decided to use a strike direction of 30^0E in the subsequent 2-D modelling.

Chapter 6

Inversion and modelling

6.1 Introduction

In the previous chapter, models were presented in which the conductivity distribution of the Earth were assumed to be known. For example, G-B decomposition was done under the assumption that 3-D local bodies are superimposed on a larger scale 2-D structure. In the thin sheet modelling, calculations of the magnetic and electric fields on the surface were performed by using specific values representing the conductivities of sea, land and underlying medium. In that type of modelling (forward modelling), one starts from a given conductivity distribution and derives a set of response functions which are then compared with the data. Attempts generally can be made to adjust the model and find the best fit to the data.

Forward modelling is one way of deriving a model compatible with the observed data. The other way which is discussed in this chapter, is by inversion of the measured data. The problem consists of going from a set of response functions (the measured data) to a resolved conductivity structure $\sigma(z)$, $\sigma(y,z)$ or $\sigma(x,y,z)$, for a 1-D, 2-D, or 3-D Earth respectively. An initial conductivity distribution σ_0 must be assumed, so in that sense the inverse problem includes one or many forward modelling problems.

Most modelling techniques usually take a starting model, calculate its response function, compare it with the observed response function and its associated errors, and then iteratively adjust the model's parameter values to reduce the misfit between the model response and the data. A model, in order to be valid, must reproduce the observed response to a degree of accuracy allowed by the response's statistical errors. A qualitative assessment of the misfit can be made by visual inspection, although quantitative statistics such as χ^2 or the rms misfit (eqs. 6.14 and 6.15 respectively), are more frequently used.

A major problem in the inversion process is that several radically different conductivity structures can have responses which are very similar. This is partly due to the presence of limitations including observational errors, restrictions of frequency

and spatial sampling. So it is possible that a large variety of models can fit the data. In that case, additional information from other geophysical or geological methods can restrict the number of acceptable models.

The best understood inversion procedures construct models in which the conductivity varies in one or two directions (1-D and 2-D models respectively). For the construction of solutions to the 1-D problem, two main classes of models exist: (i) parametric or discontinuous and (ii) continuous. The first category includes models containing a small number of layers and many data points (Larsen, 1975; Jupp and Vozoff, 1975; Fischer and Le Quang, 1981; Menke, 1984). In the second, the resistivity is treated as a continuous function of depth with small gradients, which is equivalent to using a large number of layers (Weidelt, 1972; Oldenburg, 1979; Parker, 1983). There also exist methods which give approximate models from smoothly varying estimates of the apparent resistivity, for example the Niblett-Bostick and the Schmucker (Schmucker, 1970) transformations. (A Niblett-Bostick transformation on the data is presented in section 6.4 as a preliminary 1-D modelling technique).

Based on the same principles, inversion to 2-D models has also been developed for both the continuous and discontinuous cases. In this work, the smooth inverse of Smith and Booker (1991) is used for a 2-D inversion of the MT data in Methana, leading finally to the construction of a 2-D model.

6.2 Theory

In this section, the most essential background underlying 1-D and 2-D inversion procedures is given, based mainly on the work of Oldenburg (1979), and Smith and Booker (1988, 1991), respectively. The former forms the basis for the 2-D inversion of the latter.

6.2.1 Inversion for a 1-D Earth

When the conductivity of the Earth is supposed to change only with depth, equation (2.11) becomes:

$$\frac{d^2E(z,\omega)}{dz^2} = -i\omega\mu\sigma E(z,\omega) \qquad (6.1)$$

and (2.6) in the frequency domain:

$$\frac{dE(z,\omega)}{dz} = -i\omega B(z,\omega) \qquad (6.2)$$

By definition one has:

$$R(z,\omega) = \frac{B(z,\omega)}{E(z,\omega)} \tag{6.3}$$

To construct a model $\sigma(z)$, the changes in the response for small changes in conductivity must be known. Assuming an initial conductivity distribution σ_0 and response function R_0, the perturbations $\sigma_1 = \sigma_0 + \delta\sigma$ and $R_1 = R_0 + \delta R$ can be introduced. Oldenburg (1979) used (6.1), (6.2) and (6.3) to yield the equation:

$$\delta R(0,\omega) = \int_0^\infty -\mu \left(\frac{E(z,\omega)}{E(0,\omega)}\right)^2 \delta\sigma(z)dz \tag{6.4}$$

The limits of integration at the surface and great depth are $E(0)=E_0$ and $E(\infty)=0$, respectively, where E_0 is the electric field at the surface. R is supposed to be known, so that (6.4) can be inverted for $\sigma(z)$.

6.2.2 Inversion for a 2-D Earth

In the 2-D case the EM induction equations split into two modes: TE and TM. Suppose that the electric field is parallel to the strike of the structure (x-direction), eqs.2.6 and 2.11 become:

$$\frac{\partial E_x}{\partial z} = i\omega\mu H_y \tag{6.5}$$

and $$\nabla^2 E_x = -i\omega\mu\sigma(y,z)E_x \tag{6.6}$$

Eq.6.6 can be conventionally rewritten:

$$\frac{1}{E_x}\frac{\partial^2 E_x}{\partial z^2} + \left\{\frac{1}{E_x}\frac{\partial^2 E_x}{\partial y^2}\right\} + i\omega\mu\sigma = 0 \tag{6.7}$$

It is worth noticing that now the lateral gradients of the fields are confined to the terms in braces. Without this part, eq.6.7 would be the same as the equation for induction in a 1-D model, i.e. eq.6.2.

By defining $$V = \frac{1}{E}\frac{\partial E}{\partial z} = i\omega\mu\frac{H_y}{E_x} \tag{6.8}$$

and using eqs.6.7 and 6.8, Smith and Booker (1991) solve a similar perturbation problem as for the 1-D induction (previous section) with R replaced by V, leading finally to the equation:

$$\delta V(y,\omega) = \frac{i\omega\mu}{E_0^2(y,0)}\int_0^\infty E_0^2(y,z)\delta\sigma(z)dz \tag{6.9}$$

Notice that V is closely related to the impedance $Z_{xy}=E_x/H_y$.

The above expression is complex and represents two equations at each frequency at each site. The left hand side of eq.6.9 is the residual between the measured data at each frequency and that predicted by the initial conductivity σ_0.

For the TM mode a similar expression can be derived:

$$\delta U(y,\omega) = \frac{1}{H_0^2(y,0)} \int_0^\infty E_0^2(y,z)\delta\sigma(z)dz \qquad (6.10)$$

where U is defined as $U = \frac{1}{\sigma H}\frac{\partial H}{\partial z} = \frac{E_y}{H_x} = Z_{yx}$ (6.11)

6.3 Efficiency of the inversion scheme of Smith and Booker

Usually, 2-D inversions are based on the following steps: First, the Earth is parametrized by means of a grid of prisms or nodes, each having a uniform conductivity. A starting model is guessed, and then a matrix F of partial derivatives of the data with respect to $\delta\sigma$ is calculated. This involves solutions of multiple forward models. The computer space and time that is needed to generate and store F and perform all the calculations, increases rapidly with the increasing number of data.

The inversion scheme of of Smith and Booker (1991) is based on concatenated 1D inversions incorporating 2D effects in the 1-D Frechet derivatives (eq.6.7), which is extremely CPU efficient.

In order to carry out a model construction, for example TE mode, an initial guess is made for $\sigma_0(y,z)$ and eq.6.6 is solved for $E_0(y,z)$. These fields are substituted in eq.6.9 and the equation is solved. A new value for $\sigma_0(y_i,z)$ is estimated (usually using a percentage of $\delta\sigma$), and interpolated between sites to produce a new $\sigma(y,z)$. Eq.6.6 is solved again for new estimates of E(y,z). The cycle is repeated until the data residuals become sufficiently small. The lateral gradients of the electric and magnetic field in the model are approximated by their value from the previous iteration.

A similar procedure can be applied to the TM mode. Eqs.6.9 and 6.10 can be inverted separetely or be combined together for a simultaneous inversion of the two modes.

The philosophy behind this type of inversion is the same as that of Occam's inversion (Constable et al., 1987), i.e. to seek a model with minimum structure, as *it is vain to do with more what can be done with less* (Occam's razor). Therefore, among models which equally fit the data, those with superfluous structure (not required by the data) are simply avoided. It is noticeable that the Occam2 inversion (deGroot-Hedlin and Constable, 1990) and the present inversion scheme have been

applied to the same data set, giving almost the same results (Livelybrooks et al., 1993).

A convenient way to minimise structure is to minimise a norm of the first derivative of the resistivity ρ:

$$F(\rho, f) = \int_0^{\infty} \left[\frac{d\rho}{df(z)} \right]^2 df(z) \qquad (6.12)$$

where f(z) = z or log(z).

The Smith and Booker's inversion iteratively solves for the conductivity model that fits the data (with the misfit between the model and the data normalized by the data errors) to within a prescribed chi-squared and minimises F:

$$\chi^2 = \sum_{i=1}^{2N} \left[\frac{\Delta\gamma_i}{\varepsilon_i} \right]^2 \qquad (6.13)$$

where $\Delta\gamma_i$ are the data residuals and ε_i the data standard errors. It is important here that the desired structure is one which minimises eq.6.12 and at the same time achieves the prescribed chi-squared misfit to the observations. The model is over-parameterised, and without the imposition of the smoothness constraint, the problem of finding the best-fitting solution would be ill-posed. Therefore the choice of the maximum acceptable misfit and the corresponding smoothness parameter, are crucial in determining the appearance of the resultant inversion. The best fitting model is usually very rough, and by relaxing the fit a smoother model can be formed.

The algorithm keeps the change to the model small enough at each iteration so that the whole process can be considered as linear. The rate of convergence can be monitored by the root-mean-square (rms) relative error:

$$rms = \sqrt{\frac{1}{N} \sum_{j=1}^{N} (\delta R_j / R_j^0)^2} \qquad (6.14)$$

where N is the number of observations, Rj is the calculated response function, R_j^0 is the observed datum, and $\delta R_j = R_j^0 - R_j$ for the j^{th} frequency.

The fit of the model to the data can be improved by applying robust constraints (section 4.3.2), especially when there are outliers in the data. At that stage, one must have a model which fits the data reasonably, otherwise important features of the structure can be ignored if they affect only a small percentage of the sites.

6.4 1-D Preliminary modelling

1-D modelling is the simplest and most widely used technique which transforms the response function at one site to a model in which the resistivity varies only with depth. It can be applied to simple structures with no lateral variations, but it can be useful also as a way of creating a starting model for higher dimensional modelling.

Although the analysis in the previous chapters showed the need for a multi-dimensional treatment of the data, preliminary 1-D modelling was undertaken, as the first way of assessing the information in the data. Two techniques were used, the Niblett-Bostick transformation and the inversion scheme of Fischer.

a. The Niblett-Bostick transformation takes the values of apparent resistivity (ρ_a) at each period and calculates a penetration depth (h) at period (T) using the following formula (Bostick, 1977; Jones, 1983b):

$$h = \sqrt{\frac{\rho_a(T)T}{2\pi\mu_0}} \qquad (6.15)$$

b. The inversion scheme of Fischer et al. (1981), attempts to explain the data in terms of a small number of discrete layers, each with a distinct uniform conductivity. The method is based on the fact that for a given period T, the observed response is predominantly influenced only by structures above the maximum penetration depth. The scheme starts with the shortest periods of the data and explains the apparent resistivity ρ_a and phase ϕ in terms of a simple two layer model. As the period increases, discrete new layers (corresponding to longer periods) are introduced (for more details see Fischer et al., 1981).

In fig.6.1 Bostick resistivity-depth profiles (crosses) and Fischer multi-layer models (thick lines) are shown. The sites with the best fits to 1-D models are presented. The invariant apparent resistivity (eq.2.45) was used in order to create apparent resistivity and phase models. From fig.6.1 the following comments can be made:

1. The Bostick technique indicates relatively high resistivities near to the surface, especially at site 130 (>500 Ohm m)

2. Sites 130 and 131 show very low resistivity values (1-5 Ohm m) at a depth up to 0.3-0.8 km, while still low values (<10 Ohm m) are observed up to 6 km (especially at site 130).

3. There is a tendency for higher resistivities to predominate with increasing depth.

As most of the data at T>0.5 s showed higher dimensional characteristics (section 5.4), the need for 2-D modelling was considered to be of crucial importance.

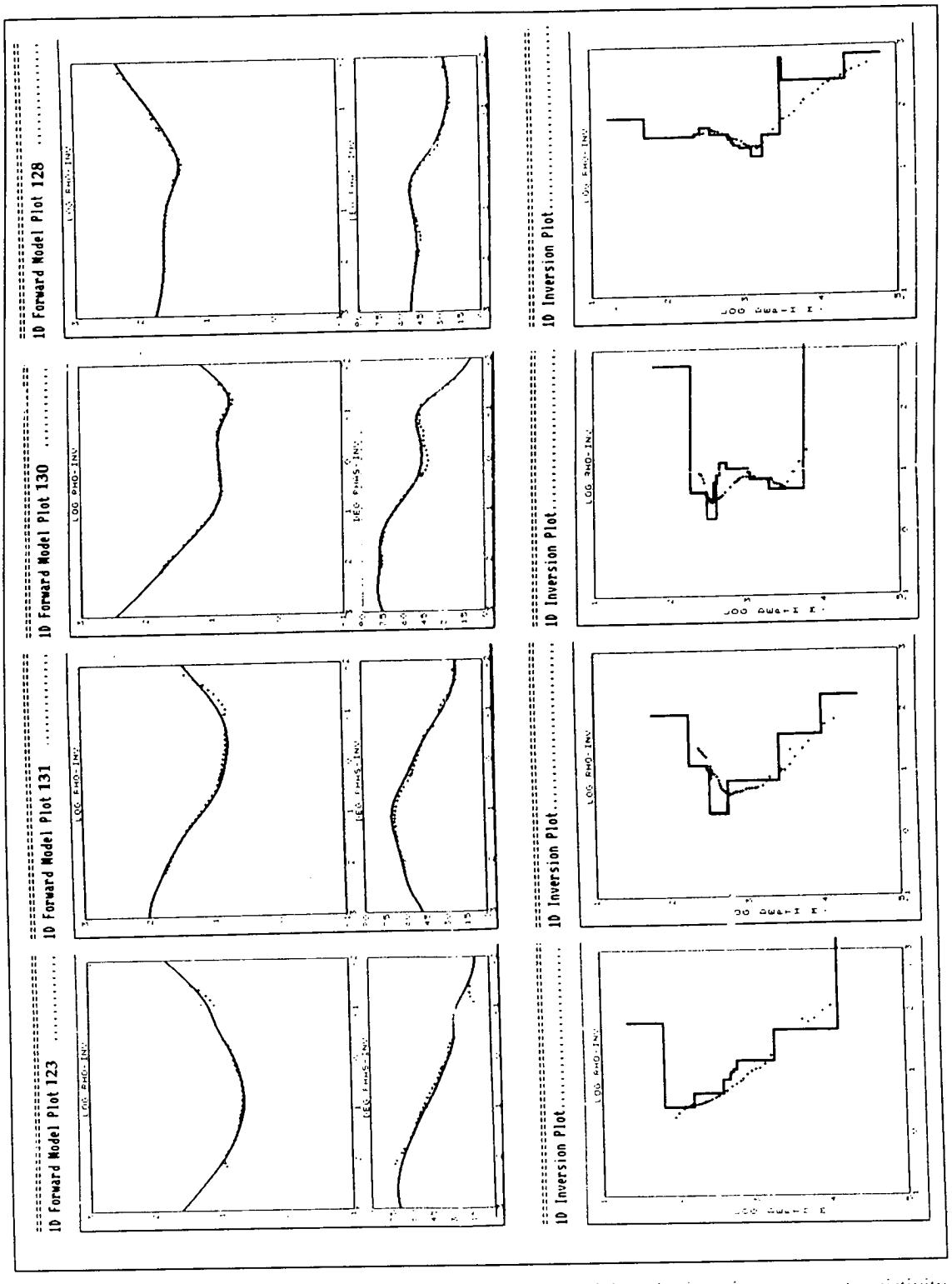

Fig. 6.1: 1-D preliminary modelling and fit of the model to the invariant apparent resistivity data. Results are shown for the 4 best fitting sites, 123, 131, 130 and 128. **Bostick depth:** crosses. **Fischer's inversion:** thick lines.

6.5 2-D inversion and modelling

6.5.1 The inverting sites

The apparent resistivities and phases (XY and YX) as they were extracted after the G-B decomposition, were compared with the unrotated curves before the decomposition. It was found that the curves were almost identical (although this was not the case for Swift's rotation method). At most of the sites also the curves before decomposition were less affected by noise than those after decomposition which shows the instability of the decomposition in the presence of noise. The static shift problem, which was present in almost all the apparent resistivity curves, could not be eliminated, and appeared on both unrotated and decomposed resistivity data. It was then decided to use the unrotated resistivity and phases for the inversion, after rotating them to the strike angle suggested by the decomposition techniques.

A second decision had to be made which concerned the sites to be inverted. The selection of sites for inversion was based on the following criteria:

1. Well defined response curves with the smallest possible error bars must be included.

2. Curves with large error bars and scattered data points over a period range of a decade or more were preferably to be avoided.

3. Data belonging to selected sites must show the smaller possible galvanic distortion (as measured by the twist and shear angles).

5. The site spacing must not be very small (less than a few hundred meters)

6. Sites should not be very close to the sea.

Although most of the recorded bands 0 and 1 show very well defined responses, too much of bands 2 and 3 poor quality data with large error bars were recorded. Sites 124, 132, and 121 were excluded from the inversion. Sites 122 and 126, which show strong influence by the sea, were also excluded. Site 120 shows large galvanic distortion (section 5.3.3) and although it was located on the main profile, was not included. Among base and remote sites, the ones with the smaller distortion parameters and the less shifted XY and YX components were chosen. The sites around the centre 130, 131 and 133 were included, although no control was provided for them in terms of a "remote site".

In fig.6.2 the profile of selected sites is shown.

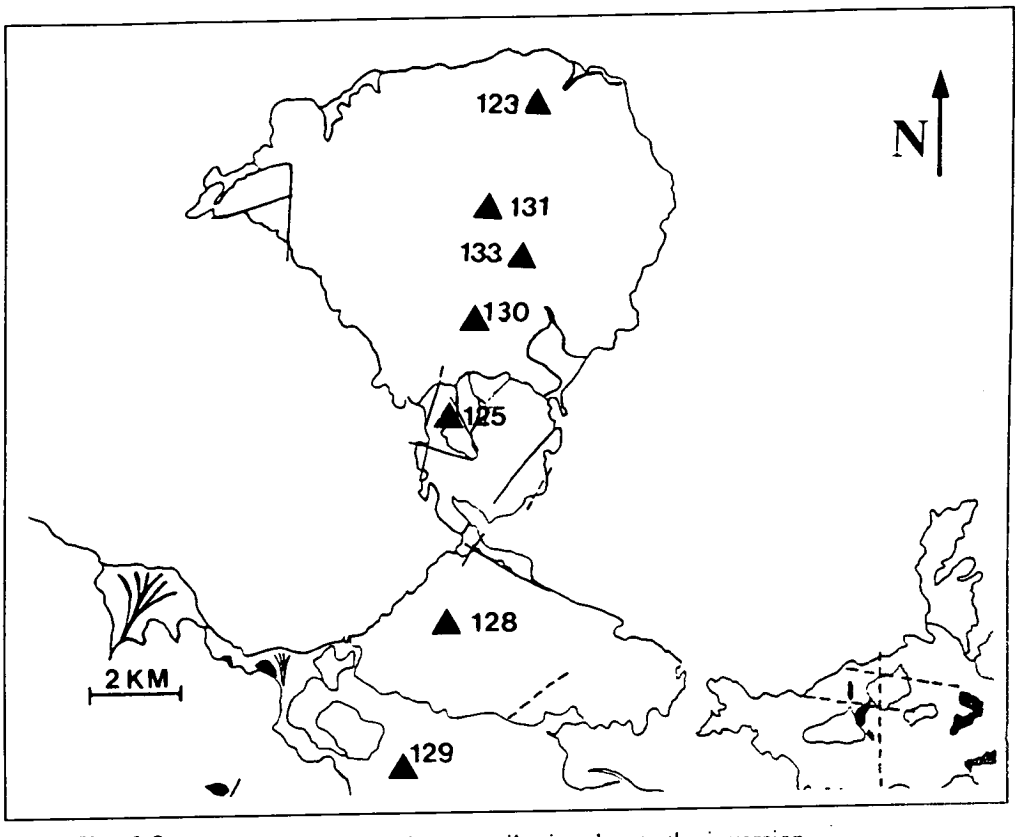

Fig.6.2: The profile and the sites contributing data to the inversion.

6.5.2 TE and TM pseudosections

In section 4.5.2, the unrotated data were presented in the form of pseudosections. However, in order to obtain an initial picture of the amount of structural detail expected in the subsequent model, the TE and TM apparent resistivities and phases for the 7 inverted sites are required (figs.6.3A-D).

As one would expect, a rotation of 30^0E does not result in crucial changes from the unrotated to the rotated data, though due to the absence of some sites the present pseudosections show small differences compared with the unrotated ones. For example, there is no vertical boundary between sites 130 and 125, which is actually due to the absence of site 120.

Up to 1 s, both TE and TM resistivity pseudosections reveal a central resistive area (sites 131 up to 130) on the top of a more conductive structure, whereas the area outside the peninsula shows also relatively high resistivities. Below 1 s, the anisotropy between the two modes is obvious as in the unrotated data (figs.6.3A and B).

Although the rotation of 30^0E did not change significantly the AMT data, this is not the case for the LMT data. The TM mode resistivity plot (fig.6.3C) appears much more resistive for both sites (123 and 125), than the YX (fig.4.4C).

The "gap" in TE phase data (which is discussed in the next section), is clearly reflected at the period range 20-200 s between sites 123 and 125, where phase values drop very rapidly from 90^0 to 0^0, a fact which (as in the unrotated case) must reflect severely noise corrupted data at that particular range. The TM mode pseudosection reveals vertical as well as horizontal transitions in the phases, but the transition towards the LMT data is much smoother than that of the TE mode.

Figs.6.3A-D (next 4 pages): Pseudosections for the TE and TM rotated apparent resistivities and phases. **Horizontal axis**: Distance between sites in km. **Vertical axis**: Pseudo-depth as a function of log (frequency). The color-scale represents gradations in the logarithm of resistivity **(6.3A, C)**, and in degrees for the phase **(6.3B, D)**. Below 5 s features should be considered as representing noise, rather than real structure.

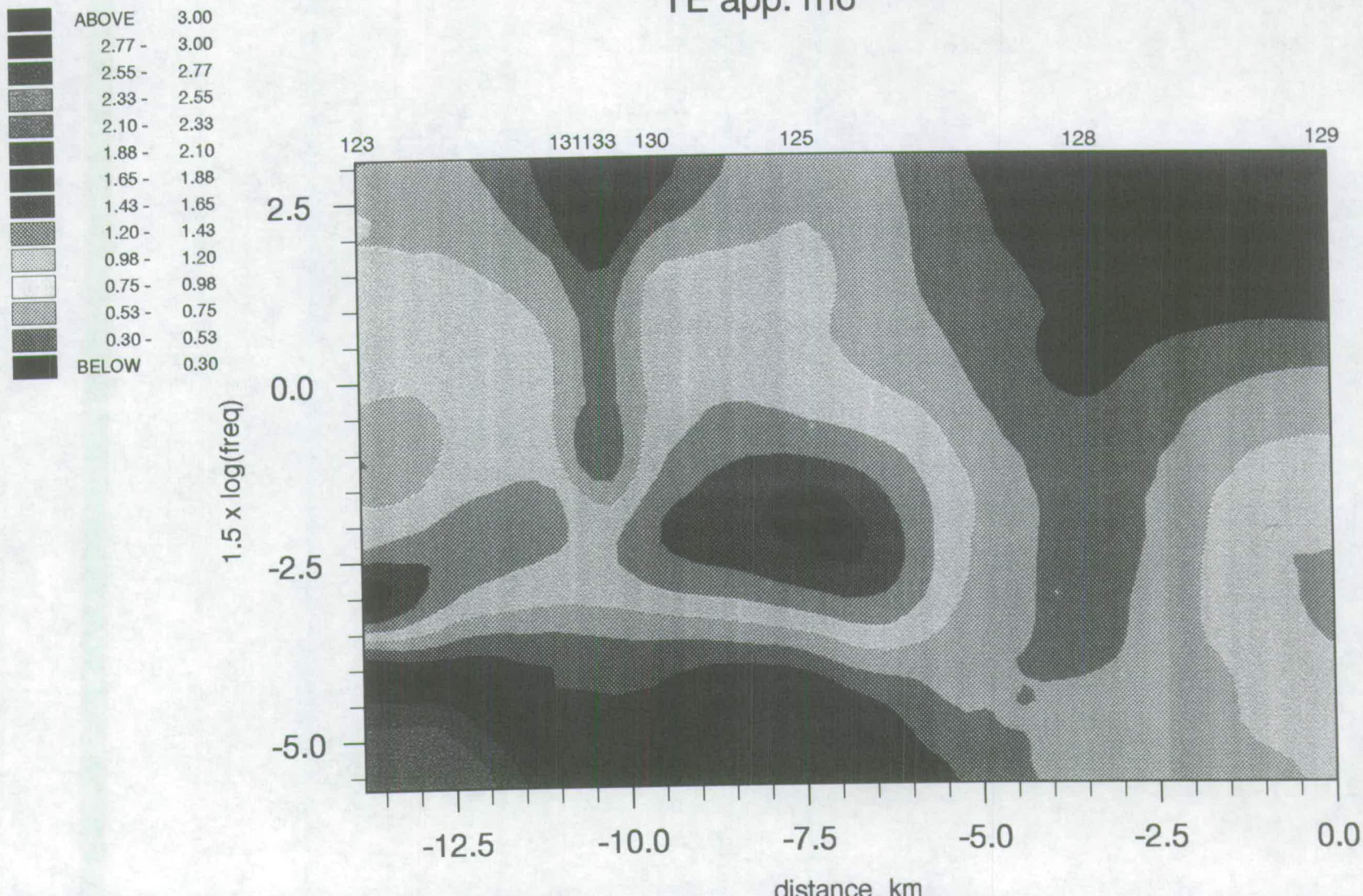
TE app. rho
ABOVE 3.00
2.77 - 3.00
2.55 - 2.77
2.33 - 2.55
2.10 - 2.33
1.88 - 2.10
1.65 - 1.88
1.43 - 1.65
1.20 - 1.43
0.98 - 1.20
0.75 - 0.98
0.53 - 0.75
0.30 - 0.53
BELOW 0.30
123
131133
130
125
128
129
2.5
0.0
-2.5
-5.0
1.5 x log(freq)
-12.5
-10.0
-7.5
-5.0
-2.5
0.0
distance, km

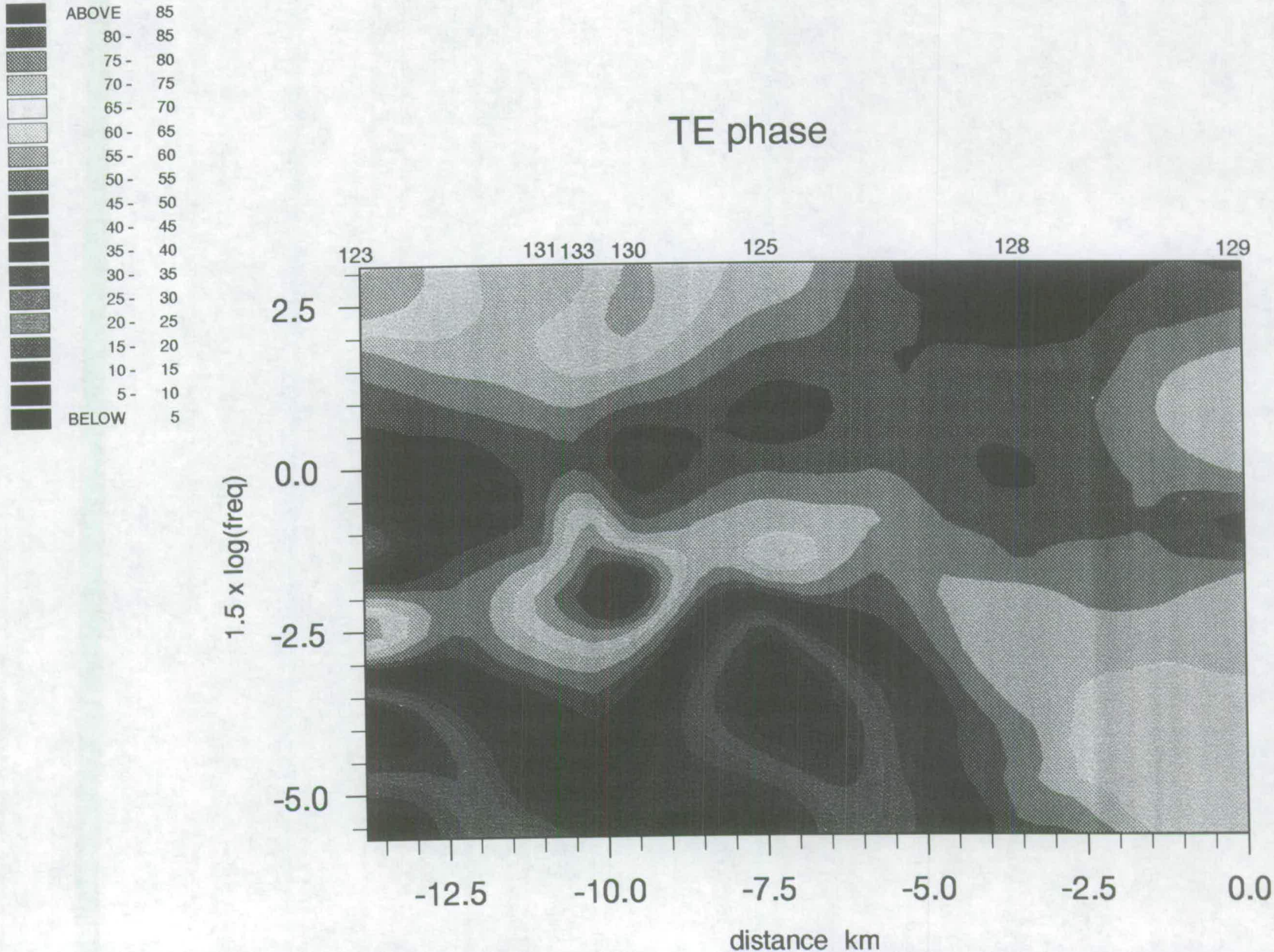
ABOVE 85
80 - 85
75 - 80
70 - 75
65 - 70
60 - 65
55 - 60
50 - 55
45 - 50
40 - 45
35 - 40
30 - 35
25 - 30
20 - 25
15 - 20
10 - 15
5 - 10
BELOW 5
TE phase
123
131
133
130
125
128
129
2.5
0.0
-2.5
-5.0
1.5 x log(freq)
-12.5
-10.0
-7.5
-5.0
-2.5
0.0
distance km

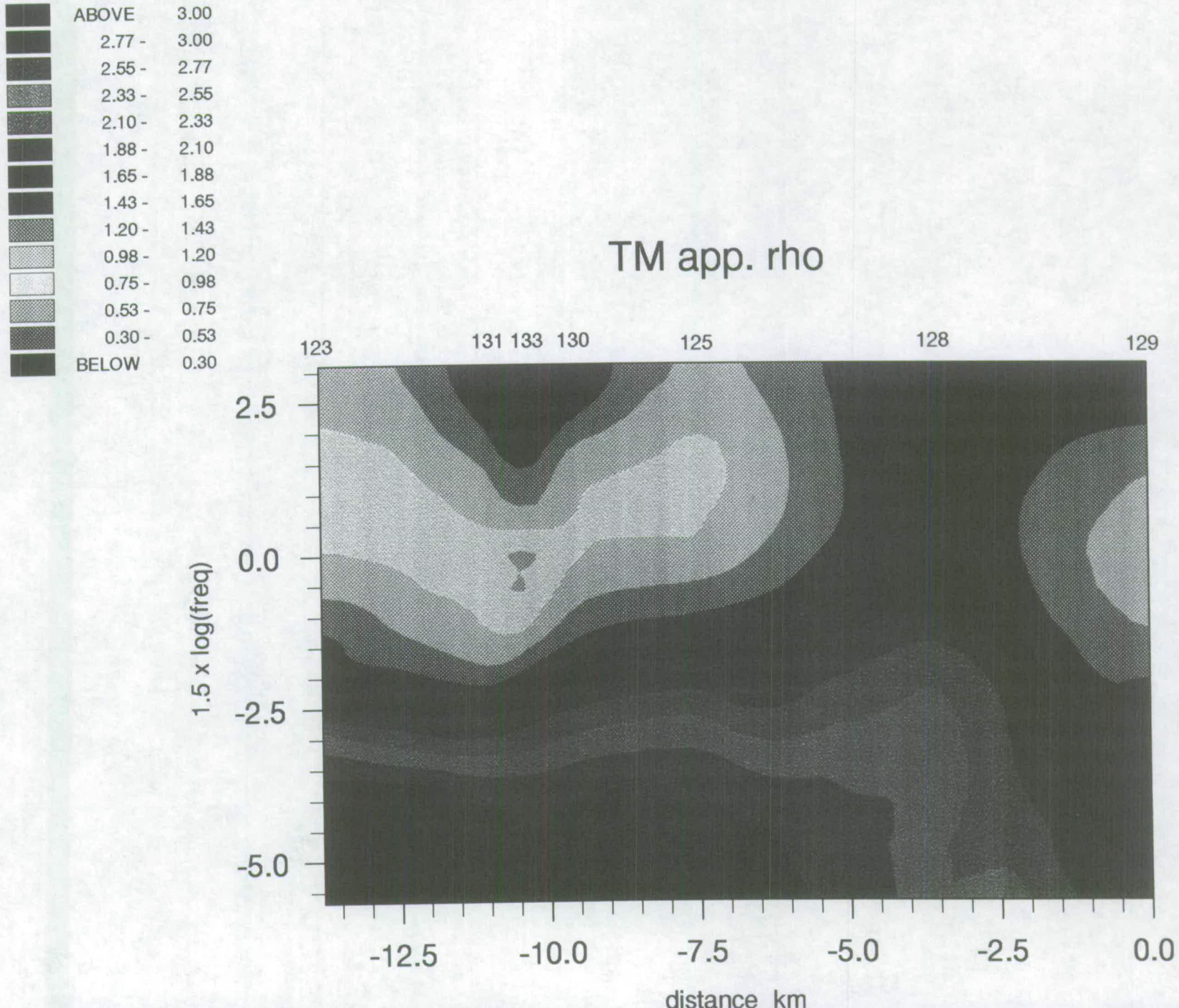
ABOVE 3.00
2.77 - 3.00
2.55 - 2.77
2.33 - 2.55
2.10 - 2.33
1.88 - 2.10
1.65 - 1.88
1.43 - 1.65
1.20 - 1.43
0.98 - 1.20
0.75 - 0.98
0.53 - 0.75
0.30 - 0.53
BELOW 0.30
TM app. rho
123
131 133 130
125
128
129
2.5
0.0
-2.5
-5.0
1.5 x log(freq)
-12.5
-10.0
-7.5
-5.0
-2.5
0.0
distance km

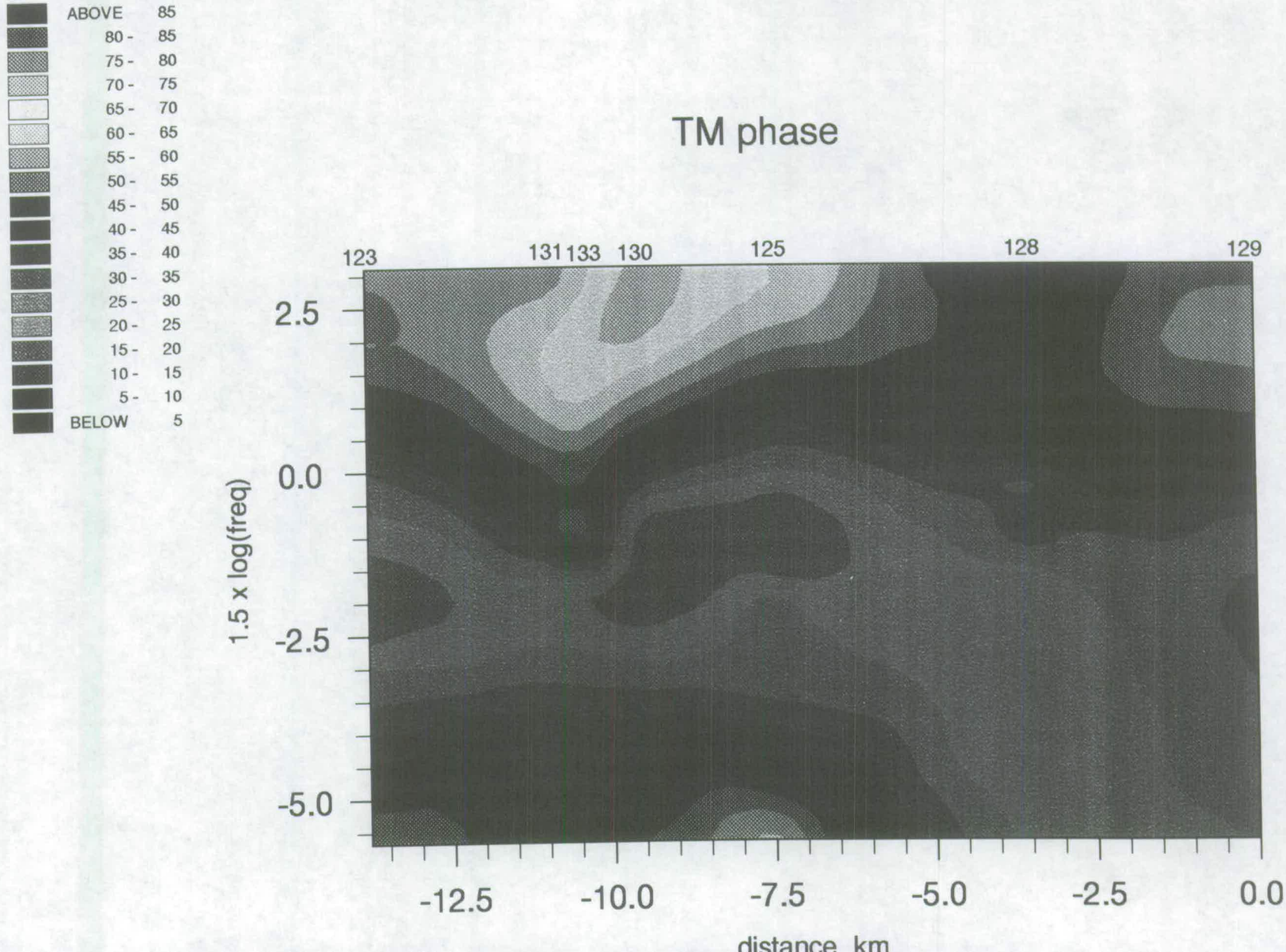
ABOVE 85
80 - 85
75 - 80
70 - 75
65 - 70
60 - 65
55 - 60
50 - 55
45 - 50
40 - 45
35 - 40
30 - 35
25 - 30
20 - 25
15 - 20
10 - 15
5 - 10
BELOW 5
TM phase
123
131
133
130
125
128
129
2.5
0.0
-2.5
-5.0
1.5 x log(freq)
-12.5
-10.0
-7.5
-5.0
-2.5
0.0
distance, km

6.5.3 Strategy for a 2-D inversion procedure to be applied

As mentioned earlier, phase values are less sensitive to galvanic distortions than apparent resistivities, so it is much wiser to attempt an inversion first on the phases. Besides, it has already be seen that most of the apparent resistivity curves are shifted relative to sites with a separation distance of a few hundred meters.

2-D inversion requires knowledge of the strike direction. From the discussion in the previous chapter it was decided to use a regional strike of 30^0E. As a final test, different rotations between 0^0-90^0E were applied to the data and then the phases were inverted. It was found that only for angles between 20^0-40^0E could the model "see" the split in the phases between 0.5-23 s, as well as "fill" partly the gap between the AMT and LMT data (figs.4.5 and 6.3). For the other angles the model fits the data only in the first 4 periods (0.01-0.1 s), while for T>0.1 s these rotation angles proved to be inappropriate.

Generally speaking, the TE and TM modes contain different kinds of information about the conductivity structure. In fact, the response curves for the two modes differ considerably at T>1 s, and as a result they lead to completely different models when inverted separetely. In order to avoid giving more weight to one or the other of the two modes, a step-wise procedure was followed, in which the output of a previous step was used as the input for the next step. The TM phases were inverted first, as they are smoother than the TE phases:

The inversion is performed in 4 steps:

Step 1: A 1-D model was constructed, from an average for each frequency of the TM resistivity and phase responses at all sites. This model was used in the next step as input for an inversion of the unaveraged TM phase data. Input to the 1-D model was a uniform halfspace of 100 Ohm m.

Step 2: The best TM phase model (output from step 1) was used as input for an inversion of the TE phase data. In order to correct the static shifts in the resistivity data, the program incorporates static shift parameters, two for each site (TE and TM modes). By inverting the phases first, one could just by visual inspection assess the amount of displacement which was present in almost all the resistivity data.

Step 3: The output from step 2 was used as input in order to generate a set of static shift factors. This was achieved by inverting the phase data only for the first highest frequency, for the two modes, and by setting free the static shift control parameters, so that the algorithm allowed the model curves to move until they fit the resistivity data. It was found that there was no significant improvement of the overall

fit after the first 10 iterations, after which the output of each iteration was examined. The static shift parameters from the model with the best fit were finally chosen.

Step 4: Static shift parameters obtained from step 3 and the output model from step 2 were used as input for a simultaneous inversion of both TE and TM apparent resistivity and phase curves.

Convergence was achieved after 20 iterations and by setting an equal misfit goal of 1 for all the sites, the inversion resulted in a rms misfit of 1.6. By applying a set of robust Huber and redescending weights, the misfit came down to 1.26 (rms). Finally, by allowing 10 smooth iterations to be made, the smoothest possible model was obtained, resulting in a slightly increased misfit (1.38).

6.5.4 The 2-D model

The final model is shown in fig.6.6, but before examining it, it is essential to look at the resistivity and phase curves which were modelled in order to show the criteria upon which the inversion was performed.

6.5.4.1 Examination of possible models

Fig.6.4 shows the rotated data for the 7 sites. It is quite clear that there is a split in the AMT phases for the two modes of induction which becomes very pronounced at the last 3 AMT periods (10-23 s). Along the profile from N to S, the split becomes larger from site 123 to 131, then reaches a maximum at sites 133 and 130, becoming finally smaller from 125 and southwards, indicating that the maximum anisotropy exists beneath sites 131 up to 130. A similar split is expected to occur also in the resistivity curves, but, except at sites 130 and 125, the split between the two modes occurs only in the last 2-3 periods.

On the other hand, the TE phases at T>24 s (the LMT part) follow a quite different pattern. The TE phases, which have reached values up to 90^0 (for the longest period of AMT data), drop suddenly to values less than 5^0. In contrast, the TM curves are much smoother. Also, the resistivity data for both modes increases with period.

The AMT data processing has shown that, except for the last two periods (13 and 23 s), the data quality between 3-10 s is not good. Even in the last 2 AMT periods although the TM mode data show small errors and high coherency, the TE data show much lower coherency values (section 4.2.2). It is possible then, that the unrealistically high TE phases may be associated with the presence of coherent noise. The LMT data processing, also, has shown that the number of acceptable data for periods between 24 and 100 s is very small and the quality poor. Therefore, the

behaviour of the TE phase data in the range between 3 and 100 s is poorly known, and information cannot be accurately considered in that period range.

Due to the above complexity, an attempt was first made to invert only the AMT data. This leads to the conclusion that the split between the TE and TM phases is caused by a conductive area (<10 Ohm m) beneath sites 131, 133 and 130, the "size" of which depends mainly on how well the model fits the highest TE phases. The better the fit, the bigger is the anomaly. The model was similar to that shown in fig.6.6B, except that the conductive anomaly beneath the centre extends down to 10 km.

It must not be forgotten that the present inversion has two aims: First to show possible shallow structures, which may be of commercial interest, and second to focus on the deep structure revealed by the LMT data, so that mechanisms at depth (and the way they are related with the shallow structure) can be better understood. So, it was considered necessary to include the LMT data in the inversion.

Attempts to invert the combined AMT+LMT data set led to the following compromise: TE phase data points exhibiting high ($>65^0$) or very low values ($<3^0$) were discarded as it was impossible to fit a 2-D model to data with such changes in resistivity. After the highest phase values were discarded, the split in the phases decreased, resulting in a conductive anomaly which extends down to 5 km (fig.6.6B).

Before the decision to present this particular model, several other models were examined. It was found that it was not possible to fit all the features of the data. As was discussed above, when attention was focused only on the AMT data, a larger conductive anomaly and lower resistivities (<10 Ohm m) were found beneath the central part of Methana. However, by allowing a better fit to the TE phase data throughout the whole AMT range, the model fails to fit the LMT data.

A simple examination of other information that support the extent of a conductive anomaly down to 5 (and not 10 km) can be done in terms of induction arrows and of the skin depth.

The induction arrows at relatively short periods (T<1 s), for sites around the centre indicate the existence of a conductive anomaly, while the remainder point towards the sea. At T>1 s, there is no such indication, as all the induction arrows (including those at the centre) point towards the sea. So, one cannot decide accurately if at depths corresponding to periods greater than 1 s, any conductive feature is due to a structure of geothermal interest, or possibly associated with the sea effect.

The skin depth at the longest AMT period (T=23 s), and for the highest resistivity suggested by the AMT model (ρ=10 Ohm m), is 7.5 km, which is less than 10 km, i.e. less than the deeper estimate of the depth of the conductor for the AMT

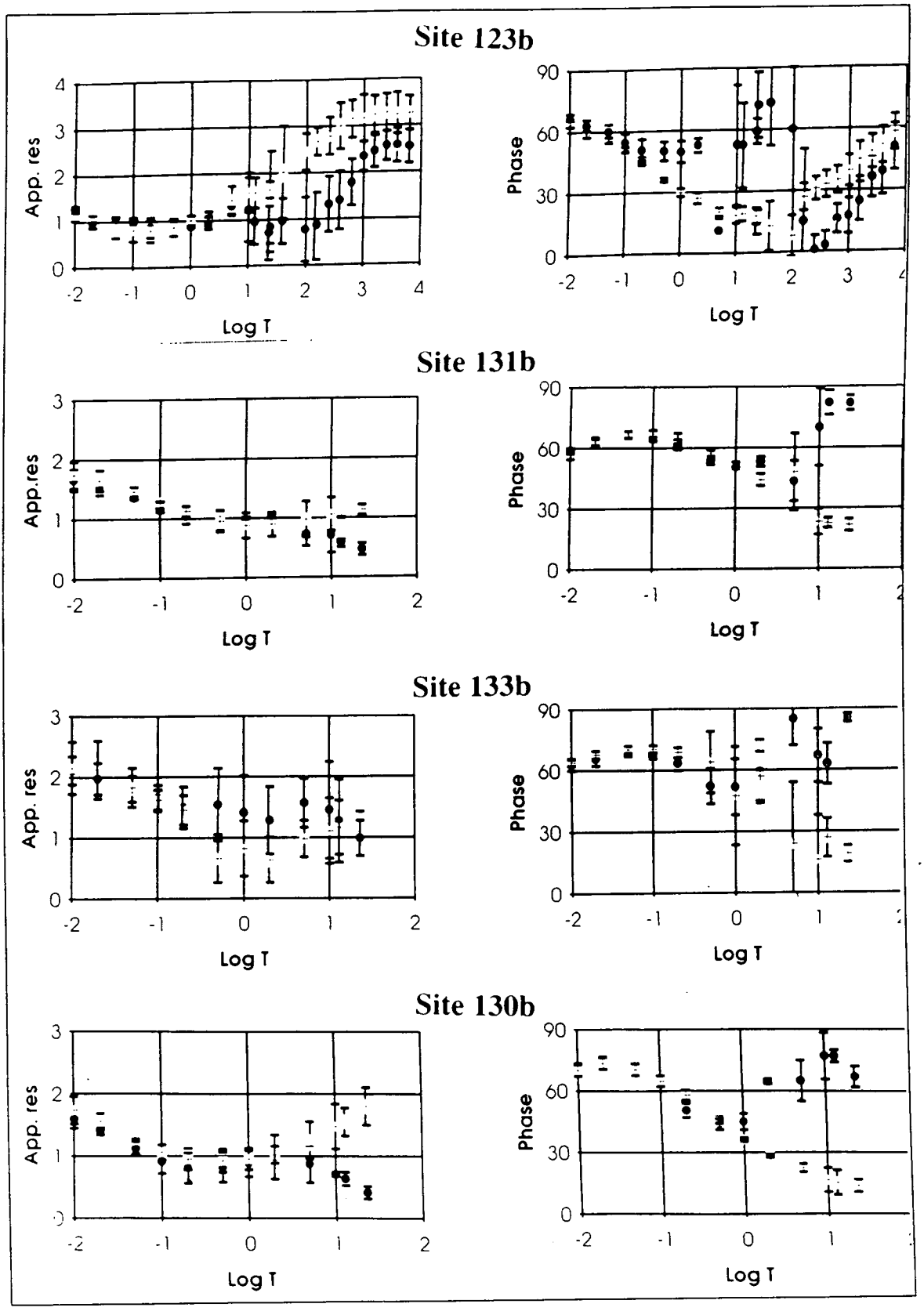

Fig 6.4 (continue): Apparent resistivity and phase data for the TE and TM modes of induction Sites 123b, 131b, 133b and 130b.

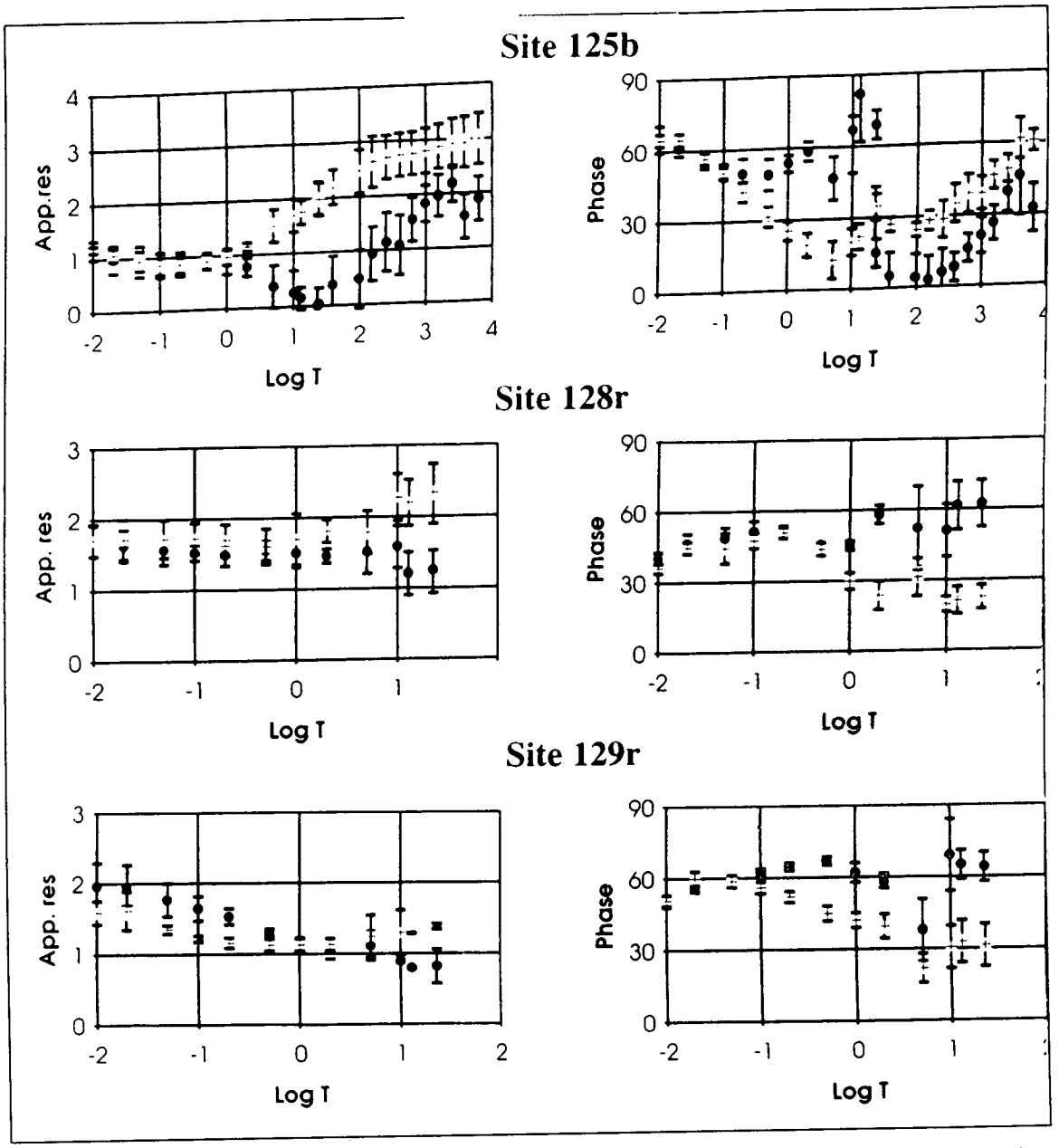

Fig 6.4 (end): Sites 125b, 128r and 129r. Apparent resistivity and phase data for the TE and TM modes of induction.

Apparent resistivity and phase data for the two modes of induction are shown in the same plot for each site, emphasing the different shapes in the curves for the TE and TM data. **Circles:** TE data **Crosses:** TM data. **b:**base site. **r:** remote site.

model. The skin depth at T=1 s and ρ=30 Ohm m is about 3 km, and gives a better estimate of the depth of the conductive anomaly for the AMT+LMT model.

6.5.4.2 Fit of the model to the data

The fit of the model to the data for individual sites is shown in fig.6.5. The TE mode is represented by circles (data) and thick lines (model); the TM mode by crosses (data) and thin lines (model). For convenience, the model can be divided into two parts, the shallow structure representing depths less than 5 km, and the deep structure (> 5 km).

a. Shallow structure (< 5 km)

The model (fig.6.6B) shows a high resistivity area (> 1500 Ohm m) below the centre of the peninsula at a depth up to 1 km. This is not surprising since apparent resistivity values for the shorter periods are higher at sites 131, 133 and 130 than at the other sites. The very thin conductive surficial patch appearing in the N at the same depth, is possibly an artifact caused by the misfit of the two first periods in the phases for site 123.

Below, a conductive area (<30 Ohm m) is indicated which extends down to 6 km. There is a minimum in resistivity of 7 Ohm m at 2-3 km beneath site 131. At about 2.5 km there is a tendency in the above anomaly to continue to the N (indicated by relatively lower values beneath site 123 at that depth), and also there is a thin conductive extension to the S in Trizina graben, due mainly to site 129, which shows resistivity values of about 25 Ohm m. For both ends (N and S) a thickness of 1 km is suggested.

A careful examination of the model shows that the split between the TE and TM phases for site 123 at T>0.1 s corresponds to the above thin conductive layer. Attempts to also model the less pronounced split in the phases at site 129 give rise to the similar conductive strip to the S. For sites 125 and 128 it was not possible to obtain a better fit for the TE phase data. A comparison between sites 123 and 125 shows that they are very similar, and also the TE phase data for site 125 in the range 0.01-1 s show the same pattern as that of 123, i.e. both phases decrease and then slightly increase (especially at site 125). So, one would expect a similar resistivity distribution beneath sites 125 and 123. But below site 125 (and 128) resistivities are considerably higher. It is then possible that the actual resistivities would be lower if the fit of the model to these site was better. If the actual resistivity values are low enough (<30 Ohm m) it might be that the two conductive "ends" are parts of the same layer, although thin (~1 km) locally. But such a continuous layer along the

profile would be detected by 1-D modelling. The 1-D modelling however, has indicated that resistivity values less than 10 Ohm m at depths greater than 2 km, occur only beneath sites 130 and 131(fig.6.1).

On the other hand, the conductive anomaly beneath the centre is well defined by the 3 closely spaced sites, whereas the conductive strips indicated at the ends of the profile are due only to sites 123 and 129 (the site spacing in Trizina graben is very poor). Therefore, apart from the central anomaly, no other significant conductive zones in the upper-middle crust beneath Methana Peninsula and Trizina graben are suggested.

b. Deep structure (> 5 km)

The skin depth for the lowest resistivity at the longest AMT period is about 5 km. This boundary coincides with the deeper indication of high conductivity areas. Unfortunately, information for the deeper structure must be confined to results from only the 2 LMT sites (123 and 125). This suggests generally increasing resistivity values with depth. A less resistive area (~100 Ohm m) under site 129, at a depth of 15 km, is probably below the depth of penetration of the AMT data (the skin depth for 30 Ohm m at the longest AMT period is 13 km), and therefore is considered as less important. Nevertheless, relatively lower resistivities appear at site 129 below 5 km, although the values are not as low as to be connected with geothermal or magmatic activity.

By looking at the fit of the model to the data (fig.6.5), the following points emerge:

1. The fit is generally better for the apparent resistivities than for the phases.
2. The TM phases fit better the model than the TE phases.
3. Although high TE phase values were discarded, the model fits part of the "split" in the phases between the two modes for the range 1-10 s (for example at sites 123 and 125), indicating the anisotropy present at that period range.
4. For the LMT data, the model shows an acceptable fit for the resistivities and the TE phases, whereas it does not fit the TM phases above 1000 s. This is possibly due to 3-D effects which are present at depth.

It was not possible to obtain a better fit to the LMT data, even when less weight was attached to achieve an acceptable fit on the AMT data. In that case, the fit to the AMT data was significantly poorer without improving the fit to the LMT data. This confirms the fact that at great depths 3-D effects are unavoidable and can cause departures from an ideal 2-D model.

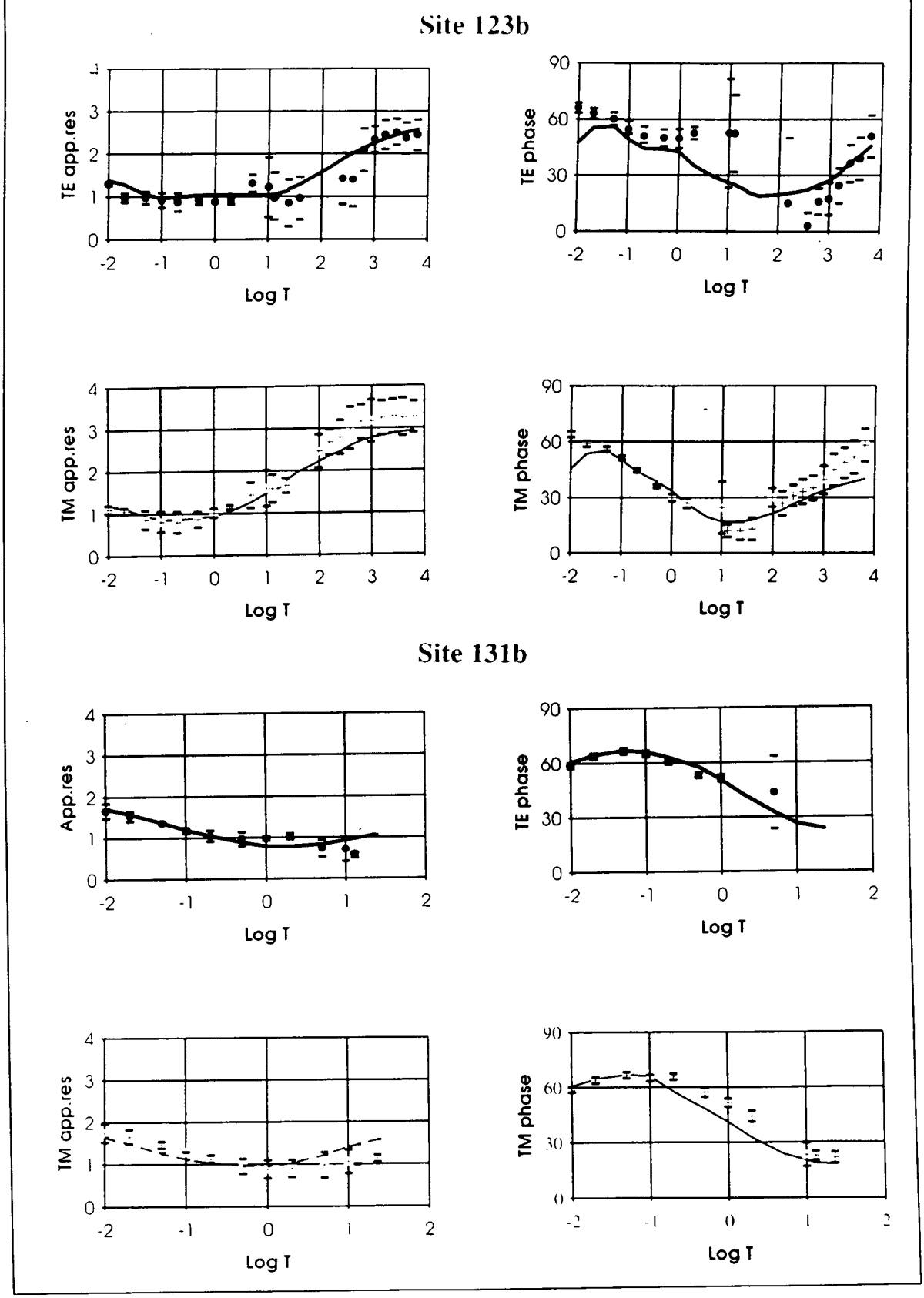

Fig.6.5 (continued): Sites 123b and 131b. Fit of the model to the data

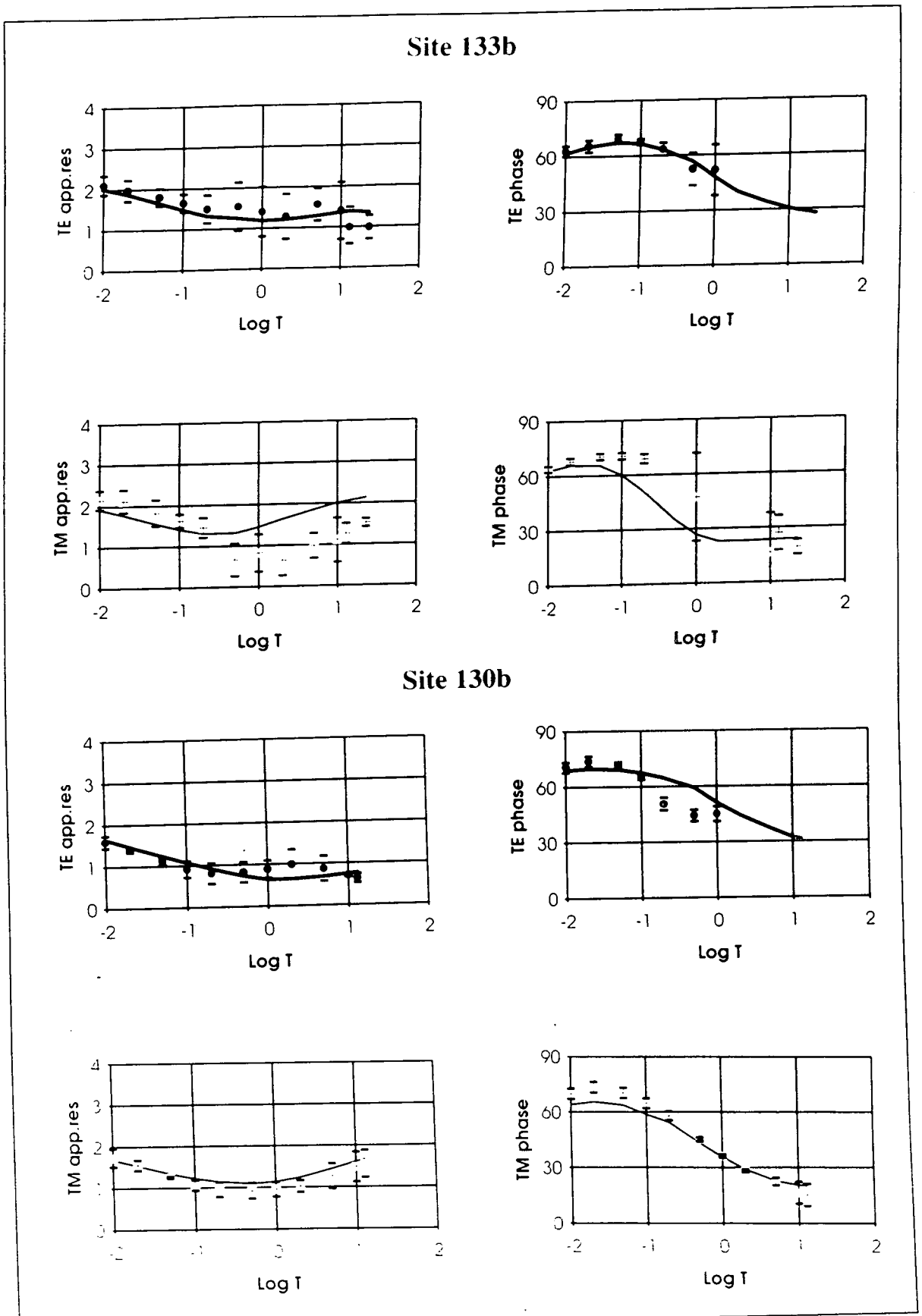

Fig.6.5 (continued): Sites 133b and 130b. Fit of the model to the data

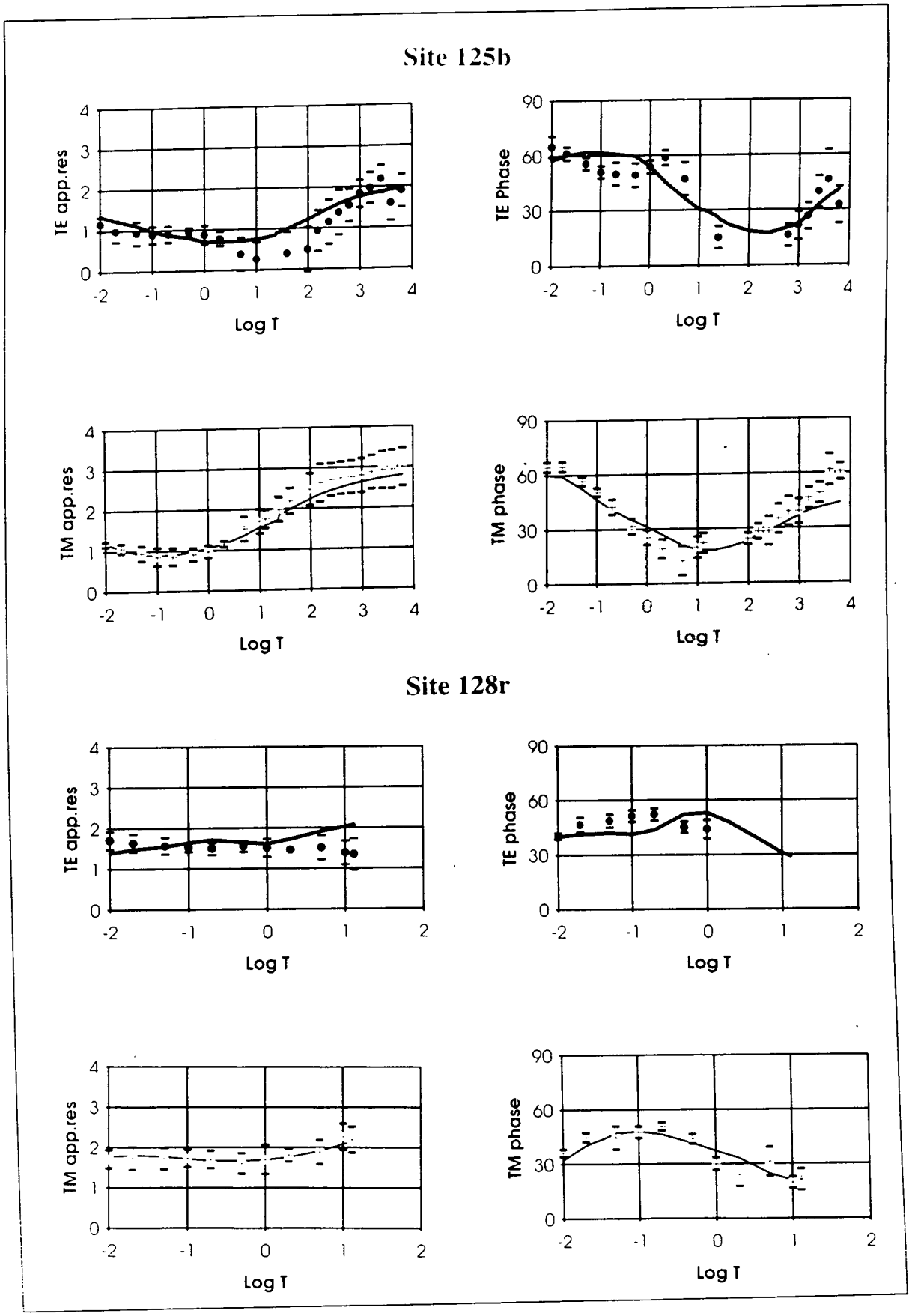

Fig.6.5 (continued): Sites 125b and 128r. Fit of the model to the data

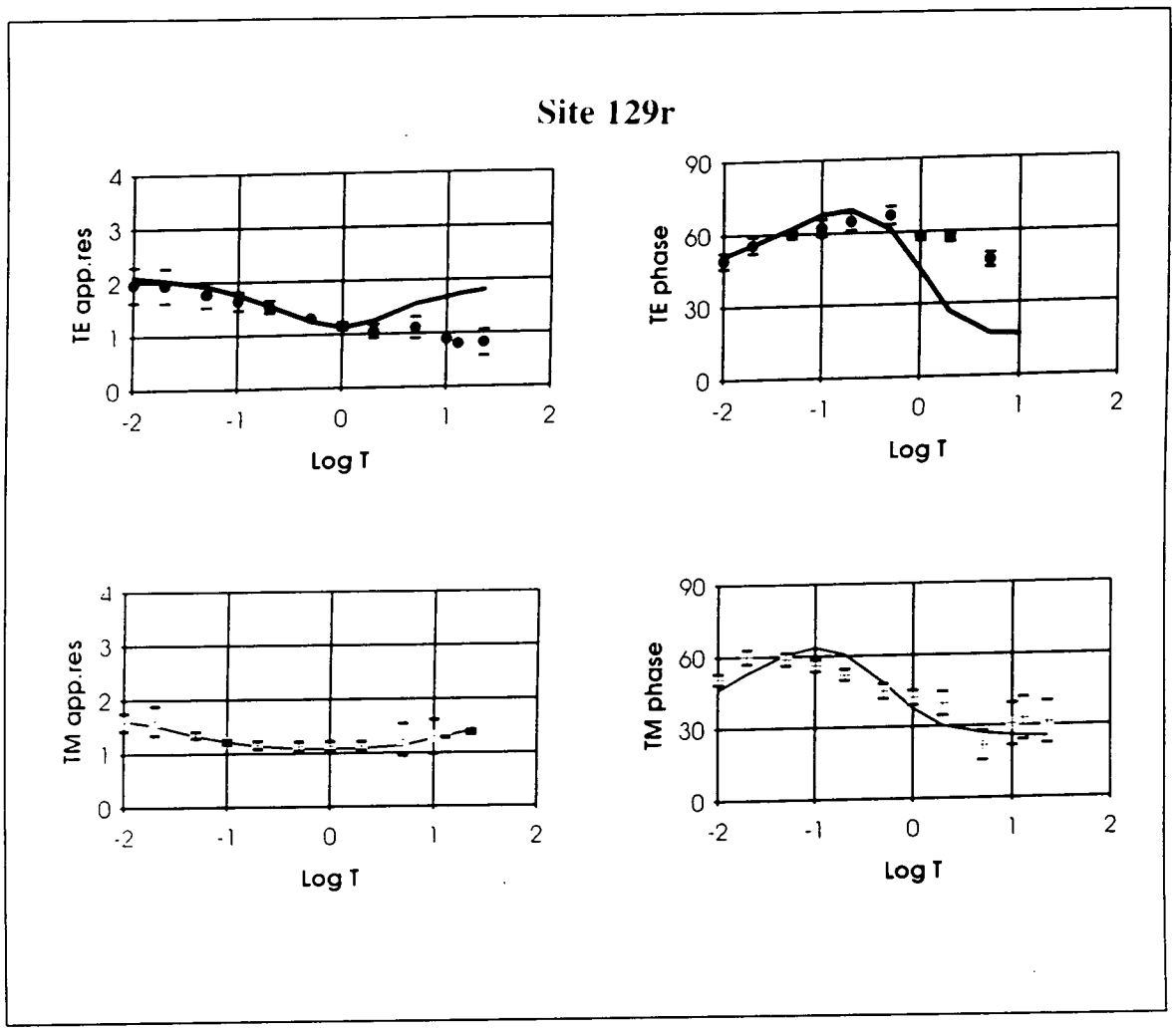

Fig.6.5(end): Site 129r.

Fig.6.5: Fit of the model to the apparent resistivity and phase data for the two modes of induction. **Circles:** TE data. **Crosses:** TM data. **Thick lines:** TE model responses. **Thin lines:** TM model responses. **b:** base site. **r:** remote site.

Fig.6.6 (next 2 pages): The 2-D model and interpretation.

Fig.6.6A: An interpretation of the 2-D model based on geological data is superimposed on the 2-D model shown in fig.6.6b. **1:** Quaternary volcanics. **2:** Tertiary flysch. **3:** Cretacious carbonates. **4:** Jurassic ophiolithes. **5:** Triassic carbonates. **6:** undefined basement. **7:** magmatic intrusion **8:** multi-fractured carbonate (?) rocks. **9:** meteoric or sea water. **10:** approximate location of thermal springs. **11:** flow of water and fluids. **12:** sea level. **13:** thrust. **14:** vents or fissures.

Fig.6.6B: The 2-D resistivity distribution beneath Methana and Trizina area as calculated from the 2-D code of Smith and Booker (1991). Resistivities are in Ohm m (Ωm).

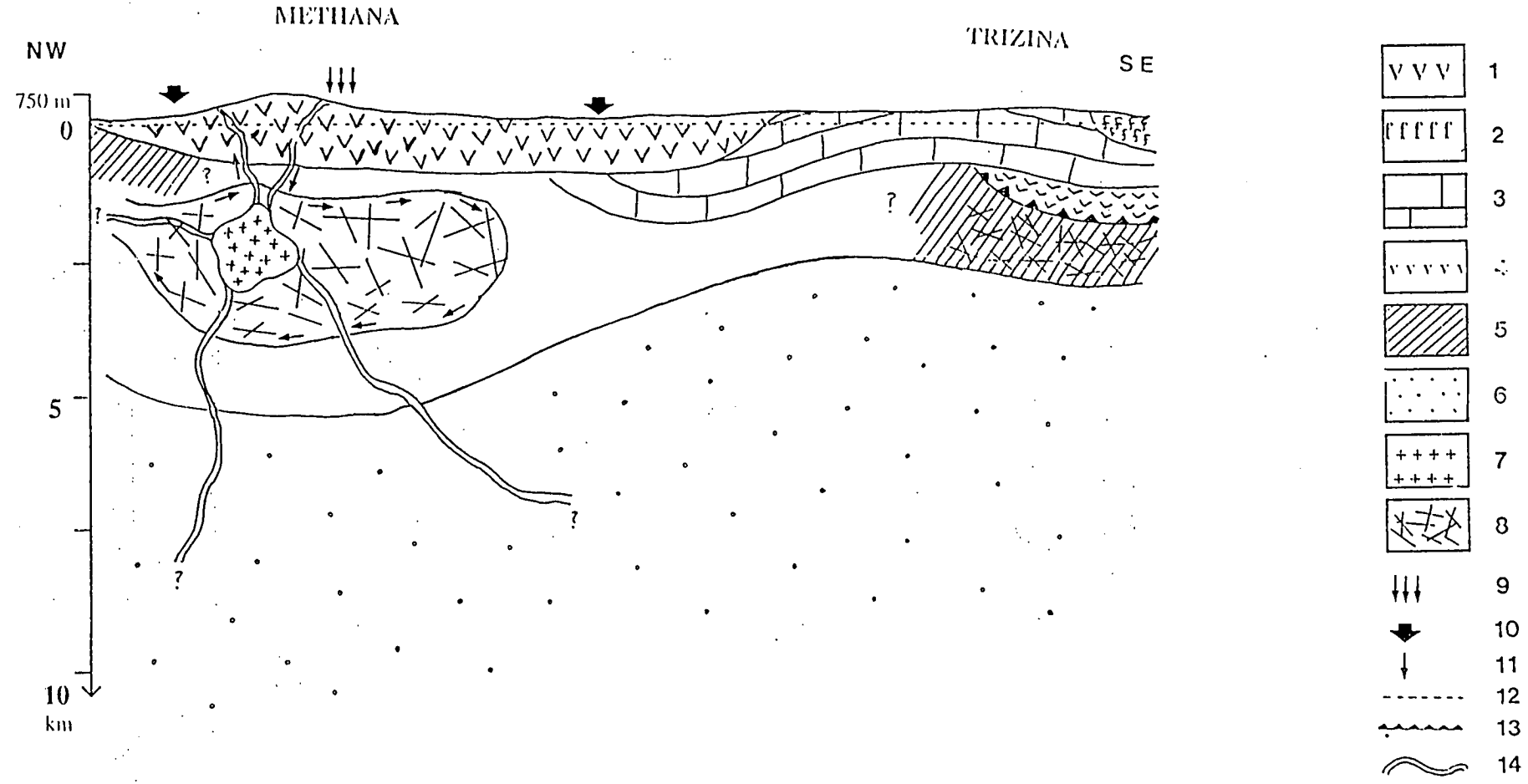
METHANA
TRIZINA
NW
SE
750 m
0
5
10
km
?
1
2
3
4
5
6
7
8
9
10
11
12
13
14

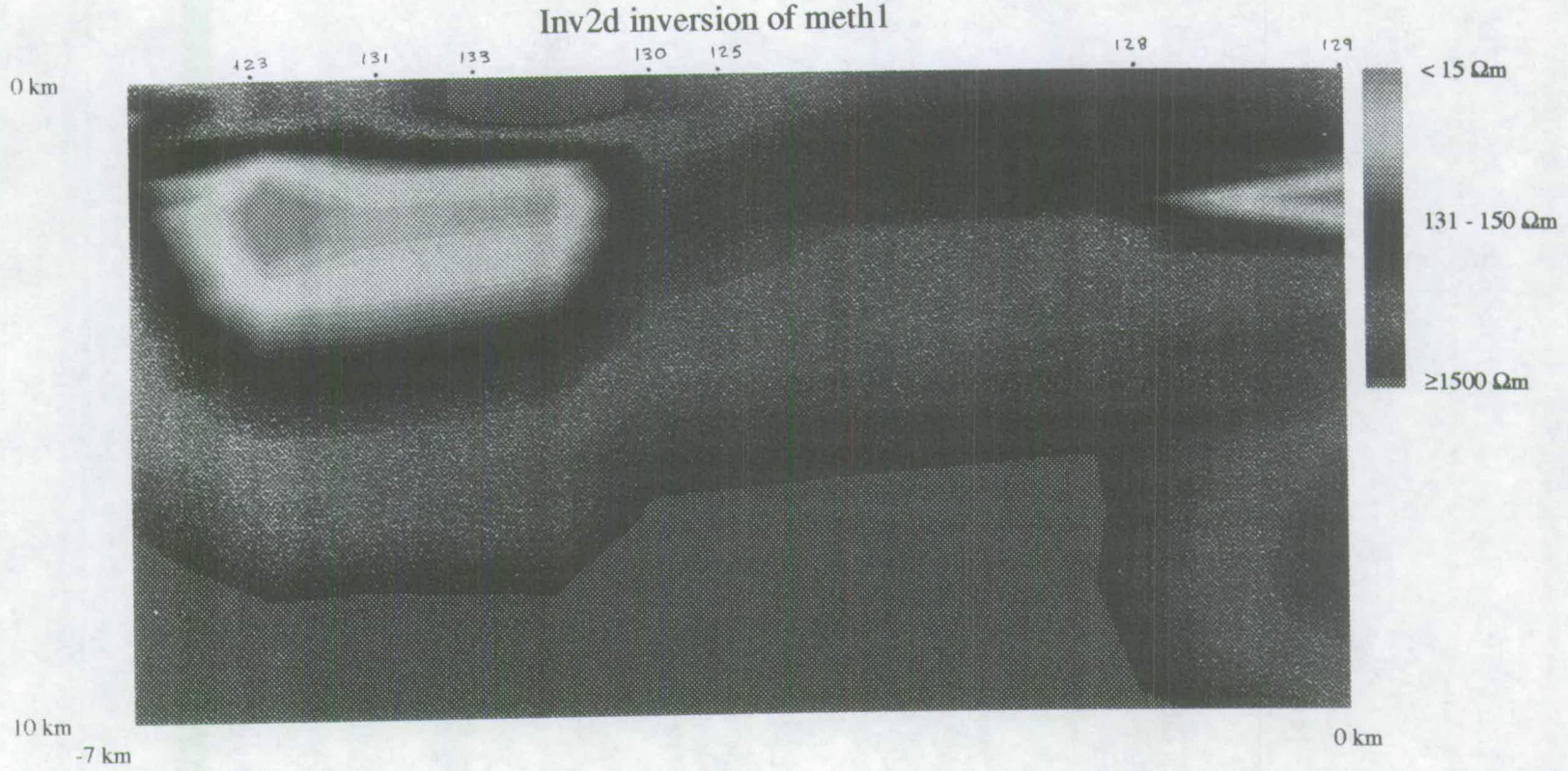
Inv2d inversion of meth1
123
131
133
130
125
128
129
0 km
< 15 Ωm
131 - 150 Ωm
≥1500 Ωm
10 km
-7 km
0 km

6.5.5 Interpretation of the 2-D model

In fig.6.6B the 2-D model is shown, while in fig.6.6A an interpretation is attempted in order to correlate the resistivity distribution, especially the low resistivity zones, with already existing information about the surficial geology (section 3.2).

6.5.5.1 Interpretation of the shallow structure (<5 km)

The discussion about the geology of the regional area (section 3.3) made it clear that two different geological environments exist, in Methana Peninsula and in Trizina graben, respectively. These differences in the surface lithology are reflected in the electrical contrasts between a more resistive block (>1500 Ohm m) under the centre of Methana, and a much less resistive (100-150 Ohm m) to the S of the peninsula. It is suggested that the first correlates with the andecite-dacite complex which reaches locally an altitude of 700 m, whereas the second represents the Cretaceous carbonates which outcrop to the S and continue under the flysch of the Trizina graben. (Although close to the surface lower resistivities are expected for the carbonates, the higher values could be due to the misfit of the model, see section 6.5.4.2). To the NW of the resistive complex, influence by the sea water and differences in the rock structure could reduce the resistivity of the volcanics. To the very S, resistivities of around 500-1000 Ohm m are typical of the flysch formation in Trizina graben.

Consulting the present 2-D model, differences in the two environments are also suggested at depths invisible to the geological mapping. A high conductivity area at depth up to 5 km beneath the volcanics is absent from Trizina graben, where only a narrow strip of values < 25 Ohm m can be seen.

From a geological point of view, the Triassic carbonates are the oldest rock outcropping to the NW of Methana therefore closer to the surface, which suggests that the Cretaceous carbonates could have been eroded there. In Trizina, the sequence is more complete: Triassic carbonates, thrust of ophiolites, Cretaceous carbonates and flysch on the top (fig.6.6A). The low resistivities in the Triassic carbonates can be connected with the presence of fractures in the rocks, due to the stress created by their tectonic contact with the ophiolites. The few lenses of ophiolites and serpentines found in Methana in contact with the Triassic carbonates, are not sufficient to justify the continuation of the ophiolitic layer under the peninsula.

As was mentioned, high conductivities (7-30 Ohm m) are confined along the profile to up to 5 km depth, being most pronounced beneath the central part of the peninsula. The lowest resistivities (7-8 Ohm m) are observed at a depth of 2-3 km close to the location of the last eruption (fig.3.6). Such a narrow anomaly could

represent a small intrusion coming from several km below, or from the N (from the volcanic island of Aegina), as a remaining part of the volcanic activity that took place in historical times. This small intrusion on its way upwards could have caused breaking and fracturing of the surrounding rocks, probably carbonates, with the obvious result of enhancing the electrical conductivity locally in the surrounding area, due to fluid circulation in the rocks' pores and fractures.

There are several possible sources of deep crustal water, such as dehydration reactions at deeper levels or water dissolved in magma (Glover et al., 1994). Also, in addition to fluids mobilised during tectonism, meteoric water can circulate to great depths in the crust (Meissner et al., 1992). Both the surface mapping of tectonic features and the detection of SP anomalies (section 3.3) have shown recent fault clusters within the volcanics which would be an effective conduit system for fluid circulation. The thermal springs could provide the means by which sea water goes downwards, interacts with the small chamber and returns back to the surface with increased temperature.

Apart from variations in fluid resistivities, other reasons which may also account for changes in the observed conductivities are a transition in mineralogy or pore shape geometry (Nesbitt, 1993).

6.5.5.2 Interpretation of the deeper structure (>5 km)

However, below 5 km a general increase in resistivity is suggested, which is not surprising since at great depths the fracture density is not so high as close to the surface, resulting in reduction of the fluid content within the rock. Therefore, although the nature and composition of rocks at these depths are not exactly known, an electrical boundary is delineated (fig.6.6A) which probably separates media of different composition and (or) different porosity and permeability. Among other reasons, permeability may be also controlled by the mineral/fluid dihedral angle (Watson and Brennan, 1987) which describes the wettability of the fluid on the mineral surface. If the value of the angle is high the fluid does not wet the surface well, so small cracks remain unsaturated with the aqueous fluid reducing pore fluid connectivity even when the pores are physically inter-connected (Hyndman and Shearer, 1989). The value of the dihedral angle can be increased with the presence of CO_2, when there is a high flux from the mantle (Harris, 1989).

In order to explain why the conductivity anomaly below the volcanic area of Methana is observed up to 5 km and not below that depth, it is necessary to consider the rocks' fluid inclusions, which usually contain dissolved gases such as CO_2, CH_4, H_2S and N_2 (Roedder, 1984). Driven by buoyancy forces, a pulse of mantle supplied

fluids can migrate rapidly upwards, leaving the lower crust in a dry state. The availability of aqueous fluids and CO_2, and their relative mobility from location to location may have a controlling influence on the presence, depth and size of high conductivity zones in the crust. In addition, the flux of CO_2 can help fluids to move to shallower depths leaving in that way a dry lower mantle (Yardley, 1986). Lateral migration of fluids is also possible by a capillary sealing mechanism by inmiscible CO_2-H_2O mixtures derived from rising volatiles (Bailey, 1994).

The above imply that no significant magmatic activity at great depths under the area of investigation takes place, or alternatively, that beneath young oceanic lithosphere more data are required in order to examine hydrothermal circulation and the presence of small scale mantle heterogeneities such as small magma chambers.

On the other hand, Parkinson arrows derived from MV data, point towards the S at the longest LMT periods (section 4.5.3), indicating a possible deep conductor of an E-W direction in the S.Aegean. Therefore the possibility of the existence of a deep magma chamber needs to be examined more carefully.

6.5.5.3 Limitations of the MT method

At this point it is worth mentioning certain limitations in the MT method: First, the MT method usually detects the limits of "large scale" geological formations, being rather insensitive to the existence of narrow zones in which hot fluids might circulate and second, its resolution decreases with depth, so that at periods corresponding to great depths there might be features which cannot be detected. Small, narrow and deep magma chambers, or the assumption of a cooling magma chamber probably not hot enough to be liquid, would not give trace on the MT data.

A third limitation concerns the nature of a 2-D model itself. It is probable that at great depths there are conductivity contrasts non-parallel to the regional azimuth, the effect of which would not be shown in the model. In reality, the misfit of the TM phases as well as the non-perpendicular relation between the regional azimuth and the induction arrows, both facts occurring at T>3000 s, could possibly be attributed to the 3-D effects which above that period become significant.

6.5.5.4 Conclusions

It is possible that the small area of lower resistivities (7-15 Ohm m) beneath the centre of the peninsula, is connected with the volcanic history of Methana. This obviously implies the existence of some feeding magma source from below, although no such indication from the inversion of the LMT data exists. From the above discussion though, it can be said that the possibility of a deep magma chamber can not be excluded. First, the parent chamber does not need to be exactly below the area of investigation, as for example it can be connected with the island of Aegina. Second, the limitations imposed on the MT method can make such detection a very difficult task (for a further discussion see section 7.3). Third, evidence of fluid mobility can have a great impact on the locations of fluid filled rocks.

The small anomaly is interpreted as being a rather limited phenomenon resulting from the cooling of former magmatic activity. Such a small magma chamber could be connected with a deep heat source through a narrow feeding channel, which used to provide fresh supplies of magma from the parent chamber, when the volcano was active. But in such cases, as soon the feeding channel freezes the apophysis becomes a small independent reservoir whose active life is limited. Such narrow pipes, by providing a way through to a deeper and central magma chamber might be responsible for the volcanic activity not only in Methana but also along the HVA.

In the next and last chapter, results from MT and MV studies belonging to other areas along the HVA will be shown. By comparing them with those from Methana, it will be seen that a similar problem of magma chamber detection by the MT data was encountered also in the island of Milos, although there was significant evidence for the existence of a thermal anomaly. In spite of this, results from MV data will support the fact that there must be a deep conductor in the S.Aegean. Finally, the regional stress field associated with the extensional tectonics in the S.Aegean will be presented, as this is related to horizontal deformations in the crust as well as with major fault zones in which hot fluids might ascend from the mantle.

Chapter 7

Electrical structure beneath the HVA- comparison with other MT studies

7.1 MT surveys along the HVA

Before the Methana project, studies in other areas, mainly islands, belonging to the Hellenic Volcanic Arc (HVA) have been carried out, in order to assess their geothermal potential. The islands of Milos, Nisyros, Kos and Santorini are considered as the most important, in which a number of geological (Keller, 1982; Fytikas, 1989; Di Paola, 1974; Pentarakis et al., 1990) and geophysical surveys have been made (Hutton et al., 1989; Galanopoulos et al., 1993; Lagios et al., 1994; Bauce et al., 1989; Dawes et al., 1991; Haak et al., 1989). All these islands show the characteristics of recent volcanism, but Milos was considered to be the most promising, as surface manifestations of its geothermal potential cover a surface of 10 km^2 (Pentarakis et al., 1990) with measured temperatures up to 100^0C (Fytikas, 1980).

Attempts to reveal the electrical structure beneath the HVA have lead to a number of broadband MT surveys, which were undertaken by the University of Edinburgh in cooperation with the Department of Geophysics and Geothermy of Athens, during the period 1986-92. These included:

a. A broadband (100 Hz-10000 s) MT survey on Milos island, aimed at locating geothermal fields indicated by high temperature gradients in the area.

b. An MT survey of Kos (100 Hz-100 s).

c. A broadband MT survey of Nisyros island, whose aim was to reveal the electrical structure beneath the caldera.

d. The installations of LMT stations on Santorini island.

During the same period, LMT stations were installed in two more areas in central Peloponnesus and in Euboea, which although they do not belong to the HVA belt, are of equal importance in a regional sense, aiming to reveal the electrical structure beneath the Aegean.

In the next section, models available from previous MT analysis are presented for Milos, Nisyros and Kos and are compared with the models constructed for Methana.

7.2 1-D and 2-D electrical models

7.2.1 1-D electrical models

As for Methana, the 1-D models constructed for the other areas are based on the invariant apparent resistivity. Fig.7.1 shows computed responses for Milos, Nisyros, Kos and Methana, and their corresponding resistivity-depth profiles. The models are characteristic for these volcanic islands and correspond to areas of geothermal activity. The Milos model corresponds to a site located in a region of high thermal gradient (Galanopoulos, 1989), the Kos model is taken from an average of all available 1-D models (Lagios,1992a), and the Nisyros model corresponds to a site situated inside the crater (Dawes and Lagios, 1991). For Methana, the 1-D model was taken from site 131 (section 6.4). Comparison between these models leads to the following conclusions:

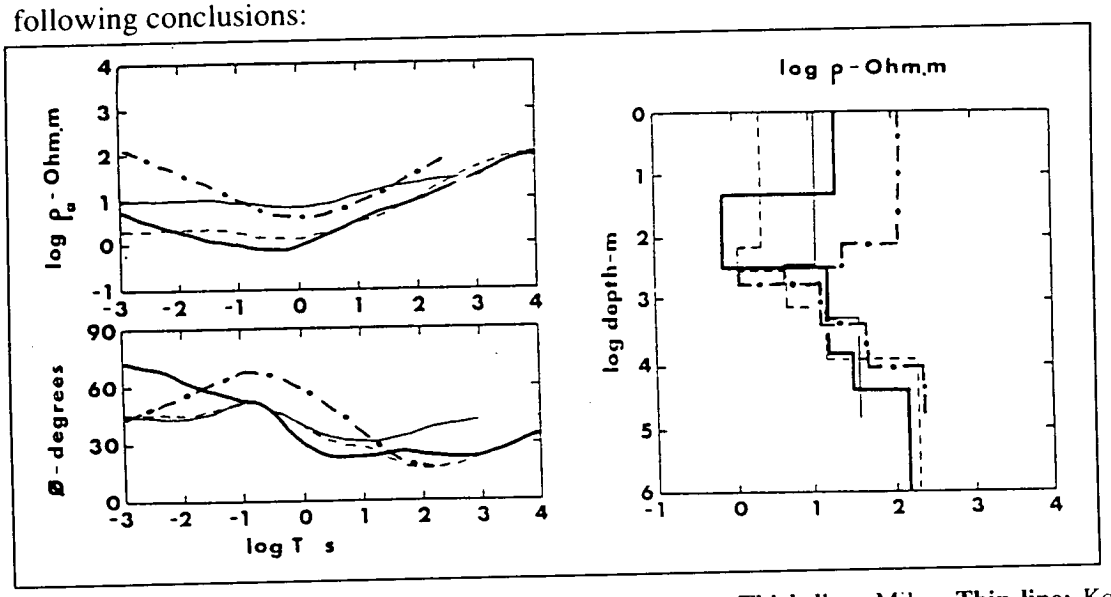

Fig.7.1: 1-D electrical models and computed responses. **Thick line:** Milos. **Thin line:** Kos. **Dashed line:** Nisyros. **Dashed and dotted line:** Methana.

1. Near the surface (first 100 m), Nisyros exhibits the lower resistivity values (< 3 Ohm m), whereas Methana the highest (200 Ohm m).

2. There is a minimum in resistivity for all areas at shallow depth (< 1 km), which is more pronounced in Milos. Values of 0.7 Ohm m are suggested for Milos, 1-4 Ohm m for Kos and Nisyros in the depth range of 100-500 m, while for Methana there is a thin layer of 10-30 Ohm m at a depth range of 300-600 m.

3. At greater depths (>10 km), there is a gradual increase in resistivity up to 30 Ohm m for Kos and up to 150-200 Ohm m for Milos and Nisyros, while at Methana the resistivity is slightly higher (~200 Ohm m).

7.2.2 2-D electrical models

In fig.7.2 TE and TM data, as well as computed responses for two sites in Milos and Methana are shown. Comparison between the two areas shows the following:

1. Both apparent resistivities show anisotropy for the two modes of induction, especially at the longer periods.

2. Apparent resistivities increase with period at T>10 s. 3. In Milos, for the longest period there are maxima in resistivity of 100 and 10 Ohm m for the TE and TM mode respectively, while in Methana the corresponding values are much higher, around 100 and 1000 Ohm m respectively.

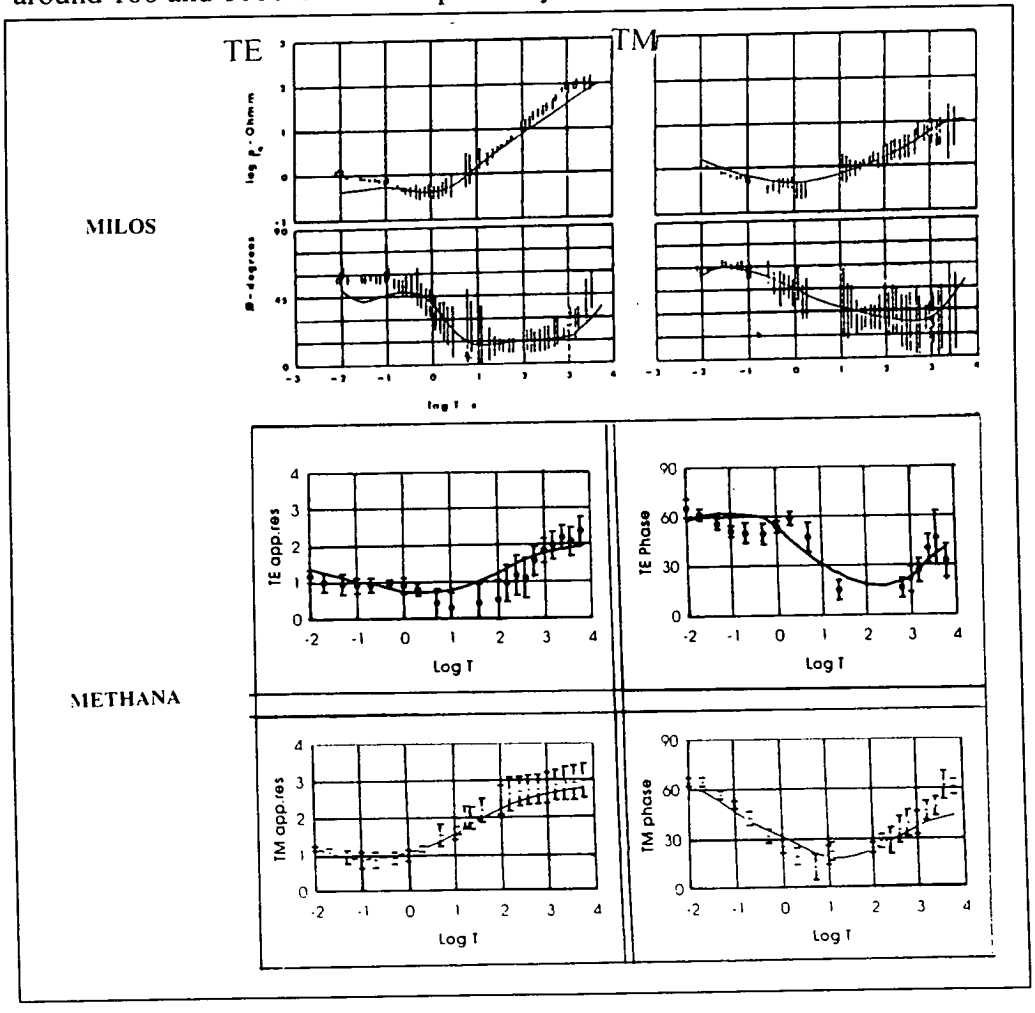

Fig.7.2: Comparison between Milos and Methana individual site model.

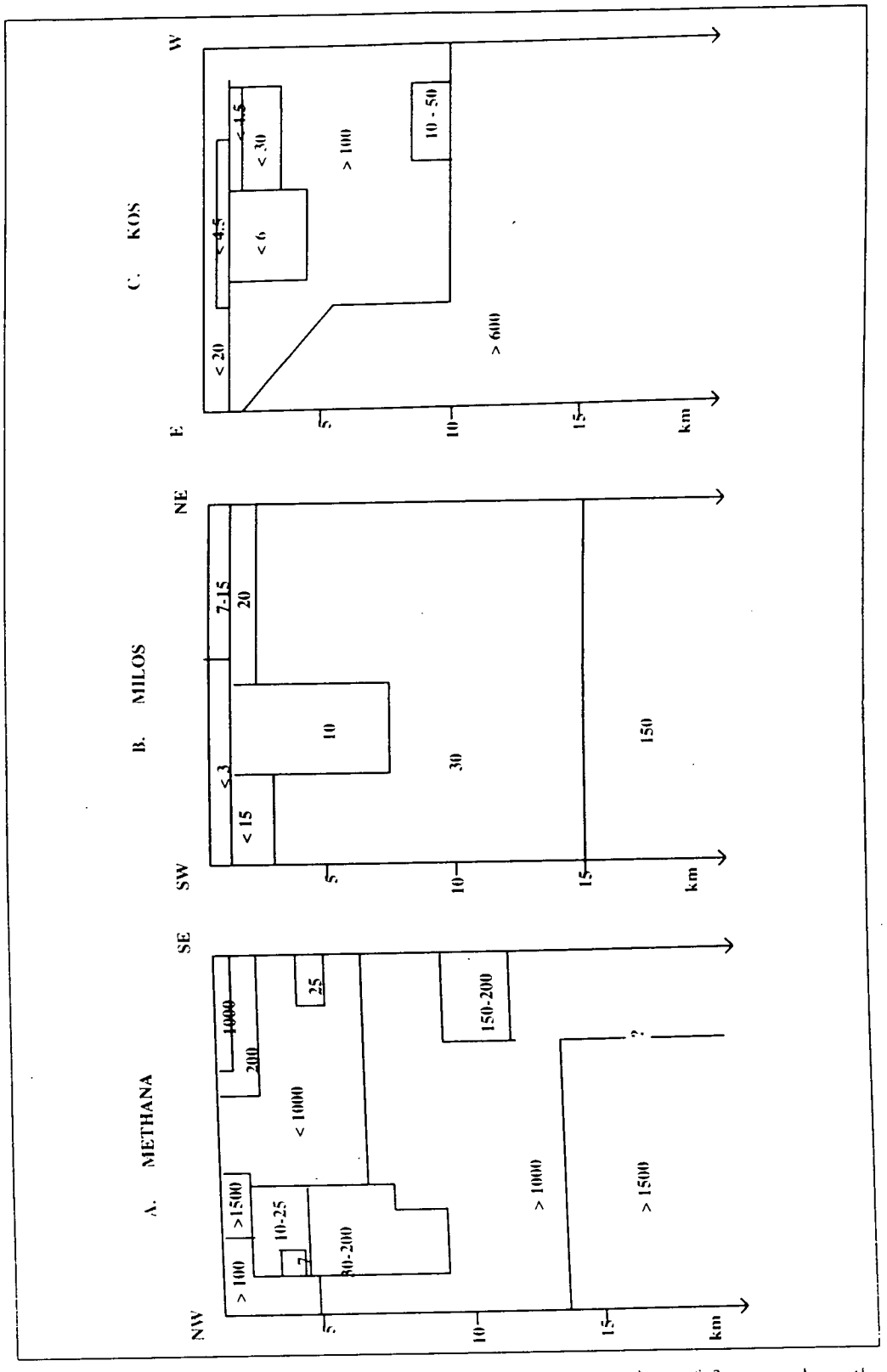

Fig.7.3: Electrical resistivity distribution for the subsurface of 3 areas along the HVA as proposed by 2-D models. **A:** Methana. **B:** Milos. **C:** Kos. Resistivities are in ohm m.

4. For Milos the TE phases are much smoother.

5. The model does not fit well the TE mode data for Milos and the TM mode data for Methana, at T > 1000 s.

A simplified sketch of a 2-D model for Milos (Galanopoulos et al., 1991) and a collation of 1-D resistivity-depth models for Kos (Lagios et al., 1994), are shown in fig.7.3. Those are compared with the 2-D model constructed for Methana in the previous chapter, a sketch of which is shown in the same figure. Comparison among these models leads to the following:

1. Low resistivity zones (0.7-30 Ohm m) are indicated in all models at depths up to 5 km (the lowest values are indicated for Milos).

2. At depths between 5-10 km there is a general increase in resistivity which is again lowest in Milos (~30 Ohm m).

3. At depths of 10-15 km, Milos shows resistivity values of about 30 Ohm m, while in Methana there is no indication of such a low resistivity zone (in Kos a similar zone is indicated between 7 and 10 km).

4. Below 15 km the resistivity increases to values of 150 Ohm m for Milos, >400 Ohm m for Kos, while for Methana resistivities rise to values > 1500 Ohm m to the N being slightly lower in the S outside the peninsula.

7.2.3 Summary

All studies along the HVA have suggested the existence of low resistivity zones within the crust. Both 1-D and 2-D modelling indicate low resistivities at relatively shallow depths, but increasing resistivities at great depths. In Milos, Nisyros, Kos and Methana very low values (<5 Ohm m) were suggested at depths <1 km (in Methana this zone is very thin).

Between 1 and 10 km, low resistivity values (10-30 Ohm m) are indicated for all the subsurface of Milos, while such low values are confined to particular locations in Kos and Methana, embedded in a more resistive structure.

At greater depths (>10 km), resistivities remain relatively low for Milos (30-150 Ohm m), whereas this is not the case for the other areas. However, although for Milos relatively low resistivities (< 10 Ohm m) were proposed at depth, these do not suggest that a magma chamber may exist in a particular location. Fytikas et al. (1989) proposed that this can be due to the presence of a cooling magma chamber, or possibly many small magma chambers which could be electrically undetected.

7.2.4 Conclusions

The results of several geophysical experiments carried out on Milos, have allowed the compilation of a possible model of a geothermal reservoir, although no support was provided for the existence of a shallow magma chamber.

(i) Apart from Milos, in which several studies have indicated (including the low resistivities of the MT data) the existence of a geothermal reservoir beneath the surface suitable for geothermal exploration, in the other areas only limited zones of low resistivities were suggested.

(ii) Especially for Methana, the limited extent of the low resistivity zone and its interpretation (i.e. due to the cooling of former magmatic activity), and the high resistivities below 10 km, do not suggest that considerable magmatic processes take place at depth.

7.3 An integrated model for the South Aegean sea

The aim of this last section is to examine more carefully the possibility of a deep magma chamber which (although undetected by the MT data) might be connected not only with the volcanic history of Methana, but with the volcanic activity generally in the S. Aegean. Although in the present work available data which might contribute to a knowledge of the regional domain are based mainly on 2 LMT sites only, an attempt is made to correlate the MT results with already existing knowledge about the S.Aegean. This concerns (i) MV results in a number of areas and (ii) the regional stress regime due to the extensional tectonics in the last 7 m.y.

7.3.1 Previous work in the S.Aegean

The general features of the subduction process between the African and Aegean plates were outlined in section 3.1.1. Over the past years various geophysical surveys have been carried out aiming to reveal the deep structure of the Aegean sea and the mechanisms connected with the volcanic activity. In systematic studies of deep earthquakes (Papazachos and Komninakis, 1971; Makris, 1977; Mackenzie, 1972,1978; Makropoulos et al., 1984) centres between the trench system and the central Aegean which reach depths of 180 km have been located. Seismic and gravity studies suggested that under Peloponnesus the crust has a thickness of 40-45 km, while towards the S.Aegean it becomes thinner, about 20 km (Makris, 1977 and 1978b). The heat flow in the Aegean is high (2.08-2.16 HFU) in comparison with other regions of thermal stability (1-1.5 HFU) (Jongsma, 1974; Fytikas et al., 1979). Positive gravity anomalies of order 120-140 mgals were observed beneath the HVA (Makris, 1977) with a maximum of +175 mgals at the Cretan trough (fig.3.2), which could be partly attributed to intrusion of dense mantle material into the crust. The stongest magnetic anomalies have also been observed at the Cretan trough (Papazachos and Komninakis, 1971) suggesting (Papazachos et al., 1971; Horvath and Berchhemer, 1982) the existence of magnetised rocks that have been intruded by volcanism.

7.3.2 Induction arrows for the S.Aegean

As was mentioned in the beginning of this chapter, LMT data have been collected during different projects for a number of areas along the HVA, including Euboea and part of Peloponnesus. For these areas Parkinson induction arrows have been calculated. These are shown together with the results from the Methana project in figs.7.4a-d, for periods in the range 230-14000 s.

For the real arrows the following points can be mentioned:

1. At T=230 s (fig.7.4a) and T=2400 s (fig.7.4b), the Parkinson arrows drawn for Methana show a similar pattern to those drawn for Euboea (to the N of Methana). At 230 s they point to the E, rotating gradually towards the SE at 2400 s.

2. At the same period range, for the islands Milos, Santorini and Nisyros the arrows point to the SW.

3. At T= 6000 s (fig.7.4c), all real arrows point to the S and SW.

4. At T=14000 s (fig.7.4d), data which are available only from two areas, show a further rotation towards the SW.

It seems that the real induction arrows at about T>6000 s point to a long deep conductor of a WNW-ESE direction.

The imaginary arrows obviously reveal a more complicated pattern. However, when compared with their real parts, the following can be noticed:

1. Imaginary arrows point obliquely to their real parts in all the areas at T< 2400 s, which is possibly connected with the presence of 3-D structures at great depths.

2. At T=6000 s, the imaginary arrows form oblique angles in central Peloponnesus, Methana, Euboea and Santorini, while in S.Peloponnesus, Milos and Nisyros they are almost antiparallel.

3. At T=14000 s, arrows in central Peloponnesus tend to be antiparallel, while in Euboea they are more oblique.

As deduced from deep earthquakes, in contrast to its northern limit, the southern limit of the Aegean microplate is well defined (McKenzie, 1970). From the discussion in section 5.7 it follows that the NW-SE tectonic trench reflects deep processes associated possibly with the morphological axis of the W part of the Hellenic arc (fig.3.2) and the limit between the Aegean and African plates.The almost antiparallel relation between the real and imaginary arrows at T>6000 s at stations located closer to the SW of the Hellenic trench, tends to support a 2-D shaped structure in the SW limit of the Aegean-African plates.

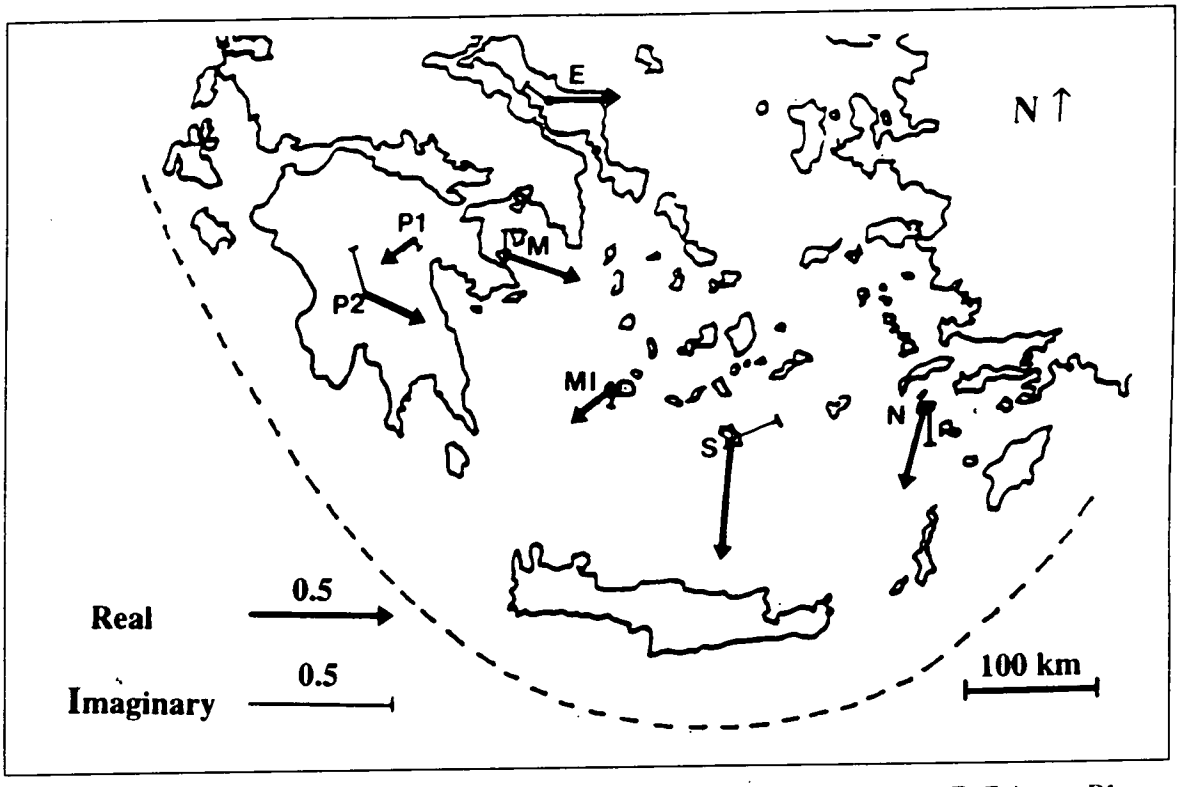

Fig.7.4a: Parkinson real and imaginary arrows in the S.Aegean. T=223-250 s. **E**: Euboea, **P1, P2**: Peloponnesus, **M**: Methana, **Mi**: Milos, **S**: Santorini, **N**: Nisyros. **Dashed line:** Hellenic trench.

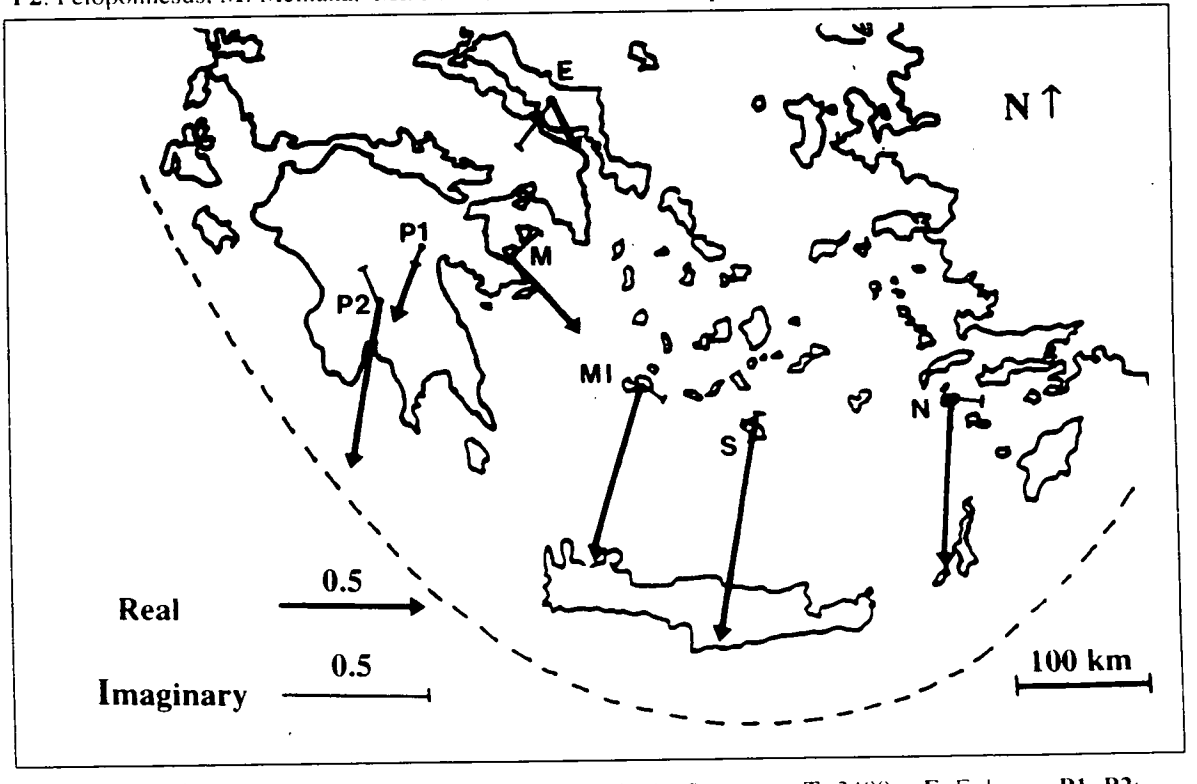

Fig.7.4b: Parkinson real and imaginary arrows in the S.Aegean. T=2400 s. **E**: Euboea, **P1, P2**: Peloponnesus, **M**: Methana, **Mi**: Milos, **S**: Santorini, **N**: Nisyros. **Dashed line:** Hellenic trench.

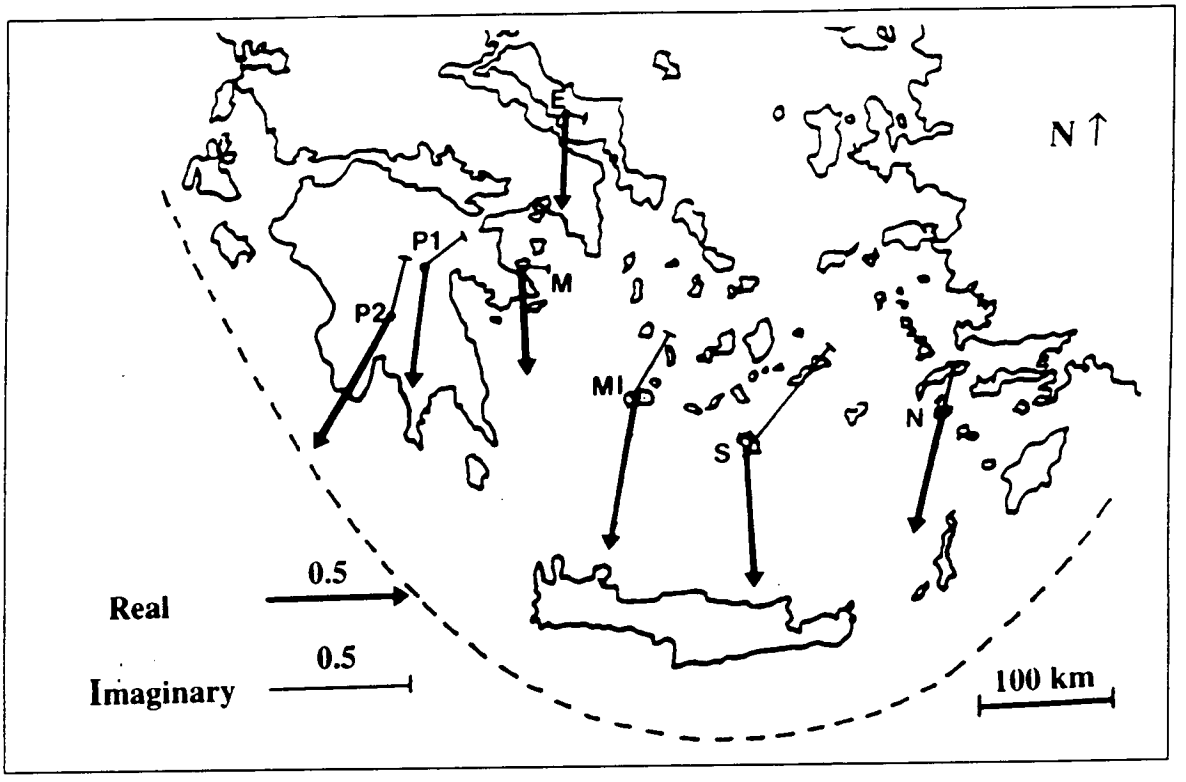

Fig.7.4c: Parkinson real and imaginary arrows in the S.Aegean. T=5800-6100 s. E: Euboea. P1, P2: Peloponnesus. M: Methana. MI: Milos. S: Santorini. N: Nisyros. **Dashed line:** Hellenic trench.

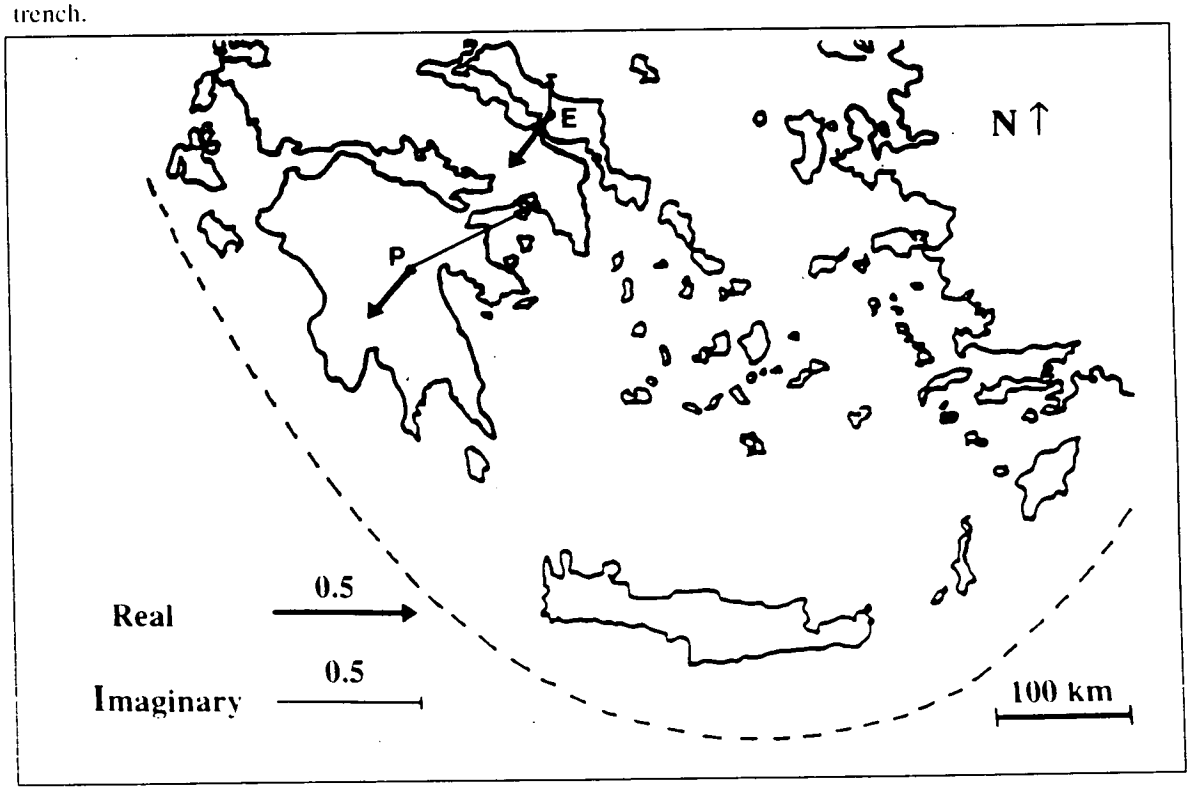

Fig.7.4d: Parkinson real and imaginary arrows in the S.Aegean. T=14000 s. E: Euboea. P: Peloponnesus. **Dashed line:** Hellenic trench.

7.3.3 The extensional tectonics of the S.Aegean

Starting from the Miocene, the entire region was affected by extensional tectonics (Le Pichon and Angelier, 1979; Angelier and al. 1982) which are still active, and commonly referred to as the neotectonic phase.

7.3.3.1 Regional stress and methods

Tectonic stress is one of the most important physical parameters for the understanding of fault patterns and tectonism generally, because it is the stress regime in a particular area that is responsible for the origin of major fault zones and movements on the faults. Assessment of the direction and magnitude of stress in a specific area can be achieved in a number of different ways. In the case of the Aegean area, data have been collected from (i) focal mechanisms of earthquakes (McKenzie 1972; Ritsema, 1973; Drakopoulos and Delibasis 1982), (ii) structural analysis of faults (Paquin et al., 1982, 1984) and (iii) aerial photographs (Angelier and al. 1982). From the earthquakes analysis, the directions of P (maximum compression) and T (maximum tension) are obtained, whereas the neotectonic faults systems are usually analysed into three orthogonal principal stresses σ_1, σ_2, and σ_3 with $\sigma_1>\sigma_2>\sigma_3$. Note that there may be agreement between the P and T trajectories and the principal σ_1, σ_2,σ_3 neotectonic stress directions (Mercier et al., 1979), although this is not always the case. These data led to several conclusions on the geometry of faults systems and permitted a sketch of some characteristic stress fields associated with the extensional process in the Aegean domain.

7.3.3.2 Stress trajectories

The extensional tectonics of the Aegean area is related to normal faulting; "extensional" means that σ_1 is vertical, σ_2 and σ_3 are horizontal, and σ_3 is the dominant direction of extension. The results are taken from Mercier et al., (1987) and Angelier et al., (1982) and are shown in figs.7.5 and 7.6 respectively. The mechanisms of extension are grouped into two categories, one for Pliocene-early Quaternary (a), and the other for Middle-Upper Pleistocene-Holocene (b). In addition, figs.7.6a and b show an attempt at reconstructing stress trajectories. As can be seen, the results from the two authors show similar stress patterns for the S.Aegean. The following points are worth mentioning:

1. In the earlier period the extensional direction σ_3 trends roughly radial to the Hellenic trench (figs 7.5a and 7.6a), whereas in the latest period stress directions tend

to align along the trench structure, especially to the NW and central area (figs 7.5b and 7.6b).

2. Comparison between the two extensional phases along the HVA shows that there is a change in direction during geological time from NE-SW to NW-SE in the W and S part of the arc, whereas in the proximity of Kos and Nisyros the change is from NNW-SSE to NNE-SSW.

3. In figs 7.6a and b, trajectories for the two horizontal principal stresses (σ_2 and σ_3) are shown. It is quite clear that the trajectories for σ_3 show an approximately E-W direction in the SW, changing gradually to N-S and NE-SW in the NE, for the Pliocene and Pleistocene respectively. However, in the very S (Crete) it seems that no predominent direction of extension can be delineated as the two horizontal axes are equal in magnitude. This was interpreted by Angelier (1979) as due to permutation of σ_2 and σ_3, suggesting a multi-directional extensional tectonics. Similar situations arise for the Pleistocene in the proximity of Methana as well as in the SE (fig.7.6b).

4. Although close to the arc boundary (Hellenic trench) the extensional processes have not changed significantly through time, along the HVA the directions of extension strike almost perpendicular for the Pleistocene compared to the Pleiocene phase.

7.3.3.3 Correlation with the MT data

Strike directions derived from analysis of MT and MV data along the HVA have been correlated with fault zones due to the extensional patterns (Galanopoulos, 1993). At Milos, information about the fault system derived from the MT data suggested a dominant NW-SE alignment of impedance at depth which was correlated with the Pliocene phase, while in Nisyros and Kos a NW-SE suggested strike was correlated with the Pleistocene phase.

Athough Trizina graben seems to have been affected by the Pleiocene NE-SW extensional tectonics (fig.3.3), the suggested 30^0E main faulting zone for Methana could be due to the latest NW-SE extensional phase, which affects the domain to the NW and N of Methana, Milos and Santorini (figs.7.5b and 7.6b).

Fig. 7.5

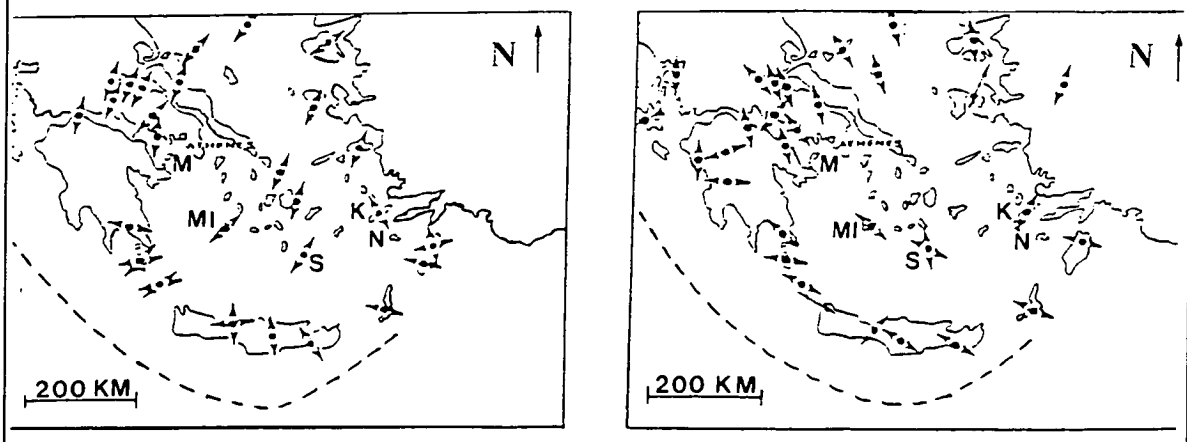

Fig. 7.6

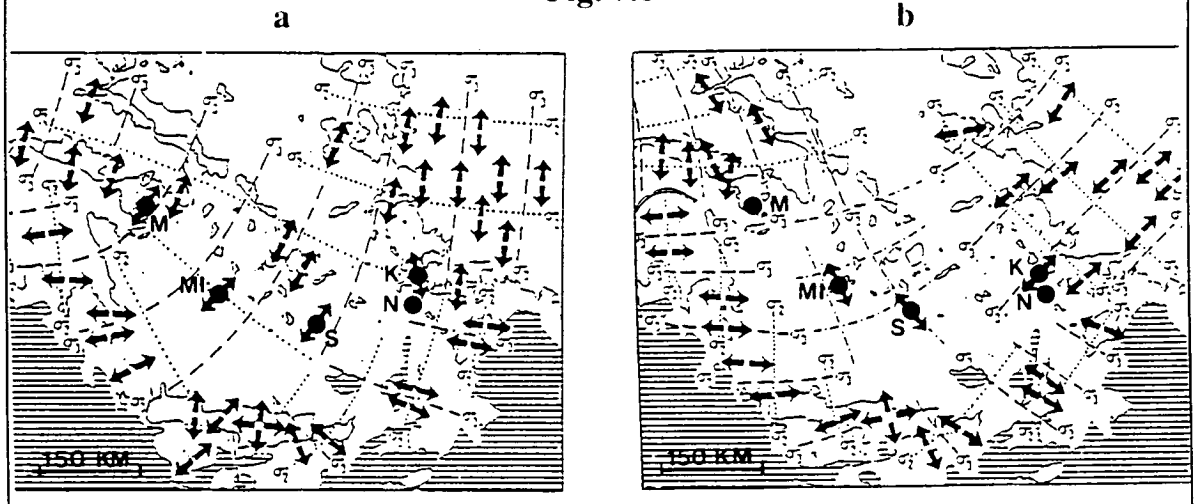

Fig.7.5a and b: Stress patterns (extensional tectonics) in the S.Aegean sea. **a:** Pliocene **b:** Pleistocene. Divergent arrows give the principal stress directions computed from striations measured on fault planes. **M:** Methana. **MI:** Milos. **S:** Santorini. **K:** Kos. **N:** Nisyros. **Dashed line:** Hellenic trench.

Fig.7.6a and b: Main directions of extension and stress trajectories in the S.Aegean sea. **a:** Pliocene **b:** Pleistocene. The areas of investigation are denoted as in fig.7.5. **Dotted lines:** trajectories of intermediate principal stress σ_2. **Dashed lines:** trajectories of minimum principal stress σ_3. **Dashed and dotted lines:** areas of stress pattern uncertainty and poorly defined fault motion.

7.3.3.4 Extensional tectonics and magma chambers

When the brittle crust is subjected to extensional stress, open cracks can exist at upper crustal levels, and if these are filled with saline fluids, the resultant conductivity is high and anisotropic. The other likely consequence of extensional stress is the penetration of melt to high levels in the crust resulting in volcanic activity.

The "stretching" of the lithosphere has certainly caused horizontal deformation of the shallow crust and is possibly responsible for the thinning of crust in the central S.Aegean (section 7.3.1). Mackenzie (1978) proposed that a possible thermal anomaly beneath the Aegean might be attributed partly to the extension, which causes the lower half of the lithosphere to be replaced by mantle at the same temperature as the asthenosphere.

The fact that the crust-mantle boundary beneath Methana (~45 km) is relatively deep might contribute to the difficulty in detecting a probable deep and small magma chamber. Also, as Tsapanos et al. (1994) mentioned, any subsequent horizontal deformation of the shallow crust, i.e caused by extension, would separate the surficial magma-related manifestations from the deeper seated magma chambers. Therefore, a magmatic intrusion occurring in the early Quaternary, could probably originate from a remote and deep source beneath the central S.Aegean, far away from the areas of investigation, causing magma to ascend through major fault zones, to form the well known volcanic centres along the HVA.

7.4 Summary and conclusions

13 MT and MV soundings (9 with the "remote electric site" technique), have been carried out in the Methana peninsula and Trizina area, positioned approximately along a N-S profile. At the majority of sites, the measurements were limited to the AMT period range (0.0085-23.3 s), except at two of them where the range was extended to include the LMT band (24-6140 s).

Impedance and transfer function estimates were calculated using robust methods and transformed into apparent resistivities and phases, and induction arrows, respectively. In order to examine the dimensionality and distortion of the data, further analysis was done (including dimensionality tests, decomposition methods and thin sheet analysis). Due to problems caused by inhomogeneous near-surface conductors, their influence was assessed in three ways: by decomposition of the impedance tensor, by analysis of the induction vectors and by thin sheet modelling of the shallow seas. It was decided that in their majority the data can be treated as 2-D, show weak distortion by 3-D effects up to 1 s and strong above 1 s, and are influenced by the sea in the 1-20 s band. A strike direction of 30^0E was chosen to represent the data for subsequent 2-D modelling.

The 2-D modelling has revealed a conductive anomaly (7-30 Ohm m) beneath the centre of Methana Peninsula at a depth of 1.5-5 km, which can be resolved by using the suggested strike angle of 30^0E. The presence of the conductive anomaly is supported by the induction arrows at periods around 0.1 s, while at longer periods the influence of the sea becomes more important.

It is proposed that the conductive anomaly beneath the centre of the peninsula corresponds to a small magmatic intrusion (connected with the volcanic history of Methana) and surrounded by highly fractured rocks, which favour the concentration of water, salts and fluids. This is consistent with the location of the former volcanic activity in Methana, whereas in Trizina graben a completely different geological environment exists (absense of volcanic activity and thermal springs), and resistivities at these depths are generally higher.

At great depths the inversion of the LMT data do not suggest the existence of a probable deep magma chamber beneath Methana, though the induction arrows at the longest periods point towards an undefined conductor to the South. Comparison between the results derived from Methana and from other MT and MV studies along the HVA has revealed the following:

1. Although under Methana Peninsula there is a limited area of high conductivity up to 5 km, when compared with the conductivity structure beneath the other areas (especially Milos), it does not seem to be of equal importance.

2. As in Milos, in Methana also no magma chambers could be located at depth. This was interpreted as due to limitations of the MT method, and (or) to a probable deep chamber far away from the areas of investigation.

3. Induction arrow directions for Methana are consistent with those calculated for a number of areas in the S.Aegean, indicating a deep conductor in a SSW-ENE direction, parallel to the front of the subducting Aegean microplate.

Similar deep conductors have been observed in island arc structures associated with subduction zones. For example, in the Ryukyu Trench-Arc system (Brown, 1994; Shimakawa et al., 1991), conductive zones beneath the island arc were interpreted by using dehydration and melting models for subduction zones (Wyllie, 1988). In the Juan De Fuca Subduction System, a thin conductor along the interface between the subducting Juan De Fuca plate and the overriding North American continent was presumed to represent partly pore water and residual sediments, as oceanic crust is carried down the subduction zone (Wannamaker et al., 1989). A similar interpretation was also given in the Vancouver Island case (Kurtz et al., 198 6).

As with the Juan De Fuca case, the resistivity manifestation of the deep HVA arc magmatism is not very strong, but consists of a sub-horizontal conductor in the middle crust below and to the West of the surficial arc which presumably represents fluids released from crystallising magmas. An imbalance between the amount of water contained in altered oceanic crust and the much lesser amount released during arc magmatism has been reported by Ito et al. (1983). A possible explanation is that most of the water carried in the altered oceanic crust is liberated well before the volcanic arc is reached (Wannamaker et al., 1989). Given the history of the volcanic activity in the western part of the HVA, the deep undefined conductor could result from hydrothermal fluids exsolved during repeated intrusion and crystallisation rather than from the presence of silicate melt in large volumes.

Finally, as a part of the attempt for an integrated model of the S.Aegean which could incorporate the MT and MV results from Methana, the regional stress field associated with the extensional regime in the S.Aegean was also presented, and impedance strike directions calculated from the MT surveys along the HVA were compared with stress patterns deduced from focal mechanisms of earthquakes and fault measurements. It is deduced that in Methana, the strike direction of 30^0E is consistent with the recent phase of the extensional process in the S.Aegean. As

implications of the extension on the location of deep magma chambers were discussed, it wass proposed that the horizontal extension has caused separation of the volcanic centres from the deeper sources responsible for the feeding of the more surficial reservoirs.

7.5 Suggestions for further work

Suggestions for further work concern mainly 3 domains: further field measurements, further modelling studies, and comparison with other geophysical methods:

a. Field measurements: **(i)** More sites around the centre of Methana would help to estimate better the horizontal extension of the conductive anomaly detected in the depth range of 1.5-6 km beneath sites 131, 133 and 130. Also, more LMT data would give more precise information about its vertical extension. In that way, a more accurate decision could be taken about the geothermal potential of the area. **(ii)** More data in the period range of 1-10 s and 24-100 s would give more reliable resistivity and phase estimates, especially in the TE mode. **(iii)** The MT profile had a low site density in the Trizina graben, whereas a number of sites (including an LMT station) in the proximity of site 129 could investigate the area of relatively low resistivities at depths around 10 km and the possible implications it might have on the deep structure. **(iv)** Investigation of the volcanic island of Aegina, located to the N of Methana, which might be associated with the magma intrusion suggested in this work.

b. 3-D Modelling: As the data have shown an increasing tendency for 3-D effects to distort the inductive response at depth, 3-D modelling would be ideal for the data at periods above 10 s. In this way, possible narrow conductive zones existing at great depths might be resolved.

c. Other geophysical methods: DC resistivity soundings and SP measurements gave an indication of the resistivity distribution in the upper 200-250 m, which was interpreted as associated with surficial effects (thermal springs, sea water). The MT method was the only one which attempted to show changes in resistivity at greater depths (> 1 km). Methods which are able to detect deep structures should be applied, as for example seismic refraction methods or the recording of microseismic activity, which can indicate zones in which fluids are concentrated. Such combinations have been carried out in Milos and Kos, where several seismic events (with hypocentric depths up to 10 km) were recorded, and linked to low resistivity zones indicated by the MT data.

References

Angelier, J., 1979. Neotectonique de l' arc egeen. These d' etat, Univ. Paris 6 Mem. Soc. Geol. du Nord, Lille, France, 3, 418 pp.

Angelier, J., Lyberis, N., Le Pichon, X., Barrier, E. and Huchon, P., 1982. The tectonic development of the Hellenic Arc and the sea of Crete: A synthesis. Tectonophysics, **86**: 159-196.

Archie, 1942. The electrical resistivity log as an aid in determining some reservoir characteristics. A.I.M.E. Trans., **146**: 54-61.

Bahr, K., 1988. Interpretation of the magnetotelluric impedance tensor: regional induction and local telluric distortion. J. Geophys. **62**: 119-127.

Bahr, K., 1991. Geological noise in magnetotelluric data: a classification of distortion types. Phys. Earth Planet. Inter. **66**: 24-38.

Bailey, R. C., 1994. Fluid trapping in mid-crustal reservoirs by H_2O-CO_2 mixtures. *Nature*, **371**: 238-240.

Banks, R. J., 1975. Complex demodulation of Geomagnetic Data and the Estimation of Transfer Functions. Geophys. J. R. astr. Soc. **43**: 87-101.

Bauce, A., Fabriol, H., Le Masne, D. and Decriaud, J.P., 1989. Test of an integrated methodology for high enthalpy exploration of the island of Milos (Greece). Geothermics **18**: 547-563.

Benderitter, Y. and Gerard, A., 1984. Geothermal study of Reunion Island: Audiomagnetotelluric survey. J. Volc. Geoth. Research **20**: 311-332.

Berckhemer, H., 1977. Some aspects of the evolution of marginal seas deduced from observations in the Aegean region. Structural history of the Mediterranean basins, edited by B. Biju-Duval, L. Montadert, Editions Technip, Paris, 303-314.

Berdichevsky, M. N., Bezruk, I. A. and Chinavera, O. M., 1973. Magnetotelluric soundings with the use of Mathematical filters (in Russian), Izv. Akad, Nauk SSSR Flz. Zeml. **3**: 72-92.

Berdichevsky, M. N. and Dmitriev, V. I., 1976. Basic Principles of Interpretation of Magnetotelluric Sounding Curves. Geoelectric and Geothermal Studies, edited by Adams, A., Budapest, Akademai Kiado, 165-221.

Berktold, A., Kemmerie, K. and Neurieder, P., 1980. Magnetotelluric measurements and geomagnetic depth sounding in the area of the Urach geothermal anomaly. Advances in European Geothermal Research, pp 911-920.

Berktold, A., 1983. Electromagnetic studies in geothermal regions. Geophys. Surveys **6**: 173-200.

Bostick, F.X. and Smith, H.W., 1962. Investigations of large scale inhomogeneities in earth by the magnetotelluric method. Proc. Inst. Radio Engineers, **50**: 2339-2346.

Bostick, F.X., 1977. A simple almost exact method of MT analysis. Workshop on Electrical Methods in Geothermal Exploration, U.S. Geol. Survey, Contact No. 14080001-8-359.

Brigham, E.O., 1974. The Fast Fourier Transform. Prentice-Hall, Englewood Cliffs, NJ, 252 pp.

Brown, C., 1993. Tectonic interpretation of regional conductivity anomalies. Surv. Geophys., **15**: 123-157.

Cagniard, L., 1953. Basic theory of the magnetotelluric method of geophysical prospecting, Geophysics, **18**: 605-635.

Cantwell, T., 1960. Detection and analysis of low frequency magnetotelluric signals, Ph.D. thesis, M.I.T., Cambridge, Mass.

Celati, R., Muse, L., Rossi, A., Squarci, P., Taffi, L. and Toro, B., 1973. Geothermal prospecting with the magnetotelluric method in the Travale area. Geothermica, **2**: 186-190.

Cevallos, C., 1986. Magnetotelluric interpretation- another approach. Ph.D. Thesis, Macquarie University, Sydney.

Chave, A. D., and Thomson, D.J. and Ander, M.E., 1987. On the robust estimation of power spectra, coherancies and transfer functions. J. Geophys. Research **92**: 633-648.

Chave, A. D. and Thomson, D.J., 1989. Some comments on magnetotelluric response function estimation. J. Geophys. Research **94**: 14,215-14,225.

Constable, S. C., Parker, R. L. and Constable, C. G., 1987. Occam's inversion: A practical algorithm for generating smooth models from EM sounding data. Geophysics, **92**: 289-300.

Cooley, J.W. and Tukey, J.W, 1965. "An algorithm for Machine Calculation of Complex Fourier Series", Math Computation, **19**: 297-301.

Cooley, J.W., Garwin, R.L., Rader, E.M., Borget, B.P. and Stockham, T.C., 1969. The 1968 Arden House workshop on fast Fourier transform processing. IEEE Trans. Audio Electroacoust., AU-17, 24 pp.

Dawes, G.J.K., 1984. Short Period Automatic Magnetotelluric (S.P.A.M.) system in a broadband tensorial magnetotelluric study in the Travale-Radiocondoli geothermal field. (Hutton et al.). EEC Final Report, Contract No. EG-A2-031-UK.

Dawes, G.J.K. and Lagios, E., 1991. A magnetotelluric survey of the Nisyros geothermal field (Greece). Geothermics, **20**: 225-235.

Dawson, T.W. and Weaver, J.T., 1979. Three-dimensional electromagnetic induction in a non-uniform thin sheet at the surface of a uniformly conductive earth, Geophys. J. R. astr. Soc. **59**: 445-462.

deGroot-Hedlin, C. and Constable, S., 1990.Occam's inversion to generate smooth, two-dimensional models from magnetotelluric data. Geophysics, **55**: 1613-1624.

Di Paola, G. M., 1974. Volcanology and petrology of Nisyros Island (Dodecanese, Greece). Bull. Volc. **38**: 944-987.

Drakopoulos, J. and Delibassis, N., 1982. The focal mechanisms of earthquakes in the major area of Greece for the period 1947-1981. Seismol. Lab. Univ. Athens Publ., **2**: 1-72.

Duba, A., 1976. Are laboratory conductivity data relevant to the earth?, Acta Geodet. Geophys. et Mont., **11**: 485-495.

Egbert , G.D. and Booker, J.R., 1986. Robust estiation of geomagnetic transfer functions, Geophys. J.R. astr.Soc. **87**: 173-194.

Eggers, D. W., 1982. An eigenstate formulation of the magnetotelluric impedance tensor. Geophysics **47**: 1204-1214.

Facca, G. and Tonani, F., 1962. Natural Steam Exploration in U.S.A. Bolletino di Geofisica Teorica ed Applicata, vol. IV, n. 14.

Fischer, G., Schnegg, P. A., Peguiron, M. and Le Quang, B. V., 1981. An analytical one dimensional magnetotelluric inversion scheme. Geophys. J.R. astr.Soc. **67**: 257-278.

Fischer, G. and Le Quang, B. V., 1981. Topography and minimization of the standard deviation in one-dimensional magnetotelluric modelling. Geophys. J.R. astr.Soc. **67**: 279-292.

Fischer, G., 1985. Some remarks on the behaviour of the magnetotelluric phase. Geophys. Prospecting, **33**: 716-722.

Fischer, G., Szarka, L., Adam, A. and Weaver, J.T., 1992. The magnetotelluric phase over 2-D structures. Geophys. J. Int., **108**: 778-786.

Fytikas, M., Giuliani, O., Innocenti, F., Marinelli, G. and Mazzuoli, R., 1976. Geochronological data on recent magmatism of the Aegean Sea. Tectonophysics **31**: 29-34.

Fytikas, M. and Kolios, N.P., 1979. Preliminary heat flow map of Greece, in Terrestrial Heat Flow in Europe, pp. 197-205, eds Cermak, V. & Rybach, L., Springer-Verlag, Berlin.

Fytikas, M., 1980. Geothermal exploration in Greece.

Fytikas, M., Innocenti, F., Manetti, P., Mazzuoli, R., Pecerillo, A. and Villari, L., 1984. Tertiary to Quaternary evolution of volcanism in the Aegean region. Geol. Soc. London, Sp. Publ. **17**: 687-699.

Fytikas, M., 1989. Updating of the geological and geothermal research on Milos island. Geothermics, **18**: 485-496.

Galanopoulos, D, 1989. Magnetotelluric studies in geothermal areas of Greece and Kenya. Ph.D. Thesis, University of Edinburgh.

Galanopoulos, D, 1993. Preliminary magnetotelluric studies along the Hellenic Volcanic Arc: implications for the collision between the African plate and the "Aegea" microplate. Phys. Earth Planet. Inter., **81**: 139-153.

Galanopoulos, D., Hutton, V.R.S and Dawes, G.J.K., 1991. The Milos geothermal field: modelling and interpretation of electromagnetic induction studies. Phys. Earth Planet. Inter., **66**: 76-91.

Georgoulis, I., 1983. Hydrogeological research assessing the geothermal interest of Poros-Methana and Loutraki-Sousaki areas. IGME. Final report (in Greek).

Glover, W. J. and Vine, F. J., 1994. Beyond KTB- Electrical conductivity of the deep continental crust. Surv. Geophys., **16**: 5-36.

Goodall, C., 1983. Examining residuals, in *Understanding Robust and Exploratory Data Analysis*, cds. Hoaglin, D.C., Mosteller, F. & Tukey, J.W., Wiley, New York.

Groom, R.W. and Bailey R..C., 1989. Decomposition of the magnetotelluric impedance tensor in the presence of local three-dimensional ganvanic distortion. J. Geophys. Res,. **94**: 1913-1925.

Haak, V.and Schwarz, G., 1980. Distribution of electrical conductivity in crust and upper mantle in the area of the geothermal anomaly of Tuscany, Italy. Advances in European Geothermal Research, 843-853.

Haak, V., Ritter, O. and Ritter, P., 1989. Mapping the geothermal anomaly on the island of Milos by magnetotellurics. Geothermics, **18**: 533-546.

Hermance, J.F. and Grillot, L.R., 1974. Constraints on temperatures beneath Iceland from magnetotelluric data. Phys. Earth Planet. Inter. **8**: 1-12.

Harris, N., 1989. Carbon dioxide in the deep crust. *Nature*, **340**: 347.

Hersir, G.P., Bjornsson, A. and Pedersen, L.B., 1984. Magnetotelluric survey across the active spreading zone on southwest Iceland. J. Volc. and Geoth. Research, **20**: 253-265.

Honkura, Y., 1974. Electrical conductivity anomalies beneath the Japan arc, J. Geomagn. Geoelec., **26**: 147-171.

Horvarth, F. and Berckhemer, H., 1982. Mediterranean backarc basins. In: H. Berckhemer and K. Hsu (Editors), Alpine-Mediterranean Geodynamics. Geodynamic Series, Vol.**7**. American Geophysical Union, Washington, DC, pp.141-173.

Huber, P. J., 1981. Robust Statistics, Wiley, New York.

Hyndman, R.D. and Shearer, P.M., 1989. Water in the lower continental crust: Modelling magnetotelluric and seismic reflection results. Geophys. J. Int. **98**: 343-365.

Hutton, V.R.S., Galanopoulos, D., Dawes, G.J.K. and Pickup, G.E., 1989. A high resolution magnetotelluric survey of the Milos geothermal project. Geothermics, **18**, No. 4, pp. 521-532.

Institute of Geological and Mineralogical Exploration (IGME) of Athens, Greece. Geological mapping of Methana Peninsula: Fytikas, M., Innocenti, F., Mazzuoli, R., 1972. Geological mapping of Trizina area: Suesskoch, H., Bannert, D., Kalkreuth, W., Walliner, P., Strauss, M., 1963-66 and 1972-74.

IGME, 1984. Methana, Poros, Loutraki, Sousaki, Platystomon, Aedipsos. Geophysical projects. Final report. Geothermica Italiana Sr2.

IGME, 1982. Geochemical investigation in Methana-Poros area. (unpublished).

IGME, 1982. Poros-Trizina area: Geoelectric direct current soundings (unpublished).

Jackobs, J.A., 1989. Geomagnetism. Vol. 3.

Jiracek, G.R., 1990. Near-surface and topographic distortions in electromagnetic induction. Surveys in Geophysics, **10**: 1-41.

Jones, A.G., 1977. Geomagnetic induction studies in Southern Scotland. Ph.D. Thesis, University of Edinburgh.

Jones, A.G., 1983a. The problem of current channelling: a critical review. Geophys. Survey, **6**: 79-133.

Jones, A.G., 1983b. On the equivalence of the Niblett and Bostick transformations in the magnetotelluric method. J. Geophys. **53**: 72-73.

Jones, P.C., 1992. An Electromagnetic Induction Study of South Cornwall, England. Ph.D. Thesis.

Jones, P.C. and Price, A. T., 1970. The perturbations of alternating geomagnetic fields by conductivity anomalies. Geophys. J. R. astron. Soc. **20**: 317-334.

Jongsma, D., 1974. Heat flow in the Aegean Sea. Geophys. J. R. astron. Soc. **37**: 337.

Jupp, D. L. B. and Vozoff, K., 1975. Stable iterative methods for the inversion of geophysical data. Geophys. J. R. astron. Soc. **42**: 957-976.

Kaufmann, A. A., 1985. Tutorial: distribution of alternating electrical charges in a conducting medium. Geophys. Prosp. **33**: 171-184.

Keller, G.V. and Frischknecht, F.C., 1966. Electrical methods in geophysical prospecting. Pergamon Press, New York.

Keller, G.V., 1971. Electrical studies of the crust and upper mantle. A.G.U. Monogr., **14**: 107-126.

Keller, J., 1982. Mediterranean island arcs. In "andesites" R.S. Thorpe Edt, 307-325, John Wiley e Sons.

Khitarov, N.I., Slutsky, A. B. and Pugin, V. A., 1970. Electrical conductivity of basalts at high T-P and phase transitions under upper mantle conditions. Phys. Earth Planet. Int., **3**: 334-342.

Kleiner, B., Martin, R.D. and Thomson, D.J., 1979. Robust estimation of power spectra. J. R. Statist. Soc. B, **41**, No 3, pp. 313-351.

Krylov, S. M., 1971. Application of electromagnetic resonance in the Earth-ionosphere cavity to magnetotelluric soundings (in Russian). In: Natural Electromagnetic Field and Investigation of the Earth's Interiors. Moscow: Nauka, pp.85-96.

Lagios, E., 1992a. Geophysical investigations in the evaluation of tectonic and geothermal regime of Kos island, Final report, submitted to the Ministry of Industry, Science and Research of Greece, Geophysics-Geothermy division, University of Athens.

Lagios, E.., Tzanis, A., Delibasis, N., Drakopoulos, J. and Dawes, G.K.J., 1994. Geothermal exploration of Kos Island, Greece: Magnetotelluric and Microseismicity studies. Geothermics, **23**: 267-281.

Larsen, J.C., 1975. Low frequency electromagnetic study of deep mantle electrical conductivity beneath the Hawaiian islands. Geophys. J. R. astr. Soc., **43**: 17-46.

La Torraca, G. A., Madden, T. R. and Korringa J., 1986. An analysis of the magnetotelluric impedance tensor for three-dimensional structures. Geophysics, **51**: 1819-1829.

Le Pichon, X. and Angelier, J., 1979. The Hellenic arc and trench syctem: a key to the Neotectonic evolution of Eastern Mediterranean. Tectonophysics, **60**: 1-42.

Livelybrooks, D., Banks, R.J., Parr, R.S. and Hutton, V.R.S., 1993. Inversion of electromagnetic induction data for the Iapetus Suture Zone in the U.K. Phys. Earth Planet. Inter. **81**: 67-84.

Long, C. L. and Kaufmann, H. E., 1980. Reconnaissance geophysics of a known geothermal resource area, Weiser, Idaho and Vale, Oregon. Geophysics, **45**: 312-322.

Lorrain, P. and Corson, D., 1970. Electromagnetic fields and waves. 2nd ed. W. H. Freeman & Co., San Fransisco.

Mackenzie, D., 1970. Plate tectonics of the Mediterranean region. Nature, **226**: 239-243.

Mackenzie, D., 1972. Active tectonics of the Mediterranean region. Geophys. J. R. astr. Soc., **30**: 109-185.

Mackenzie, D., 1978. Active tectonics of Alpine-Himalayan belt: the Aegean Sea and surrounding regions. Geophys. J. R. astr. Soc., **55**: 217-254.

McKirdy, D. McA., Weaver, J. T. and Dawson, T. W., 1985. Induction in a thin sheet of variable conductance at the surface of a stratified earth. Geophys. J. R. astr. Soc., **80**: 177-194.

Madden, T.R. and Swift, C.M., 1969. Magnetotelluric studies of electrical conductivity structure of the crust and upper mantle. In: The Earth 's crust and upper mantle (ed. P.J. Hart). Geophys. Monogr. A.G.V., 469-479.

Makris, J., 1977. Geophysical investigations of the Hellenides, Hamburger Geophys. Einzelchriften, **34**, Wittenborn, Hamburg, 124 pp.

Makris, J., 1978b. The crust and upper mantle of the Aegean region from deep seismic soundings, Tectonophysics, **46**: 269-284.

Makropoulos, K. C. and Burton, P. W., 1984. Greek tectonics and seismicity. Tectonophysics **106**: 175-304.

Meissner, R. and Wever, Th., 1992. The possible role of fluids for the structuring of the continental crust. Earth Sci. Rev. **32**: 19-32.

Menke, W., 1984. Geophysical data analysis. Discrete inverse theory (Florida: Academic press).

Mercier, J. L., Delibassis, N., Gauthier, A., Jarrige, J.J., Lemeille, F., Philip, H., Sebrier, M. and Sorel, D., 1979. La neotectonique de l' arc egeen. Rev. Geol. Dyn. Geogr. Phys., **21** (1): 67-92.

Mercier, J. L., Sorel, D. and Simeakis, K., 1987. Changes in the state of stress in the overriding plate of a subduction zone: the Aegean Arc from the Pliocene to the Present. Annales Tectonicae, Vol.1, n. **1**: 20-39.

Mufler, L.J.P., 1976. Tectonic and hydrologic control of the nature and distribution of geothermal resources. In Proc. Sec. U.N. Symp. on the Dev. and Use of geotherm. Resources, San Fransisco, p.499-507.

Nesbitt, B., 1993. Electrical resistivities of crustal fluids. J. Geoph. Research **98**: 4301-4310.

Nicholls, I. A., 1971. Petrology of Santorini volcano. Cyclades, Greece. J. Petrol. **12**: 67-119.

Oldenburg, D. W., 1979. One-dimensional inversion of natural source magnetotelluric observations. Geophysics **44**: 1218-1244.

Orlicky, O., 1984. Paleomagnetism of selected Plio-Quaternary volcanic rocks of Methana peninsula and small volcanic centres in NW Aegean Arc in Greece. Sbor. geol. ved. Uzita geof. **20**: 83-102.

Papanikolaou, D., 1984. Tectonic evolution of the Hellenides. 27th Intern. Geological Congress, Moscow, Abstracts III, 351-352.

Papazachos, B. C. and Komninakis, P.E., 1971. Geophysical and tectonic features of the Aegean Arc. J. Geoph. Research **76**: 8517-8533.

Paquin, C., Froidevaux, C., Bloyet J., Ricard Y. and Angelidis, C., 1982. Tectonic stress on the mainland of Greece: In-situ measurements by overcoring. Tectonophysics, **86**: 17-27.

Paquin, C., Froidevaux, C., Bloyet J., Ricard Y. and Angelidis, C., 1984. Tectonic stress on the boundary of the Aegean domain: In-situ measurements by overcoring. Tectonophysics, **110**: 145-150.

Park, S., 1988. A systematic approach to the interpretation of magnetotelluric data in volcanic environments with applications to the quest for magma in Long Valley, California. J. Geoph. Research **93**: 13,265-13,283.

Parker, R. L., 1983. The magnetotelluric inverse problem. Geophys. Surv. **6**: 5-25.

Parkinson, W. D., 1962. The influence of continents and oceans on geomagnetic variations. Geophys. J. R. astr. Soc., **6**: 441-449.

Parr, R. S., 1991. Development of MT processing and modelling procedures - Application to Northern England. Ph.D. Thesis.

Pe, G. G., 1974. Volcanic rocks of Methana (South Aegean Arc, Greece). Bull. Volc. **38**: 270-290.

Pentarakis, L., Pippos, H., Fytikas and M., Karayiannis, P., 1990. Assesment, development and.. of the geothermal fieds in Greece. Submitted to the Ministry of Industry, Energy and Technology. IGME (in Greek).

Petiau, G. and Dupis, A., 1980. Noise, temperature coefficient, and long time stability of electrodes for telluric observations. Geophys. Prospecting, **28**: 792-804.

Price, A.T., 1949. The induction of electric currents in non-uniform thin sheets and shells. Q. J. Mech. Appl. Math. **2**, 385-410.

Price, A.T., 1962. The theory of magnetotelluric method when the source field is considered. J. Geophys. Res. **67**: 1907-1918.

Richards, M.L., Schmucker, U. and Steveling, E., 1980. Magnetovariational and magnetotelluric soundings in Reingraben and Schwarzwald. Advances in European Geothermal Research, pp. 893-903.

Rikitake, T., 1950. Bull. Earthq. Res. Int., Tokyo University, **28**: 45-219.

Ringwood, A.E., 1975. Composition and Petrology of the Earth's Mantle. McGraw Hill, N.Y., 618 p.

Ritsema, A.R., 1973. Proceedings of the seminar of the seismotectonic map of the Balkan region, Skopje 1974.

Roedder, E., 1984. Fluid inclusions. Rev. Mineral.**12**: 644.

Rokityansky, I. I., 1961. On the application of the magnetotelluric method to anisotropic and inhomogeneous masses. Bull. (Izv.) Acad. Sci. USSR, Geophys. Series, **11**: 1607-1613.

Rokityansky, I. I., 1982. Geoelectromagnetic Investigation of the Earth's Crust and Mantle.

Scholl, D.W., Marlow, M. S. and Cooper, A. K., 1977. Sediment subduction and offscraping at Pacific margins, in: Island Arcs, Deep Sea Trenches and Back-Arc Basins, M. Talwani and W.C. Pitman III, eds., Maurice Ewing Ser. **1**: 199-210.

Shankland, T.J., 1975. Electrical conduction in rocks and minerals: parameters for interpretation. Phys. Earth Planet. Int. **10**: 209-219.

Shimakawa, Y. and Honkura, Y., 1991. Electrical conductivity structure beneath the Ryukyu Trench-Arc system and its relation to the subduction of the Phillipines Sea Plate, J. Geomagn. Geoelectr. **43**: 1-20.

Sims, W. E., Bostick, F. X. and Smith, R. W., 1971. The estimation of magnetotelluric impedance tensor elements from measured data. Geophysics **36**: 938-942.

Smith, J.T. and Booker, J.R., 1988. Magnetotelluric inversion for minimum structure. Geophysics **53**: 1565-1576.

Smith, J.T. and Booker, J.R., 1991. Rapid inversion of two- and three-dimensional magnetotelluric data. J. Geophys. Res. **96**: 3905-3922.

Schmucker, U., 1970. Anomalies in geomagnetic variations in the southwestern U.S.A. Bull. Scripps Inst. Oceanogr., **13**, 23.

Swift, C.M. Jr., 1967. A magnetotelluric investigation of an electrical conductivity anomaly in the south western U.S. PhD thesis, M.I.T., 211.

Telford, W. M., Geldart, L. P., Sheriff, R.E. and Keys, D. A., 1981. Applied Geophysics. Cambridge University Press, Cambridge, U.K.

Thanasoulas, K. and Ksanthopoulos, N., 1991. A geophysical survey in Methana Peninsula- implication on the thermal springs (in Greek). Final report, Institute of Geological and Mineral Exploration (I.G.M.E.), Greece.

Tikhonov, A.V., 1950. Determination of the electrical characteristics of the deep strata of the earth 's crust. Dokl. Akad. Nauk. **73**: 295-297.

Tsapanos, T.M., Galanopoulos D. and Burton, P.W, 1994. Seismicity in the Hellenic Volcanic Arc: relation between seismic parameters and the geophysical fields in the region. Geophys. J. Int. **117**: 677-694.

Valiant, M. J., 1976. N.E.R.C. (Natural Enviromental Research Council) geologger technical handbook, IGS magnetic observatory, Hartland.

Vozoff, K., 1972. The magnetotelluric method in the exploration of sedimentary basins. Geophysics **37**: 98-141.

Vozoff, K., 1990. Magnetotellurics: Principles and practice. Proc. Indian Acad. Sci. (Earth Planet. Sci.), **99**, No. 4, 441-471.

Wannamaker, P.E., Booker, J.R., Filloux, J.H., Jones, A.G., Jiracek, G.R., Chave, A.D., Tarits, P., Waff, H.S., Egbert, G.D., Young, C.T., Stodt, J.A., Mario Martinez, G., Law, L.K., Yukutake, T., Segawa, J.S., White, A. and Green, A.W.Jr., 1989. Resistivity cross-section across the Juan de Fuca Subduction Zone in the EMSLAB Project. JGR **94**: 14,111-14,125.

Wannamaker, P.E., Wright, P. M., Zhou Zi-xing, Li Xing-bin and Zhao Jing-xiang, 1991. Magnetotelluric transect of Long Valley caldera: Resistivity cross-section, structural implications, and the limits of a 2-D analysis. Geophysics **56**: 926-940.

Wait, J.R., 1962. Electromagnetic waves in stratified media. Oxford, Pergamon press.

Watson, E. B. and Brennan, J. M., 1987. Fluids in the lithosphere, 1. Experimentally-determined wetting characteristics of H_2O-CO_2 fluids and their implications for fluid transport, host rock physical properties and fluid inclusion formation, Earth Planet Sci. Lett. **85**: 497-515.

Weaver, J.T., 1982. Regional induction in Scotland: an example of three-dimensional numerical modelling using the thin sheet approximation, Phys. Earth Planet. Int. **28**: 161-180.

Weaver, J., 1994. Mathematical methods for Geo-Electromagnetic Induction. Research Studies Press, Taunton, England.

Weidelt, P., 1972. The inverse problem of geomagnetic induction. J. Geophys. **38**: 257-289.

Wight, D.E. and Bostick, F.X., 1980. Cascade decimation- A technique for real time estimation of power spectra. Proceedings IEEE International Conference on Acoustic Speech and Signal Processing, Denver, CO. pp. 626-629.

Wyllie, P. J., 1988. Magma genesis, Plate Tectonics and Chemical differentiation of the Earth. Rev. Geophys. **26**: 370-404.

Yardley, B.W.D., 1986. Is there water in the deep continental crust? *Nature* **323**: 111.

Yannetakis, K., Karageorgiou, E., Mastoris, K., Kallergis, J. and Oikonomou, P., 1972. Consequences of the exploration of limestones in the SW part of Asprovouni (Methana), on the Methana thermal springs (in Greek). Final rapport, Inst. Geol. and Underground Exploration, Athens.

Appendix

In the following pages, figs.A.1-18 show the azimuths and skew values as calculated by the methods of Swift and Bahr for all the sites (except those shown in section 5.1.1).

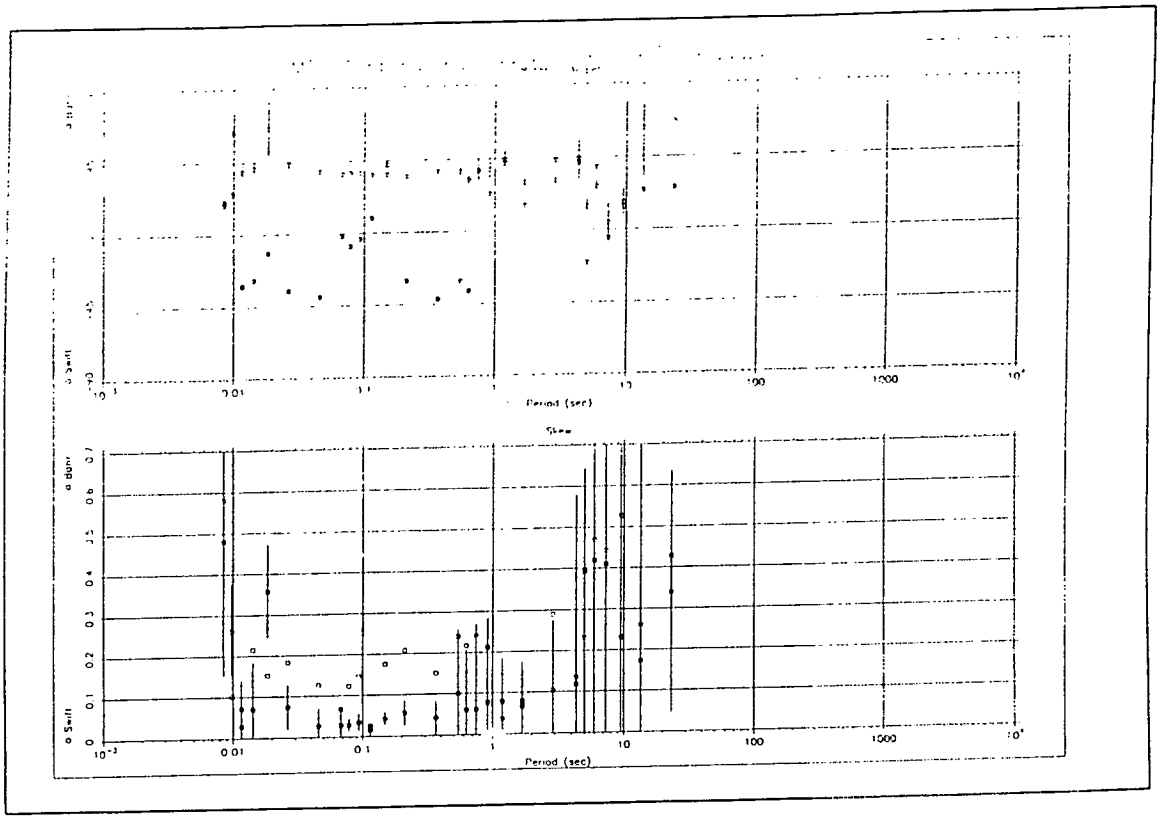
Period (sec)
Skew
Period (sec)

Fig.A.1

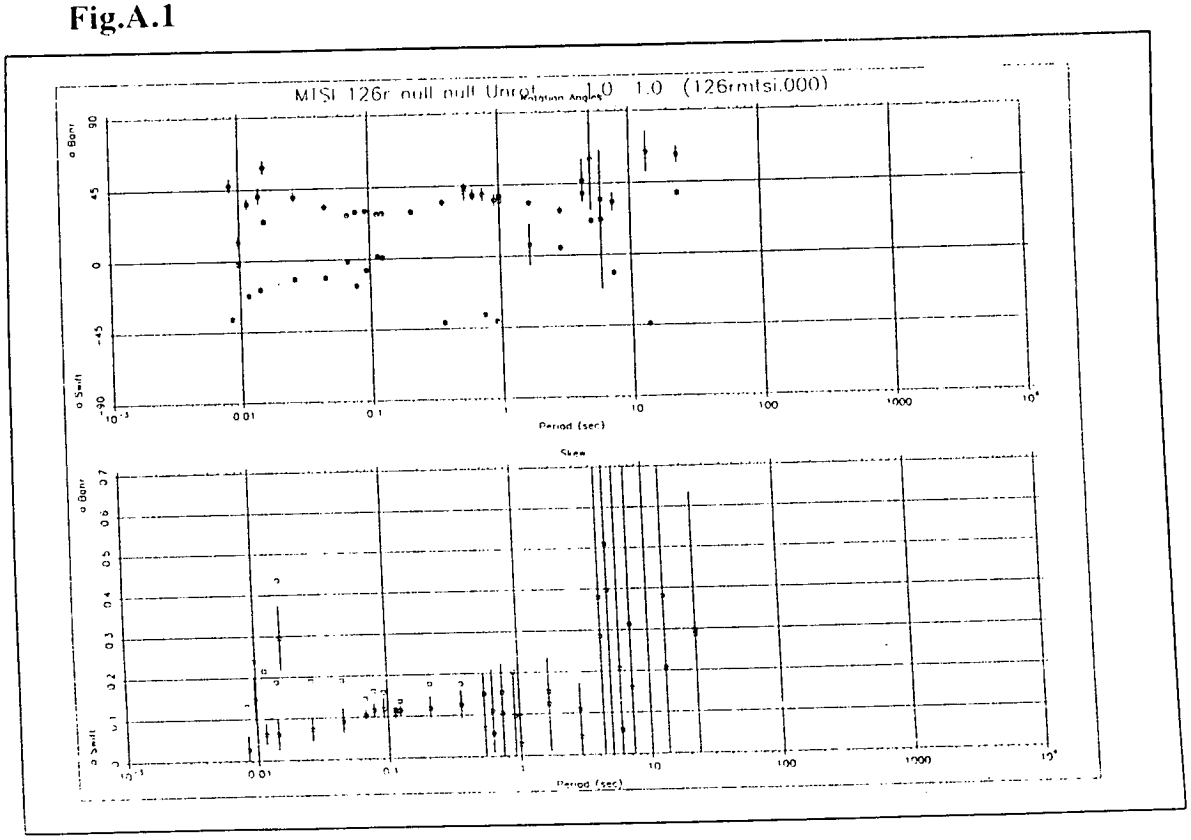
MTSI 126r null null Unrot 1.0 1.0 (126rmtsi.000)
Period (sec)
Skew
Period (sec)

Fig.A.2

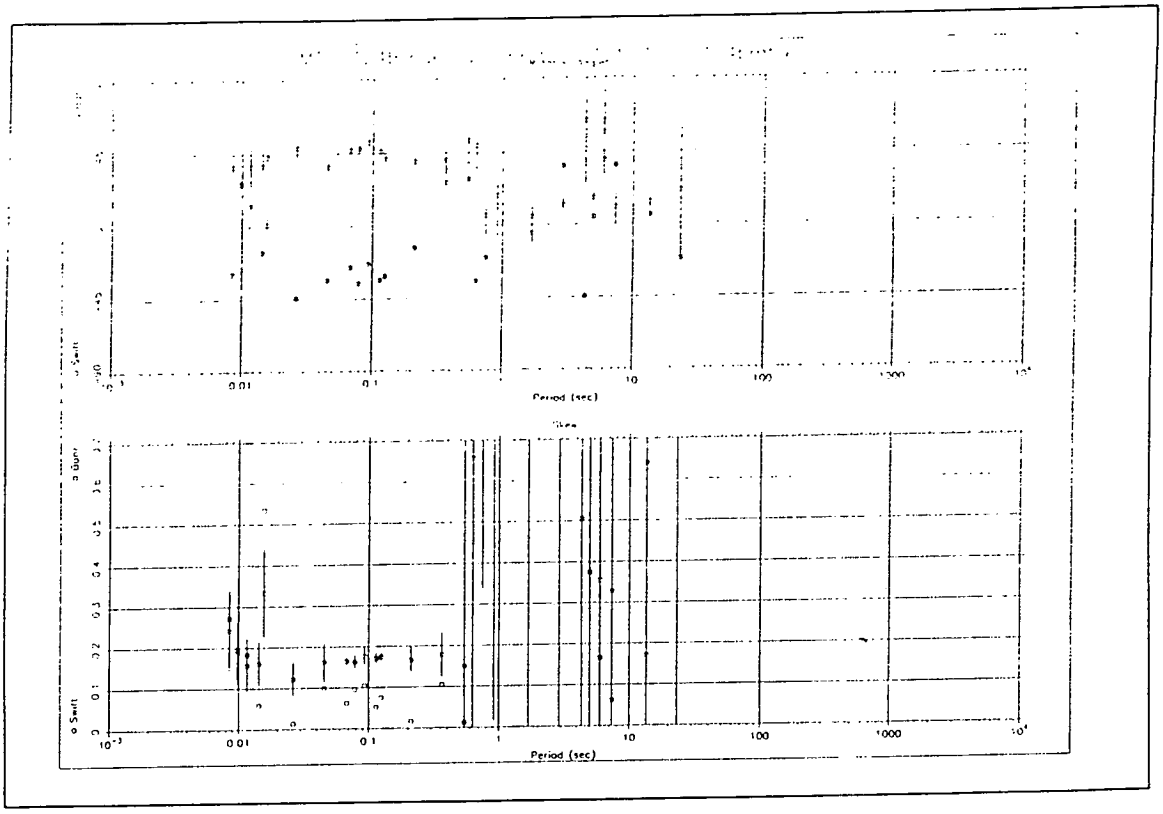
Period (sec)
Skew
Period (sec)

Fig.A.3

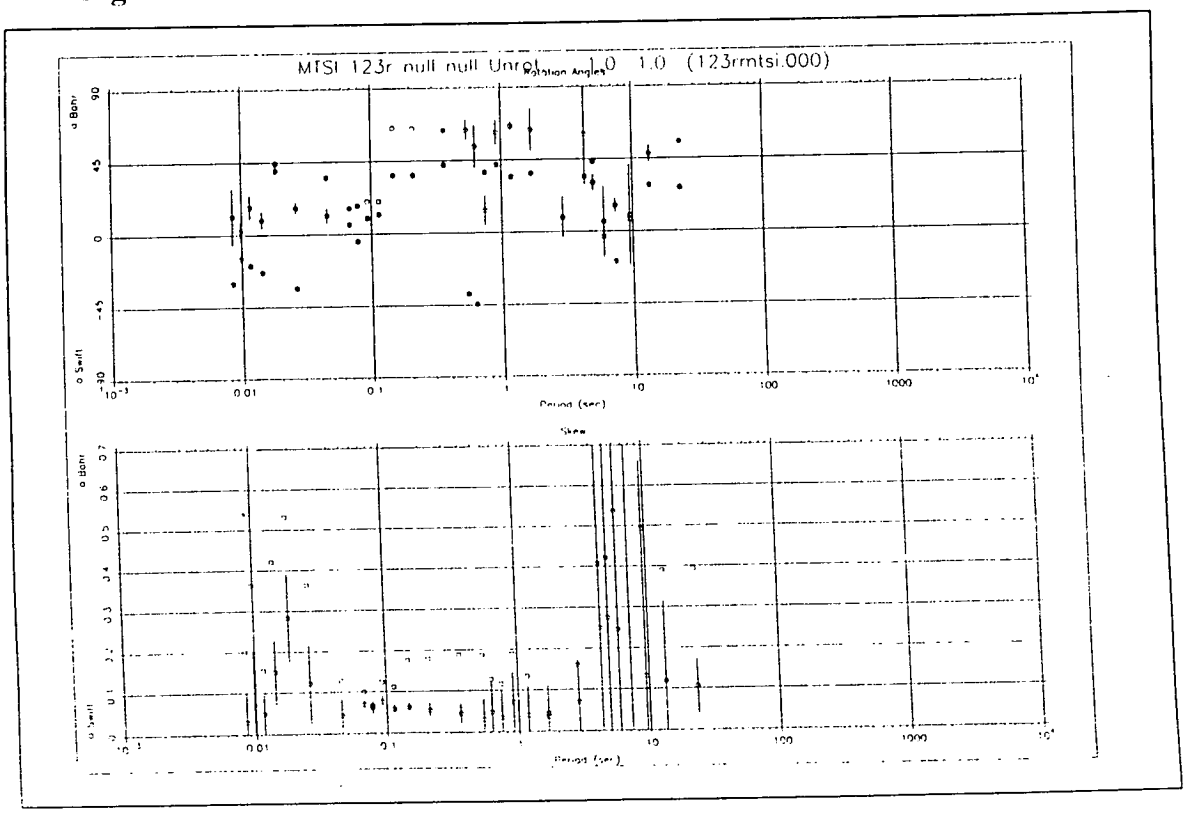
MTSI 123r null null Unrot 1.0 1.0 (123rmtsi.000)
Rotation Angles
Period (sec)
Skew

Fig.A.4

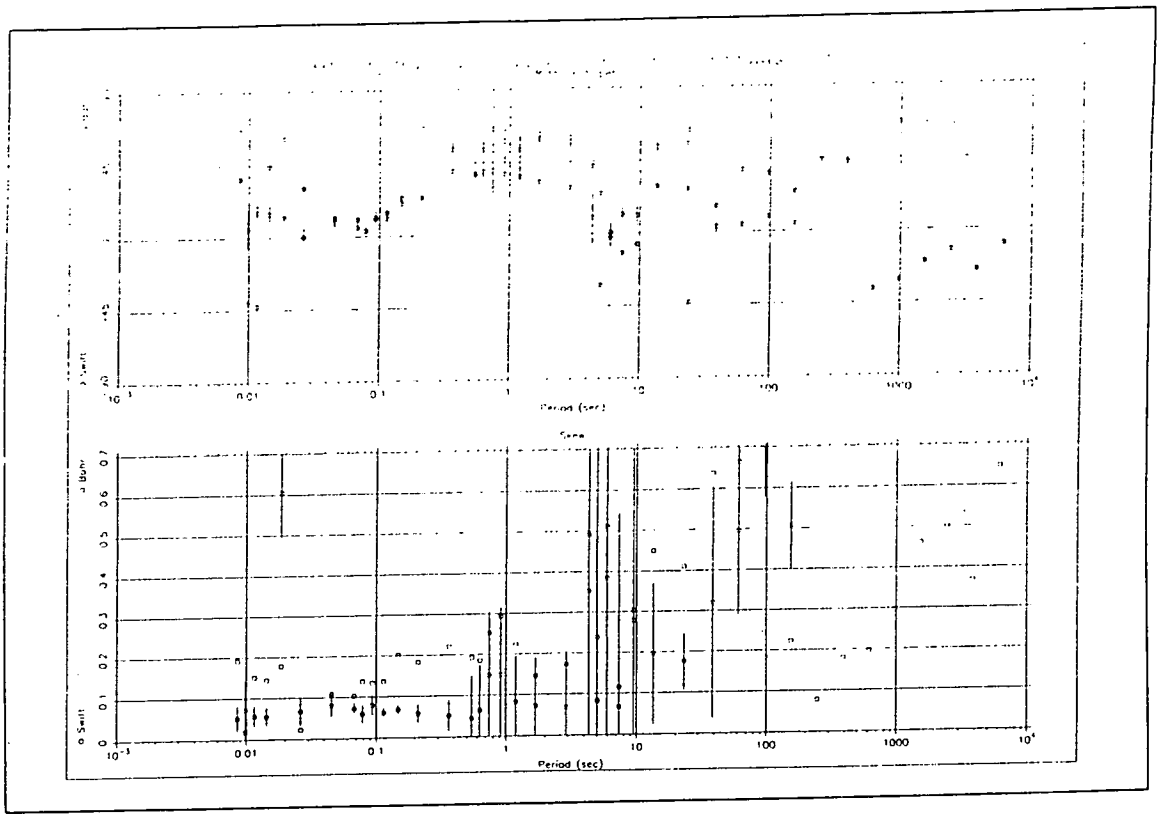
Period (sec)
Skew
Period (sec)

Fig.A.5

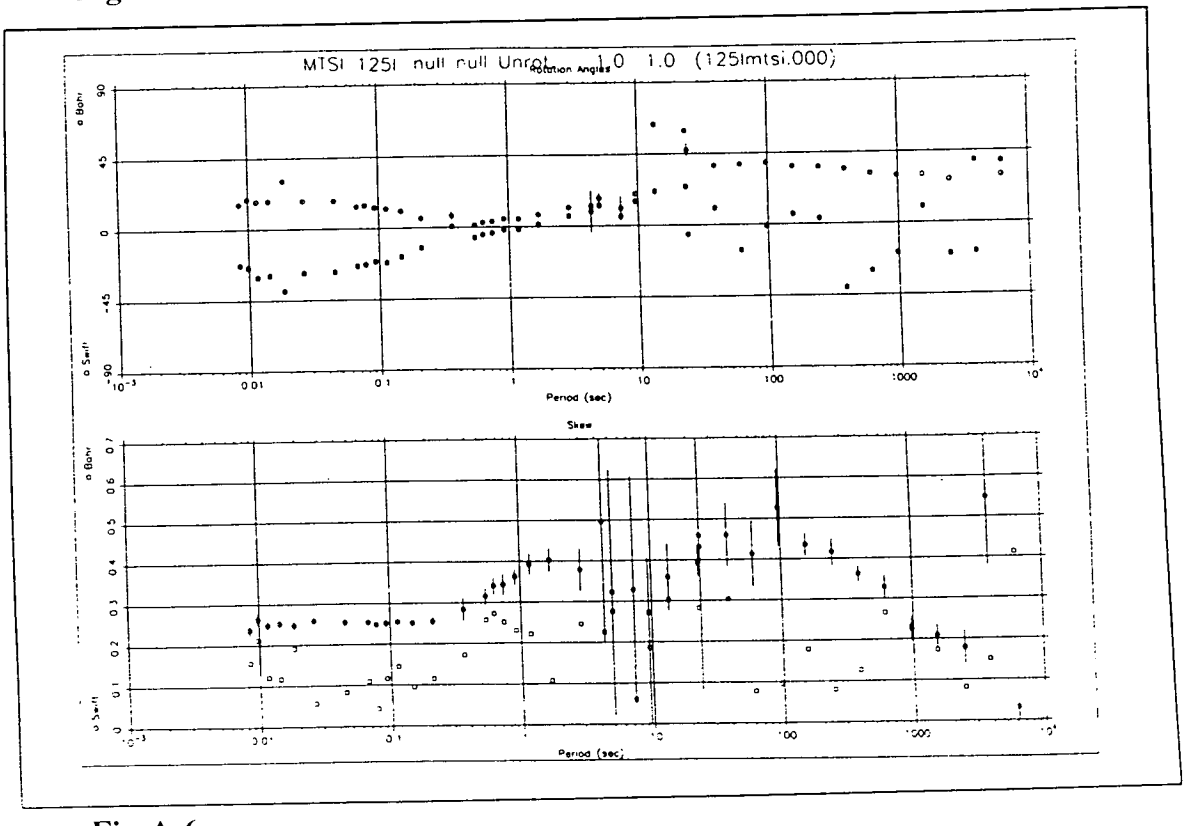
MTSI 125I null null Unrot 1.0 1.0 (125Imtsi.000)
Rotation Angles
Period (sec)
Skew
Period (sec)

Fig.A.6

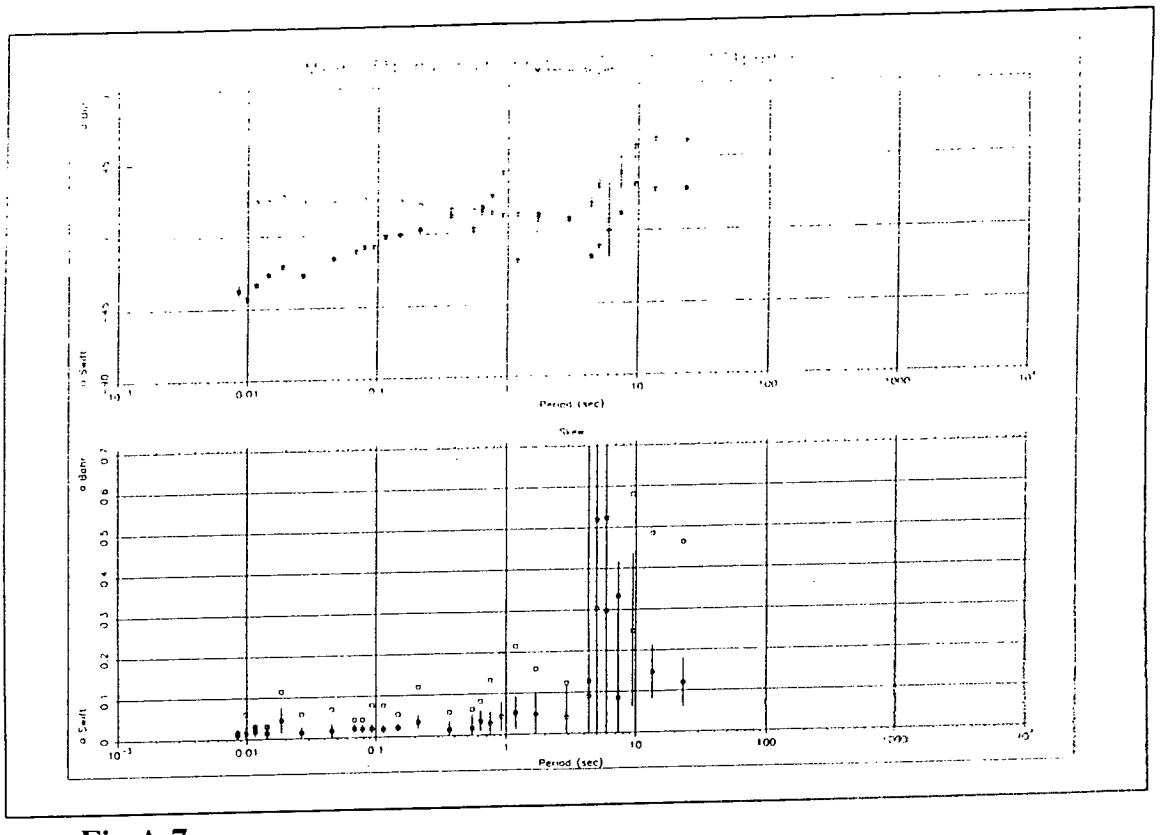
Period (sec)
Skew
Period (sec)

Fig.A.7

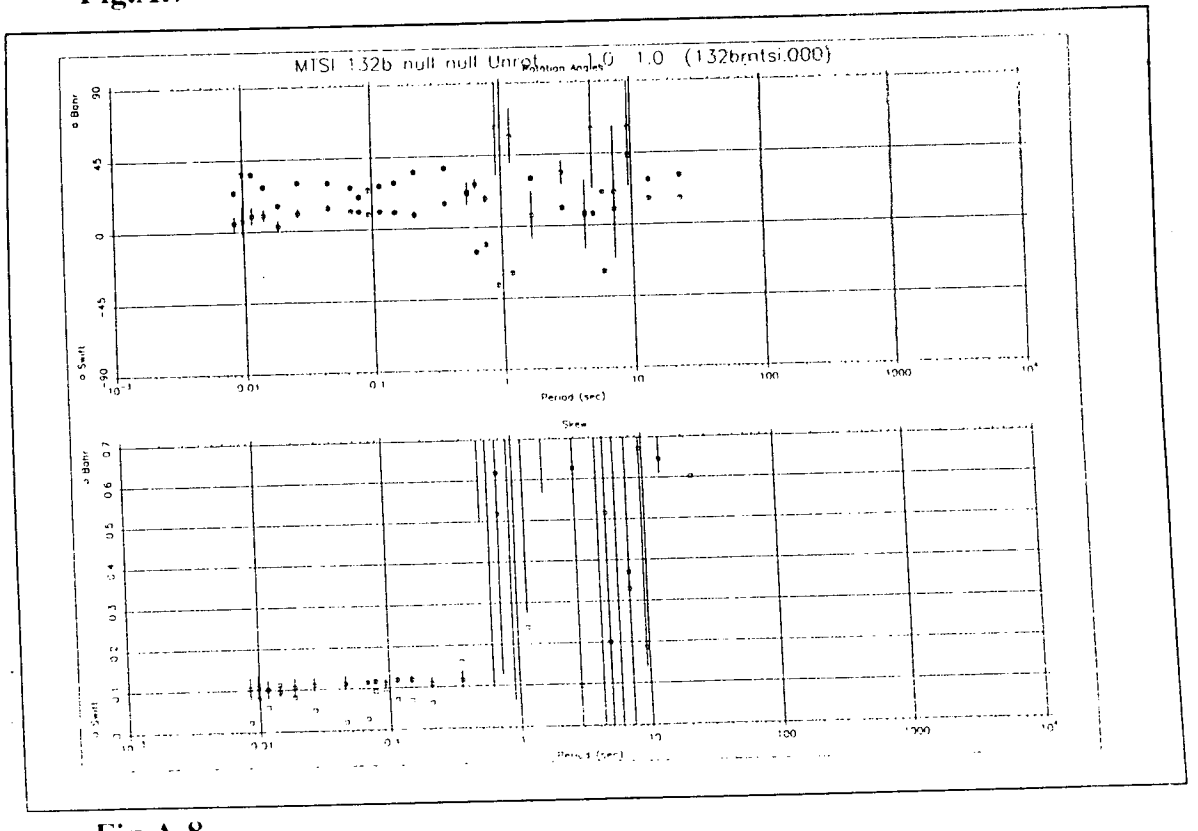
MTSI 132b null null Unrot 1.0 1.0 (132brntsi.000)
Rotation Angles
Period (sec)
Skew

Fig.A.8

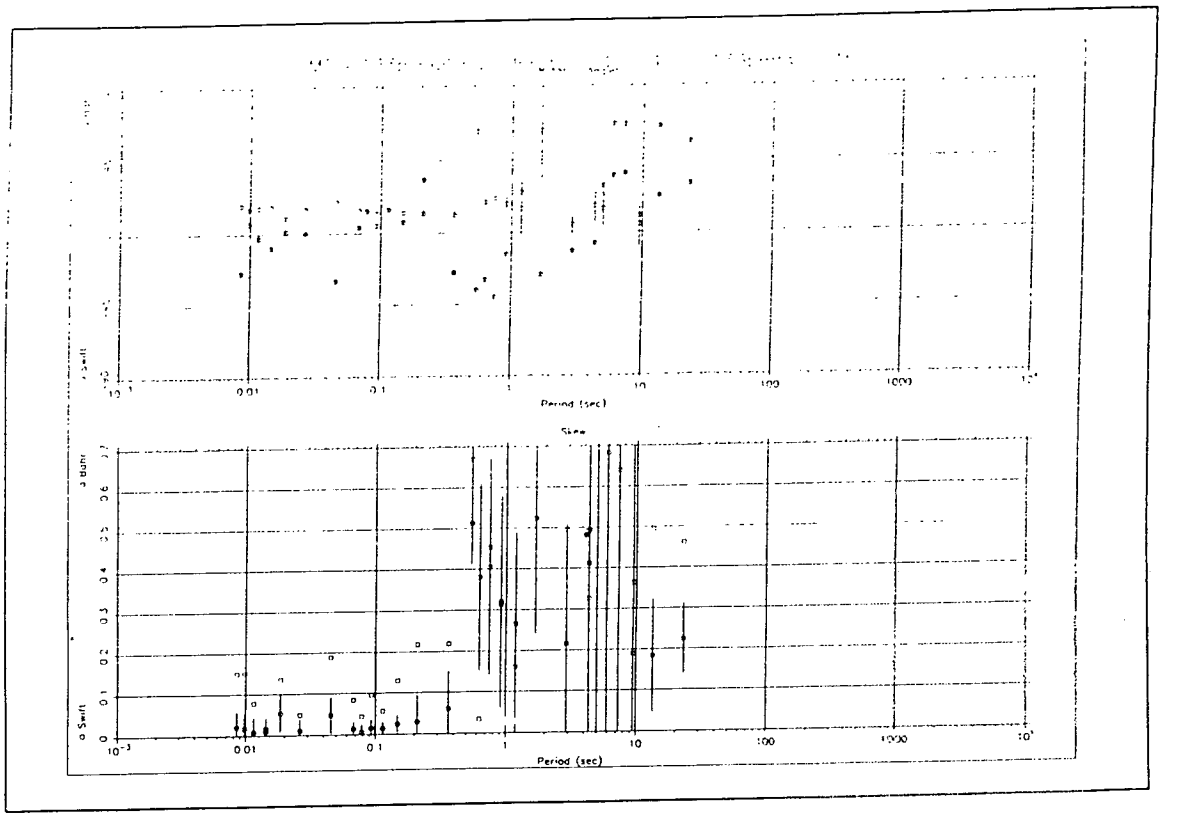

Fig.A.9

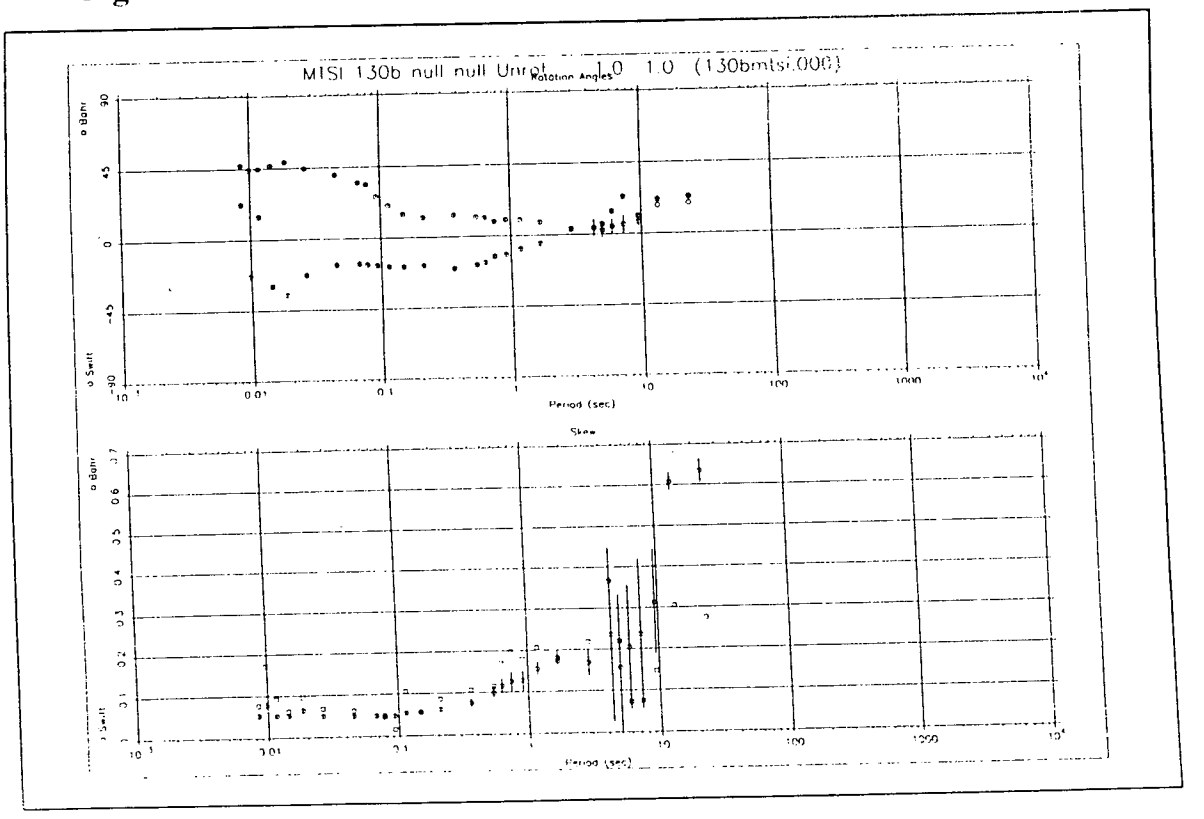

Fig.A.10

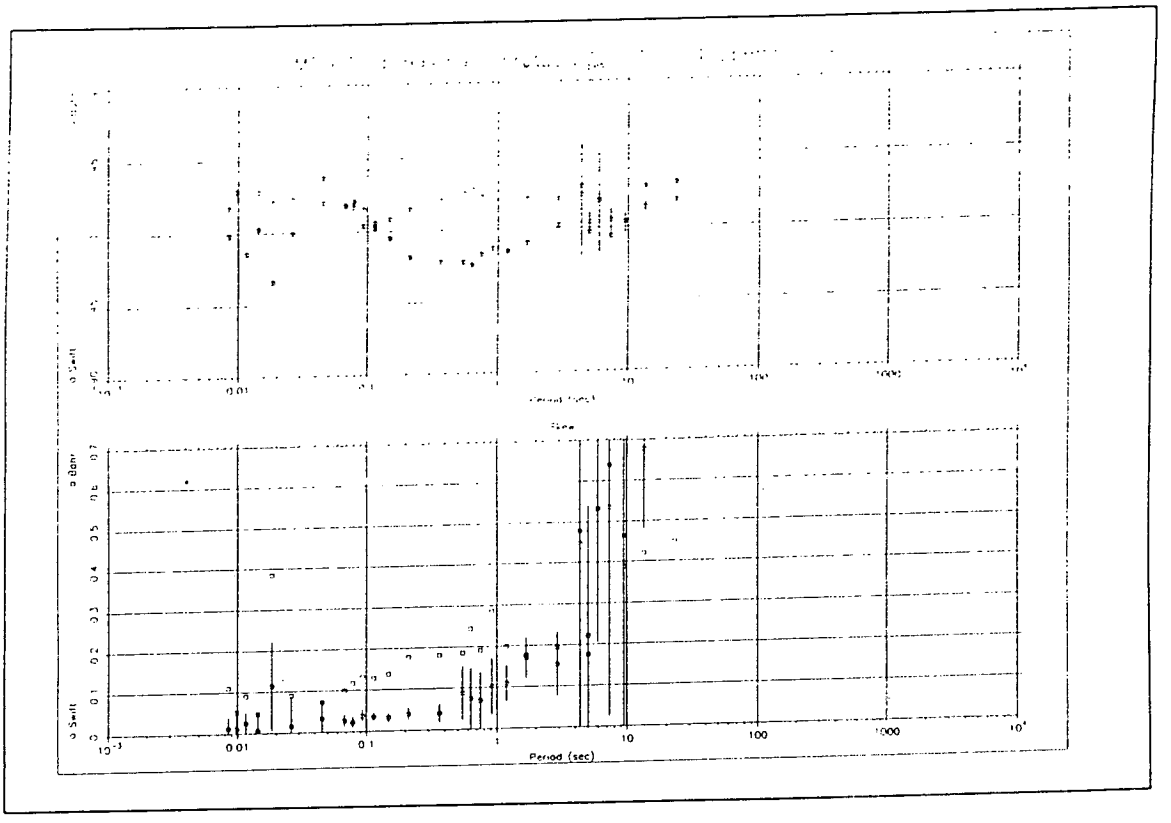

Fig.A.11

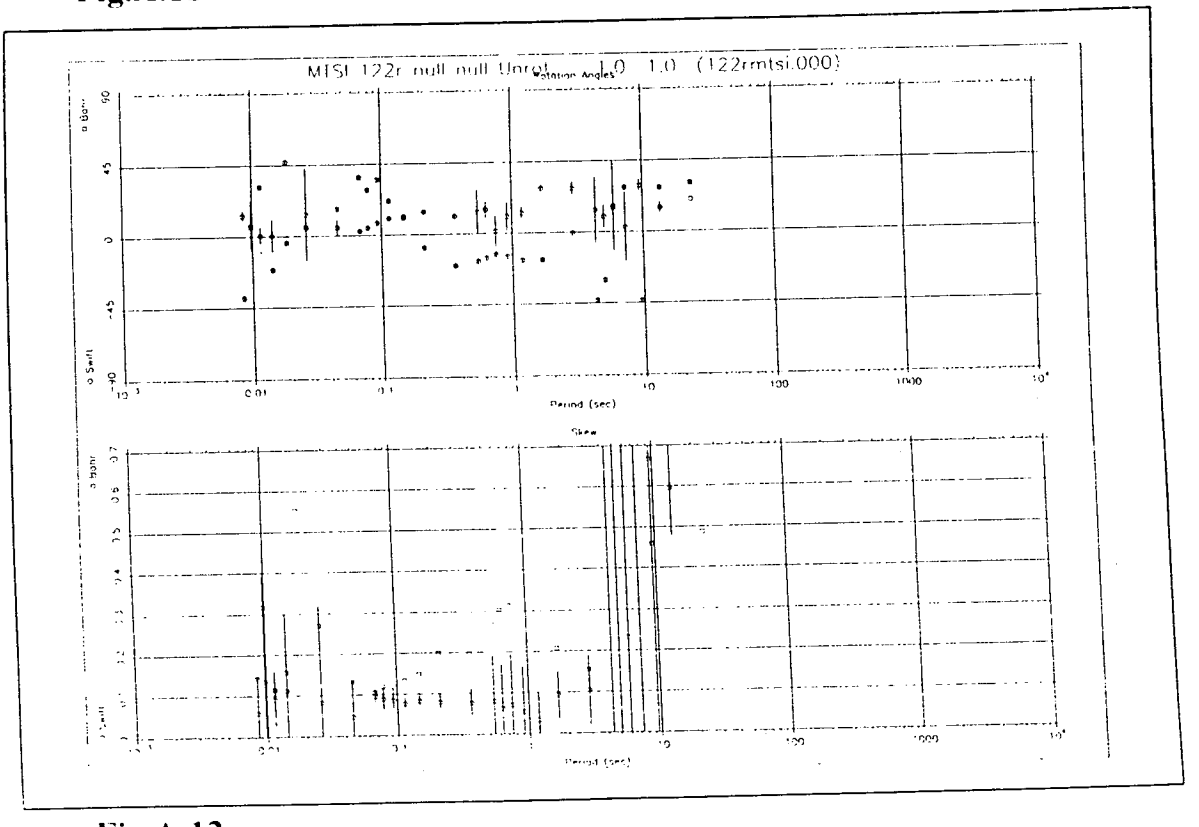

Fig.A.12

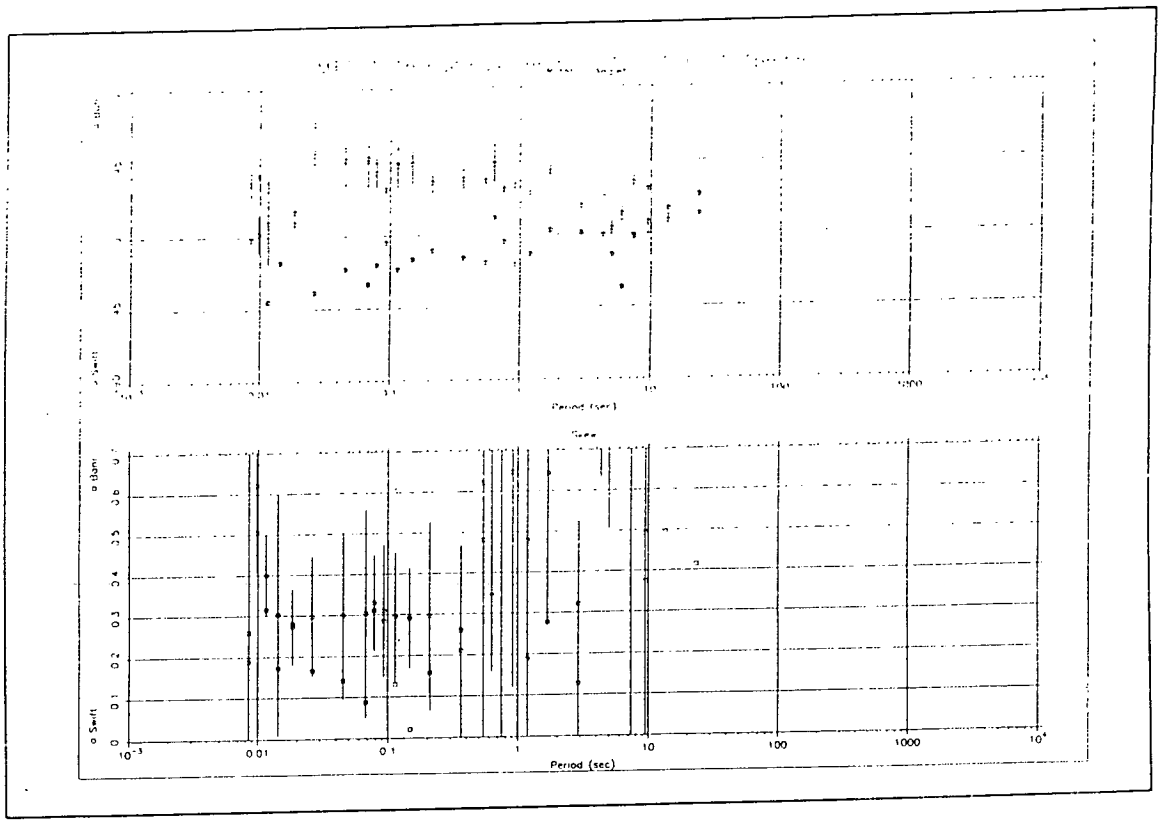

Fig.A.13

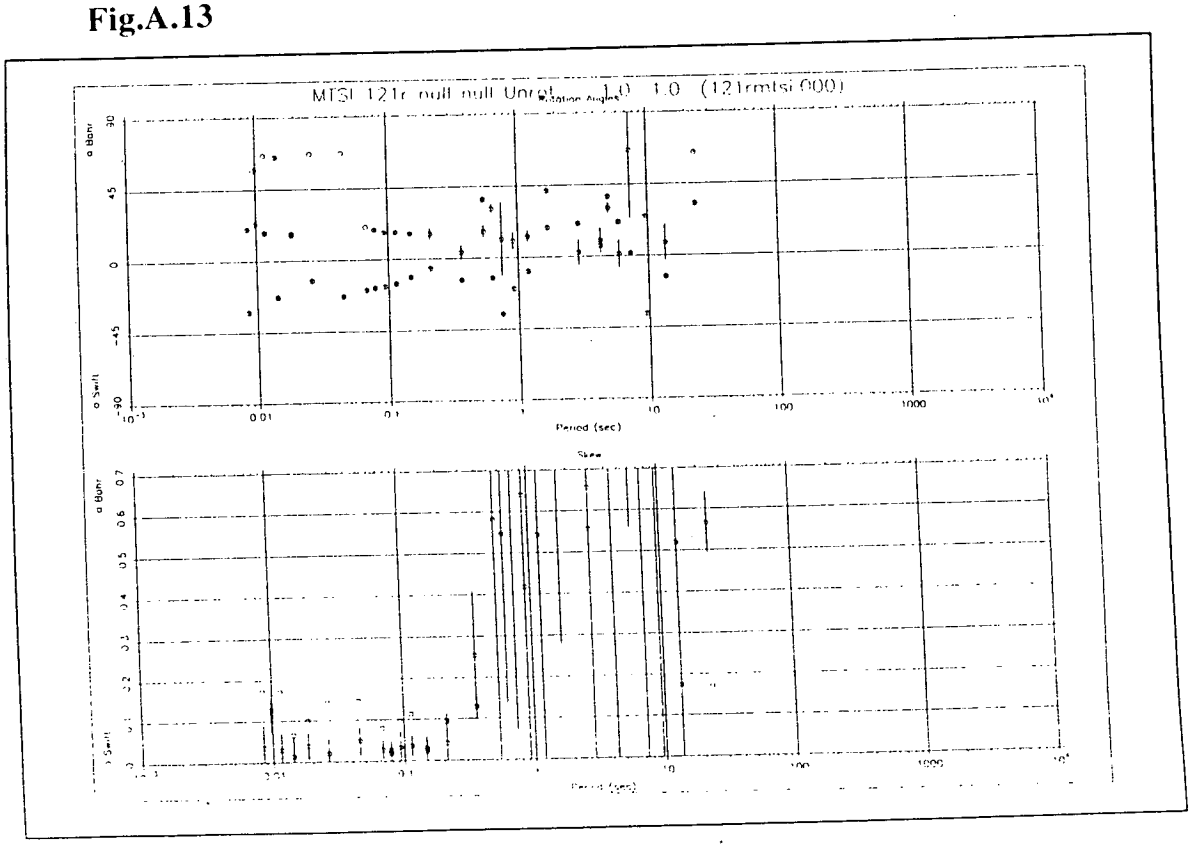

Fig.A.14

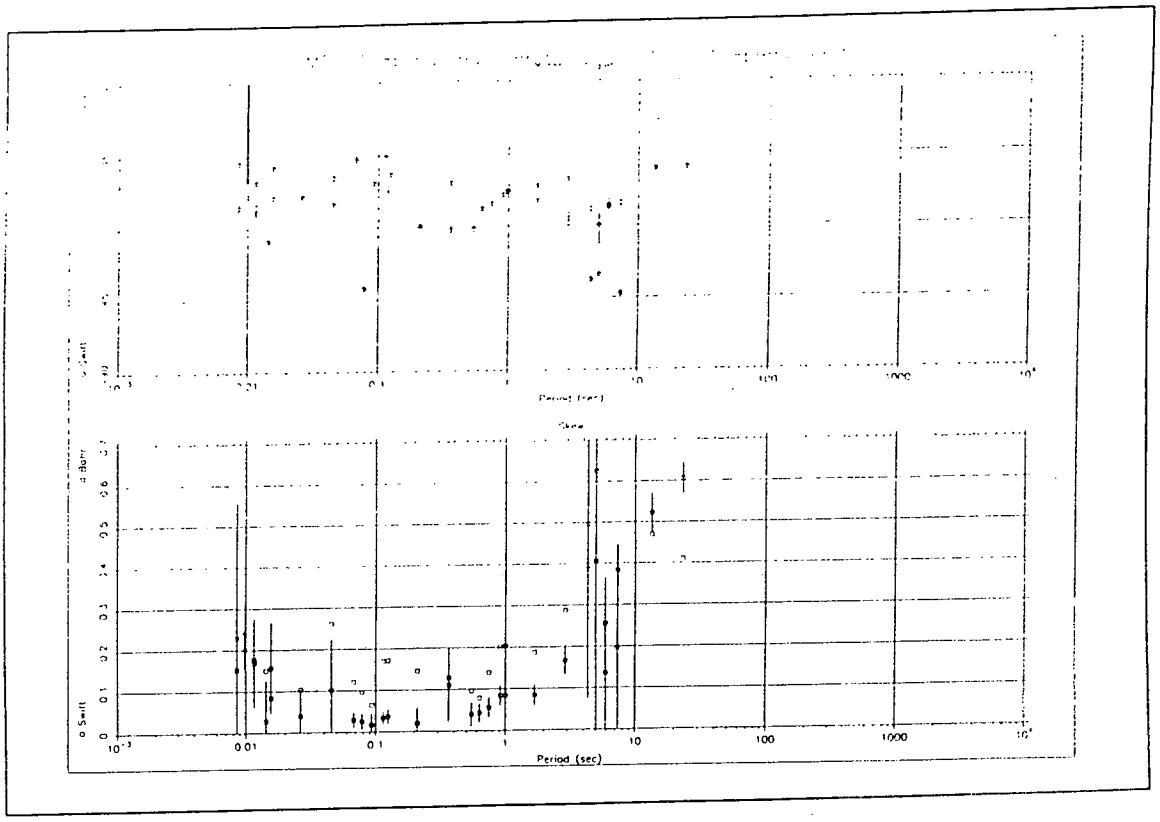

Fig.A.15

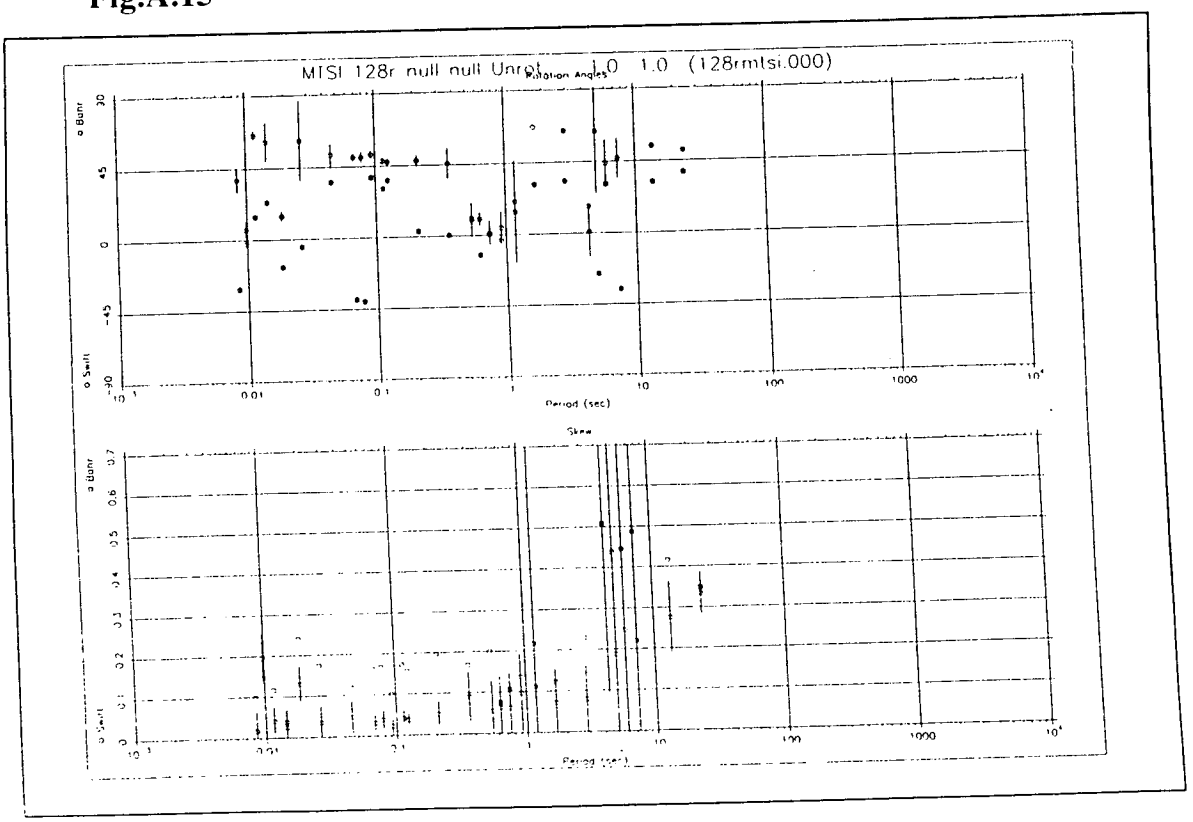

Fig.A.16

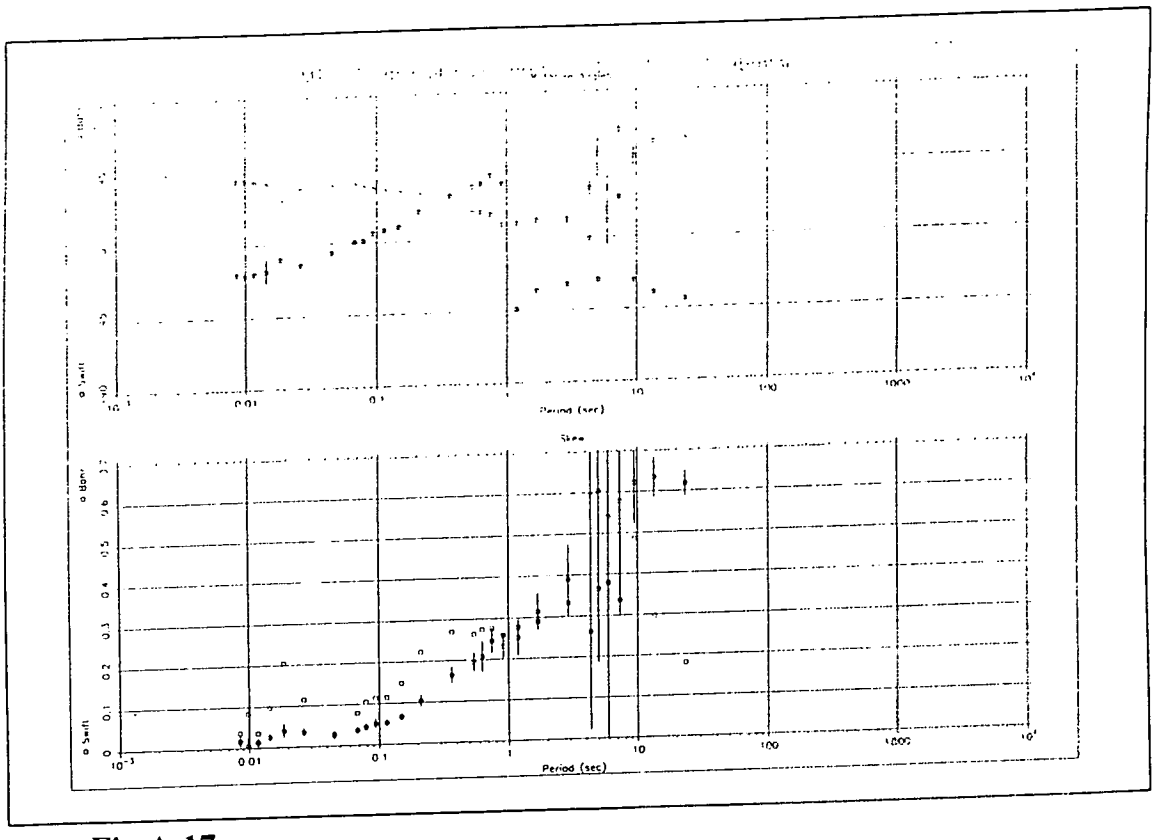

Fig.A.17

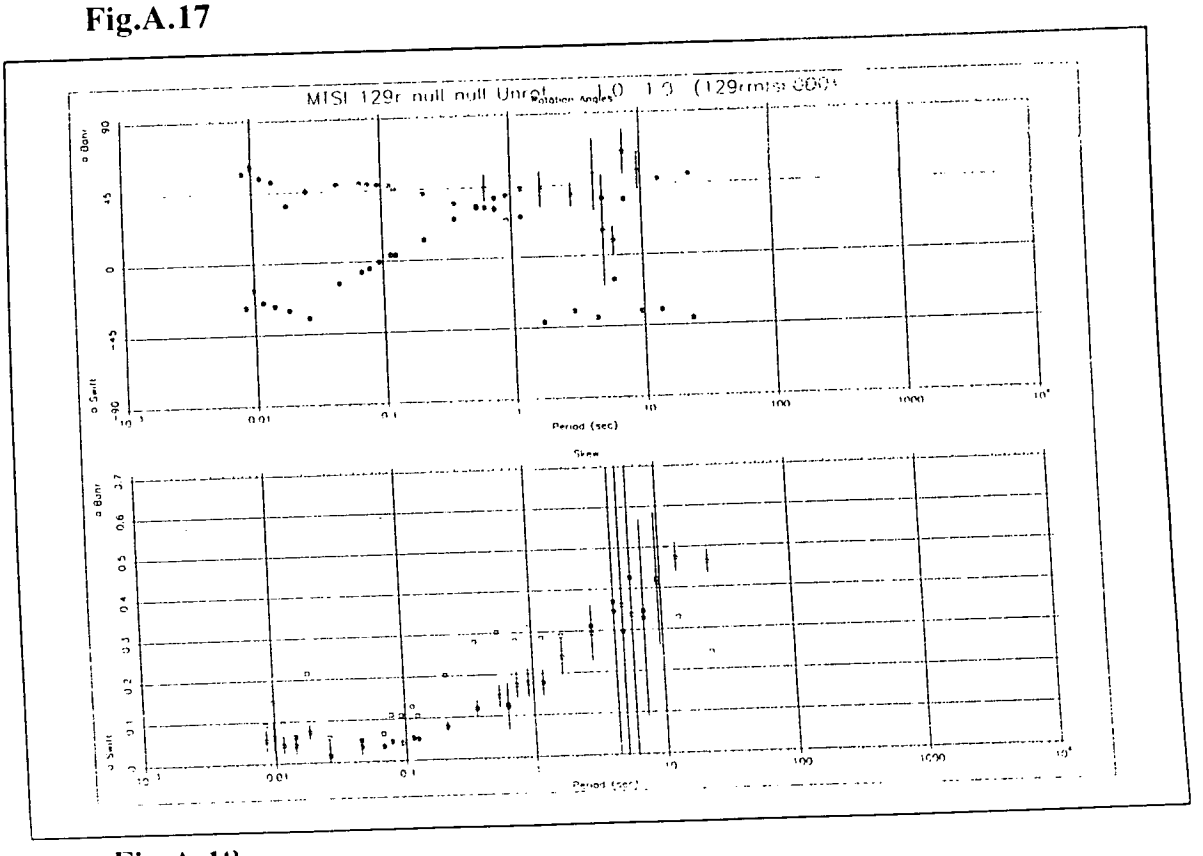

Fig.A.18

Figs.A.1-A.18: Azimuths and skew values as calculated by the methods of Swift and Bahr. **squares:** Bahr's values. **circles:** Swift's values. No errors are shown for Bahr's skew values.